UNIVERSITY OF SOUTHAMPTON

Faculty of Social and Human Sciences

School of Mathematics

Light–matter interaction in liquid crystal cells

by

Keith Richard Daly

A thesis submitted in partial fulfillment for the
degree of Doctor of Philosophy

January 2011

UNIVERSITY OF SOUTHAMPTON

ABSTRACT

FACULTY OF SOCIAL AND HUMAN SCIENCES
SCHOOL OF MATHEMATICS

Doctor of Philosophy

by Keith Richard Daly

In this thesis we study the interactions between light and matter in photorefractive liquid crystal cells. To model the liquid crystal alignment we develop a fast and accurate approximation of the normally stiff equations which minimise the Landau-deGennes free energy of a nematic liquid crystal. The resulting equations are suitable for all configurations in which defects are not present, making them ideal for device simulation. Specifically, they offer an increase in computational efficiency by a factor of 100 while maintaining an error of order (10^{-4}) when compared to the full stiff equations. As this approximation is based on a $\mathcal{Q}$–tensor formalism, the sign reversal symmetry of the liquid crystal is respected. We consider both the simplified case, where the director is restricted to a plane, and the full three-dimensional case. An approximation of the error is also given. We use the liquid crystal model to understand two different optical effects. The first of these is optical coupling. This effect is observed in liquid crystals in both the Bragg and Raman–Nath regimes. To account for this behaviour we develop an extension to the coupled wave theory which is suitable for all regimes of coupling. The model assumes that the refractive index grating, generated by the liquid crystal, has an arbitrary profile in one direction and is periodic (but not necessarily sinusoidal) in the other. Higher order diffracted terms are considered and appropriate mismatch terms dealt with. It is shown that this model is analytically equivalent to both the Bragg and Raman–Nath regime coupling models under an appropriate set of assumptions. This model is also verified through comparison to finite element simulations of Maxwell's equations. The second effect we model is the coupling of surface plasmon polaritons at the interface between a metal layer and a photorefractive liquid crystal cell. We implement existing numerical models to gain a thorough understanding of the system. These models are qualitatively compared with experimental observations. Analytic approximations to describe the coupling of surface plasmon polaritons at the surface of the liquid crystal cell are developed. These expressions provide a great deal of insight into the coupling mechanisms and will be of fundamental importance in optimising these systems.

Contents

List of Figures

List of Publications

1. K.R. Daly, G. D'Alessandro, and M. Kaczmarek. Regime independent coupled-wave equations in anisotropic photorefractive media. *Appl. Phys. B: Lasers Opt.*, 95(3):589–596, 2009.
2. K.R. Daly, G. D'Alessandro, and M. Kaczmarek. An efficient Q-tensor based algorithm for liquid crystal alignment away from defects. *SIAM Journal on Applied Mathematics*, 70:2844-2860, 2010.
3. M. Herrington, K.R. Daly, O. Buchnev, G. D'Alessandro, and M. Kaczmarek. Two–beam coupling in nematic crystals with an applied AC field. *Submitted to Optics Letters*, 2010.

DECLARATION OF AUTHORSHIP

I, **Keith Richard Daly**, declare that the thesis entitled **Light–matter interaction in liquid crystal cells** and the work presented in the thesis are both my own, and have been generated by me as the result of my own research. I confirm that:

- this work was done wholly or mainly while in candidature for a research degree at this University;
- if any part of this thesis has previously been submitted for a degree or any other qualification at this University or any other institution, this has been clearly stated;
- where I have consulted the published work of others, this is always clearly attributed;
- where I have quoted from the work of others, the source is always given. With the exception of such quotations this thesis entirely my own work;
- I have acknowledged all main sources of help;
- where the thesis is based on work done by myself jointly with others, I have made clear exactly what was done by others and what I have contributed myself;
- parts of this work have been published.

Signed:

Date: *7th January 2011*

Acknowledgements

First and foremost I would like to thank my supervisors; Dr Giampaolo D'Alessandro and Professor Malgosia Kaczmarek for giving me the opportunity to study applied mathematics at PhD level and for their help and guidance throughout my studies.

I would also like to acknowledge Professor Tim Sluckin, Dr David Chillingworth, Dr Ian Hawke and the liquid crystals group at UCL for help with the liquid crystal chapter, Mark Herrington, Dr Oleksandr Buchnev and Nina Podoliak for experimental input in the beam coupling chapter and Dr David Smith and Stephen Abbot for experimental input for the surface plasmons chapter.

A special thanks goes to my friends within the department. Particularly Chris Catt and Richard Slessor who were always willing to discuss problems and proof read sections of work.

Finally I would like to thank my fiancée Kathy for putting up with me throughout the PhD and feigning interest when I insist on discussing work.

To my fiancée Kathy …

Chapter 1

Introduction

This thesis is concerned with the interaction of electromagnetic fields with liquid crystals in photorefractive cells. These cells consist of a sample of liquid crystals sandwiched between two alignment layers, at least one of which is photoconductive, see Figure 1.1. The combination of light incident on the photoconductor and an applied DC electric field causes a change in the voltage applied to the liquid crystal layer. This realigns the liquid crystal causing apparent non-linear interactions between the liquid crystals and the incident optical field.

We have studied two different but related optical interactions, the second of which builds on the effects modelled in the first situation. The first is the coupling of energy between optical plane waves in a bulk liquid crystal cell. This effect is similar to photorefraction. The second effect is the propagation of optical surface waves, known as surface plasmon polaritons, at an interface between a liquid crystal cell and a metal. There are three main problems of interest in modelling these systems, each of which forms a chapter of this thesis. A formal introduction to the problems including a review of the relevant literature is given in the introduction of each chapter and a brief summary of each of the problems is given below.

1.1 Layout of Thesis

This thesis is arranged as follows: The remainder of this chapter provides a brief introduction to Maxwell's equations which are used to determine the electric field distribution in the liquid crystal cell and relevant for the optical modelling in the later chapters.

In Chapter 2 we consider the modelling of the alignment of liquid crystals under the influence of an applied electric field. Whilst powerful numerical tools exist [1], these involve finding the solution to a set of stiff non-linear coupled partial differential equations. The numerical stiffness is due to the separation in time scales between the elastic and temperature dependent properties of the liquid crystal. Under appropriate assumptions, relevant for a photorefractive liquid crystal cell, an approximate set of equations are developed. This method, based on a perturbation

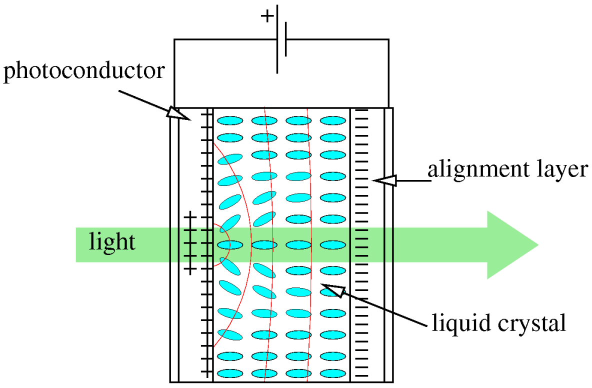

FIGURE 1.1: *Schematic of a photorefractive liquid crystal cell: A layer of liquid crystals is sandwiched between two alignment layers, one of which is a photoconductor. A DC electric potential is applied to the cell creating an electric field which aligns the liquid crystal. This alignment can be altered by application of a spatially varying optical field. This changes the conductivity of the alignment layer and, hence, the electric field in the cell and the liquid crystal alignment.*

expansion technique, offers an increase in computational efficiency by a factor of 100 whilst maintaining an error of order (10^{-4}) when compared to the full stiff equations. Derivations and numerical verification is given for both the simplified case where the liquid crystal is restricted to a plane and the more general case where the liquid crystal alignment is unrestricted.

Chapters 3 and 4 describe two different, but related, optical effects observed in liquid crystal cells. Chapter 3 considers the modelling of the photorefractive–like coupling observed in the bulk liquid crystal cell. The interference of two beams in the photoconducting layer of the cell produces a conductivity modulation. Combined with an applied DC field the electric field in the cell becomes spatially modulated with fundamental period equal to the pitch of the interference pattern of the two beams. The effect of this is to align the liquid crystal periodically and create a refractive index grating which scatters each of the two beams into a discrete set of directions. This is modelled using a multiple scales expansion technique. The resulting equations prove to be fast and accurate when compared to existing models and to finite element simulations of Maxwell's equations. Some predictions of the model are analysed in detail and suggestions for improving the performance of the system are considered.

The final problem, considered in Chapter 4, is the plasmonic diffraction at the surface of the photorefractive cell. Adding a thin gold layer adjacent to the photoconductor allows the photorefractive liquid crystal cell to support surface plasmon polaritons. These surface waves are of fundamental importance in many optical applications and are limited by their short propagation length. To overcome this energy can be pumped into the plasmons using a refractive index grating. To gain an understanding of the system a numerical model is developed based on existing techniques [2]. The resulting code allows us to probe the effects of different parameters on the system. Analytic tools, based on the equations from Chapter 3, are developed and compared to the numerical model. The resulting models will be of fundamental importance in the optimisation of these systems.

Finally, in Chapter 5, we provide a summary of the work done in this thesis and conclude by considering possible future work and addressing open questions raised by the preceding chapters.

A copy of each of the publications which have come from this work are included at the end of this thesis.

1.2 Maxwell's equations

The majority of Chapters 3 and 4, and small sections of Chapter 2, make frequent use of Maxwell's equations. Here we provide the briefest of introductions to these equations. Further information, including a historical introduction can be found in the opening chapters of Born and Wolf [3]. Maxwell's equations are the fundamental laws of electromagnetism and are comprised of four linear partial differential equations. These may be summarised as follows: Faraday's law of induction, first published in 1831 ,

$$\boldsymbol{\nabla} \times \boldsymbol{E}(\boldsymbol{x}, t) = -\frac{\partial \boldsymbol{B}(\boldsymbol{x}, t)}{\partial t}, \tag{1.1a}$$

Ampère's circuital law, published in 1826 and extended by Maxwell in 1861,

$$\boldsymbol{\nabla} \times \boldsymbol{H}(\boldsymbol{x}, t) = \frac{\partial \boldsymbol{D}(\boldsymbol{x}, t)}{\partial t} + \boldsymbol{J}(\boldsymbol{x}, t), \tag{1.1b}$$

Gauss' law applied to electrostatics, derived in 1835 but not published until 1867,

$$\boldsymbol{\nabla} \cdot \boldsymbol{D} = \rho \tag{1.1c}$$

and the corresponding law for magnetism

$$\boldsymbol{\nabla} \cdot \boldsymbol{B} = 0. \tag{1.1d}$$

Here $\boldsymbol{E}$ is the electric field, $\boldsymbol{D}$ is the electric displacement, $\boldsymbol{H}$ is the magnetic field, $\boldsymbol{B}$ is the magnetic induction, $\boldsymbol{J}$ is the free current density and ρ is the free charge density. These fundamental quantities are related by the materials equations $\boldsymbol{D} = \epsilon \boldsymbol{E}$, $\boldsymbol{B} = \mu \boldsymbol{H}$ and $\boldsymbol{J} = \sigma \boldsymbol{E}$. The quantities ϵ, μ and σ are the dielectric constant (or permittivity), permeability and conductivity respectively. These equations are exact under the assumption that the photon mass is zero. The error induced by a non-zero rest mass is observed in deviations from the $1/r^2$ predicted by Gauss' law for the dependence of electric field at a distance r from a point charge. To first order, this error is approximated with a $1/r^{2+q}$ dependence. The exact value of q is undetermined however bounds have been established by means of null experiments, for a review see [4]. The current upper bound, $q = (2.7 \pm 3.1) \times 10^{-16}$, was established in 1971 by Williams et al [5]. This degree of accuracy means, for the systems studied in this thesis, that Maxwell's equations may be considered exact.

In the majority of cases considered here we are interested in travelling wave solutions in the absence of free charges and free currents. Therefore, an explicit time dependence $e^{-i\omega t}$ is assumed, where ω is the optical angular frequency. On substitution into Maxwell's equations we obtain the simplified relations for the electric and magnetic fields,

$$\begin{aligned} \boldsymbol{\nabla} \times \boldsymbol{H} &= i\omega\epsilon\boldsymbol{E}, & \boldsymbol{\nabla} \times \boldsymbol{E} &= -i\omega\mu\boldsymbol{H}, \\ \boldsymbol{\nabla} \cdot \epsilon\boldsymbol{E} &= 0, & \boldsymbol{\nabla} \cdot \mu\boldsymbol{H} &= 0. \end{aligned} \tag{1.2}$$

From these equations it is clear that only the first two equations need to be solved. In Chapter 4 we will see that, under certain assumptions, this statement also holds for conductive materials. Therefore, throughout this thesis we generally need only consider Maxwell's curl equations.

For travelling wave solutions it is often easier to deal with the wave equation. This is derived from Maxwell's equations by taking the curl of either Faraday's law or Ampère's law,

$$\boldsymbol{\nabla} \times \boldsymbol{\nabla} \times \boldsymbol{E} = \omega^2\mu\epsilon\boldsymbol{E} \tag{1.3}$$

and will be used to model wave propagation throughout this thesis. In general the materials constants can be written as $\epsilon = \epsilon_0\epsilon_r$ and $\mu = \mu_0\mu_r$ where ϵ_0 and μ_0 are the permittivity and permeability of free space which define the speed of light $c = 1/\sqrt{\epsilon_0\mu_0}$. As the materials considered here are non-magnetic $\mu_r = 1$. For anisotropic materials, such as the liquid crystal, ϵ_r is a tensor function of frequency, space and time. Here the spatial and temporal dependences are determined by the alignment properties of the liquid crystal. From equations (1.3) it can be seen that there is a coupling between a materials dielectric properties and the electromagnetic field. This coupling enables the control of optical fields using a liquid crystal cell and is the basis for all liquid crystal optics.

Chapter 2

An efficient algorithm for liquid crystal alignment away from defects

In this chapter we use perturbation techniques to develop a new approximate method which can be used to calculate the alignment of liquid crystals. The resulting equations are suitable for all configurations in which defects are not present, making them ideal for device simulation. This method, which is based around the widely used Landau–deGennes (LdG) phenomenological description of liquid crystals, is shown to be both accurate and computationally efficient. Specifically the approximation offers an increase in computational efficiency by a factor of 100 whilst maintaining an error of order (10^{-4}) when compared to the full LdG model.

This chapter is arranged as follows: In Section 2.1 we provide an introduction to liquid crystals and existing modelling methods. In Section 2.2 we derive the Frank Oseen (FO) model for liquid crystal alignment restricted to a plane. This will be used in comparison to the approximation derived here. In Section 2.3 we introduce the equations governing the LdG free energy of the liquid crystal and make an analogy between our approximation method and the Signorini method originally developed in elasticity [6, 7, 8]. In Section 2.4, to illustrate the method, we derive a simplified two dimensional model for the case where liquid crystal alignment is restricted to a plane. Equations for alignment are given and an estimate of the accuracy of the method is derived. In Section 2.5 we apply the ideas and methods used in the two dimensional case to derive equations for the three dimensional case. A method to approximate the error is also given. Finally, Section 2.6 details comparisons with the FO and LdG models that show that the approximation we derive is both computationally fast and accurate.

2.1 Introduction

The liquid crystalline phase is a state of matter which exists between the isotropic liquid phase and the crystalline solid phase. As such the liquid crystal phase has properties of both solids and

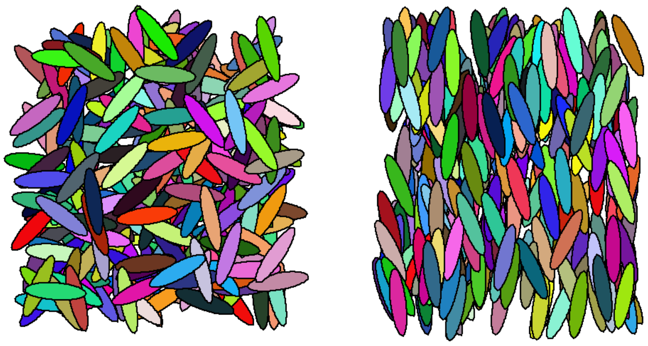

FIGURE 2.1: *Phases of matter. The left hand image shows the isotropic liquid phase, the molecules are randomly positioned with random alignment. The right hand image shows the nematic liquid crystal phase. As in the isotropic phase the molecules are randomly positioned, however, they have a degree of orientational order.*

liquids. Specifically, liquid crystals can flow like a liquid, however, they have a degree of orientational ordering to their molecular structure similar to a solid, see Figure 2.1. Materials which exhibit a liquid crystalline phase have effectively two melting points, the point at which they transform from solid to liquid crystal and the point at which they transform from liquid crystal to liquid. The high molecular ordering of the liquid crystal phase gives them a large optical and dielectric anisotropy. Coupled with their strong electro–optic response this has lead to the successful application of liquid crystals in display technology, for a review see [9]. These properties can also be used in a wide variety of linear and non-linear optical devices. The modelling and simulation of liquid crystal alignment for device purposes is an active area of research with a wide variety of applications [10, 11]. In this chapter we use perturbation techniques to develop a new approximate method which can be used to calculate the alignment of liquid crystals.

A comprehensive history of liquid crystals is beyond the scope of this thesis. A detailed historical review can be found in [12]. Here we wish to simply highlight important milestones in the development of liquid crystal modelling. Liquid crystals were originally discovered by Friedrich Reinitzer in 1888 [13, 14]. Reinitzer observed that certain cholesterol exhibit two melting points. The liquid crystalline nature of these materials was confirmed through microscopy measurements by Lehmann [15, 16] who also observed materials with two or three melting points. Whilst Lehmann observed the multiple melting points he did not realise that this constituted a new phase of matter. It was not until 1922 that liquid crystals were recognised as a fourth phase of matter [17, 18]. It is this paper by Friedel in which much of the present terminology is introduced. Friedel introduced the term mesophases to describe liquid crystalline materials and observed that these can be further categorised into Nematic, Cholesteric and Smectic phases. He also recognised that cholesteric phases are chiral Nematic phases and predicted that Smectic phases form layers, this was later verified by x–ray diffraction [19, 20]. The main phases of interest for device application are the Nematic and Smectic phases, of which the most commonly used are the nematic phases. Therefore we will concentrate on these for the remainder of this chapter.

Liquid crystals can be further classified into two different groups, thermotropic and lyotropic. The liquid crystals discovered by Reinitzer are thermotropic liquid crystals, these are materials which form liquid crystal phases due to temperature. Lyotropic liquid crystals are materials which form liquid crystal phases due to changes in concentration, see [12], and are of interest in biophysics and biochemistry. Throughout this thesis we will only be concerned with thermotropic liquid crystals and will not discuss lyotropic liquid crystals further.

The alignment of liquid crystals by electromagnetic fields is one of their key properties which makes them useful in device applications. The orientation of liquid crystals by a magnetic field was first observed by Mauguin in 1911 [21]. He observed that samples of liquid crystals sandwiched between two glass layers could be made to align such that they were optically homogeneous by application of a magnetic field in the direction normal to the glass layers. The alignment of liquid crystal reorientation driven by an electric field was first reported in 1904, for details see [12]. One of the most important discoveries relating to the electromagnetic response of liquid crystals was the threshold behaviour displayed by liquid crystals. That is, for a sample of liquid crystals between two glass plates with defined alignment at the boundaries there is a threshold field above which the elastic alignment energy of the liquid crystal is overcome and the liquid crystal will align to the applied field. This effect is known as the Frederiks transition and was first quantified in 1929 [22].

The most successful and well known application of this alignment effect is the twisted nematic cell used in liquid crystal displays. The invention of this devices, which builds on a great deal of previous theoretical and experimental work, is usually attributed to Schadt and Helfrich [23]. The cells consist of liquid crystals sandwiched between two glass plates. Alignment treatments are applied to the glass plates such that the liquid crystal is aligned in the plane of the glass plates at each interface, however, there is a 90 degree twist in alignment between the two. Between crossed polarisers this device will appear transparent. When a voltage is applied the liquid crystals will realign. For a sufficiently large voltage [24] the twisted structure within the cell is broken and the cell becomes opaque

The mathematical modelling of liquid crystals falls into two main categories, the molecular field theories and the continuum theories. Molecular field theories, such as the theory developed by Maier and Saupe in 1958 [25, 26], concentrate on the intermolecular forces and degree of order for a sample of liquid crystals. Such theories involve writing down the intermolecular interactions between a pair of molecules before averaging over a large sample. Continuum theories make use of phenomenological expressions to describe the free energy of a liquid crystal sample, these theories began with the work of Oseen in 1933 [27] and Frank in 1958 [28]. Both continuum and molecular field theories provide different insights into the behaviour of liquid crystals and attempts have been made to align the two [29, 30]. In this thesis we are concerned with the alignment of liquid crystals to electric fields rather than detailed studies on the molecular level. Therefore we make use of the continuum theories and will not consider the molecular field theories further.

FIGURE 2.2: *The three common liquid crystal disclinations, all of which have a different elastic constant. The left hand image shows the splay disclination, this has elastic constant* K_1*. The middle image shows the twist disclination, this has the elastic constant* K_2*. The right hand image shows the bend disclination, this has elastic constant* K_3*.*

The original theories put forward by Frank and Oseen are static theories, these describes the liquid crystal in terms of a unit vector $\hat{\boldsymbol{n}}$, also referred to as the director. The equilibrium alignment of the liquid crystal is found by associating a free energy to the liquid crystal in terms of the various possible disclinations, see Figure 2.2, The resulting free energy is minimised in terms of the director orientation angles. These theories were developed and reformulated by Ericksen [31] in 1962. The dynamic theories of liquid crystals began in the early 60s with a theory developed by Ericksen [32]. However, this theory proved too simplistic to describe the dynamics of a liquid crystal cell. In 1966 Leslie published his first paper on the dynamical theory of liquid crystals [33]. However, this theory failed to reduce to the Ericksen reformulation of the FO model in the static limit. In 1968 Leslie published a second paper, in which he added contributions from the elastic interactions between liquid crystals [34]. This time the theory did reduce to the static model in the appropriate limit. This model is computationally very efficient. However, although the vector representation of the liquid crystal may be considered quite intuitive, it is physically incorrect as it does not respect the inversion symmetry of the liquid crystal, i.e. $\hat{\boldsymbol{n}}$ and $-\hat{\boldsymbol{n}}$ represent the same state of the liquid crystal. This limits the application of the FO model to geometries in which the liquid crystal orientation angle is bounded between 0 and $\pi/2$. Further, the microscopic order of the nematic phase, which depends on temperature, is not considered. This makes the model unsuitable for geometries in which defects, non smooth variations in $\hat{\boldsymbol{n}}$, can occur.

To overcome these problems an approach was developed by deGennes in which the liquid crystal alignment is represented by a tensor, $\mathcal{Q}$ which is proportional to $\hat{\boldsymbol{n}}\otimes\hat{\boldsymbol{n}}$ [26, 35]. This tensor is invariant with respect to the transformation $\hat{\boldsymbol{n}} \rightarrow -\hat{\boldsymbol{n}}$. Further, this theory takes into account the orientational order of the liquid crystal through the temperature dependent bulk energy, sometimes referred to as the thermotropic energy, and can therefore be used to describe situations in which defects, occur. The direct solution of the Euler-Lagrange equations which minimises this free energy requires the integration of 9 coupled non–linear PDE's. This can be simplified through the method of Schopohl and Sluckin [36] who used Lagrange multipliers to impose the traceless symmetric properties of the system. Direct elimination of the Lagrange multipliers reduces the dimension of the problem to 5. Alternatively the method of Sonnet can be used [37]. This method involves writing the free energy on the orthonormal basis of traceless symmetric tensors and again reduces the dimension of the problem to 5. These methods are commonly used in the numerical simulation of liquid crystal alignment to date. The main disadvantage of the LdG method is that, due to the difference in time scales between the thermotropic and elastic properties of the liquid crystals, the final equations are numerically stiff, making computation expensive.

Typically continuum theories involve writing down free energy expressions for the elastic, electrostatic, thermotropic and surface interactions in the liquid crystal cell. In the tensor based models these usually take the form of Landau power series expansions. Typically only the lowest order terms are retained. A great deal of work has been done to obtain the most general possible expressions for these energies. Expressions for the elastic and bulk free energies are invariant with respect to rotation of the sample and have been obtained up to $\mathcal{Q}^4$ [38, 39]. The surface free energy for a liquid crystal sample is present due to the non-infinite anchoring strength between the liquid crystal and the boundaries. The strength of this alignment is dependent on the method used to align the liquid crystals, for a review see [40]. Finite anchoring strength in director based models is usually based on the formalism of Rapini and Papoular [41] which was also described by Berreman [42, 43] and has been shown to give good agreement with experimental measures [44]. Anchoring strength in tensor based models has been described in the simplest possible case by Nobili [45]. Here the anchoring strength is assumed to be isotropic, i.e. the liquid crystal can move out of the plane of the boundary as easily as it can rotate in the plane. This theory provides a method of modelling finite anchoring strength. However, in general the anchoring strength will be anisotropic, i.e. the liquid crystal may move away from the interface plane more easily than it can twist in the plane. To overcome this anisotropic anchoring strengths have been considered [46]. These are based on a power series expansion where different penalty energies are associated with movement in and out of plane.

A great deal of work has gone into the study of continuum models. Some groups have produced detailed simulations regarding the structure of point defects, [47, 48], hedgehog configurations [49, 50, 51, 52] for a review see [53], disclination lines [54, 55, 56] and order reconstruction [48, 57]. Whilst other groups have worked on large scale numerical simulations, often based around finite element [1, 58, 59] or finite difference [60, 61] discretisation methods, of the continuum equations. The finite element models have proved highly successful and are used in a variety of optical applications [62, 63].

Often the advantages of using a $\mathcal{Q}$–tensor model outweigh the disadvantage of increased computation time. However, there are devices, such as photorefractive cells [64] or spatial light modulators [65], in which the FO model is inappropriate as the liquid crystals may rotate in an unbounded way. However, as there are no defects in these cells, the LdG $\mathcal{Q}$-tensor model is unnecessarily expensive to compute.

Numerical methods to overcome the stiffness of the full $\mathcal{Q}$ tensor equations include: The scaling of the elastic and electrostatic coefficients [66] and the renormalisation of the liquid crystal director after each time step [67]. Codes also exist which solve the full stiff equations. These are usually based around finite element simulations with adaptive meshing techniques to eliminate the need for dense grids away from defects [1, 46].

Although the separation in scales makes the $\mathcal{Q}$-tensor equations computationally expensive, the small parameters involved can be used to our advantage. In this chapter we develop a new approximation which uses a multiple scales expansion technique to separate the two time scales and overcome the numerical stiffness. On the timescale of interest, i.e. the slow reorientation time of the liquid crystal, the fast timescale equations, which determine the order parameter, can be considered as having reached equilibrium. The resulting equations for the slow timescale are non-stiff and can be solved in a fraction of the time of the full equations. This approximation reduces the computation time by a factor of approximately 100 and is suitable for any geometry in which the variation in the scalar order parameter may be assumed to be small.

2.2 Frank–Oseen director model

2.2.1 Free energy

The FO free energy of a liquid crystal sample is given by $\tilde{\mathcal{F}}(\hat{\boldsymbol{n}}) = \tilde{\mathcal{F}}_d(\hat{\boldsymbol{n}}) + \tilde{\mathcal{F}}_e(\hat{\boldsymbol{n}})$, where $\tilde{\mathcal{F}}_d$ is the elastic free energy and $\tilde{\mathcal{F}}_e$ is the electrostatic free energy. We model the orientation of the liquid crystal on a macroscopic level in terms of a unit director $\hat{\boldsymbol{n}}$, which tells us the average alignment of liquid crystal molecules over a small sample. Typically this is written in terms of polar coordinates

$$\hat{\boldsymbol{n}} = \begin{pmatrix} \sin\theta_{FO}\cos\phi_{FO} \\ \sin\theta_{FO}\sin\phi_{FO} \\ \cos\theta_{FO} \end{pmatrix}, \tag{2.1}$$

where θ_{FO} and ϕ_{FO} are the standard spherical coordinate angles.

The elastic free energy is modelled in terms of the FO free energy expression [27, 28],

$$\tilde{\mathcal{F}}_d = \frac{1}{2}K_1\left[\boldsymbol{\nabla}\cdot\hat{\boldsymbol{n}}\right]^2 + \frac{1}{2}K_2\left[\hat{\boldsymbol{n}}\cdot\left(\boldsymbol{\nabla}\times\hat{\boldsymbol{n}}\right)\right]^2 + \frac{1}{2}K_3|\hat{\boldsymbol{n}}\times\left(\boldsymbol{\nabla}\times\hat{\boldsymbol{n}}\right)|^2, \tag{2.2}$$

where K_1, K_2, K_3 are the splay, twist and bend elastic constants respectively, see Figure 2.2. To model alignment in the most general case all three of these elastic constants are needed. However, our purpous is to give the simplest possible derivation of the FO model such that it is suitable for comparison with the $\mathcal{Q}$ tensor approach. Therefore, to simplify the derivation we use the one elastic constant approximation, $K_j = K$, where $j = 1, 2, 3$. For an appropriate geometry the liquid crystal orientation is restricted to the x, z plane (see Figure 3.1). As such we may assume our system to be twist free, $\phi_{FO} = 0$. Substituting the director expression (2.1) into the Oseen Frank free energy expression (2.2) yields:

$$\tilde{\mathcal{F}}_d = \frac{K}{2}\left(\boldsymbol{\nabla}\theta_{FO}\right)^2. \tag{2.3}$$

The second part of the free energy is the electrostatic free energy which is derived by substituting the expression for the dielectric tensor

$$\epsilon_{ij} = \epsilon_u \delta_{ij} + \Delta\epsilon \left(\hat{n}_i \hat{n}_j - \frac{\delta_{ij}}{3} \right) \tag{2.4}$$

into the expression for electrostatic energy

$$\tilde{\mathcal{F}}_e = -\frac{1}{2}\epsilon_0 \epsilon_{ij} \partial_i \tilde{\psi} \partial_j \tilde{\psi}, \tag{2.5}$$

where $\tilde{\psi}$ is the electric potential throughout the cell and

$$\Delta\epsilon = \epsilon_{||} - \epsilon_{\perp}, \qquad \epsilon_u = \frac{\epsilon_{||} + 2\epsilon_{\perp}}{3}. \tag{2.6}$$

Retaining only terms which depend on the alignment gives the electrostatic energy for the liquid crystal cell

$$\tilde{\mathcal{F}}_e = -\frac{1}{2}\epsilon_0 \Delta\epsilon \left(\boldsymbol{\nabla}\tilde{\psi} \cdot \hat{\boldsymbol{n}} \right)^2. \tag{2.7}$$

The total free energy is the sum of the expressions for elastic energy (2.3) and electrostatic energy (2.7). We non-dimensionalise it to obtain

$$\mathcal{F} = \frac{1}{2}\left(\boldsymbol{\nabla}\theta_{FO}\right)^2 - \frac{1}{2}\chi_{FO}\left(\boldsymbol{\nabla}\psi \cdot \hat{\boldsymbol{n}}\right)^2, \tag{2.8}$$

where $\chi_{FO} = \dfrac{\epsilon_0 \Delta\epsilon}{K}\psi_0^2$ and ψ_0 is a constant potential which non-dimensionalises the system, $\psi = \tilde{\psi}/\psi_0$. The liquid crystal alignment can now be determined by minimising equation (2.8) in terms of θ_{FO}. To minimise the free energy over the whole domain we substitute equation (2.8) into the Euler–Lagrange equation

$$\frac{\partial F}{\partial y_n} - \partial_i \frac{\partial F}{\partial(\partial_i y_n)} = 0, \tag{2.9}$$

where $i = x, y, z$. Equation 2.9 is derived in Appendix A and minimises a function F with respect to a set of variables y_n. After some manipulation we obtain the Euler Lagrange equation for θ_{FO}

$$\frac{\partial\theta_{FO}}{\partial\tau_{FO}} = \nabla^2\theta_{FO} + \frac{1}{2}\chi_{FO}\left[\sin 2\theta_{FO}\left(E_x^2 - E_z^2\right) + 2\cos 2\theta_{FO} E_x E_z\right], \tag{2.10}$$

where $\tau_{FO} = t\left[K/(L_x^2\gamma_1)\right]$, L_x is the characteristic length of the system, $(x, z) = (\tilde{x}, \tilde{z})/L_x$ and γ_1 is Leslie's rotational viscosity. The equation for ψ is derived by substituting equation (2.4) into Maxwell's equation $\boldsymbol{\nabla} \cdot \boldsymbol{D} = 0$. After some manipulation this yields

$$\boldsymbol{\nabla}^T \begin{pmatrix} 1 - \alpha_{FO}\cos 2\theta_{FO} & \alpha_{FO}\sin 2\theta_{FO} \\ \alpha_{FO}\sin 2\theta_{FO} & 1 + \alpha_{FO}\cos 2\theta_{FO} \end{pmatrix} \boldsymbol{\nabla}\psi = 0, \tag{2.11}$$

where $\alpha_{FO} = \Delta\epsilon/(\epsilon_{||} + \epsilon_{\perp})$ is the electrostatic coupling strength.

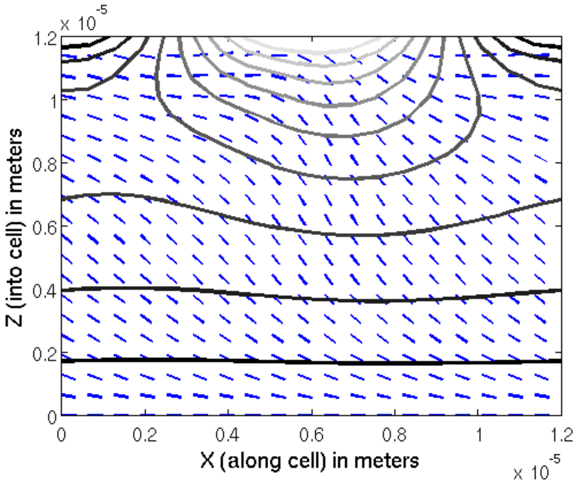

FIGURE 2.3: *Typical plot for director field under the application of a sinusoidal electric field with planar boundary conditions. The contour lines show the equipotentials in the cell.*

The coupled differential equations (2.10) and (2.11) can, assuming small director reorientation and neglecting the electrostatic coupling, be solved analytically [68, 69]. However, here we solve them as a numerical boundary value problem, the details of which can be found in Appendix B. A typical plot for the director angles under the application of a sinusoidal electric field is given in Figure 2.3. Here the interaction between the electric field and the director alignment can be clearly seen, in the absence of this coupling the potential would be symmetric. The asymmetric alignment of the liquid crystal is caused by the molecular pretilt at one of the cell boundaries.

2.3 $\mathcal{Q}$–tensor model

2.3.1 Free energy

In the $\mathcal{Q}$–tensor model we consider a dimensional liquid crystal free energy of the form $\tilde{\mathcal{F}} = \tilde{\mathcal{F}}_e(\tilde{\mathcal{Q}}) + \tilde{\mathcal{F}}_d(\tilde{\mathcal{Q}}) + \tilde{\mathcal{F}}_t(\tilde{\mathcal{Q}})$, where $\tilde{\mathcal{F}}_e$, $\tilde{\mathcal{F}}_d$ and $\tilde{\mathcal{F}}_t$ are respectively the electrostatic, elastic and bulk free energies. The general form of the biaxial liquid crystal alignment tensor,$\tilde{\mathcal{Q}}$, written in terms of the orthogonal unit directors $\hat{\boldsymbol{n}}$ and $\hat{\boldsymbol{m}}$, which define the major and minor crystal axis respectively, is

$$\tilde{\mathcal{Q}} = \sqrt{\frac{3}{2}}\tilde{S}\left(\overbracket{\hat{\boldsymbol{n}} \otimes \hat{\boldsymbol{n}}}\right) + \sqrt{\frac{3}{2}}\tilde{\beta}\left(\overbracket{\hat{\boldsymbol{m}} \otimes \hat{\boldsymbol{m}}}\right) \tag{2.12}$$

where $\tilde{S}$ is the scalar order parameter, $\tilde{\beta}$ the biaxiality parameter, I is the identity matrix and $\overbracket{\hat{\boldsymbol{n}} \otimes \hat{\boldsymbol{n}}} = (\hat{\boldsymbol{n}} \otimes \hat{\boldsymbol{n}} - 1/3I)$ denotes a traceless symmetric tensor. The total free energy may be obtained by integrating over the cell volume. In the absence of external forces, such as electromagnetic fields or boundaries, this free energy reduces to just the elastic and thermotropic free energies which are $SO(3)$ invariant. Much work has been done to obtain comprehensive expressions for the thermotropic and elastic free energies [38, 39].

Throughout the remainder of this chapter we shall assume the simplest possible expressions for these free energies. It should be noted however that this restriction is not a necessary condition for this method to work, rather it is a simplification used to clarify the derivation.

The elastic free energy in its simplest form is derived using the one elastic constant approximation. This can be written as

$$\tilde{\mathcal{F}}_d = \frac{L}{2}\left|\boldsymbol{\nabla}\tilde{\mathcal{Q}}\right|^2, \tag{2.13}$$

where L is defined as $L = K/(3\tilde{S}^2)$ and K is the liquid crystal elastic constant. The electrostatic free energy of the liquid crystal takes the form

$$\tilde{\mathcal{F}}_e = -\frac{1}{3}\epsilon_0\Delta\epsilon\mathrm{Tr}\left(\tilde{\mathcal{Q}}\tilde{\mathcal{E}}\right), \tag{2.14}$$

where

$$\tilde{\mathcal{E}} = \sqrt{\frac{3}{2}}\,\overline{\tilde{\boldsymbol{E}}\otimes\tilde{\boldsymbol{E}}}, \tag{2.15}$$

ϵ_0 is the permittivity of free space, $\Delta\epsilon$ the anisotropic relative permittivity and the electric field $\tilde{\boldsymbol{E}} = -\boldsymbol{\nabla}\tilde{\psi}$, where $\tilde{\psi}$ is the electric potential. The effect of temperature on the liquid crystal alignment is described by the bulk free energy, written in terms of a Landau power series expansion of $\tilde{\mathcal{Q}}$ [26]

$$\tilde{\mathcal{F}}_t = \frac{1}{2}A(T-T^*)\mathrm{Tr}\left(\tilde{\mathcal{Q}}^2\right) - \sqrt{6}B\mathrm{Tr}\left(\tilde{\mathcal{Q}}^3\right) + \frac{1}{2}C\mathrm{Tr}^2\left(\tilde{\mathcal{Q}}^2\right), \tag{2.16}$$

where A, B and C are the bulk thermotropic coefficients which are assumed to be independent of temperature. The temperature dependence of this energy is described entirely by $T - T^*$, where T^* is the pseudocritical temperature at which the isotropic phase becomes unstable.

To ensure the traceless symmetric properties of our $\tilde{\mathcal{Q}}$ and $\tilde{\mathcal{E}}$ are respected we express the free energy on the basis of traceless symmetric tensors [37],

$$\tilde{\mathcal{Q}} = \sum_{p=1}^{5}\tilde{a}_p T^{(p)} \quad \text{and} \quad \tilde{\mathcal{E}} = \sum_{p=1}^{5}\tilde{e}_p T^{(p)},$$

where

$$\begin{aligned}
T^{(1)} &= \frac{1}{\sqrt{6}}\left(-\boldsymbol{e}_x\otimes\boldsymbol{e}_x - \boldsymbol{e}_y\otimes\boldsymbol{e}_y + 2\boldsymbol{e}_z\otimes\boldsymbol{e}_z\right)\\
T^{(2)} &= \frac{1}{\sqrt{2}}\left(\boldsymbol{e}_x\otimes\boldsymbol{e}_x - \boldsymbol{e}_y\otimes\boldsymbol{e}_y\right), \quad T^{(3)} = \frac{1}{\sqrt{2}}\left(\boldsymbol{e}_x\otimes\boldsymbol{e}_y + \boldsymbol{e}_y\otimes\boldsymbol{e}_x\right),\\
T^{(4)} &= \frac{1}{\sqrt{2}}\left(\boldsymbol{e}_x\otimes\boldsymbol{e}_z + \boldsymbol{e}_z\otimes\boldsymbol{e}_x\right), \quad T^{(5)} = \frac{1}{\sqrt{2}}\left(\boldsymbol{e}_y\otimes\boldsymbol{e}_z + \boldsymbol{e}_z\otimes\boldsymbol{e}_y\right).
\end{aligned} \tag{2.17}$$

We rescale the order parameter $S = \frac{3C}{2B}\tilde{S}$, the biaxiality parameter $\beta = \frac{3C}{2B}\tilde{\beta}$, the tensor field $\mathcal{Q} = \frac{3C}{2B}\tilde{\mathcal{Q}}$ and the component fields $a_p = \frac{3C}{2B}\tilde{a}_p$ and $e_p = \tilde{e}_p/\psi_0^2$, where ψ_0 is a typical potential, $\psi = \tilde{\psi}/\psi_0$. For compactness of notation, from now on we adopt the convention of summing over repeated indices, unless stated otherwise. We also indicate with $\boldsymbol{a}$ and $\boldsymbol{e}$ the vectors with components a_p and e_p. Finally we non-dimensionalise to obtain the scaled free energy,

$$\mathcal{F} = \frac{\xi_0^2}{2}|\boldsymbol{\nabla a}|^2 - \chi_a \boldsymbol{a}\cdot\boldsymbol{e} + \frac{T_0}{2}|\boldsymbol{a}|^2 + \frac{1}{2}|\boldsymbol{a}|^4 - \sqrt{6}\sum_{p,q,r}\mathrm{Tr}\left(T^{(p)}T^{(q)}T^{(r)}\right)a_p a_q a_r. \qquad (2.18)$$

The non-dimensional elastic constant ξ_0^2, the electrostatic coefficient χ_a and the scaled temperature T_0 are

$$\xi_0^2 = \frac{9C}{2B^2}\frac{L}{L_x^2}, \quad \chi_a = \frac{9\epsilon_0\Delta\epsilon C^2}{2L_x^2B^3}\psi_0^2, \quad T_0 = \frac{T-T^*}{T_c-T^*},$$

where T_c is the clearing point temperature and L_x is the characteristic length of the geometry studied. We have rescaled space so that $(x,z) = (\tilde{x},\tilde{z})/L_x$. Typically $T_0 \sim O(1)$ whilst $\xi_0^2 \sim O(10^{-7})$ and $\chi_a \sim O(10^{-6})$.

The separation in scales between the various terms in the free energy cause the Euler-Lagrange equations, which minimise equation (2.18), to be stiff. As a result the computing times required for even relatively simple geometries become very large. In situations where the elastic and electrostatic free energies remain small we can initially consider only the critical points of the bulk free energy. The elastic and electrostatic free energies can then be considered as a perturbation. It is this assumption that makes this method inappropriate for defect modelling.

2.3.2 Critical points under slightly broken symmetry

Before we consider the case of the liquid crystal it is useful to consider a general free energy of the type given in equation (2.18). The free energy $\mathcal{F}(\boldsymbol{a})$ consists of a symmetric bulk free energy perturbed by a small symmetry breaking contribution from the elastic and electrostatic energies. We denote these terms $\mathcal{F}_t(\boldsymbol{a})$ and $\mathcal{L}(\boldsymbol{a})$ respectively, where $\mathcal{L}(\boldsymbol{a})$ $\mathcal{F}_t(\boldsymbol{a}) \in \mathbb{R}^5$ in the three dimensional case and $\mathcal{L}(\boldsymbol{a})$ $\mathcal{F}_t(\boldsymbol{a}) \in \mathbb{R}^2$ in the two dimensional case. For simplicity we consider here the case that $\mathcal{L}(\boldsymbol{a})$ has only the electrostatic energy component, so that the liquid crystal state is described by a single five dimensional vector $\boldsymbol{a}$, rather than a five-component vector field $\boldsymbol{a}(\boldsymbol{x})$. This allows us to describe the perturbation scheme in very general terms as the effect of a symmetry breaking perturbation on an invariant manifold of solutions of a set of ordinary differential equations. In the more general case where the elastic energy is also considered we would have to deal with partial differential equations for vector fields: however, we expect that the main ideas outlined here would remain valid.

As the bulk energy is $SO(3)$ invariant the critical points of $\mathcal{F}_t(\boldsymbol{a})$ will form an orbit of solutions in the five dimensional component space. Specifically, for the general case corresponding to a biaxial minimiser, the group orbit will be a 3-manifold, whilst in the special case corresponding to uniaxial minimisers the orbit reduces to a 2-manifold.

The effect of the first order perturbation $\mathcal{L}(\boldsymbol{a})$ is to break the symmetry and to collapse the invariant manifold of critical points to a smaller set near the manifold. This setting is very similar to the Signorini perturbation scheme, originally derived in the context of elastostatics [6, 7, 8, 70],

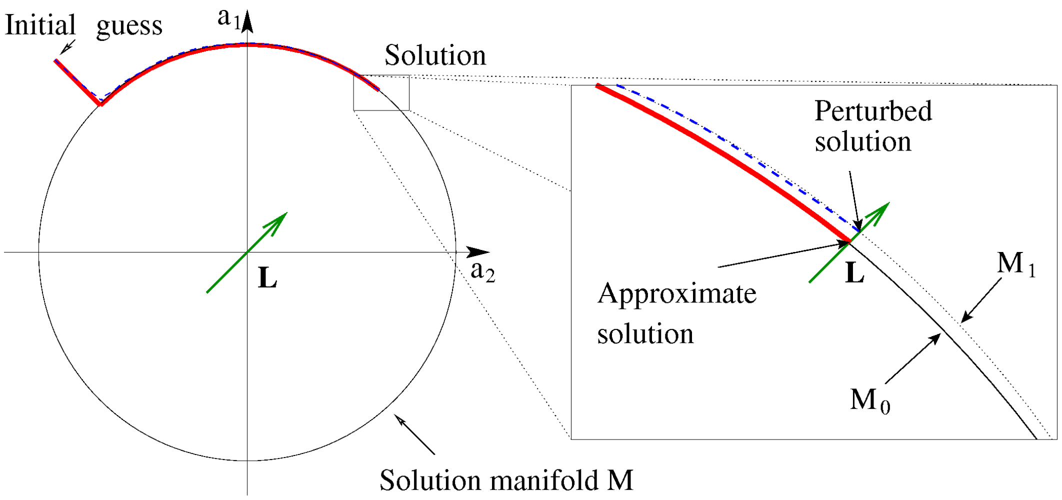

FIGURE 2.4: *Graphical representation of the Signorini perturbation scheme. For some initial point in the phase space (a_1, a_2) there is rapid convergence at a rate τ_0 to the solution manifold. Motion along the manifold, driven by the flow $\boldsymbol{L}$, occurs much more slowly at a rate τ_1. The critical point on M_0 is found when $\boldsymbol{L}$ is orthogonal to $T_{\boldsymbol{a}}M_0$. As M_0 is close to the perturbed manifold M_1 the solution can be approximated by the point on M_0 whose surface normal intersects M_1 close to the perturbed solution.*

but of wider potential application [71]. This scheme determines the equilibrium configuration of an elastic body under the effect of applied stresses using a perturbation expansion in powers of the applied stress. In the context of liquid crystals, the role of the "applied stresses" is played by the (small) elastic and electrostatic forces and our approximation is the first step of a standard Signorini expansion.

We consider an orbit M_0 consisting of the critical points of the bulk energy $\mathcal{F}_t(\boldsymbol{a})$ with tangent space $T_{\boldsymbol{a}}M_0$ at $\boldsymbol{a} \in M_0$. As M_0 consists entirely of critical points then $T_{\boldsymbol{a}}M_0 \subset \ker(\mathcal{H})$, where $\mathcal{H}$ is the Hessian of the bulk free energy. If the critical points of the bulk free energy are non-degenerate in the direction normal to the manifold then the tangent space coincides with the kernel, $T_{\boldsymbol{a}}M_0 = \ker(\mathcal{H})$. Therefore, M_0 is a normally hyperbolic invariant manifold for the flow, $-\boldsymbol{\nabla}_{\boldsymbol{a}}\mathcal{F}_t(\boldsymbol{a})$, where $\boldsymbol{\nabla}_{\boldsymbol{a}}$ denotes differentiation with respect to the components of the vector $\boldsymbol{a}$.

The effects of the perturbative terms can be understood by invariant manifold theory. If the perturbed flow, $-\boldsymbol{\nabla}_{\boldsymbol{a}}(\mathcal{F}_t+\mathcal{L})$ and its first derivative are sufficiently close to the unperturbed flow then there exists a smooth invariant manifold M_1 close to M_0. The behaviour of the perturbed flow along M_1 will be comparable to the flow restricted to M_0 [70]. Specifically, a point p_0 on M_0 will correspond to a point p_1 on M_1, where p_1 is the intersection of the normal to M_0 at p_0 and M_1. If all non-zero eigenvalues of $\mathcal{H}$ are positive then the dynamical behaviour of the flow close to the manifold will consist of exponential attraction towards the manifold followed by a slow drift along it [72].

As the perturbation $-\boldsymbol{\nabla}_{\boldsymbol{a}}\left(\mathcal{F}_t + \mathcal{L}\right)$ is also a gradient vector field then the local minima on M_1 will be attracting stationary points. For non-degenerate critical points these are in $1:1$

correspondence with the local minima of the perturbed function restricted to the unperturbed manifold M_0. The critical points restricted to M_0 are found when the flow $\boldsymbol{L} = -\boldsymbol{\nabla}_{\boldsymbol{a}}\mathcal{L}$ is orthogonal to $T_{\boldsymbol{a}}$. This is represented graphically for the simplified two dimensional case in Figure 2.4.

In the simple two dimensional case considered in Section 2.4 the symmetry group is $SO(2)$ under the action of rotation on $\mathbb{R}^2$. In this case there will be two critical points on the perturbed manifold. These correspond to an unstable maximum and a stable minimum.

In the three dimensional case, Section 2.5, the situation is more complicated. The bulk energy minimisers form an orbit of the conjugacy action of $SO(3)$ on the five dimensional space of traceless symmetric matrices (see Section 2.5.2). This orbit is parametrised locally by the direction of the major axis of the liquid crystal molecule (two dimensions) together with a circle corresponding to the orientation of the minor axis. For uniaxial minimisers of the bulk free energy these circles of critical points shrink to radius 0. The result is that liquid crystal orientation can only be determined in terms of the major axis. To determine the orientation of the minor axis in cases where the perturbation induces biaxiality, a further step in the expansion is required.

2.4 2D case

As an example to illustrate the approximation method it is helpful to look at a simplified two dimensional case where the liquid crystal director is restricted to the x, z plane. The alignment tensor is a 2×2 uniaxial tensor,

$$\mathcal{Q}_{ij} = \sqrt{2}S\left(\hat{n}_i\hat{n}_j - \frac{1}{2}\delta_{ij}\right). \tag{2.19}$$

We can proceed exactly as in Section 2.3.1 with the simplified basis set of 2×2 traceless symmetric tensors:

$$T_1 = \frac{1}{\sqrt{2}}\begin{pmatrix} -1 & 0 \\ 0 & 1 \end{pmatrix}, \qquad T_2 = \frac{1}{\sqrt{2}}\begin{pmatrix} 0 & 1 \\ 1 & 0 \end{pmatrix}. \tag{2.20}$$

Hence

$$\mathcal{Q} = \sum_{p=1}^{2} a_p T^{(p)}.$$

In this notation the scalar order parameter is $S^2 = \mathrm{Tr}(\mathcal{Q}^2) = a_1^2 + a_2^2$. The Euler–Lagrange equations of motion, derived using the simplest form of the free energy, are

$$\partial_\tau a_n = \xi_0^2\nabla^2 a_n - T_0 a_n - 2a_n\left(a_1^2 + a_2^2\right) + \chi_a e_n, \tag{2.21}$$

where $n = 1, 2$, $\tau = t/\tau_d$, $\tau_d = \left[9C/(2B^2)\right]\zeta$ and the viscosity, ζ, is related to Leslie's rotational viscosity γ_1 by $\zeta = \gamma_1/(3\tilde{S}^2)$.

2.4.1 Invariant manifold

Due to the smallness of ξ_0^2 and χ_a equation (2.21) can be seen to have two different time scales. Taking $\eta = \xi_0^2$ as the small parameter we can write the time derivatives in equation (2.21) as $\partial_\tau = \partial_{\tau_0} + \eta\partial_{\tau_1}$. Substituting into equation (2.21) gives

$$\partial_{\tau_0} a_n + \eta\partial_{\tau_1} a_n = \eta\nabla^2 a_n - T_0 a_n - 2a_n\left(a_1^2 + a_2^2\right) + \eta\chi_0 e_n, \tag{2.22}$$

where $\chi_0 = \chi_a/\xi_0^2$ is $O(1)$. Observing that only the bulk free energy changes on the fast timescale we assume that this scale determines only the scalar order parameter. As we are only interested in the slow timescale, i.e. the timescale over which the liquid crystal aligns, we can make the assumption that the fast timescale behaviour has reached equilibrium, i.e. $\partial_{\tau_0} = 0$. The slow scale behaviour, which is present due to the small elastic and electrostatic terms, will be obtained from the first order correction.

To proceed the component representation of the liquid crystal is rewritten as a power series expansion in η:

$$a_n = \quad a_{n,0} + \eta a_{n,1} + O(\eta^2), \tag{2.23}$$

where $a_{n,j}$ is the n–th component of j–th order. Substituting into equation (2.22) and retaining terms only to $O(\eta^0)$ allows us to write

$$\left[T_0 + 2\left(a_{1,0}^2 + a_{2,0}^2\right)\right] a_n = 0, \tag{2.24}$$

which is satisfied if $\left(a_{1,0}^2 + a_{2,0}^2\right) = -T_0/2$. As $S^2 = a_1^2 + a_2^2$, equation (2.24) defines the leading order approximation to the scalar order parameter,

$$S_0^2 = -T_0/2. \tag{2.25}$$

This equation can also be derived by minimising the corresponding Landau deGennes free energy in terms of the scalar order parameter. As described in Section 2.3.2 equation (2.25) defines a manifold of critical points in the component space $(a_{1,0}, a_{2,0})$. For uniaxial liquid crystals the critical points of the free energy are non-degenerate as $T_0 < 0$. We consider the effects of the elastic and electrostatic free energies as a symmetry breaking perturbation. In the context of the Signorini expansion this defines the flow along the manifold with, in this case, a unique stable minimum, found using the first step of the Signorini expansion.

2.4.2 Kernel of adjoint (tangent space)

This minimum, and hence the liquid crystal alignment, can be found from the first order expansion of equation (2.21). Retaining terms to $O(\eta)$ and using equation (2.24) we obtain:

$$4\begin{pmatrix} a_{1,0}^2 & a_{1,0}a_{2,0} \\ \\ a_{1,0}a_{2,0} & a_{2,0}^2 \end{pmatrix}\begin{pmatrix} a_{1,1} \\ \\ a_{2,1} \end{pmatrix} = \begin{pmatrix} \nabla^2 a_{1,0} + \chi_0 e_1 - \partial_{\tau_1} a_{1,0} \\ \\ \nabla^2 a_{2,0} + \chi_0 e_2 - \partial_{\tau_1} a_{2,0} \end{pmatrix}. \tag{2.26}$$

This is a system of linear equations for $a_{n,1}$ that can be written as $\mathcal{H}\boldsymbol{a}_1 = \boldsymbol{L}$. Recall that $\mathcal{H}$ is the Hessian of the bulk free energy. However, in this case this equation has no unique solution as det$(\mathcal{H}) = 0$. The Hessian is a symmetric real valued function, therefore, $\mathcal{H}^\dagger = \mathcal{H}$, where $\mathcal{H}^\dagger$ denotes the adjoint of $\mathcal{H}$. Therefore, as stated in Section 2.3.2, for a non-trivial solution to exist $\boldsymbol{L}$ must be orthogonal to ker$(\mathcal{H})$. As this is a two dimensional system, the kernel of $\mathcal{H}$ is a single vector $\boldsymbol{V}$. This gives us the solvability condition $\boldsymbol{L} \cdot \boldsymbol{V} = 0$, where $\boldsymbol{V} = (-a_{2,0}, a_{1,0})^T$ is the eigenvector of zero eigenvalue of $\mathcal{H}$.

Using the solvability condition, $\boldsymbol{L} \cdot \boldsymbol{V} = 0$, we obtain the following equation for $a_{1,0}$ and $a_{2,0}$,

$$a_{1,0}\partial_{\tau_1} a_{2,0} - a_{2,0}\partial_{\tau_1} a_{1,0} = a_{1,0}\nabla^2 a_{2,0} - a_{2,0}\nabla^2 a_{1,0} + a_{1,0}\chi_0 e_2 - a_{2,0}\chi_0 e_1. \tag{2.27}$$

Equation (2.27) can be solved simultaneously with equation (2.24) to determine the liquid crystal dynamics on the solution manifold.

2.4.3 Parameterisation of the solution

By correctly parameterising the components $a_{1,0}$ and $a_{2,0}$ we can force the director onto the solution manifold removing the need to solve the leading order equation. As the leading order solution manifold is $SO(2)$ invariant we parameterise the solutions in terms of the polar angles $\vartheta \in [0, 2\pi]$. If we write

$$a_{1,0} = S_0 \sin\vartheta, \quad \text{and} \quad a_{2,0} = S_0 \cos\vartheta$$

then equation (2.25) is automatically satisfied. This representation can be used in equation (2.27) to determine the time evolution of $a_{n,0}$:

$$S_0^2 \frac{\partial a_{n,0}}{\partial \tau_1} = V_n \left(a_{1,0}\nabla^2 a_{2,0} - a_{2,0}\nabla^2 a_{1,0} + a_{1,0}\chi_0 e_2 - a_{2,0}\chi_0 e_1 \right), \tag{2.28}$$

where V_n is the nth component of $\boldsymbol{V}$. This equation confirms that the motion of the director field is in the direction tangent to the manifold.

Equation (2.28) is an initial value problem for $a_{n,0}$ which can be solved using standard numerical techniques for an initial set of $a_{n,0}$ on the manifold. It is important to note that we need never calculate ϑ, as equation (2.28) is solved purely in terms of the component representation, $a_{n,0}$. This ensures that the singularities expected in a director model are overcome.

2.4.4 Order one accuracy check

To determine the accuracy of the expansion we consider the perturbed manifold M_1. The equations derived above are suitable only in the case where M_1 is sufficiently close to M_0.

Physically the minimum distance between the leading order solution and M_1 represents the correction S_1 to the scalar order parameter, $S = S_0 + \eta S_1 + O(\eta^2)$. In general this can be calculated from the singular value decomposition of the $O(\eta)$ equation (2.26). However, in 2D the correction can be calculated analytically. After a little algebra we obtain

$$S_1 = \frac{1}{\sqrt{-2T_0^3}} \left[\boldsymbol{a}_0 \cdot \nabla^2 \boldsymbol{a}_0 + \chi_0 \boldsymbol{a}_0 \cdot \boldsymbol{e} \right]. \tag{2.29}$$

The magnitude of S_1 can be used to determine the validity of the perturbation expansion. If ηS_1 becomes comparable with S_0 then the expansion breaks down and the liquid crystal has large variation in order parameter. If this happens then the full stiff equations (2.21) must be solved.

2.5 3D case

The three dimensional Euler–Lagrange equations are computed in a similar way to the two dimensional case,

$$\eta \frac{\partial a_1}{\partial \tau_1} = \eta \left(\nabla^2 a_1 + \chi_0 e_1 \right) - T_0 a_1 + 3 \left(a_1^2 - a_2^2 - a_3^2 \right) + \frac{3}{2} \left(a_4^2 + a_5^2 \right) - 2 a_1 \sum_{k=1}^{5} a_k^2, \tag{2.30a}$$

$$\eta \frac{\partial a_2}{\partial \tau_1} = \eta \left(\nabla^2 a_2 + \chi_0 e_2 \right) - T_0 a_2 - 6 a_1 a_2 + \frac{3\sqrt{3}}{2} \left(a_4^2 - a_5^2 \right) - 2 a_2 \sum_{k=1}^{5} a_k^2, \tag{2.30b}$$

$$\eta \frac{\partial a_3}{\partial \tau_1} = \eta \left(\nabla^2 a_3 + \chi_0 e_3 \right) - T_0 a_3 - 3 \left(2 a_1 a_3 - \sqrt{3} a_4 a_5 \right) - 2 a_3 \sum_{k=1}^{5} a_k^2, \tag{2.30c}$$

$$\eta \frac{\partial a_4}{\partial \tau_1} = \eta \left(\nabla^2 a_4 + \chi_0 e_4 \right) - T_0 a_4 + 3 a_1 a_4 + 3\sqrt{3} \left(a_2 a_4 + a_3 a_5 \right) - 2 a_4 \sum_{k=1}^{5} a_k^2, \tag{2.30d}$$

$$\eta \frac{\partial a_5}{\partial \tau_1} = \eta \left(\nabla^2 a_5 + \chi_0 e_5 \right) - T_0 a_5 + 3 a_1 a_5 + 3\sqrt{3} \left(a_3 a_4 - a_2 a_5 \right) - 2 a_5 \sum_{k=1}^{5} a_k^2, \tag{2.30e}$$

where, as in the two dimensional case, $\eta = \xi_0^2$ and $\chi_0 = \chi_a / \xi_0^2$. The fast time derivatives have been neglected as, on the timescale of interest, these variations will have reached equilibrium.

At this point, for compactness of notation, it is useful to define the first order perturbation L_m in terms of the elastic and electrostatic contributions,

$$L_m = \nabla^2 a_{m,0} + \chi e_m - \frac{\partial a_{m,0}}{\partial \tau_1}, \tag{2.31}$$

where $m = 1, \ldots, 5$.

2.5.1 Invariant manifold

In the two dimensional case the leading order equations are those which minimise the free energy in terms of the scalar order parameter. This minimisation fixes the liquid crystal director onto the solution manifold in the two dimensional space (a_1, a_2). A similar method can be used in the three dimensional case using the biaxial $\mathcal{Q}$ tensor representation (2.12). It can be shown that the stationary points of the leading order free energy function, of the form given in equation (2.16), are either uniaxial or isotropic [30]. As such the biaxiality parameter β must vanish at leading order. Minimising the free energy in terms of the scalar order parameter S, as in the two dimensional case, allows us to obtain the fast timescale equations. The Euler–Lagrange equation of motion that minimises the leading order scalar order parameter, S_0, is

$$\frac{\partial S_0}{\partial \tau_0} = -2{S_0}^3 + 3{S_0}^2 - T_0 S_0, \tag{2.32}$$

which can be solved for steady uniaxial state to obtain

$$S_0 = \frac{3 + \sqrt{9 - 8T_0}}{4}. \tag{2.33}$$

Equation (2.33) defines the solution manifold in the five dimensional component space. The critical points on this manifold are non-degenerate providing T_0 is below the super heating limit, $T_0 = 9/8$ [51]. In terms of the component representation the scalar order parameter is given by

$$S_0^2 = \sum_{n=1}^{5} a_n^2. \tag{2.34}$$

To fix the biaxiality to zero we require that $\mathcal{Q}$ has two only two unique eigenvalues, hence,

$$a_{1,0}^3 + 3a_{1,0}^2\left(S_0 - a_{1,0}\right) + \frac{3\sqrt{3}}{2}\left[a_{2,0}\left(a_{4,0}^2 - a_{5,0}^2\right) + 2a_{3,0}a_{4,0}a_{5,0}\right] = S_0^3. \tag{2.35}$$

These two equations define a 3–manifold in the five dimensional component space. However, as the leading order minimisers are uniaxial there are only two undefined parameters which relate to the angles the liquid crystal makes with the coordinate axis. Therefore, as described in Section 2.3.2, the 3–manifold corresponding to the biaxial stationary points must reduce to a 2–manifold leading to a degeneracy in the first order correction. Specifically this allows us to determine only the direction of the major crystal axis uniquely.

2.5.2 Kernel of adjoint (tangent space)

As in the two dimensional case we now need to find the first order correction to the leading order components which will determine the unique solution on the manifold. Motion across the manifold is determined by the first order perturbation L_m. The first order contribution from the bulk energy is invariant with respect to motion on the leading order manifold. Therefore, for the equation to have a non-trivial solution we require that the perturbation L_m is orthogonal to the kernel of $\mathcal{H}$. As Ker$(\mathcal{H}) = T_{\boldsymbol{a}}M_0$ the solvability condition is

$$L_m \frac{\partial a_{m,0}}{\partial s} = 0, \tag{2.36}$$

where s parameterises motion along the tangent space to the manifold. The derivative of $a_{m,0}$ is found by considering the tensor $\mathcal{Q}_{ij}(0)$ which satisfies the perturbed Euler–Lagrange equations. The motion of $\mathcal{Q}_{ij}(0)$ along the manifold by rotation in a spherical coordinate system is defined by the rotation matrix $R_{ij}(s)$ which acts on $Q_{ij}(0)$ by the conjugacy action $\mathcal{Q}_{ij}(s) = R_{ip}(s)R_{jq}(s)\mathcal{Q}_{pq}(0)$. The rotation matrix $R_{ij}(s)$ is orthogonal, i.e. $R_{ik}(s)R_{jk}(s) = \delta_{ij}$ and $R_{ij}(0) = \delta_{ij}$. Motion along the manifold written in terms of the component representation is

$$a_{m,0}(s) = \left[T^{(m)}_{ji} R_{ip}(s)R_{jq}(s)T^{(l)}_{pq}\right] a_{l,0}(0). \tag{2.37}$$

The derivative of $a_{m,0}$ is found by differentiating equation (2.37) at $s = 0$:

$$\frac{\partial a_{m,0}}{\partial s} = T^{(m)}_{ji} \left[R'_{ip}(0)\delta_{jq}T^{(l)}_{pq} + \delta_{ip}R'_{jq}(0)T^{(l)}_{pq}\right] a_{l,0}(0). \tag{2.38}$$

To proceed we need to determine $R'_{ij}(0)$, this can be obtained by differentiating the identity $R_{ip}(s)R_{jp}(s) = \delta_{ij}$ at $s = 0$,

$$R'_{ip}(0)\delta_{jp} + \delta_{ip}R'_{jp}(0) = 0. \tag{2.39}$$

For this equation to be satisfied $R'_{ij}(0)$ must be a skew symmetric tensor. therefore, it can be expressed on the basis $W^{(n)}$, defined as

$$\begin{aligned} W^{(1)} &= \frac{1}{\sqrt{2}}\left(\boldsymbol{e}_y \otimes \boldsymbol{e}_x - \boldsymbol{e}_x \otimes \boldsymbol{e}_y\right), \\ W^{(2)} &= \frac{1}{\sqrt{2}}\left(\boldsymbol{e}_x \otimes \boldsymbol{e}_z - \boldsymbol{e}_z \otimes \boldsymbol{e}_x\right), \\ W^{(3)} &= \frac{1}{\sqrt{2}}\left(\boldsymbol{e}_z \otimes \boldsymbol{e}_y - \boldsymbol{e}_y \otimes \boldsymbol{e}_z\right). \end{aligned} \tag{2.40}$$

For each $W^{(n)}$ we obtain a different $\partial a_{m,0}/\partial s$ and thus three vectors, $\boldsymbol{V}^{(n)}$, that span the kernel. The solvability conditions can be written as

$$L_m V^{(n)}_m = 0, \tag{2.41}$$

where the spanning vectors can be explicitly written as

$$V_m^{(n)} = T_{ki}^{(m)} \left(T_{ij}^{(p)} W_{jk}^{(n)} - W_{ij}^{(n)} T_{jk}^{(p)} \right) a_{p,0}, \tag{2.42}$$

In terms of the $O(\eta^0)$ components the spanning vectors, $\boldsymbol{V}^{(n)}$ formed by each $W^{(n)}$ are:

$$\boldsymbol{V}^{(1)} = \begin{pmatrix} 0 \\ -2a_{3,0} \\ 2a_{2,0} \\ -a_{5,0} \\ a_{4,0} \end{pmatrix}, \quad \boldsymbol{V}^{(2)} = \begin{pmatrix} -\sqrt{3}a_{4,0} \\ a_{4,0} \\ a_{5,0} \\ \sqrt{3}a_{1,0} - a_{2,0} \\ -a_{3,0} \end{pmatrix}, \quad \boldsymbol{V}^{(3)} = \begin{pmatrix} \sqrt{3}a_{5,0} \\ a_{5,0} \\ -a_{4,0} \\ a_{3,0} \\ -\sqrt{3}a_{1,0} - a_{2,0} \end{pmatrix}. \tag{2.43}$$

The first order equations require equation (2.41) to be satisfied in the direction of each spanning vector. This gives us three equations, one for each of the skew symmetric tensors $W^{(n)}$. Substituting equation (2.31) into the equation (2.41) the time dependent equations are obtained

$$V_m^{(n)} \frac{\partial}{\partial \tau_1} a_{m,0} = V_m^{(n)} \left(\nabla^2 a_{m,0} + \chi e_m \right), \tag{2.44}$$

where $m = 1..5$.

2.5.3 How to solve equations/parameterisation of equations

Equations (2.44) describe the dynamics of the critical point structure on the generic 3–manifold. However, as the bulk minimisers are uniaxial these 3 equations must reduce to 2 corresponding to the reduction in the dimension of the manifold. Using guidance from the two dimensional case we exploit the $SO(3)$ invariance of the bulk energy and parameterise the component representation $\boldsymbol{a}_0$ in terms of the uniaxial $\mathcal{Q}$–tensor with principal axis defined by the spherical coordinate angles $[\theta, \phi]$:

$$\boldsymbol{a}_0 = S_0 \begin{pmatrix} 1 - \frac{3}{2}\sin^2\theta \\ \frac{\sqrt{3}}{2}\sin^2\theta \left(2\cos^2\phi - 1\right) \\ \sqrt{3}\sin^2\theta\cos\phi\sin\phi \\ \sqrt{3}\cos\theta\sin\theta\sin\phi \\ \sqrt{3}\cos\theta\sin\theta\cos\phi \end{pmatrix}. \tag{2.45}$$

For a free energy which supports biaxial phases the appropriate representation for the component field would be a biaxial tensor expressed in terms of all three Euler angles. Substituting into equation (2.44) we can simplify the time derivatives to obtain equations for the time derivatives of θ and ϕ:

$$\begin{aligned} 3{S_0}^2\frac{\partial\theta}{\partial\tau_1} &= \Big(\cos\phi V_m^{(2)} - \sin\phi V_m^{(3)}\Big)\Big(\nabla^2 a_{m,0} + \chi e_m\Big), \\ 3{S_0}^2\frac{\partial\phi}{\partial\tau_1} &= \frac{1}{\sin^2\theta} V_m^{(1)}\Big(\nabla^2 a_{m,0} + \chi e_m\Big). \end{aligned} \tag{2.46}$$

These can be used to describe the time dependent liquid crystal alignment in all cases except where the liquid crystal is aligned close to the coordinate singularity $\theta = 0, \pi$. If this is the case then we need to use a multigrid method [73]. We choose a different set of coordinates $(\tilde{\theta}, \tilde{\phi})$, formed by rotating the existing coordinates about the y axis. This second coordinate system produces a set of components which give time dependent equations

$$\begin{aligned} 3{S_0}^2\frac{\partial\tilde{\theta}}{\partial\tau_1} &= \Big(\cos\tilde{\phi} V_m^{(2)} - \sin\tilde{\phi} V_m^{(1)}\Big)\Big(\nabla^2 a_{m,0} + \chi e_m\Big), \\ 3{S_0}^2\frac{\partial\tilde{\phi}}{\partial\tau_1} &= -\frac{1}{\sin^2\tilde{\theta}} V_m^{(3)}\Big(\nabla^2 a_{m,0} + \chi e_m\Big). \end{aligned} \tag{2.47}$$

The second coordinate system is singular at $\tilde{\theta} = 0, \pi$, equivalent to $\theta = \pi/2$ and $\phi = 0, \pi$. As such the two coordinate systems cannot be simultaneously singular for a given director. Using the different coordinate systems the time derivatives of $a_{p,0}$ can be found from the least singular coordinate system as either

$$\frac{\partial a_p}{\partial\tau_1} = V_p^{(1)}\frac{\partial\phi}{\partial\tau_1} - \Big(\sin\phi V_p^{(3)} - \cos\phi V_p^{(2)}\Big)\frac{\partial\theta}{\partial\tau_1}, \tag{2.48a}$$

or

$$\frac{\partial a_p}{\partial\tau_1} = -V_p^{(3)}\frac{\partial\tilde{\phi}}{\partial\tau_1} + \Big(\cos\tilde{\phi} V_p^{(2)} - \sin\tilde{\phi} V_p^{(1)}\Big)\frac{\partial\tilde{\theta}}{\partial\tau_1}. \tag{2.48b}$$

The strength of the singularity in each coordinate system is determined by the size of θ and $\tilde{\theta}$. This can be directly measured from the size of the x and z components of the director. An appropriate choice of representation, chosen arbitrarily to allow for some overlap between the two, is to use $[\theta, \phi]$ if $|n_z| \leq 4/(3\sqrt{2})$ and $[\tilde{\theta}, \tilde{\phi}]$ if $|n_x| \leq 4/(3\sqrt{2})$. If both these conditions are satisfied an average value of $\partial a_p/\partial\tau_1$ obtained from each of the two representations is used.

2.5.4 Order one accuracy check

As in the two dimensional case we wish to determine the correction to the scalar order parameter as an approximation of the accuracy of our method. Unlike the two dimensional case an analytic expression cannot be obtained. Instead we use the method of singular value decomposition. Given the degenerate $O(\eta)$ equation $\mathcal{H}\boldsymbol{a}_1 = \boldsymbol{L}$ we calculate the perturbed manifold M_1

corresponding to the $O(\eta)$ correction to the components $\boldsymbol{a}_1$, where

$$\begin{aligned}
\mathcal{H}_{11} &= (4a_{1,0}-6)a_{1,0}+T_0+2\textstyle\sum_{n=1}^{4}a_{n,0}^2,\\
\mathcal{H}_{22} &= 4a_{2,0}^2+6a_{1,0}+T_0+2\textstyle\sum_{n=1}^{4}a_{n,0}^2,\\
\mathcal{H}_{33} &= 4a_{3,0}^2+6a_{1,0}+T_0+2\textstyle\sum_{n=1}^{4}a_{n,0}^2,\\
\mathcal{H}_{44} &= 4a_{4,0}^2-3a_{1,0}-3\sqrt{3}a_{2,0}+T_0+2\textstyle\sum_{n=1}^{4}a_{n,0}^2,\\
\mathcal{H}_{55} &= 4a_{5,0}^2-3a_{1,0}+3\sqrt{3}a_{2,0}+T_0+2\textstyle\sum_{n=1}^{4}a_{n,0}^2,\\
\mathcal{H}_{12} &= (6+4a_{1,0})a_{2,0}, & \mathcal{H}_{24} &= (4a_{2,0}-3\sqrt{3})a_{4,0},\\
\mathcal{H}_{13} &= (6+4a_{1,0})a_{3,0}, & \mathcal{H}_{25} &= (4a_{2,0}+3\sqrt{3})a_{5,0},\\
\mathcal{H}_{14} &= (4a_{1,0}-3)a_{4,0}, & \mathcal{H}_{34} &= 4a_{3,0}a_{4,0}-3\sqrt{3}a_{5,0},\\
\mathcal{H}_{15} &= (4a_{1,0}-3)a_{5,0}, & \mathcal{H}_{35} &= 4a_{3,0}a_{5,0}-3\sqrt{3}a_{4,0},\\
\mathcal{H}_{23} &= 4a_{2,0}a_{3,0}, & \mathcal{H}_{45} &= 4a_{4,0}a_{5,0}-3\sqrt{3}a_{3,0},
\end{aligned}$$

and $\mathcal{H}_{ij}=\mathcal{H}_{ji}$. The order parameter correction S_1 is then determined from the components of $\boldsymbol{a}_1$ orthogonal to the manifold, $S_1=\boldsymbol{a}_0\cdot\boldsymbol{a}_1/S_0$.

2.6 Examples

To demonstrate the use of the non stiff approximate liquid crystal equations we consider a planar cell filled with liquid crystals. A spatially periodic voltage is applied to one boundary whilst the other is set to a uniform zero Volts. This is a realistic model for a photorefractive liquid crystal cell [64, 74], a device used for optical coupling and as an optically addressable spatial light modulator. This is an interesting device for testing this algorithm as it allows for three dimensional orientation of the liquid crystal directors whilst having a simple geometry.

Under appropriate conditions the test geometry is a square in the x, z plane. Periodic conditions are imposed in the x direction such that $\boldsymbol{a}(x+L_x,z)=\boldsymbol{a}(x,z)$ and Dirichlet boundary conditions, corresponding to infinite anchoring strength, are imposed at $z=0$ and $z=L_z$. The liquid crystal is aligned by application of a spatially modulated voltage $\psi(x,L_z)=\psi_a\sin^2(\pi x/L_x)$ at one boundary, where ψ_a is the applied voltage amplitude, whilst the other is earthed, $\psi(x,0)=0$.

First we verify the two dimensional liquid crystal model derived in Section 2.4. This is done through comparison to the full stiff time dependent $\mathcal{Q}$-tensor equations and through comparison to a time dependent FO model. In this case the director orientation is restricted to the x, z plane by the planar, in plane boundary conditions. As is typical, due to the alignment layers used in these cells, a small pretilt is applied at $z=L_z$. The parameters used in our simulation are given in Table 2.1. The spatial derivatives are calculated using a pseudo-spectral method [75] and, for ease of implementation, the time derivative is calculated using the MATLAB multistep solver ODE113. A public domain version of the MATLAB code is available at [76] and further details

$K = 20 \times 10^{-12}\mathrm{N}$
$A = 0.13 \times 10^{6}\mathrm{J\,K^{-1}m^{-3}}$
$B = 1.6 \times 10^{6}\mathrm{Jm^{-3}}$
$C = 3.9 \times 10^{6}\mathrm{Jm^{-3}}$
$T_0 = -10$
$\epsilon_{\|} = 9.1$
$\epsilon_{\perp} = 4.1$
$S = 3.65\hat{S}$
$L = 6.05 \times 10^{-12}\mathrm{N}$
$L_x = 12 \times 10^{-6}\mathrm{m}$
$L_z = 12 \times 10^{-6}\mathrm{m}$
$\gamma_1 = 0.081\mathrm{Pa\,s}$
$\zeta = 0.037\mathrm{Pa\,s}$
$\tau_d = 2.56 \times 10^{-7}\mathrm{s}$
$\xi_0^2 = 4.39 \times 10^{-7}$
$\chi_a = 5.13 \times 10^{-6}\psi_0^2$
$\chi_I = 3.25 \times 10^{-5}\psi_0^2$
$\psi_0 = 1\mathrm{V}$

TABLE 2.1: Numerical values of non-dimensional constants for a typical photorefractive LC cell filled with the liquid crystal compound TL205

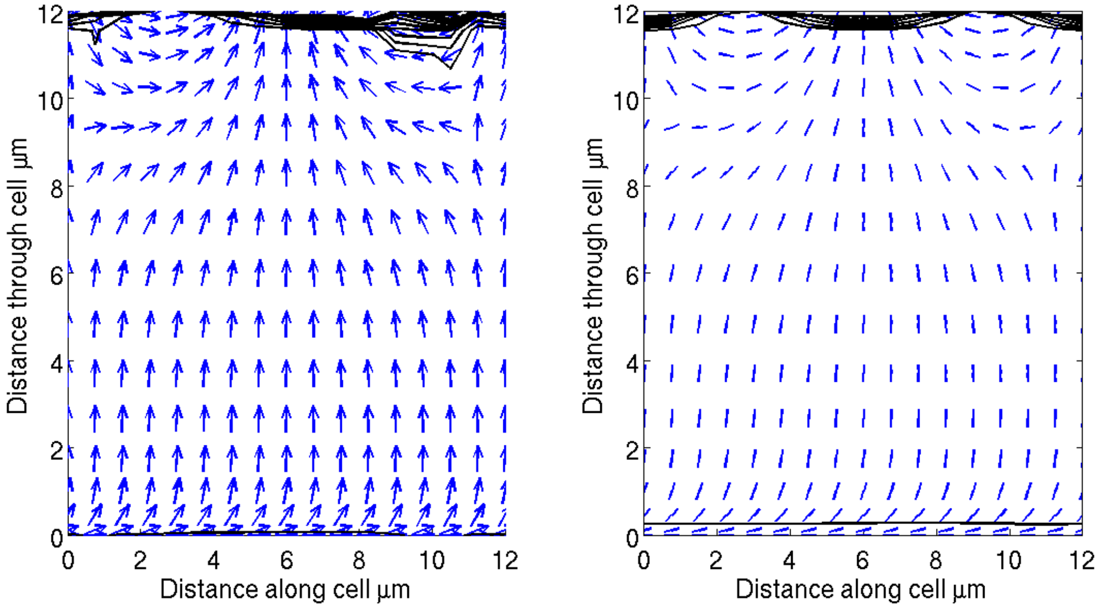

FIGURE 2.5: *Comparison of liquid crystal alignment. The left and right images show the director alignment for the FO model and the approximate Q-tensor model respectively. Director fields for both models are plotted, contour lines show areas of equal elastic energy, $|\boldsymbol{\nabla}\theta_{FO}|^2 = C$ in the FO model and $|\boldsymbol{\nabla}\boldsymbol{a}|^2 = C$ in the LdG model. The inaccuracy of the FO model can be seen in the asymmetry of $|\boldsymbol{\nabla}\theta_{FO}|^2$ near the boundary.*

of the code can be found in Appendix B.

Starting from the same initial conditions the FO and Q-tensor models are integrated till steady state is reached. The resulting configurations are compared and the differences are computed.

First we compare the FO model, derived in Section 2.2, with the approximate Q-tensor model. We observe that there is an area of the FO model which does not show good agreement with the Q-tensor model. By plotting the resulting director field as vectors and comparing the numerical gradient it can be seen that these errors correspond to the points where the FO model predicts unphysical gradients, Figure 2.5.

Similarly we can compare the full stiff Q-tensor equations with the non-stiff approximate equations derived in Section 2.4. Figure 2.6 shows a plot of the error in the approximate equation calculated using both the first order correction to the order parameter, equation (2.29), and the difference in the two simulations divided by the leading order scalar order parameter, equation

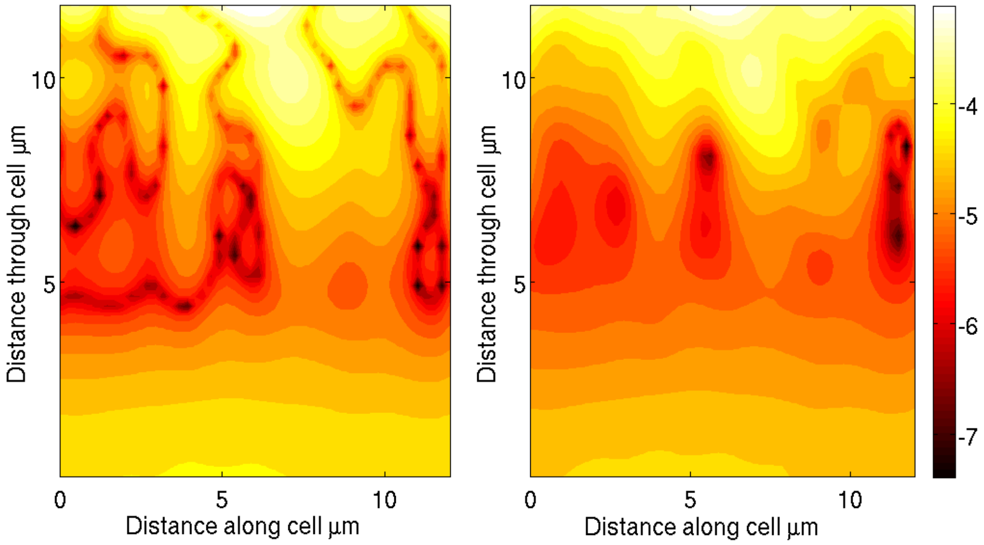

FIGURE 2.6: *2D director field error calculation for a 10 Volt spatially modulated electric field as described in text. The liquid crystal has strong planar anchoring boundary conditions at* $z = 0$ *and* $z = L_z$ *and periodic boundary conditions in the* x *direction. The error is calculated both through calculation of the correction to the scalar order parameter* $log_{10}(S_1/S_0)$ *(left) and through comparison to the full stiff equations* $log_{10}(\delta a)$*(right) where* δa *is given in equation (2.49).*

(2.33),

$$\delta a = \frac{1}{S_0}\left|\left|\boldsymbol{a}_{approx} - \boldsymbol{a}_{stiff}\right|\right|. \tag{2.49}$$

Not only is the error very low but when the two error plots are compared it can be seen that the approximate error is qualitatively comparable with the difference between the full stiff equations and the approximations derived here. In both plots the error peaks around the points of highest liquid crystal variation. This is expected as these points correspond to those with highest elastic energy.

Secondly we compare the 3D model, derived in Section 2.5, with the full stiff $\mathcal{Q}$-tensor model. In this case the boundary conditions fix the director out of plane in the y direction to allow for full 3D reorientation.

The steady state alignment results are shown in Figure 2.7. The comparison to the full stiff equations is shown in Figure 2.8 with error calculated using both the correction to the scalar order parameter and the percentage error given in equation (2.49). Again it can be seen that the difference between the two methods is very low and that the error approximation using the singular value decomposition method is comparable with the true error. We find for the same number of grid points, 12 in each spatial dimension, that the stiff code takes over an hour to converge whilst the approximate code converges to a solution with $\delta a \sim O(10^{-4})$ in a time of ≈ 45 seconds.

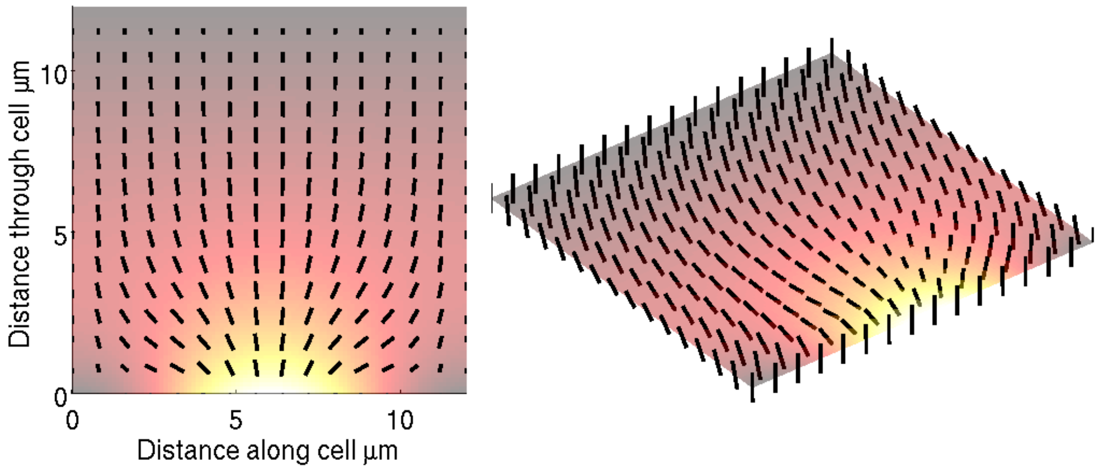

FIGURE 2.7: *Typical director field plot calculated using approximate equations for a 5 Volt spatially modulated electric field as described in text. The colour corresponds to the voltage throughout the cell. The liquid crystal alignment is parallel to the surface but twisted out of plane, this forces full three dimensional orientation of the liquid crystal when subject to a spatially modulated electric field.*

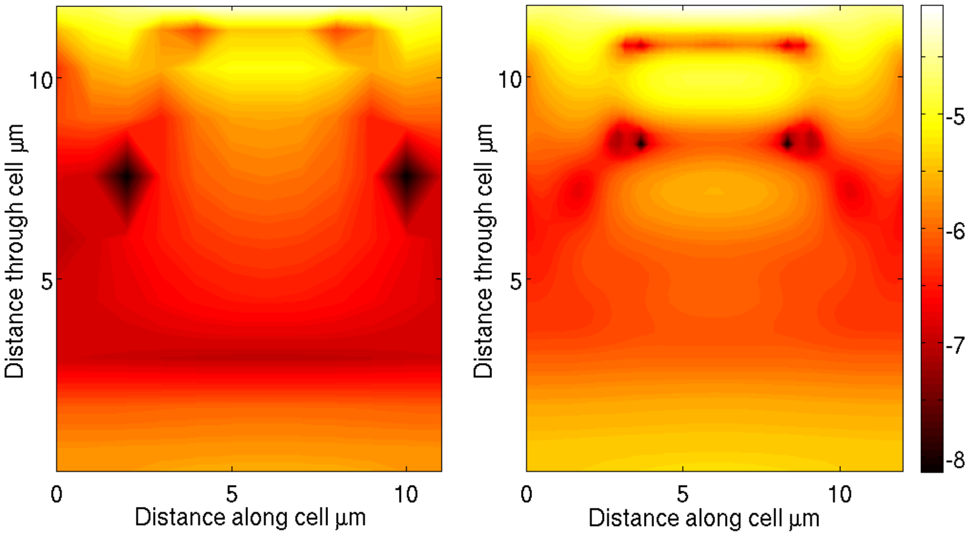

FIGURE 2.8: *3D director field error calculation for a 5 Volt spatially modulated electric field. The liquid crystal has strong out of plane anchoring boundary conditions at $z = 0$ and $z = L_z$ and periodic boundary conditions in the x direction. The error is calculated both through calculation of the correction to the scalar order parameter $log_{10}(S_1/S_0)$ (left) and through comparison to the full stiff equations $log_{10}(\delta a)$ (right) where δa is given in equation (2.49).*

2.7 Conclusion

The approximate equations derived in this chapter determine the liquid crystal alignment which minimises the Landau-deGennes free energy in the absence of defects. They can be solved in a fraction of the time required to solve the full stiff equations.

We have derived equations for both a two and three dimensional case and have implemented both as non-stiff initial value problems in MATLAB. Estimates of the accuracy of these equations have been derived in terms of the first order correction to the component values and have been shown to give strong qualitative agreement with the deviation of the approximation from the full stiff equations.

It should be noted that the free energy functions used in this paper are the simplest possible forms of the free energy. However, generalisation to other free energy functions, whose bulk energy minimisers are uniaxial, is relatively straightforward. Generalising this method to situations where the free energy supports biaxial states is also possible. In this case M_0 is a 3–manifold and expressions must be found for the equations of motion using a biaxial tensor representation with major and minor axis determined using all three Euler angles.

The major advantage of these equations with respect to the full stiff minimisers is that they can be computed in 1% of the time whilst producing results with error $\sim O(10^{-4})$. This will be of great importance in medium to large scale models where computational efficiency becomes an issue. The assumption that the elastic and electrostatic free energies remain small makes these equations suitable for geometries in which defects do not occur. As such these approximate equations will be of most use in applications where defects are undesirable. This is the case in many optical devices where smooth alignment of the liquid crystal is important, but, the FO model predicts unphysical configurations.

Chapter 3

Regime-independent coupled wave equations

In this chapter we derive a semi-analytic model to describe the coupling of optical beams as they propagate through a periodically modulated liquid crystal cell. This model is particularly useful as it can be used independently of the liquid crystal geometry. The model is combined with the liquid crystal model, derived in the previous chapter, to provide a thorough description of the system. A detailed analysis of the features of the photorefractive liquid crystal cell is provided and a simplified model for the electrical properties of the cell is developed.

This chapter is arranged as follows: In Section 3.1 we introduce optical coupling including a brief description of the different coupling regimes. In Section 3.2 we provide an introduction to existing methods to model beam coupling, including their derivations and limitations. In Section 3.3 we consider some of the problems involved in modelling beam coupling in a photorefractive liquid crystal cell. In Section 3.4 we derive a new model suitable for modelling beam coupling in all geometries. This model is verified in Section 3.5 through comparison to existing models and numerical simulations of Maxwell's equations we also consider in detail some of the features predicted by this model with reference to recent experiments. Finally, in Section 3.6, we use a simplified electrical circuit to model the electrical properties of the cell and comment on work which could be done to optimise these systems.

3.1 Introduction

The optical transfer of energy from one beam to another via diffraction from a refractive index grating has been observed in a variety of non-linear materials. This effect, known as beam coupling, or optical coupling, has a number of possible applications. These include: optical beam deflection, pattern recognition and image amplification [77]. Beam coupling is observed due to the non-linear way in which light and matter interact. Generally a non-linear material is one whose refractive index is dependent on the electric field at any given point. Beam coupling is observed in materials whose refractive index is related to the modulus square of the electric field. This effect is observed in, but not limited to, photorefractive crystals. These are non-linear optical materials which, when illuminated with an optical interference pattern, form a refractive index grating which is $\pi/2$ out of phase with the incident optical field.

Photorefractive crystals have been extensively used to observe beam coupling; for example large coupling coefficients have been observed in $\mathrm{BaTiO_3}$ and $\mathrm{Rh:BaTiO_3}$ crystals [78]. More recently efficient beam coupling was shown in a wide range of organic materials, such as fullerene [79] and CdSe doped [80] liquid crystals, polymer-dispersed [81] and ferroelectric liquid crystals [82], polymeric composites [83], hybrids with liquid crystals [84, 85, 86], light valves [86], photoconductive polymer-liquid crystal structures [87, 88] and photorefractive polymers [89, 90].

Physically beam coupling occurs due to the interference of two beams in a bulk photorefractive crystal. This sinusoidal interference pattern will create a sinusoidal modulation of the refractive index, which will scatter the beams. As the wave vector of the refractive index grating is equal to the difference between the wave vectors of the two beams, the diffraction of one beam into the direction of the other will be in phase, and will interfere constructively. Photorefractive like effects have also been observed at low power in liquid crystal cells using either a photoconducting [91] or photorefractive [92] alignment layer. Liquid crystals are an attractive choice for such applications due to their high birefringence and strong electro–optic response.

In this chapter we study the coupling effects of two beams incident on a planar cell containing liquid crystals sandwiched between a polyimide (PI) and a photoconducting polyvinyl-carbazole doped with C_{60} (PVK:C_{60}) layer as shown in Figure 3.1. The superposition of the two coherent incident beams on the photoconductor creates a modulation in the conductivity which, when combined with the applied DC voltage, produces the modulated electric field across the cell. This aligns the liquid crystals and modulates the refractive index. Such systems have been realised experimentally [84, 93], including the setup available in our group [91].

Theoretically there is no complete model of this system and those that exist simplify the system to one which can be described analytically. Here we look briefly at how the existing models have been developed and how their approaches differ from ours.

The coupling of light due to diffraction from inhomogeneous, anisotropic materials has been studied for many years [94, 95, 96, 97, 98, 99] and is often referred to as occurring in one of two distinct regimes, Bragg and Raman-Nath, see Figure 3.2.

Bragg regime coupling is characterised by the presence of only two beams and was initially described in 1969 by the coupled wave theory of Kogelnik [94] for an isotropic medium. This work was extended in 1997 by Montemezzani and Zgonik [95] to include optically anisotropic materials.

Raman-Nath diffraction is characterised by multiple diffracted output beams and was initially

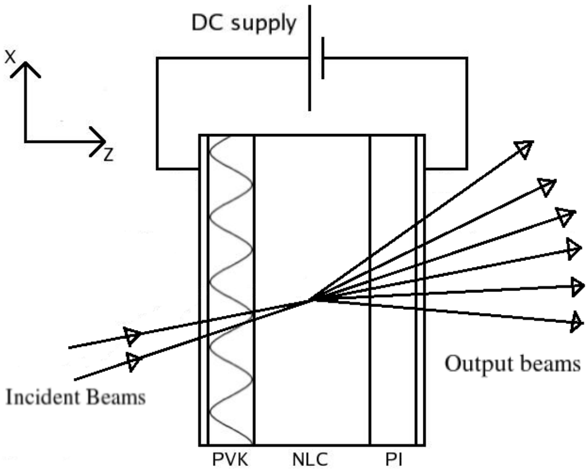

FIGURE 3.1: *Schematic of the system modelled: a nematic liquid crystal layer is sandwiched between two alignment layers, a photoconductor (PVK) and an insulator (PI). An electric potential is applied by means of transparent electrodes at either side of the cell. The system is assumed to be infinitely extended in the y direction and as such reduces to a two dimensional problem.*

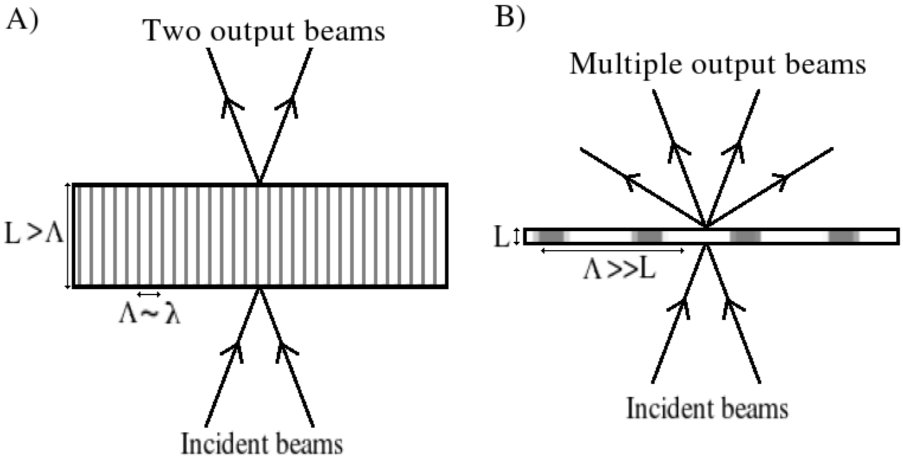

FIGURE 3.2: *Beam coupling effects in A) the Bragg regime and B) the Raman-Nath regime.*

modelled using the assumption that the grating is thin. Diffraction in this regime was first studied in 1936 [96]. This system is modelled by considering the modulated refractive index as a phase grating and neglecting any anisotropy in the materials. In the past couple of years modelling in the Raman-Nath regime has been extended using an approach similar to that of Kogelnik and Montemezzani to describe Raman-Nath diffraction in anisotropic media [97, 98].

Although the models just described offer ease of implementation and high computational efficiency they are restricted to specific regimes. Differentiation between the Bragg and Raman-Nath regimes is not always straightforward as both the thickness of the medium and the refractive index profile affect the nature of the diffracted beams. The first criteria used to distinguish the two regimes were suggested by Kogelnik [94], based on the dimensionless parameter

$$q = \frac{2\pi\lambda L}{n_u \Lambda^2}, \tag{3.1}$$

where Λ is the grating period, λ the free space wavelength of the light, n_u the homogeneous part of the refractive index and L the thickness of the medium. The Bragg regime is then defined as $q \gg 1$ and the Raman-Nath regime as $q \ll 1$. However, since then a variety of criteria have been suggested, as reviewed in [100], and more appropriate criteria for both Bragg and Raman-Nath [101] coupling regimes have been established based not only on q but also the Raman-Nath grating strength.

From the analysis of these criteria, it is clear that there is no distinct cut off point between Bragg and Raman-Nath regimes. Indeed, there is an intermediate regime in which neither theory is appropriate. It is this intermediate regime, in which little work has been done, which is of importance here. A more rigorous method, suitable for this regime, has been developed. This is based on direct substitution of the refractive index profile into Maxwell's equations and is suitable for both isotropic [2] and anisotropic [102] materials. This method has also been used for cascaded gratings with the constraint that the dielectric profile has the same period at the boundary between two gratings [103]. It has been shown to agree numerically with both the coupled wave approach and the Raman-Nath phase grating approach. Although it is in good agreement with the simpler theories this approach is less computationally efficient as it involves solving $4n$ coupled ODEs for n discrete wave vectors. Further, although highly flexible, the resulting system of equations must be solved independently for each geometry. This makes the model computationally inefficient for optimisation.

Although the early theories provide a good deal of insight into the coupling mechanisms, experimental geometries such as photorefractive liquid crystal cells are not as straightforward to model for a number of reasons. Firstly, due to the non-linear alignment of the liquid crystals with the applied electric field, liquid crystal refractive index profiles are non-uniform in the z direction and contain many harmonics of the fundamental grating vector in the x direction. Secondly, as nematic liquid crystal molecules are symmetric with respect to inversion, it is necessary to have a non-normal incidence angle for the bisector of the two incident beams in order to obtain the correct grating vector [92]. This means that as the grating is created by the superposition of the beams at the cell surface, there are no waves which can be perfectly matched by the fundamental grating vector. Finally, diffraction in these cells has been observed in both the Bragg [104] and the Raman-Nath [105] regimes. Simple changes in the geometry of the incident beams will move the system continuously from the Bragg to the Raman-Nath regime, through the intermediate regime. As such, a model has to be capable of describing both of these behaviours.

There are two main theoretical models for the diffraction of light by liquid crystal cells. Both of these models consider a linearisation of the equations governing the liquid crystal alignment. This is equivalent to considering small variation in the director angle and that the electric field is decoupled from the liquid crystal alignment. Jones and Cook [68] considered photorefractive liquid crystal cells in the Bragg regime. Their optical analysis is based in the Bragg coupling regime making their model inappropriate for the Raman-Nath regime. Further, they only consider the effects of the anisotropy on the refractive index seen by the beams as they propagate. This neglects fundamental polarisation effects observed in anisotropic crystals. Kubytskyi et al [99] consider photorefractive liquid crystal cells in the Raman-Nath regime. Their analysis is based on a geometrical optics approach suitable for thin gratings and has been verified by numerical simulation [106]. Whilst both of these approaches are appropriate only for specific coupling regimes, they each provide a great deal of insight into the coupling mechanisms involved. This allows clear identification of the key parameters involved in obtaining a strong optical coupling effect.

Here we model the liquid crystal alignment using the approximate $\mathcal{Q}$–tensor model developed in Chapter 2. We also propose a new model for beam coupling in the liquid crystal cell. This model does not make any assumptions which could restrict the models use to the Bragg or Raman-Nath regime. We take into account all possible scattered optical waves in the cell and their superposition. The model is developed for a cell with refractive index which is periodic (but not necessarily sinusoidal) in one direction and has arbitrary profile in the other. This profile has been chosen as it accurately reflects the profile of the liquid crystal cell. We have verified this model by comparison with finite element simulations and proved it to be accurate. We have also shown that the model is, under appropriate assumptions, analytically equivalent to existing models for beam coupling in specific regimes.

3.2 Modelling beam coupling

In order to understand how beam coupling works in liquid crystal cells we first consider some existing models. Suppose we have two coherent plane waves incident on a medium whose conductivity at any point is proportional to the intensity of the light at that location. If the waves are in the (x, z) plane and have wave vectors $\boldsymbol{k}_1$ and $\boldsymbol{k}_2$ we write the scaled intensity pattern at the surface of the medium $(z = 0)$ as

$$I = \left| A_1 e^{i\left(\frac{2\pi}{\lambda}\hat{\boldsymbol{k}}_1\cdot\boldsymbol{x}-\omega t\right)} + A_2 e^{i\left(\frac{2\pi}{\lambda}\hat{\boldsymbol{k}}_2\cdot\boldsymbol{x}-\omega t\right)} \right|^2 \tag{3.2}$$

where λ is the free space wavelength. After some manipulation equation (3.2) gives

$$I = A_1^2 + A_2^2 + 2A_1A_2\cos\left[\frac{2\pi}{\lambda}\left(\hat{\boldsymbol{k}}_1 - \hat{\boldsymbol{k}}_2\right)\cdot\boldsymbol{x}\right]. \tag{3.3}$$

This gives us a modulated intensity and hence a modulated conductivity with wave vector $\boldsymbol{K} = \boldsymbol{k}_1 - \boldsymbol{k}_2 = 2\pi/Lambda$ and Λ is the grating period. If this material is used as a boundary for a liquid crystal cell then, combined with an applied DC electric field, we obtain a modulated potential at the liquid crystal boundary and hence, a modulated electric field across the liquid crystal layer with a phase shift of $\frac{\pi}{2}$ from the incident intensity. The modulated electric field causes the liquid crystal to realign and produces a modulated refractive index in the cell. Beam coupling is caused by the superposition of the diffracted waves produced by this refractive index modulation.

3.2.1 Raman-Nath regime

In the case of Raman-Nath diffraction we consider a single plane wave incident at angle θ on a medium with periodically modulated refractive index where the interaction length L is small enough that the medium acts as a phase grating [96]. This approach is valid in the limit of thin gratings, this limit can be quantified by the dimensionless parameter q defined in equation (3.1). The Raman–Nath analysis is valid when $q \ll 1$. We write the modulation of the refractive index as

$$n_m = n_0 + \Delta n \sin(\boldsymbol{K} \cdot \boldsymbol{x}), \tag{3.4}$$

and the incident plane wave as

$$E = Ae^{i(\boldsymbol{k}\cdot\boldsymbol{x}-\omega t)}, \tag{3.5}$$

where $\boldsymbol{k}$ is the wave vector of the incident beam and ω the optical angular frequency, the wave at the far side of the medium can then be expressed as

$$E = A \exp\left\{ i \left[n_0 \boldsymbol{k} \cdot \boldsymbol{x} + \frac{2\pi \Delta n L}{\lambda \cos\theta} \sin(\boldsymbol{K} \cdot \boldsymbol{x}) - \omega t \right] \right\}. \tag{3.6}$$

We use the Jacobi-Anger identity for Bessel functions,

$$e^{i\delta \sin x} = \sum_{m=-\infty}^{\infty} J_m(\delta) e^{imx}, \tag{3.7}$$

to repackage the expression for electric field as a series of plane waves,

$$E_t = E_0 \sum_{m=-\infty}^{\infty} J_m(\delta) e^{in_0(\boldsymbol{k}+m\boldsymbol{K})\cdot\boldsymbol{x}} e^{-i\omega t}, \tag{3.8}$$

where

$$\delta = \frac{2\pi \Delta n L}{\lambda \cos(\theta)}. \tag{3.9}$$

The m–th order wave propagates with wave vector $\boldsymbol{k}_m = \boldsymbol{k} + m\boldsymbol{K}$ which propagates at angle $\sin\theta_m = m\lambda/(n_0\Lambda)$. Using equations (3.9) and (3.8) we can obtain the intensity for the diffraction beams at different order,

$$I_m = E_0^2 J_m^2(\delta). \tag{3.10}$$

A typical plot for the Raman-Nath intensity distribution as a function of distance through the cell is shown in Figure 3.3. It can be seen that over a short distance the energy from the incident wave is transferred first into the ±1 diffracted order, then from there into the next order and so on. As the distance into the cell increases the energy is spread between more waves, with no single large amplitude diffracted order occurring. For the case of two input beams the coupling can be described as the superposition of equation (3.10) for two different inputs.

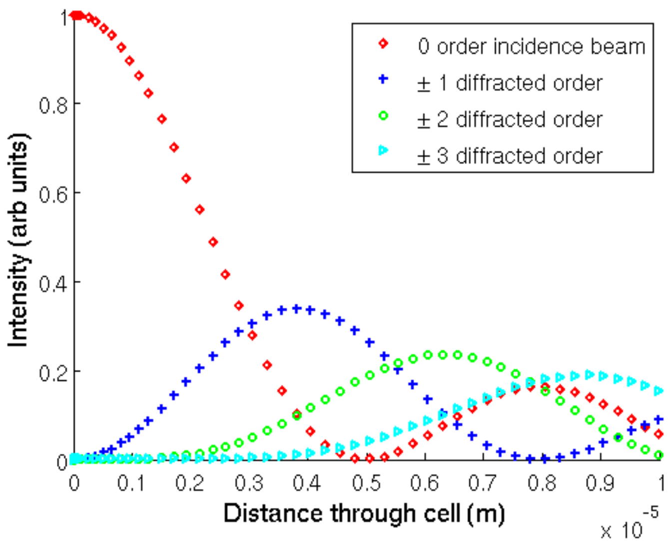

FIGURE 3.3: *Typical plot for Raman-Nath intensity distribution as a function of distance through cell.*

3.2.2 Bragg regime

Beam coupling in the Bragg regime is modelled by neglecting all diffracted orders except the two incident beams. This analysis holds whenever the regime parameter $q \gg 1$, where q is defined in equation 3.1. We substitute the non-homogeneous dielectric constant

$$\epsilon = \epsilon_u + \eta \Delta\epsilon \cos\left(\boldsymbol{K} \cdot \boldsymbol{x} + \varphi\right) \tag{3.11}$$

into the wave equation (1.3) [94]. Here φ is the phase shift between the optical interference pattern and the refractive index grating, ϵ_u is the homogeneous part of the dielectric constant, $\Delta\epsilon$ is the non-homogeneous part and $\eta \ll 1$ is a scaling parameter. It is important to note that the role of the φ in these systems is slightly different to the role of phase shift in a conventional photorefractive system (this will be discussed in Section 3.3.3). The method of multiple scales, which will be described in detail in Section 3.4, is used to obtain an expression for the slowly varying wave amplitudes

$$\hat{\boldsymbol{k}_1} \cdot \boldsymbol{\nabla} A_1 = i\frac{|\boldsymbol{k_0}|\Delta\epsilon}{4n}\left(\hat{\boldsymbol{e}}_1 \cdot \hat{\boldsymbol{e}}_2\right) A_2 e^{-i\varphi}, \tag{3.12a}$$

$$\hat{\boldsymbol{k}_2} \cdot \boldsymbol{\nabla} A_2 = i\frac{|\boldsymbol{k_0}|\Delta\epsilon}{4n}\left(\hat{\boldsymbol{e}}_2 \cdot \hat{\boldsymbol{e}}_1\right) A_1 e^{i\varphi}. \tag{3.12b}$$

Here $n = \sqrt{\epsilon_u}$ is the uniform part of the refractive index. These equations assume that the medium is thick and any higher order diffracted waves will be evanescent. As such they will be attenuated as they propagate. Beam coupling equations for the Bragg regime have also been derived in the case of an anisotropic medium [95] in which case ϵ is a tensor.

Equations (3.12) are usually solved as an eigenvalue problem. The simplest case is obtained by

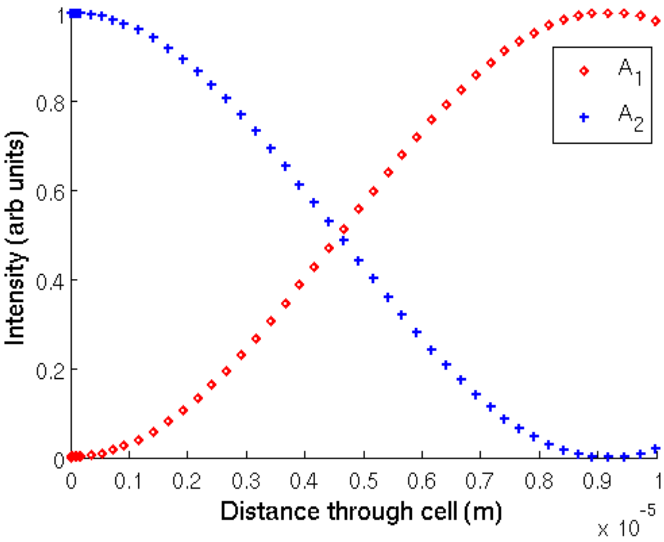

FIGURE 3.4: *Typical plot for Bragg intensity distribution as a function of distance through cell.*

choosing the coordinates such that the waves propagate in the x, z plane with polarisation in the y direction. The bisector of the two beams is also assumed to be normal to the x, y plane. This allows us to write equation (3.12) as

$$\begin{aligned} \frac{d\tilde{A}_1}{d\tilde{z}} &= i\tilde{A}_2 \\ \frac{d\tilde{A}_2}{d\tilde{z}} &= i\tilde{A}_1, \end{aligned} \tag{3.13}$$

where we have introduced the new variables $\tilde{A}_1 = A_1 e^{-i\varphi/2}$ and $\tilde{A}_2 = A_2 e^{i\varphi/2}$, and the scaled spatial variable

$$\tilde{z} = \frac{|\boldsymbol{k_0}|\Delta\epsilon}{4n\cos\theta} z. \tag{3.14}$$

Here θ is the angle at which the waves propagate with respect to the z axis. Equation (3.13) has solution

$$\begin{aligned} \tilde{A}_1 &= \frac{\tilde{A}_1(0) - \tilde{A}_2(0)}{2} e^{i\tilde{z}} + \frac{\tilde{A}_1(0) + \tilde{A}_2(0)}{2} e^{-i\tilde{z}}, \\ \tilde{A}_2 &= -\frac{\tilde{A}_1(0) - \tilde{A}_2(0)}{2} e^{i\tilde{z}} + \frac{\tilde{A}_1(0) + \tilde{A}_2(0)}{2} e^{-i\tilde{z}}, \end{aligned} \tag{3.15}$$

where the constants $\tilde{A}_1(0)$ and $\tilde{A}_2(0)$ are the initial amplitudes of the two beams. The coupling strength depends not only on the input optical intensities but also on the relative phase of the beams with the grating. A typical plot for the Bragg regime intensities is shown in Figure 3.4.

In this case it can be seen that the energy transfers entirely from the incident beam A_1 into A_2 before beginning to transfer back. All the energy is confined to one of two different directions, this is in contrast to the Raman-Nath case where the energy progressively spreads throughout the diffracted orders.

These two models are well established and have been used to describe coupling in the different regimes successfully. We wish to extend these models such that they can be used to model Bragg, Raman-Nath and the intermediate regimes.

3.3 Beam coupling in a liquid crystal cell

In this section we consider some of the properties of the photorefractive liquid crystal cells which make them different from standard photorefractive crystals. These properties require careful consideration during the derivation of the regime independent model.

3.3.1 Anisotropy

To understand how light behaves in such a medium we consider the wave equation (derived in Section 1.2)

$$\boldsymbol{\nabla} \times \boldsymbol{\nabla} \times \boldsymbol{E} = \omega^2 \mu \epsilon \boldsymbol{E}. \tag{3.16}$$

where $\mu = \mu_0 \mu_r$ is the permeability of the medium, $\epsilon = \epsilon_0 \epsilon_r$ is the dielectric permittivity and ∂_t is the derivative with respect to time and $\boldsymbol{E}$ is the electric field. For an anisotropic material ϵ_r is a tensor. We assume equation (1.3) has a solution in the form of a plane wave

$$\boldsymbol{E} = \boldsymbol{A} e^{i(\boldsymbol{k} \cdot \boldsymbol{x} - \omega t)}, \tag{3.17}$$

where $\boldsymbol{k} = \frac{\omega}{c} n \hat{\boldsymbol{k}}$ and n the refractive index in that direction. Substituting into equation (1.3), we obtain

$$n^2 \boldsymbol{A} - n^2 \hat{\boldsymbol{k}} (\hat{\boldsymbol{k}} \cdot \boldsymbol{A}) = \epsilon_u \mu_r \boldsymbol{A} \tag{3.18}$$

Equation (3.18) is simplified by choosing the coordinate axes so that they coincide with the principal optical axes of the medium. Hence, the dielectric tensor is diagonal:

$$\epsilon_r = \begin{pmatrix} n_x^2 & 0 & 0 \\ 0 & n_y^2 & 0 \\ 0 & 0 & n_z^2 \end{pmatrix}, \tag{3.19}$$

where n_x, n_y, n_z are the refractive indices in the x, y and z directions respectively. Substituting (3.19) into (3.18) allows us to write an expression for the electric field components

$$A_i = \frac{n^2 \hat{k}_i (\hat{\boldsymbol{k}} \cdot \boldsymbol{A})}{n^2 - \mu_r \epsilon_i}. \tag{3.20}$$

We multiply both sides by $\hat{k}_i$ and sum over i to obtain

$$\frac{\hat{k}_x^2}{n^2 - \mu_r \epsilon_x} + \frac{\hat{k}_y^2}{n^2 - \mu_r \epsilon_y} + \frac{\hat{k}_z^2}{n^2 - \mu_r \epsilon_z} = \frac{1}{n^2}. \tag{3.21}$$

This is Fresnel's equation of wave normals [3], which we wish to solve to find the eigenvelocities at which light travels through the birefringent medium. This allows us to define the refractive indices, the direction in which the waves propagate and hence, using equation (3.20), the polarisation. We follow the method of Born and Wolf [3] and multiply equation (3.21) by n^4 and use the fact that $\hat{k}_x^2 + \hat{k}_y^2 + \hat{k}_z^2 = 1$. We obtain the following quadratic equation for the phase velocity $v_p^2 = c/n^2$

$$\hat{k}_x^2(v_p^2 - v_y^2)(v_p^2 - v_z^2) + \hat{k}_y^2(v_p^2 - v_z^2)(v_p^2 - v_x^2) + \hat{k}_z^2(v_p^2 - v_x^2)(v_p^2 - v_y^2) = 0, \tag{3.22}$$

where the component velocities are $v_i = c/\sqrt{\mu_r \epsilon_i}$. At present the only assumption we have made is that the coordinate axes coincide with the principal optical axes of the crystal. No assumptions have been made about the nature of the crystal. Nematic liquid crystals are known as uniaxial crystals, meaning that they have one axis of complete rotational symmetry. Hence they have only two refractive indices, $n_x = n_y = n_o$ and $n_z = n_e$ where the subscripts o and e refer to the ordinary and extraordinary refractive indices respectively. This means we can write the component form of the velocities as $v_x = v_y = v_o$ and $v_z = v_e$ where v_o and v_e are the ordinary and extraordinary velocities respectively. We write $\hat{\boldsymbol{k}}$ in spherical coordinates in order to simplify equation (3.22)

$$\hat{\boldsymbol{k}} = \begin{pmatrix} \sin\theta_i \cos\phi_i \\ \sin\theta_i \sin\phi_i \\ \cos\theta_i \end{pmatrix}, \tag{3.23}$$

where θ_i and ϕ_i are the standard spherical coordinate angles. We use this and equation (3.22) to obtain a simpler expression for phase velocity

$$(v_p^2 - v_o^2)[\sin^2\theta_i(v_p^2 - v_e^2) + \cos^2\theta_i(v_p^2 - v_o^2)] = 0. \tag{3.24}$$

This equation has two roots which tell us the velocities at which the wave propagates in any given direction. It is worth noting that as we are solving for v_p^2 there will be four solutions for v_p. These will form equal and opposite pairs which correspond to propagation in opposite directions. By inspection the two roots are

$$\begin{aligned} v_{p1}^2 &= v_o^2, \\ v_{p2}^2 &= v_o^2 \sin^2\theta_i + v_e^2 \cos^2\theta_i. \end{aligned} \tag{3.25}$$

The phase velocities of the light rays propagating through the medium are independent of the angle the ray makes with the ordinary axis. It is only the angle which the ray makes with the extraordinary axis which is important in determining these velocities as shown in Figure 3.5.

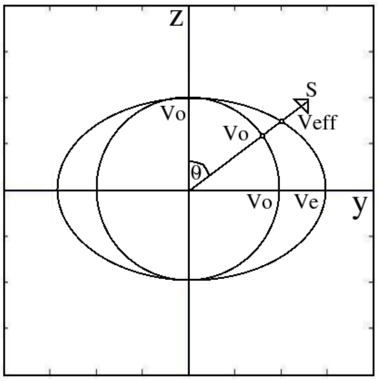

FIGURE 3.5: *Phase velocity for ordinary and extraordinary waves.*

Using the eigenvelocities we can calculate the eigen–indices of refraction for the system:

$$\begin{aligned} n_1 &= n_o, \\ n_2 &= \frac{n_e n_o}{\sqrt{n_e^2 \cos^2\theta_i + n_o^2 \sin^2\theta_i}}. \end{aligned} \tag{3.26}$$

It is usual to name these refractive indices as the ordinary refractive index n_o which has no direction dependence and the effective refractive index n_{eff} which depends on the direction of propagation.

As an aside, these expressions can be used to experimentally verify the liquid crystal model through cross polarised intensity experiments. Cross polarised intensity is the light intensity observed for a beam transmitted through two polarisers at an angle of $\frac{\pi}{2}$ to each other, as shown in Figure 3.6. If the first polariser is placed such that it makes an angle of $\frac{\pi}{4}$ to the x, z plane then we can write light transmitted through the polariser in the z direction in terms of its polarisation components

$$\boldsymbol{E} = E_0 e^{i(kz-\omega t)} \left[\cos\left(\frac{\pi}{4}\right)\hat{\boldsymbol{x}} + \sin\left(\frac{\pi}{4}\right)\hat{\boldsymbol{y}}\right] = \frac{E_0}{\sqrt{2}} e^{i(kz-\omega t)} \left[\hat{\boldsymbol{x}} + \hat{\boldsymbol{y}}\right]. \tag{3.27}$$

A birefringent material is placed between the polarisers with its optical axis is in the x, z plane. At its exit facet one the component of light polarised in plane will be phase shifted by an amount $\Delta\varphi$ with respect to the other. Hence, the electric field can be written as

$$\boldsymbol{E} = \frac{E_0}{\sqrt{2}} e^{i(kz-\omega t)} \left(e^{i\Delta\varphi}\hat{\boldsymbol{x}} + \hat{\boldsymbol{y}}\right). \tag{3.28}$$

This light is then transmitted through the analyser (a second polariser making an angle of $\frac{\pi}{2}$ to the first polariser). The electric field of the beam transmitted through the analyser is

$$\boldsymbol{E}_\perp = \frac{E_0}{2} e^{i(kz-\omega t)} \left(1 - e^{i\Delta\varphi}\right)\left(-\hat{\boldsymbol{e}}_x + \hat{\boldsymbol{e}}_y\right). \tag{3.29}$$

From here the cross polarised intensity can be calculated by multiplying the electric field by its

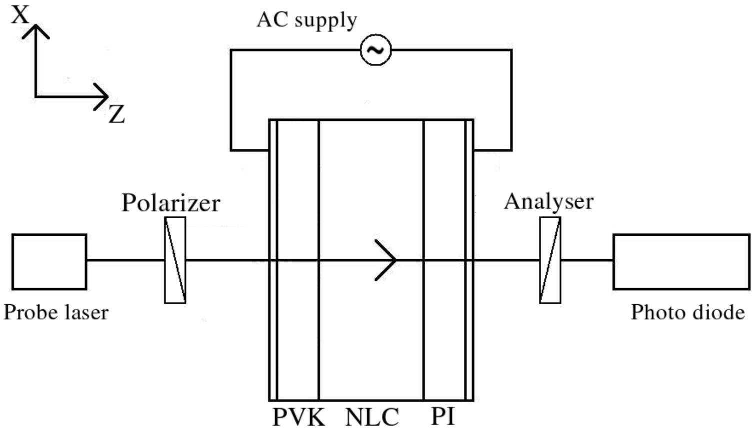

FIGURE 3.6: *Experimental setup for cross polarised intensity experiment. Polarised light is transmitted through the photorefractive liquid crystal cell before being measured using an analyser (a second polariser at $\pi/2$ to the first) and a photodiode. As voltage is applied to the liquid crystal cell the molecules realign creating an additional phase shift in one polarisation component. The result is a variation in light intensity measured at the photo diode.*

complex conjugate to obtain

$$I_{\perp} = \sin^2 \frac{\Delta\varphi}{2}. \tag{3.30}$$

Equation (3.30) can be used to verify that the liquid crystal models can accurately predict the director orientation under different applied voltage forms. In order to do this we need to determine the phase shift $\Delta\varphi$ as a function of propagation through the liquid crystal. In calculating the cross polarised intensity we assume that only the phase of the light is affected by the liquid crystals medium and that the optical axis is restricted to the x, z plane.

We now consider the original problem of a normal incidence plane wave passing through two polarisers. After the first polariser the light will be polarised at $45°$ to the x, z plane. The out-of-plane component will see the ordinary refractive index whilst the in-plane component will see the effective refractive index. Over a small distance dz the in plane and out of plane waves will develop a phase shift,

$$d\Delta\varphi = \frac{2\pi}{\lambda} \left(n_o - n_{eff}\right) dz, \tag{3.31}$$

over the length of the cell this gives a total phase shift

$$\Delta\varphi = \frac{2\pi}{\lambda} \int_0^L \left(n_o - n_{eff}\right) dz. \tag{3.32}$$

Substituting equation (3.32) into equation (3.30), gives a cross polarised intensity,

$$I_{\perp} = \sin^2 \left[\frac{\pi}{\lambda} \int_0^1 \left(n_o - n_{eff}\right) dz\right]. \tag{3.33}$$

Equation (3.33) is solved using a numerical Clenshaw-Curtis quadrature scheme (see Appendix B.5) and is coupled to the liquid crystal model to allow us to plot the cross polarised intensity of light transmitted through the cell, at the boundary $z = L$, as a function of cell thickness and voltage. This numerical model can then be directly compared with experimental observations. We compare the predictions of the numerical models with experimental results for two different liquid crystal cells, one containing the liquid crystal compound E7 and the other TL205. The cross polarised intensity is obtained from both the director and tensor liquid crystal models in the case of TL205 and only from the director model in the case of E7. This is because the splay and bend elastic constants in TL205 are very similar and, as such, the single elastic constant approximation used in the tensor model is valid. However, in the case of E7 the difference in elastic constants is not small and, as such, experimental comparison using the single elastic constant is not possible.

Experimentally the system is set up as described above: the input laser beam is split into two beams, the intensity of one beam is measured directly, the other is measured after it has passed through the crossed polarisers and the liquid crystal cell, allowing us to compensate for any modulation in the laser intensity. The cross-polarised intensity is measured for a variety of different AC voltages, and the experiments are run first increasing the voltage from 0 to V_{max} then decreasing back to 0. Comparison of the two curves allows us to ensure the liquid crystal has reached steady state alignment.

The fitting algorithm uses a non-linear least squares method to determine the elastic constants which best fit the experimental behaviour. First however, the cell length is determined from the total phase shift observed in the experiment. At high voltage all the liquid crystal will be aligned in the z–direction. Therefore, the in plane and out of plane components of the field will see the same refractive index. This means the the cross polarised intensity will asymptote to zero. Using this knowledge, the initial value of $I_\perp$ and the number of times $I_\perp$ oscillates with voltage we can determine the total phase shift of the beam. Combining this with the optical wavelength we can obtain the cell thickness.

The E7 cell is compared first, this cell is calculated as 11.1μm thick with liquid crystal refractive indices, $n_e = 1.764$, $n_o = 1.522$, and DC dielectric constants, $\epsilon_\perp = 5.17$, $\epsilon_\| = 19.54$, the optical wavelength of light used is $\lambda = 543.5$nm and the molecular pretilt is 0° on the PVK side and 2° on the PI side. Figure 3.7 shows the comparison of theoretical and experimental cross polarised intensities. The fitting parameters used are the elastic constants for bend and splay, the best fit is obtained from $K_1 = 11.08$pN and $K_3 = 22.67$pN, these values are comparable to those found in the literature $K_1 = 11.7$pN and $K_3 = 19.5$pN [107].

Figures 3.8 gives the experimental comparison for the TL205 cell, using the director model. This cell is approximately 11.8μm thick with liquid crystal refractive indices, $n_e = 1.745$, $n_o = 1.527$, and dielectric constants, $\epsilon_\perp = 4.9$, $\epsilon_\| = 9.1$, the optical wavelength, pretilt angles and anchoring strengths used are the same as in the E7 case. The best fit values for the splay and bend elastic constants are $K_1 = 16.11$pN and $K_3 = 15.83$pN, these are slightly smaller than the known values, $K_1 = 17.3$pN and $K_3 = 20.4$pN.

The experimental comparison for the TL205 cell with the $\mathcal{Q}$ tensor model is shown in Figure 3.9. Here the cell parameters used are the same as for the director model of the TL205 cell. In

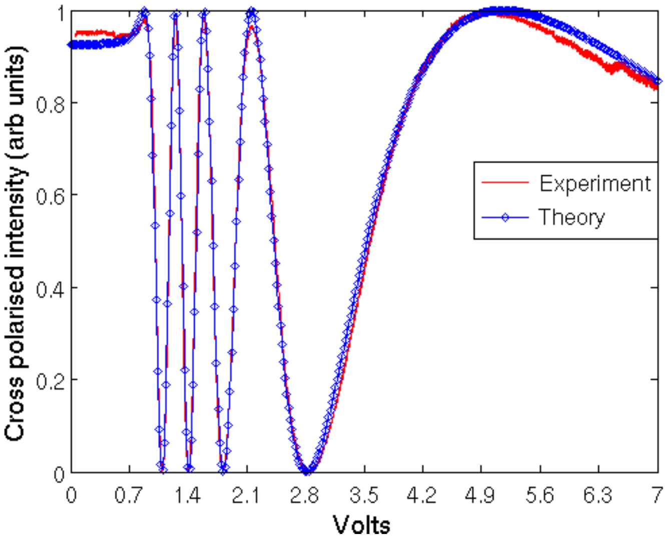

FIGURE 3.7: *Experimental comparison for E7 liquid crystal using director model. The cell length is calculated from the total observed phase shift and the fit is obtained using the elastic constants K_1 and K_3 as fitting parameters. Experimental data by Mark Herrington and Malgosia Kaczmarek*

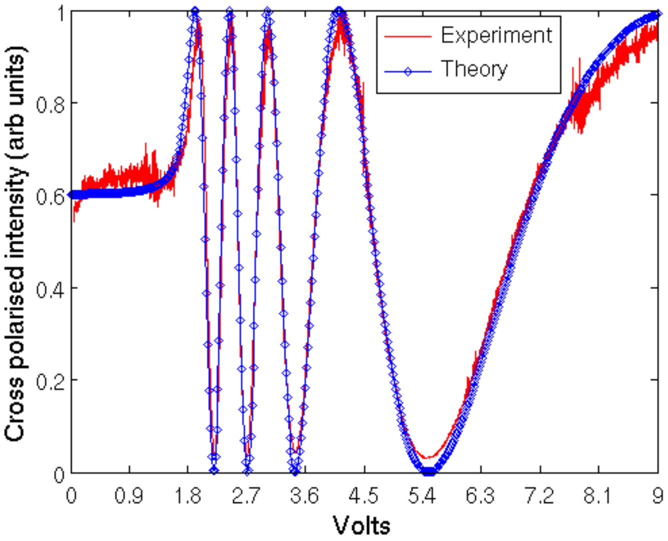

FIGURE 3.8: *Experimental comparison for TL205 liquid crystal using director model. The cell length is calculated from the total observed phase shift and the fit is obtained using the elastic constants K_1 and K_3 as fitting parameters. Experimental data by Mark Herrington and Malgosia Kaczmarek*

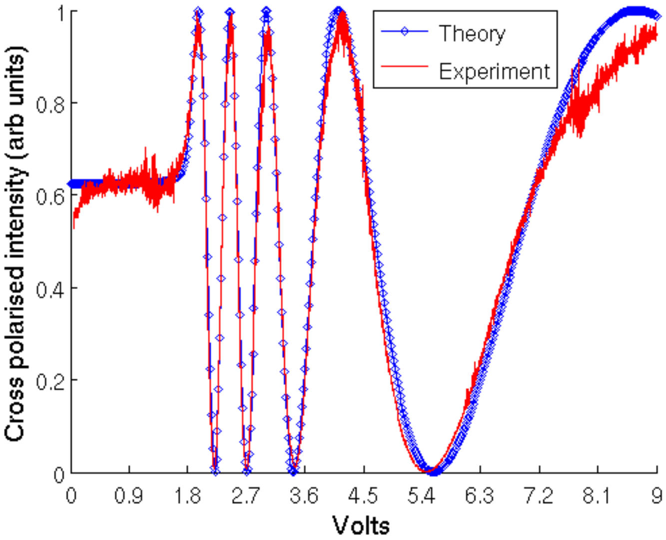

FIGURE 3.9: *Experimental comparison for TL205 liquid crystal using Q tensor model. The cell length is calculated from the total observed phase shift and the fit is obtained using the single elastic constant K as fitting parameter. Experimental data by Mark Herrington and Malgosia Kaczmarek*

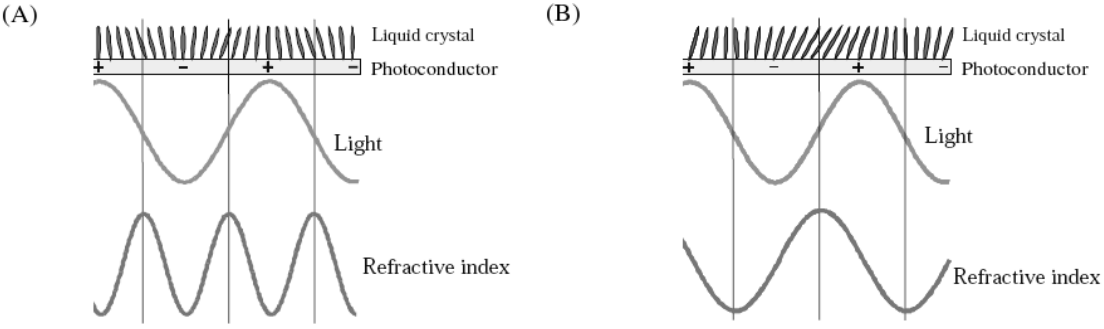

FIGURE 3.10: *Symmetry breaking in liquid crystal cell, reproduced from [74]. (A) Refractive index profile seen by normal incidence light for zero pretilt. (B) Refractive index profile seen by normal incidence light with pretilt.*

this case we have only one elastic constant to used as a fitting parameter. However, it can be seen from Figure 3.9 that this is enough. The fitted value for the elastic constant is $K = 15.9$pN, this was calculated using a scalar order parameter $S = 1$.

It is clear from these results that, for a uniform AC applied voltage, the director model for the liquid crystal cell is sufficiently accurate. Also for the case of the TL205 cell a single elastic constant approach as used in the Q–tensor model is an accurate assumption as the splay and bend constants are similar. Whilst the Q–tensor model developed here is not appropriate for the E7 cell it is worth noting that this can be overcome by using a more general form of the elastic free energy and is not a limitation of the Q–tensor approach in general.

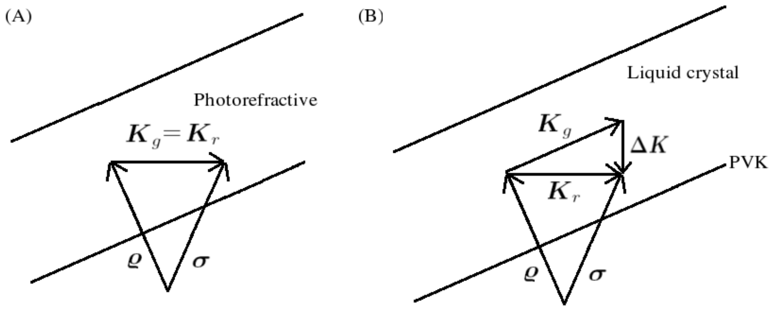

FIGURE 3.11: *Grating vectors seen in typical beam coupling experiments. (A) Photorefractive material, refractive index grating vector is the one required to match the two waves regardless of cell tilt. (B) Liquid crystal cell with mismatch between refractive index grating and optical grating.*

3.3.2 Geometry and symmetry considerations

Beam coupling in a liquid crystal cell differs from beam coupling in a photorefractive material in two ways, both of which are due to the way in which the grating is formed. Firstly, due to the symmetries of a liquid crystal cell, i.e. the fact that a liquid crystal aligned at $+\vartheta$ has the same refractive index to one aligned at $-\vartheta$ the fundamental refractive index grating vector will be of twice the length of that required to couple the two incident beams. At first glance this would suggest that the normal incidence gain is zero in a Bragg regime setup. However, as we will see when we analyse the regime independent model in Section 3.5.4, a small amount of gain can still be observed in this situation. Typically the problem of small gain is overcome by either tilting the liquid crystal cells or by using liquid crystal cells with a large molecular pre-tilt on the photoconducting side, see Figure 3.10. Secondly, in a photorefractive crystal the materials non-linearity causes the refractive index grating vector to be exactly the difference between the two incident optical wave vectors. As such energy is transferred between two adjacent beams with no phase mismatch, see Figure 3.11(A). However, in a liquid crystal cell the grating is produced due to the interaction of the incident optical field with the very thin photoconducting layer. The modulation in conductivity in this layer then causes the refractive index grating vector to be tangential to the photoconducting layer regardless of the cell orientation. This means that the fundamental grating vector is different to the one required to match the two incident beams as shown in Figure 3.11(B).

Before we develop the regime independent beam coupling model, it is important to understand the role of these two effects in detail. The first of these requires that the liquid crystal cell has some asymmetry in order to produce the correct grating vector to match the incident beams whilst the second requires low cell tilt in order to minimise the mismatch induced by this effect.

The refractive index profile of a liquid crystal beam coupling cell seen by a single incidence beam is determined by equation (3.26). The alignment of the liquid crystal is determined by the intensity interference pattern. Therefore, a good approximation for ϑ, the angle the optical axis makes with the z–axis, is $\vartheta = \vartheta_0 \sin(\boldsymbol{K}_g \cdot \hat{\boldsymbol{x}})$, where $\boldsymbol{K}_g$ is the grating vector required to produce photorefractive gain, then the refractive index seen by a beam incident at angle ϑ_i to the surface normal is given by

$$n_{eff} = \frac{n_e}{\sqrt{1 + \left(\frac{n_e^2 - n_o^2}{n_o^2}\right) \cos^2\left(\vartheta_0 \sin(\boldsymbol{K}_g \boldsymbol{\cdot} \hat{\boldsymbol{x}}) + \vartheta_i\right)}}. \tag{3.34}$$

Linearising equation (3.34) by assuming $\vartheta_i \ll 1$, $\vartheta_0 \ll 1$ and $n_e^2 - n_o^2 \ll n_o^2$ allows us to obtain an approximation for the refractive index seen by a beam incident on the cell:

$$n_{eff} \approx n_e \left\{ 1 - \frac{1}{4}\left(\frac{n_e^2 - n_o^2}{n_o^2}\right)\left[2 - 4\vartheta_i\vartheta_0 \sin(\boldsymbol{K}_g \boldsymbol{\cdot} \hat{\boldsymbol{x}}) - \vartheta_0^2(1 - \cos(2\boldsymbol{K}_g \boldsymbol{\cdot} \hat{\boldsymbol{x}})) + O\left(\vartheta_0^3\right)\right] \right\}. \tag{3.35}$$

For any $\theta_i \neq 0$ we can see that the input beam will see the fundamental component of the grating vector and be diffracted. However, for normal incidence i.e. $\theta_i = 0$ there will be no coupling through the fundamental grating vector. At first glance this suggests that any angle of incidence can be chosen with the exception of normal incidence. However, if we have two beams incident on the photoconducting layer separated by angle 2α, with bisector normal to the cell surface then the two input beams will each see the fundamental grating vector. However, the grating seen by beam 1 will be shifted by π with respect to the grating seen by beam 2. As the two beams do not see the same grating the result will be no energy transfer. Whilst this analysis seems somewhat incomplete we will see in Section 3.5.4 that it provides a good approximation to the full analysis of normal incidence beam coupling.

Therefore in order to obtain photorefractive gain it is necessary to have either a large pre-tilt on the molecular surface alignment or to tilt the cell. The most common of these two methods is to tilt the cell as large pre-tilt angles are hard to obtain using conventional alignment layers. Unfortunately there is a price to be paid in doing this: the mismatch between the two beams, which is larger the greater the cell tilt. The two incident beams defined above have wave vectors defined as

$$\boldsymbol{\varrho}_i = k_0 n_i \left[\cos(\beta_i - \alpha_i)\hat{\boldsymbol{e}}_z + \sin(\beta_i - \alpha_i)\hat{\boldsymbol{e}}_x\right] \tag{3.36a}$$

and

$$\boldsymbol{\sigma}_i = k_0 n_i \left[\cos(\beta_i + \alpha_i)\hat{\boldsymbol{e}}_z + \sin(\beta_i + \alpha_i)\hat{\boldsymbol{e}}_x\right], \tag{3.36b}$$

where, $k_0 = 2\pi/\lambda_0$, λ_0 is the free space wavelength and n_i is the refractive index outside the liquid crystal cell. On entering the cell these beams will refract and as such can be written as

$$\boldsymbol{\varrho}_t = k_0 n_t \left[\cos(\beta_t - \alpha_t)\hat{\boldsymbol{e}}_z + \sin(\beta_t - \alpha_t)\hat{\boldsymbol{e}}_x\right] \tag{3.37a}$$

and

$$\boldsymbol{\sigma}_t = k_0 n_t \left[\cos(\beta_t + \alpha_t)\hat{\boldsymbol{e}}_z + \sin(\beta_t + \alpha_t)\hat{\boldsymbol{e}}_x\right], \tag{3.37b}$$

where the subscript t refers to the transmitted wave angles. Snell's law in this case states that

$$n_i \sin(\beta_i \pm \alpha_i) = n_t \sin(\beta_t \pm \alpha_t). \tag{3.38}$$

As such, the tangential part of the electric field is conserved across the boundary as expected due to Maxwell's boundary condition. The grating vector within the liquid crystal is based only on the tangential component within the photoconducting layer, and can be written as

$$\boldsymbol{K}_g = k_0 n_t \left[\sin\left(\beta_t - \alpha_t\right) - \sin\left(\beta_t + \alpha_t\right)\right] \hat{\boldsymbol{e}}_x. \tag{3.39}$$

However, the grating vector, $\boldsymbol{K}_r = \boldsymbol{\varrho}_t - \boldsymbol{\sigma}_t$, required to match the two waves in the medium is

$$\boldsymbol{K}_r = k_0 n_t \left[\left(\sin\left(\beta_t - \alpha_t\right) - \sin\left(\beta_t + \alpha_t\right)\right) \hat{\boldsymbol{e}}_x + \left(\cos\left(\beta_t - \alpha_t\right) - \cos\left(\beta_t + \alpha_t\right)\right) \hat{\boldsymbol{e}}_z\right]. \tag{3.40}$$

Therefore, there is a grating vector mismatch equal to the difference between $\boldsymbol{K}_g$ and $\boldsymbol{K}_r$,

$$\boldsymbol{\Delta K} = k_0 n_t \left(\cos\left(\beta_t - \alpha_t\right) - \cos\left(\beta_t + \alpha_t\right)\right) \hat{\boldsymbol{e}}_z. \tag{3.41}$$

From this analysis we can see that for $\beta_t = 0$ the mismatch vanishes. This is also the condition for the fundamental refractive index component to be zero. As such there must be some optimum angle at which the mismatch is small, yet the fundamental refractive index grating component is non-zero.

3.3.3 Phase shift

In typical photorefractive crystals the phase shift between the grating and the beams is of fundamental importance for coupling to take place [108]. In liquid crystal cells this is not the case as the following analysis demonstrates. This has already been observed in [99] but the authors did not pursue this point in any detail.

To understand the role of the phase shift in these systems it is important to first understand the role of phase shift in a conventional photorefractive system. In these systems the refractive index grating at any point in the cell is defined by the electric field at that point in space. Therefore two waves of the form $E_1(\boldsymbol{x}) = R(\boldsymbol{x})e^{i(k_x x + k_z z - \omega t)}$ and $E_2(\boldsymbol{x}) = S(\boldsymbol{x})e^{i(-k_x x + k_z z - \omega t)}$ will interfere to form a grating which can be written as,

$$I = R(\boldsymbol{x})S(\boldsymbol{x})\left[e^{i(2k_x x)} + e^{-i(2k_x x)}\right]. \tag{3.42}$$

As there is an implicit phase shift φ_g between the intensity interference pattern and the dielectric profile, the dielectric profile will take the form,

$$\epsilon = \epsilon_u + \Delta\epsilon R(\boldsymbol{x})S(\boldsymbol{x})\left[e^{i(2k_x x + \varphi_g)} + e^{-i(2k_x x + \varphi_g)}\right]. \tag{3.43}$$

After substitution into the wave equation we can derive the scaled coupled wave equations for a photorefractive material [109],

$$\frac{dR(\boldsymbol{x})}{d\hat{z}} = iR(\boldsymbol{x})|S(\boldsymbol{x})|^2 e^{i\varphi_g} \tag{3.44a}$$

$$\frac{dS(\boldsymbol{x})}{d\hat{z}} = iS(\boldsymbol{x})|R(\boldsymbol{x})|^2 e^{-i\varphi_g}. \tag{3.44b}$$

As $R(\boldsymbol{x})$ and $S(\boldsymbol{x})$ are complex quantities they can be written in modulus argument form $R(\boldsymbol{x}) = \sqrt{I_r(\boldsymbol{x})}e^{-i\varphi_r(\boldsymbol{x})}$ and $S(\boldsymbol{x}) = \sqrt{I_s(\boldsymbol{x})}e^{-i\varphi_s(\boldsymbol{x})}$. Substituting into equation (3.44) gives us the following equations for the intensities and phases

$$\begin{aligned} \frac{dI_r}{dz} &= -2I_r I_s \sin\varphi_g, \quad & \frac{dI_s}{dz} &= 2I_r I_s \sin\varphi_g, \\ \frac{d\phi_r}{dz} &= I_s \cos\varphi_g, & \frac{d\phi_s}{dz} &= I_r \cos\varphi_g. \end{aligned} \tag{3.45}$$

It can be seen that for $\varphi_g = 0$ these equations decouple and there is no energy transfer between the two beams. Physically this can be thought of as the grating shifting in space with the interference pattern: although the phase of the two beams changes in space there is no overall phase shift in the system. In photorefractive systems the phase shift is $\varphi_g = \pi/2$ throughout the crystal. In our cells this is not the case as the grating is fixed by the boundary of the cell. Therefore, regardless of the phase shift between the grating and the intensity interference pattern we will see energy exchange induced by the phase shift which develops between the two beams during propagation. Starting from the linear beam coupling equations in the Bragg regime,

$$\frac{dR(\boldsymbol{x})}{d\hat{z}} = iS(\boldsymbol{x})e^{i\varphi_g} \tag{3.46a}$$

$$\frac{dS(\boldsymbol{x})}{d\hat{z}} = iR(\boldsymbol{x})e^{-i\varphi_g}, \tag{3.46b}$$

we can make the same substitution, $R(\boldsymbol{x}) = \sqrt{I_r(\boldsymbol{x})}e^{-i\varphi_r(\boldsymbol{x})}$ and $S(\boldsymbol{x}) = \sqrt{I_s(\boldsymbol{x})}e^{-i\varphi_s(\boldsymbol{x})}$ and obtain:

$$\begin{aligned} \frac{dI_r}{dz} &= -2\sqrt{I_r I_s}\sin\left(\varphi_g - \varphi_r(\boldsymbol{x}) + \varphi_s(\boldsymbol{x})\right), \quad & \frac{dI_s}{dz} &= 2\sqrt{I_r I_s}\sin\left(\varphi_g - \varphi_r(\boldsymbol{x}) + \varphi_s(\boldsymbol{x})\right), \\ \frac{d\phi_r}{dz} &= I_s \cos\left(\varphi_g - \varphi_r(\boldsymbol{x}) + \varphi_s(\boldsymbol{x})\right), & \frac{d\phi_s}{dz} &= I_r \cos\left(\varphi_g - \varphi_r(\boldsymbol{x}) + \varphi_s(\boldsymbol{x})\right). \end{aligned} \tag{3.47}$$

In this case we can see that these equations decouple when $\varphi_g - \varphi_r(\boldsymbol{x}) + \varphi_s(\boldsymbol{x}) = 0$. In this case the solution to equations (3.47) is $I_r = C_0$, $I_s = C_1$, $\varphi_r = I_s z + C_2$ and $\varphi_s = I_r z + C_3$, where C_j are arbitrary constants. These equations are consistent if

$$\varphi_g - I_s z + C_2 + I_r z + C_3 = 0. \tag{3.48}$$

Equation 3.48 must be satisfied for all z, this is only the case if $I_r = I_s$. From this analysis we can conclude that we will always see energy transfer between the two beams, even for $\varphi_g = 0$, except in the case where $I_r = I_s$. In this case the two beams will propagate through the grating with no change in intensity and will develop a phase shift proportional to the distance travelled. In other words, for the special case of equal input intensities the two beams will propagate through the material unaltered by the grating. Physically this can be thought of as the two beams each coupling energy into the other at the same rate, this results in zero net energy transfer. In general at the cell boundaries the photorefractive liquid crystal cells, like general photorefractive crystals, have a phase shift $\varphi_g = \pi/2$. However, the overall phase shift between the interference pattern and the grating is not $\pi/2$ throughout the cell. Hence, the cells are only truly photorefractive at the PVK:C$_{60}$ boundary.

3.4 Derivation of regime independent coupling model

To derive the regime independent coupling model, we start from the wave equation (1.3), derived in Section 1.2. We consider a medium which contains a periodic refractive index grating in the (x, z) plane with a fundamental grating with wavenumber $K = \frac{2\pi}{\Lambda}$ in the x direction and any number of higher grating harmonics pK where $p = 2, 3, ...$ and Λ is the grating period. We further assume that the medium is birefringent and that each Fourier component of the dielectric tensor, $\Delta\epsilon^{(p)}$, may vary slowly in the z direction so that the dielectric tensor may be expressed as:

$$\epsilon_r(x, z) = \epsilon_u + \eta\frac{1}{2}\sum_{p=-\infty}^{\infty} \Delta\epsilon^{(p)}(\eta z)e^{i\left(pKx+\varphi^{(p)}\right)}, \tag{3.49}$$

where, $\eta \ll 1$ is a smallness parameter, ϵ_u is the uniform part of the dielectric tensor and $\varphi^{(p)}$ is the phase shift of the p-th grating Fourier component. We assume that the optical axis of ϵ_u is in the plane formed by the complete set of optical wave vectors as this is typically the case for a liquid crystal photorefractive cell. For compactness of notation we assume the z–dependence to be implicit in $\Delta\epsilon^{(p)}$ and absorb the phase into the complex tensor Fourier coefficients. These will eventually be obtained from a complex Fourier transform of the liquid crystal alignment profile.

The non-homogeneous part of ϵ_r is small. Therefore, to leading order we can neglect it. As such we obtain a set of ordinary and extraordinary eigenmodes with wave vectors $\hat{\boldsymbol{k}}_o^{(m)}$ and $\hat{\boldsymbol{k}}_e^{(m)}$ respectively. These have out of plane polarisation $\hat{\boldsymbol{e}}_o^{(m)}$ for the ordinary mode and in plane polarisation $\hat{\boldsymbol{e}}_e^{(m)}$ for the extraordinary mode. The derivation of these polarisations and wave vectors is described in Section 3.3.1. The coupling between modes is described by the $O(\eta)$ correction to the amplitudes and is found using the method of multiple scales. This coupling takes two forms, coupling between the different Fourier components of the field and coupling between the ordinary and extraordinary components. The coupling between the Fourier components can be achieved by diffraction from the fundamental grating vector and any of its higher harmonics, as illustrated in Figure 3.12 A and B. It should be noted that if the bisector of the two incident waves is not normal, none of the wave vectors will be perfectly matched by the fundamental grating vector, see Section 3.3.2. Therefore, the coupling strength will depend not only on the amplitude of the appropriate coupling harmonic, but also on the size of the mismatch term $\Delta K^{(m,n)} = k_z^{(m)} - k_z^{(n)}$.

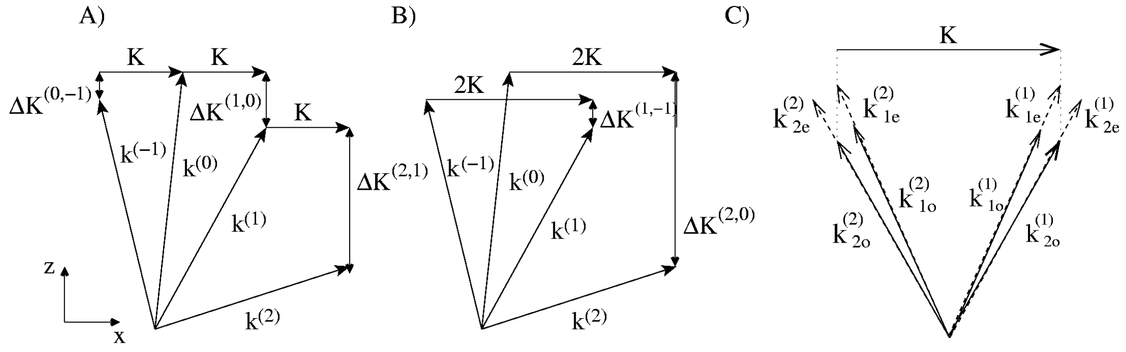

FIGURE 3.12: *Possible couplings and associated mismatch terms for ordinary and extraordinary waves A) Coupling of Fourier components by the fundamental grating period. B) Coupling of Fourier components by the second harmonic. C) Coupling of ordinary and extraordinary waves by the fundamental Fourier component. This is the minimum number of components it is possible to consider if we want to obtain consistent equations.*

Coupling between the ordinary and extraordinary modes is illustrated in Figure 3.12 C. For the most general case of arbitrary input polarisation there are two sets of ordinary and extraordinary waves required to match the boundary conditions. Coupling occurs between the waves generated at the boundary, $\hat{\boldsymbol{k}}_{1e}^{(m)}$ and $\hat{\boldsymbol{k}}_{2o}^{(m)}$, and their corresponding ordinary and extraordinary parts. The processes of coupling between different Fourier components and different polarisations occur simultaneously in any general photorefractive system. However, as these two processes make the derivation rather complex we consider a simplified system. For a first order dielectric tensor restricted to the plane formed by the incoming grating vectors then we need only consider the coupling between the Fourier components. This significantly simplifies the algebra and the resulting equations. Whilst this assumption may seem restrictive it is generally true for the case of a photorefractive cell. However, for completeness we consider the more general case where the optical axis of $\Delta\epsilon^{(p)}$ points in an arbitrary direction in Appendix C.

As the non-homogeneous part of the dielectric constant is small we observe a separation of scales in this system. We use this to set up a multiple scale expansion in terms of the scaled spatial variables: $\boldsymbol{x}_0 = \boldsymbol{x}$ and $\boldsymbol{x}_1 = \eta\boldsymbol{x}$ and the scaled derivatives

$$\begin{aligned}\frac{\partial}{\partial \boldsymbol{x}} &= \frac{\partial \boldsymbol{x}_0}{\partial \boldsymbol{x}}\frac{\partial}{\partial \boldsymbol{x}_0} + \frac{\partial \boldsymbol{x}_1}{\partial \boldsymbol{x}}\frac{\partial}{\partial \boldsymbol{x}_1} \\ &= \frac{\partial}{\partial \boldsymbol{x}_0} + \eta\frac{\partial}{\partial \boldsymbol{x}_1},\end{aligned} \tag{3.50}$$

which, for compactness of notation can be written $\boldsymbol{\nabla} = \boldsymbol{\nabla}_0 + \eta\boldsymbol{\nabla}_1$. The electric field in the material is written as a power series expansion in η, where we need only retain the lowest order terms, $\boldsymbol{E}^{(m)} = \boldsymbol{E}_0^{(m)} + \eta\boldsymbol{E}_1^{(m)} + O(\eta^2)$ and the fields at each order are assumed to be a superposition of the ordinary and extraordinary plane waves which may be perfectly matched by the grating vectors in the x direction. Hence the field is periodic in x with fundamental wave number K. We expand it in a Fourier series in x to obtain

$$\boldsymbol{E}_j = \sum_{m=-N}^{N} \boldsymbol{A}_{1e,j}^{(m)}(\boldsymbol{x}_1)\, e^{i\boldsymbol{k}_{e,j}^{(m)}\cdot\boldsymbol{x}-i\omega t}, \tag{3.51}$$

where the subscript j refers to the term of order j in the expansion and the subscripts o, e refer to the ordinary and extraordinary waves respectively. Assuming the optical axis of $\Delta\epsilon^{(p)}$ is in plane then we need only consider the fields $\boldsymbol{A}_{1e,j}^{(m)}$. As these are the only fields we drop the subscript $1e$. The amplitude is assumed to vary spatially with the inhomogeneity in the dielectric constant and $\boldsymbol{k^{(m)}} = mK\hat{\boldsymbol{e}}_x + k_z^{(m)}\hat{\boldsymbol{e}}_z$, with the constraint that $|\boldsymbol{k^{(m)}}| = k_0 n^{(m)}$. Here k_0 is the free space wavenumber, $n^{(m)}$ is the refractive index seen by the m-th wave and we assume that the evanescent waves may be neglected. Therefore, the total number of optical components is $2N+1$ where $N = \frac{k_0}{|\boldsymbol{K}|}$. Substituting equations (3.51) and (3.49) into (1.3) we expand to first order to obtain a set of coupled wave equations in terms of the scaled spatial variable $\boldsymbol{x}_1$ for the amplitudes $\boldsymbol{A}_0^{(m)}$

$$\begin{aligned} \boldsymbol{\nabla}_0 \times \boldsymbol{\nabla}_0 \times \boldsymbol{E}_1 - \frac{\omega^2}{c^2}\epsilon_u \boldsymbol{E}_1 = \\ -\boldsymbol{\nabla}_0 \times \boldsymbol{\nabla}_1 \times \boldsymbol{E}_0 - \boldsymbol{\nabla}_1 \times \boldsymbol{\nabla}_0 \times \boldsymbol{E}_0 + \frac{k_0^2}{2}\sum_{p=-\infty}^{\infty} \Delta\epsilon^{(p)} e^{ipKx}\boldsymbol{E}_0. \end{aligned} \tag{3.52}$$

This is a non-homogeneous equation for $\boldsymbol{E}_1$ of the form $\mathcal{L}_0\boldsymbol{E}_1 = \mathcal{L}_1\boldsymbol{E}_0$, where $\mathcal{L}_j$ refers to the order j linear operator. Solving the homogeneous part of this equation we find that $\boldsymbol{E}_{1h}$, the homogeneous part of $\boldsymbol{E}_1$, has the same spatial dependence as $\boldsymbol{E}_0$. Solving the non-homogeneous part of equation (3.52) would therefore require a trial solution which grows linearly in $\boldsymbol{x}_0$ resulting in unbounded growth. As the energy of the system is finite we must require that $\boldsymbol{E}_1$ is bounded. Therefore, the solvability condition is that the coefficients of the terms resonant with $\boldsymbol{E}_{1h}$ in the non-homogeneous part of (3.52) must be zero,

$$\boldsymbol{\nabla}_0 \times \boldsymbol{\nabla}_1 \times \boldsymbol{E}_0 + \boldsymbol{\nabla}_1 \times \boldsymbol{\nabla}_0 \times \boldsymbol{E}_0 = \frac{k_0^2}{2}\sum_{p=-\infty}^{\infty} \Delta\epsilon^{(p)} e^{ipKx}\boldsymbol{E}_0. \tag{3.53}$$

Substituting equation (3.51) into equation (3.53), using the identity (which can be derived graphically from Figure 3.12)

$$\boldsymbol{k}_e^{(m)} = \boldsymbol{k}_e^{(n)} + (m-n)K\hat{\boldsymbol{e}}_x + \left(k_z^{(m)} - k_z^{(n)}\right)\hat{\boldsymbol{e}}_z, \tag{3.54}$$

and collecting terms with the same $\boldsymbol{x}_0$ dependence allows us to obtain

$$\begin{aligned} ik^{(m)}\left[(\hat{\boldsymbol{k}}^{(m)}\cdot\hat{\boldsymbol{e}}^{(m)})\boldsymbol{\nabla}_1 + \hat{\boldsymbol{k}}^{(m)}(\hat{\boldsymbol{e}}^{(m)}\cdot\boldsymbol{\nabla}_1) - 2\hat{\boldsymbol{e}}^{(m)}(\hat{\boldsymbol{k}}^{(m)}\cdot\boldsymbol{\nabla}_1)\right]A^{(m)} = \\ \frac{k_0^2}{2}\sum_{n=-N}^{N}\Delta\epsilon^{(n-m)}\hat{\boldsymbol{e}}^{(n)}A^{(n)}e^{i(k_z^{(n)}-k_z^{(m)})z_1} \end{aligned} \tag{3.55}$$

The phase detuning term on the right hand side of (3.55) comes from equation (3.54) and is considered to be a function of the slow spatial variable z_1. This assumption requires that $k_z^{(m)} \ll |\boldsymbol{k}^{(m)}|$. It is clear than although this is not always the case, in general it holds that $k_z^{(m)} < |\boldsymbol{k}^{(m)}|$. However, as $k_z^{(m)}$ becomes comparable with $|\boldsymbol{k}^{(m)}|$ it can be seen that very little coupling will take place and the variation in the amplitude becomes $O(\eta)$. Therefore, we would expect that the error induced by this assumption is not of significant effect on the results obtained. We see later, through comparison to finite element simulations of Maxwell's equations, that this is the case. Equation (3.55) is a vector equation and it must be satisfied in all of its components. To ensure this is the case we project it onto the directions $\hat{\boldsymbol{e}}^{(m)}$, $\hat{\boldsymbol{k}}^{(m)}$ and the magnetic field polarisation direction $\hat{\boldsymbol{h}}^{(m)}$. Projecting onto $\hat{\boldsymbol{h}}^{(m)}$, equation (3.55) becomes

$$ik^{(m)}(\hat{\boldsymbol{k}}^{(m)} \cdot \hat{\boldsymbol{e}}^{(m)})\hat{\boldsymbol{h}}^{(m)} \cdot \boldsymbol{\nabla}_1 A^{(m)} = \frac{k_0^2}{2} \sum_{n=-N}^{N} \hat{\boldsymbol{h}}^{(m)} \Delta\epsilon^{(n-m)} \hat{\boldsymbol{e}}^{(n)} A^{(n)} e^{i(k_z^{(n)} - k_z^{(m)})z_1}. \tag{3.56}$$

At this point we notice that the first order dielectric tensor is in plane whilst $\hat{\boldsymbol{h}}^{(m)}$ is out of plane. Therefore the right hand side of equation (3.56) is zero. This means that the amplitude is constant in the direction orthogonal to the plane of propagation. This agrees with the symmetry argument that the system is invariant in the direction orthogonal to the plane of propagation. However, had the first order dielectric tensor been out of plane, then equation (3.56) would be in violation of the systems symmetries. To overcome this we would require the inclusion of the full set of possible wave vectors, see Appendix C. Projecting onto the wave vector $\hat{\boldsymbol{k}}^{(m)}$ gives the equation

$$ik^{(m)}\boldsymbol{d}^{(m)} \cdot \boldsymbol{\nabla}_1 A^{(m)} = \frac{k_0^2}{2} \sum_{n=-N}^{N} \hat{\boldsymbol{k}}^{(m)} \Delta\epsilon^{(n-m)} \hat{\boldsymbol{e}}^{(n)} A^{(n)} e^{i(k_z^{(n)} - k_z^{(m)})z_1} \tag{3.57}$$

where $\boldsymbol{d}^{(m)} = \hat{\boldsymbol{e}}^{(m)} - \left(\hat{\boldsymbol{k}}^{(m)} \cdot \hat{\boldsymbol{e}}^{(m)}\right) \hat{\boldsymbol{k}}^{(m)}$. This is simply a statement of the divergence equation $\boldsymbol{\nabla} \cdot \epsilon_r \boldsymbol{E} = 0$ to $O(\eta)$ and describes the variation of the amplitudes in the direction of the electric displacement vector. The coupled wave equations are found by projecting onto the electric field polarisation, the resulting equations are

$$\begin{gathered} 2ik^{(m)} \left[(\hat{\boldsymbol{k}}^{(m)} \cdot \hat{\boldsymbol{A}}^{(m)})\hat{\boldsymbol{A}}^{(m)} - \hat{\boldsymbol{k}}^{(m)}\right] \cdot \boldsymbol{\nabla} A^{(m)} = \\ \frac{k_0^2}{2} \sum_{n=-N}^{N} \left[\hat{\boldsymbol{A}}^{(m)} \Delta\epsilon^{(n-m)}(z) \hat{\boldsymbol{A}}^{(n)} A^{(n)} e^{-i\Gamma\varphi^{(n-m)}} e^{i(k_z^{(n)} - k_z^{(m)})z_1}\right] \end{gathered} \tag{3.58}$$

The bracketed term on the left hand side of equation (3.58) can be written as $-\hat{\boldsymbol{u}}^{(\boldsymbol{m})} g^{(m)}$. Here

$$\hat{\boldsymbol{u}} = \frac{\boldsymbol{A} \times \boldsymbol{H}}{|\boldsymbol{A} \times \boldsymbol{H}|} \tag{3.59}$$

is the unit Poynting vector, $g^{(m)} = \left(\hat{\boldsymbol{A}}^{(\boldsymbol{m})} \cdot \hat{\boldsymbol{D}}^{(\boldsymbol{m})}\right)$ and $\hat{\boldsymbol{D}}$ is the electric displacement unit vector. By writing $k^{(m)} = n^{(m)}k_0$, introducing the new variable

$$A^{(m)} = \tilde{A}^{(m)} e^{-ik_z^{(m)} z_1} \tag{3.60}$$

and, based on the translational symmetry of the system, requiring that the amplitudes are invariant in the x direction we obtain the first order correction to the field amplitudes,

$$\frac{d\tilde{A}^{(m)}}{dz_1} = ik_z^{(m)}\tilde{A}^{(m)} + ik_0 \sum_{n=-N}^{N} \frac{\hat{e}^{(m)}\Delta\epsilon^{(n-m)}\hat{e}^{(n)}}{4n^{(m)}g^{(m)}\hat{u}_z^{(m)}}\tilde{A}^{(n)}. \tag{3.61}$$

Equation (3.61) can, for the simple case of $\Delta\epsilon^{(n-m)}$ being constant in z, be solved as an eigenvalue problem. For all other cases the equations are solved using a Runge Kutta method in MATLAB. A typical plot for the intensities produced by this model is shown in Figure 3.13: plots are shown for Bragg, Raman-Nath and the intermediate regime of coupling. The parameters used to generate these plots are the same as those used to generate the typical Bragg and Raman-Nath plots (Figures 3.4 and 3.3) to aid comparison.

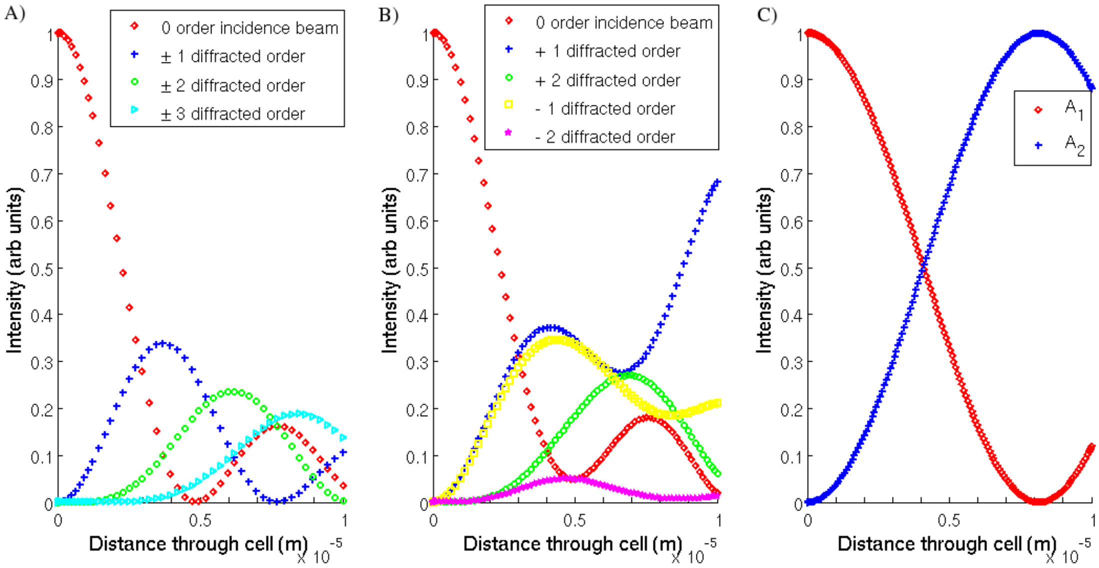

FIGURE 3.13: *Typical plot for intensities produced by the regime independent model: A) Raman-Nath regime $q = 0.03$. B) Intermediate regime, $q = 3.02$. C) Bragg regime, $q = 46.50$.*

It can be seen that Figure 3.13 A and C are identical to the plots for Bragg and Raman-Nath regime coupling given earlier. The intermediate diffraction regime (Figure 3.13) shows behaviour which is similar to both Bragg and Raman-Nath regimes. Energy is transfered to higher diffracted orders, however, the majority of the energy still stays in the incidence beam and the $+1$ diffracted order.

Equation (3.61) is the fundamental result of this chapter, it describes the coupling of an arbitrary number of beams in a system whose dielectric profile is slowly varying in the z direction and modulated with fundamental period Λ in the x direction. This extension to the anisotropic coupled wave theory has been derived to allow us to model systems in the Bragg, Raman-Nath and intermediate regimes. The model developed here takes into account all possible coupling combinations between the various optical waves propagating though the medium and all possible mismatch terms for an in plane dielectric tensor. The general equations for an arbitrary tensor are dealt with in Appendix C. The use of a general grating profile in the z direction makes the model useful for more complex systems such as the liquid crystal cell.

3.5 Model verification

In this section we show that the model derived to describe optical coupling in a liquid crystal cell is accurate. This analysis is split into two parts. First the model is compared to the standard models for the different regimes. Secondly, finite element simulations are used to verify the model independently of the coupling regime.

3.5.1 Comparison to existing models

The existing Bragg and Raman-Nath diffraction models have been successfully used previously for simple geometries to model optical coupling. Here we show that as well as being numerically equivalent for these geometries and optical incidence angles, the equations are analytically identical for an appropriate set of assumptions.

The Bragg case is straightforward. Under the assumption of a single grating Fourier component, a constant dielectric profile in the z direction and the presence of only two waves, equation (3.61) becomes

$$\begin{aligned}\hat{u}_z^{(1)}\frac{dA^{(1)}}{dz} &= \frac{ik_0}{4n^{(1)}g^{(1)}}\hat{\boldsymbol{A}}^{(1)}\Delta\epsilon\hat{\boldsymbol{A}}^{(2)}A^{(2)}e^{i\boldsymbol{\Delta K}\cdot\boldsymbol{x}},\\ \hat{u}_z^{(2)}\frac{dA^{(2)}}{dz} &= \frac{ik_0}{4n^{(2)}g^{(2)}}\hat{\boldsymbol{A}}^{(2)}\Delta\epsilon\hat{\boldsymbol{A}}^{(1)}A^{(1)}e^{-i\boldsymbol{\Delta K}\cdot\boldsymbol{x}}.\end{aligned} \tag{3.62}$$

These expressions become equal to those derived by Montemezzani [95], once the assumption of zero absorption has been made.

The comparison to Raman-Nath phase grating theory is less obvious. Again, we begin by making the assumptions of a single grating Fourier component of large wavelength, and a constant dielectric profile in the z direction. As the grating wavelength is large the deviation in propagation angles of the beams is small. Hence the mismatch term $k_z^{(n)} - k_z^{(m)}$ is small and may be neglected for thin materials. For comparison, the system is simplified for an isotropic material with all waves polarised out of the plane. If we then make the standard Raman-Nath assumption of a $\pi/2$ phase shift and a single normal incidence input beam with amplitude A_0, we may write equation (3.61) as

$$2\cos\theta^{(m)}\frac{2n}{k_0\Delta\epsilon}\frac{dA^{(m)}}{dz} = \left[A^{(m-1)} - A^{(m+1)}\right], \tag{3.63}$$

where $\theta^{(m)}$ is the angle with respect to the surface normal at which the m-th wave propagates. Using the assumption that the wave propagation directions differ by a small amount we may approximate $\theta^{(m)}$ by the propagation angle of the incident beam $\theta^{(i)}$. To proceed we make the following change of variable

$$\zeta = \frac{k_0 \Delta\epsilon}{2n\cos\theta_i} z. \tag{3.64}$$

Making use of the Bessel recurrence relation,

$$2\frac{dJ_m}{dz} = \left[J_{m-1} - J_{m+1}\right], \tag{3.65}$$

it can be seen that equation (3.63) is satisfied by the m-th order Bessel function $A_0 J_m(\zeta)$. This gives the optical envelope $A^{(m)} = A_0 J_m(\zeta)$. By writing the non-homogeneous dielectric constant in terms of the refractive indices we can write the intensity of the m-th order wave, with free space wavelength λ, after propagation through a material of thickness L as

$$I^{(m)} = A_0^2 J_m^2 \left(\frac{2\pi\Delta n L}{\lambda\cos\theta_i}\right) \tag{3.66}$$

which is identical to the optical envelope predicted by the Raman-Nath phase grating theory, see equation (3.10).

This analysis demonstrated how equation (3.61) is, under realistic assumptions, equivalent to either Bragg or Raman-Nath theory.

3.5.2 Comparison to Maxwell's equations

The regime independent model has been compared against the standard models for Bragg and Raman-Nath diffraction. We now use Comsol Multiphysics, a finite element modelling package, to solve Maxwell's equations directly and hence verify its accuracy for the intermediate regime, $0.1 \geq q \geq 10$, see equation (3.1).

We define a rectangular geometry with sides parallel to the x and z axis. The boundary conditions are periodic in the x-direction with periodicity of the refractive index. The finite element simulations are carried out with an optical wavelength of 1μm, as shorter wavelengths would require an extremely fine finite element mesh and, hence, considerable computation time.

We first verify that the model behaves correctly for a single grating component K which is constant for all z. To ensure that q lies in the intermediate regime the following parameters are used: $L = 12\mu$m, $\Lambda = 11.5\mu$m, which give the regime parameter $q = 1.4210$. The incident electric field is normal to the cell boundary $z = 0$. The refractive indices chosen in this system correspond to those of a typical liquid crystal, $n_o = 1.5$ and $n_e = 1.7$ giving the dielectric profile as

$$\epsilon_r = \begin{pmatrix} n_o^2 & 0 \\ 0 & n_e^2 \end{pmatrix} + \begin{pmatrix} -0.1 & 0.05 \\ 0.05 & 0.1 \end{pmatrix} \cos\left(Kx\right). \tag{3.67}$$

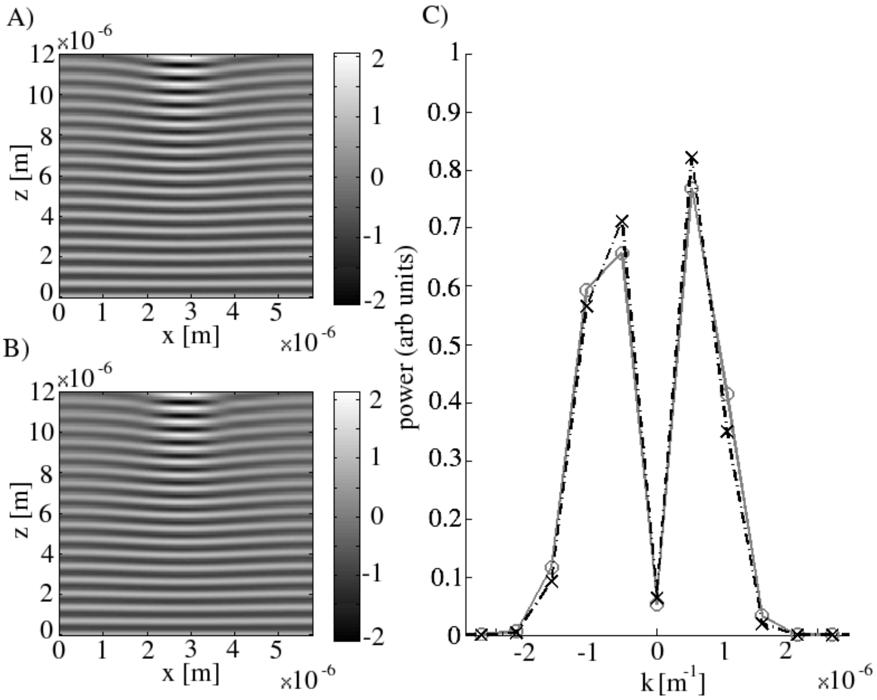

FIGURE 3.14: *Finite element comparison for the case of a single grating Fourier component: A) x-component of electric field in cell for coupled wave model, the coloured fringes correspond to the optical amplitude as shown in the adjacent colourbar. B) x-component of electric field in cell for finite element simulation. C) Optical power spectrum at output of cell where '○' is the coupled wave approximation and '×' is the finite element simulation.*

Figure 3.14 A and B compares the field calculated within the cell by the coupled wave model and the finite element method. Part C compares the power spectra calculated by each method. From the power spectrum it can be seen that the optical energy has coupled almost completely from the incident beam into its two closest neighbours. The slight asymmetry in the coupling is due to the presence of the off diagonal components in the dielectric tensor (this is considered in more detail in Section 3.5.3). The optical power spectrum and field inside the cell show good agreement with the finite element simulation. The differences in the power spectra are less than 10%. This verifies the model's ability to predict the component amplitudes of each wave and hence the electric field within the medium. We now wish to make full use of the model's features by considering a system with the same fundamental period but also with second and third harmonics present. Furthermore, to make the system even more realistic with respect to the experimental system we choose some arbitrary profiles for these higher harmonics. Therefore we choose as dielectric tensor

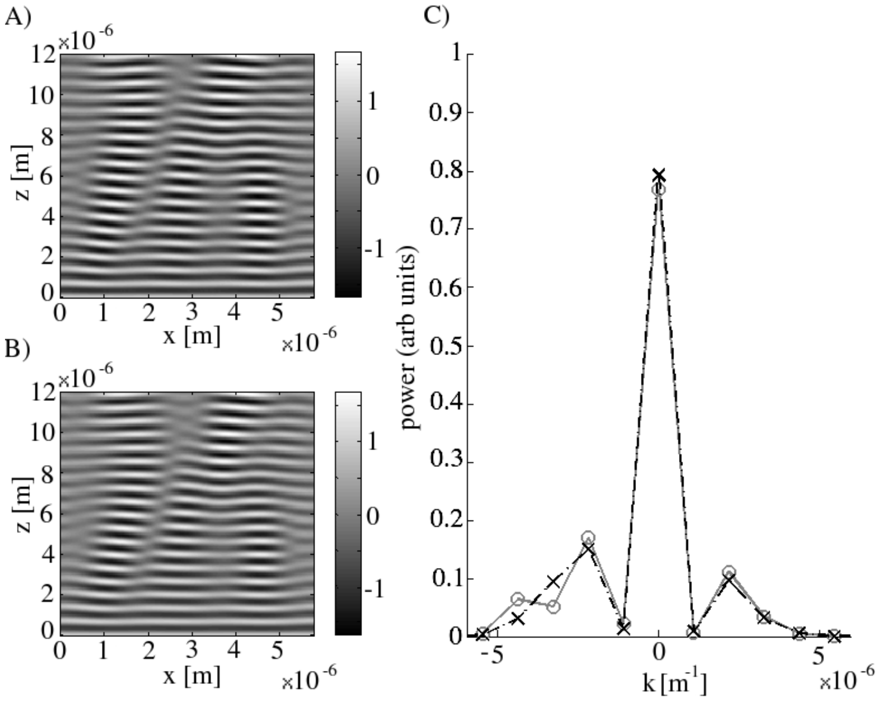

FIGURE 3.15: *Finite element comparison for the case of multiple grating wave vectors with varying profile in the z direction: A) x-component of electric field in cell for coupled wave model, the coloured fringes correspond to the optical amplitude as shown in the adjacent colourbar. B) x-component of electric field in cell for finite element simulation. C) Optical power spectrum at output of cell where '$\circ$' is the coupled wave approximation and '$\times$' is the finite element simulation.*

$$\begin{aligned}\Delta\epsilon = & \begin{pmatrix} -0.05 & 0.03 \\ 0.03 & 0.05 \end{pmatrix} \cos(\boldsymbol{K}\cdot\boldsymbol{x}) + \\ & \begin{pmatrix} -0.1 & 0.05 \\ 0.05 & 0.1 \end{pmatrix} e^{-\frac{(z-L_z/2)^2}{L_z^2}} \cos(2\boldsymbol{K}\cdot\boldsymbol{x}) + \\ & \begin{pmatrix} -0.05 & 0.1 \\ 0.1 & 0.05 \end{pmatrix} e^{\frac{z}{L_z}} \cos(3\boldsymbol{K}\cdot\boldsymbol{x}). \end{aligned} \tag{3.68}$$

The field throughout the cell and the comparison with the finite element modelling in this case is shown in Figure 3.15. Unlike the previous test case the majority of the energy remains in the incident beam $k_x = 0$ with energy transferring past the nearest neighbours into the second diffracted order beams. Again we see good agreement between the electric fields and the optical power spectrum with error less than one part in ten. This comparison verifies the ability of the model to handle the higher harmonics and arbitrary spatial profiles of the grating. The only difference between this and the liquid crystal profile is the addition of higher harmonics and the possibility of less smooth spatial profiles. For the liquid crystal test case, we solve the $\mathcal{Q}$ tensor model with an applied voltage of the form

$$V_{app} = V_0 \cos^2\left(\frac{\pi}{\Lambda}x\right). \tag{3.69}$$

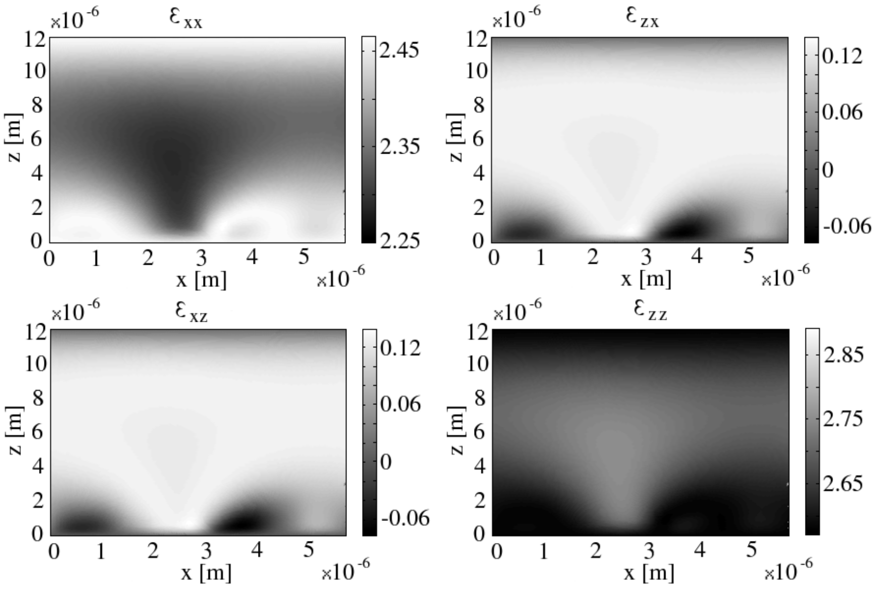

FIGURE 3.16: *In-plane components of the dielectric tensor for the anisotropic liquid crystal. The four images show the different components of the dielectric tensor.*

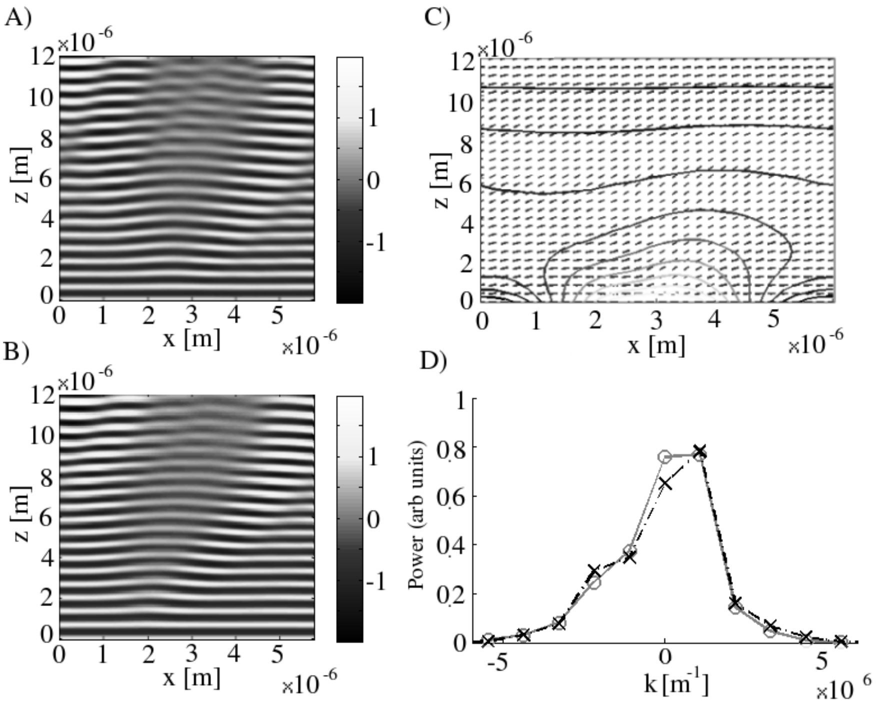

FIGURE 3.17: *A) x-component of electric field in cell for: A) Coupled wave model, the coloured fringes correspond to the optical amplitude as shown in the adjacent colourbar. B) Finite element simulation. C) Liquid crystal director profile showing molecular orientation and contour lines showing equipotentials. D) Optical power spectrum at output of cell where '$\circ$' is the coupled wave approximation and '$\times$' is the finite element simulation.*

The voltage amplitude $V_0 = 5$ has been chosen to give an interesting dielectric profile containing harmonics of the grating vector and a non-uniform profile in the z direction. Figure 3.16 shows the in plane components of the dielectric tensor throughout the cell. The second coupling harmonic is confined close to the cell boundary whilst the fundamental grating vector penetrates further into the cell. The component values a_0 and a_1 are substituted into equation (3.61), this is then solved to give the amplitude of the different optical wave vectors. Figure 3.17 shows the comparison of the electric field in the liquid crystal with the finite element modelling. In this case the energy can be seen to transfer with a large asymmetry. In this case the asymmetry is larger than in Figure 3.14 due to the size of the off diagonal elements of the dielectric tensor, see Section 3.5.3.

Comparison to existing theories has been shown analytically in both Bragg and Raman-Nath regimes. In terms of computation speed the finite element simulation typically takes approximately one minute to run with a wavelength of 1μm whilst the coupled wave approach takes less than one second for a non-trivial refractive index profile. For shorter wavelengths the coupled wave approach will be significantly quicker as its computation time does not scale with wavelength whilst the finite element simulation time does. The model shows good agreement with the finite element simulations in all cases tested and will be a useful tool for modelling optical coupling in more complex systems where computational speed and efficiency are required. We now want to consider some of the predictions of this model in detail.

3.5.3 Asymmetric coupling

The comparison between the coupled wave approach and the finite element simulations detailed in Section 3.5.2 showed an asymmetry developing between the positive and negative diffracted orders. This can be explained by considering the off–diagonal elements in the dielectric tensor. For a system whose coordinate axis have been chosen such that they coincide with the principal axis of the dielectric tensor the refractive index is given by equation (3.26). In this case the refractive index seen by a wave propagating at an angle θ to the optical axis will see the same refractive index as one propagating at an angle of $-\theta$. In other words, the ellipsoid of refraction for this system will be aligned such that its major axis coincide with the coordinate axis and the whole system is symmetric.

However, in the case of the beam coupling model the dielectric tensor is not completely diagonal. The non-homogeneous part of the dielectric tensor has off diagonal components, and as such we need a different method to define the refractive index. The simplest way is to consider the wave equation in terms of the magnetic field $\boldsymbol{H}$,

$$\boldsymbol{\nabla}\times\epsilon^{-1}\boldsymbol{\nabla}\times\boldsymbol{H} = \frac{\omega^2}{c^2}\boldsymbol{H}. \tag{3.70}$$

Rearranging the left hand side of this equation and using Maxwell's equation $\boldsymbol{\nabla}\cdot\boldsymbol{H} = 0$ we obtain,

$$\boldsymbol{k}^T\epsilon^{-1}\boldsymbol{k} = \frac{\omega^2}{c^2}, \tag{3.71}$$

where $\boldsymbol{k} = nk_0\left(\sin\theta, \cos\theta\right)$ is the optical wave vector. We assume a dielectric tensor which has a small traceless symmetric part containing off diagonal elements,

$$\epsilon = \begin{pmatrix} \epsilon_{11} - \eta\epsilon_d & \eta \\ \eta & \epsilon_{22} + \eta\epsilon_d \end{pmatrix}, \tag{3.72}$$

where $\eta \ll 1$. Substituting into equation (3.71), we can obtain a more general expression for the refractive index,

$$\frac{1}{n^2} = \epsilon_{22}\sin^2\theta + \epsilon_{11}\cos^2\theta + \eta\left[\epsilon_d\left(\cos^2\theta - \sin^2\theta\right) - 2\cos\theta\sin\theta\right]. \tag{3.73}$$

This expression is no longer invariant with respect to $x, -x$ reflections due to the final term on the right hand side. An anisotropic medium not described by a diagonal tensor will not be symmetric. This is true for the case of the beam coupling theory; the off diagonal elements of the dielectric tensor mean that the true symmetry for the system is $x, -x$, $\eta, -\eta$ and $\epsilon_d = -\epsilon_d$. Physically the effect of the off diagonal components of the tensor is to rotate the ellipsoid of refraction from the coordinate axis of the system making the interaction of the anisotropic medium with the optical field asymmetric.

3.5.4 Beam coupling at normal incidence

In Section 3.3.2 we mentioned that, without some form of symmetry breaking, for two beams incident on a liquid crystal cell whose bisector is normal to the cell surface we will see no gain. We supported this statement with some simplified analysis based on the Fourier components present in the refractive index grating seen by each beam. After recent experimental observation of normal incidence gain from Dr O. Buchnev and Professor M. Kaczmarek we want to see if a more in depth analysis based on our model allows us to observe and quantify this gain.

We start from equation (3.61) and consider the simplest possible normal incidence case, Bragg regime coupling where only two beams are present. As such, equation (3.61) can be rewritten as:

$$\frac{d}{dz}\begin{pmatrix} \tilde{A}^{(1)} \\ \tilde{A}^{(2)} \end{pmatrix} = i\begin{pmatrix} k_z^{(1)} + \frac{ik_0\left(\hat{\mathbf{e}}^{(1)}\Delta\epsilon^{(0)}\hat{\mathbf{e}}^{(1)}\right)}{4n^{(1)}g^{(1)}\hat{u}_z^{(1)}} & \frac{ik_0\left(\hat{\mathbf{e}}^{(1)}\Delta\epsilon^{(1)}\hat{\mathbf{e}}^{(2)}\right)}{4n^{(1)}g^{(1)}\hat{u}_z^{(1)}} \\ \frac{ik_0\left(\hat{\mathbf{e}}^{(2)}\Delta\epsilon^{(1)*}\hat{\mathbf{e}}^{(1)}\right)}{4n^{(2)}g^{(2)}\hat{u}_z^{(2)}} & k_z^{(2)} + \frac{ik_0\left(\hat{\mathbf{e}}^{(2)}\Delta\epsilon^{(0)}\hat{\mathbf{e}}^{(2)}\right)}{4n^{(2)}g^{(2)}\hat{u}_z^{(2)}} \end{pmatrix}\begin{pmatrix} \tilde{A}^{(1)} \\ \tilde{A}^{(2)} \end{pmatrix} \tag{3.74}$$

where we have absorbed the phases into the dielectric tensor and a superscript $*$ denotes the complex conjugate. It can be seen that beam coupling will only take place if the off diagonal elements in the matrix are non-zero. As the dielectric tensor and, hence, the coupling matrix is symmetric then the condition which must be satisfied for coupling to take place is

$$\hat{\boldsymbol{e}}^{(1)} \cdot \Delta\epsilon^{(1)} \hat{\boldsymbol{e}}^{(2)} \neq 0. \tag{3.75}$$

To keep the calculations simple we neglect the anisotropy of the liquid crystal in the derivation of the polarisations. This is equivalent to $\epsilon_u = \epsilon_u I$, where I is the identity matrix. Therefore, the polarisations of the two fields are given by

$$\hat{\boldsymbol{e}}^{(1)} = \begin{pmatrix} \sin(\beta+\alpha) \\ 0 \\ \cos(\beta+\alpha) \end{pmatrix} \quad \text{and} \quad \hat{\boldsymbol{e}}^{(2)} = \begin{pmatrix} \sin(\beta-\alpha) \\ 0 \\ \cos(\beta-\alpha) \end{pmatrix}, \tag{3.76}$$

where β is the angle the bisector of the two input beams makes with the cell normal and α is the angle each beam makes with the bisector. Substituting this form of the polarisations into equation (3.75) and using the knowledge that the dielectric tensor is traceless and symmetric we obtain

$$\begin{aligned} \hat{\boldsymbol{e}}^{(1)} \cdot \Delta\epsilon^{(1)} \hat{\boldsymbol{e}}^{(2)} = \; & \Delta\epsilon^{(1)}_{11} \left(\sin^2\beta\cos^2\alpha - \cos^2\beta\sin^2\alpha\right) + \\ & \Delta\epsilon^{(1)}_{13} \left(2\cos\beta\sin\beta\right) + \\ & \Delta\epsilon^{(1)}_{33} \left(\cos^2\alpha\cos^2\beta - \sin^2\alpha\sin^2\beta\right). \end{aligned} \tag{3.77}$$

For normal incidence, i.e. $\beta = 0$ this becomes

$$\hat{\boldsymbol{e}}^{(1)} \cdot \Delta\epsilon^{(1)} \hat{\boldsymbol{e}}^{(2)} = -\Delta\epsilon^{(1)}_{11}\sin^2\alpha + \Delta\epsilon^{(1)}_{33}\cos^2\alpha. \tag{3.78}$$

Note that if the liquid crystal is aligned in plane then $\Delta\epsilon_{11} = -\Delta\epsilon_{33}$ and $\hat{\boldsymbol{e}}^{(1)} \cdot \Delta\epsilon^{(1)} \hat{\boldsymbol{e}}^{(2)} = -\Delta\epsilon_{11}$. We now consider the case of a liquid crystal cell with a modulated applied electric field. We assume that the modulation of the liquid crystal due to the electric field is small with respect to the bulk alignment to the unmodulated part of the field. As the applied field is modulated, the spherical angles which express the liquid crystals alignment (θ and ϕ) can be expressed as a Fourier series which we write in the form

$$\theta = \theta_0 + \eta \sum_{n=1}^{\infty} \theta_n(\eta z) e^{inK_g z} + \theta_n^*(\eta z) e^{-inK_g z}, \tag{3.79a}$$

$$\phi = \phi_0 + \eta \sum_{n=1}^{\infty} \phi_n(\eta z) e^{inK_g z} + \phi_n^*(\eta z) e^{-inK_g z}, \tag{3.79b}$$

where $\eta \ll 1$. To determine the coupling strength we need an expression for the Fourier tensor coefficient of the first order Fourier component. This is obtained by first writing the director as a Fourier series and neglecting terms $O(\eta^2)$

$$\hat{\boldsymbol{n}} = \hat{\boldsymbol{n}}_0 + \eta \left[\hat{\boldsymbol{n}}_1 \sum_{n=1}^{\infty} \left(\theta_n e^{inK_g z} + \theta_n^* e^{-inK_g z}\right) + \sin\theta_0 \hat{\boldsymbol{m}}_1 \sum_{n=1}^{\infty} \left(\phi_n e^{inK_g z} + \phi_n^* e^{-inK_g z}\right) \right], \tag{3.80}$$

where $\hat{\boldsymbol{n}}_0 = (\sin\theta_0\cos\phi_0, \sin\theta_0\sin\phi_0, \cos\theta_0)^T$, $\hat{\boldsymbol{n}}_1 = (\cos\theta_0\cos\phi_0, \cos\theta_0\sin\phi_0, -\sin\theta_0)^T$

and $\hat{\boldsymbol{m}}_1 = (-\sin\phi_0, \cos\phi_0, 0)^T$. Interestingly, if $\theta_0 = 0$ (as is the case for strongly aligned liquid crystal cells) then the modulation out of plane makes no difference to the coupling, at least to first order in the modulation amplitude. This is exactly the case derived in Section 3.4, which suggests that the extended analysis in Appendix C is only required for weakly aligned liquid crystals. The tensor coefficients are then proportional to the product $\overline{\hat{\boldsymbol{n}} \otimes \hat{\boldsymbol{n}}}$, excluding terms $O(\eta^2)$ we obtain

$$\begin{aligned}\overline{\hat{\boldsymbol{n}} \otimes \hat{\boldsymbol{n}}} = \quad & \hat{\boldsymbol{n}}_0 \otimes \hat{\boldsymbol{n}}_0 - \frac{1}{3}Id + \eta \left\{ [\hat{\boldsymbol{n}}_1 \otimes \hat{\boldsymbol{n}}_0 + \hat{\boldsymbol{n}}_0 \otimes \hat{\boldsymbol{n}}_1] \sum_{n=1}^{\infty} \left(\theta_n e^{inK_g z} + \theta_n^* e^{-inK_g z}\right) + \right. \\ & \left. \sin\theta_0 \left[\hat{\boldsymbol{n}}_0 \otimes \hat{\boldsymbol{m}}_1 + \hat{\boldsymbol{m}}_1 \otimes \hat{\boldsymbol{n}}_0\right] \sum_{n=1}^{\infty} \left(\phi_n e^{inK_g z} + \phi_n^* e^{-inK_g z}\right) \right\} + O(\eta^2).\end{aligned} \tag{3.81}$$

It is interesting to look at the different order terms separately as these provide a great deal of insight into the coupling mechanisms. As the modulation of the liquid crystal occurs at $O(\eta)$ it can be seen that there is no coupling induced by the $O(\eta^0)$ terms. The tensor Fourier coefficients at $O(\eta^1)$ are

$$\Delta\epsilon_{11} = 2\theta_1 \hat{n}_{0x}\hat{n}_{1x} + 2\phi_1 \sin\theta_0 \hat{n}_{0x}\hat{m}_{1x}, \tag{3.82a}$$

$$\Delta\epsilon_{33} = 2\theta_1 \hat{n}_{0z}\hat{n}_{1z} + 2\phi_1 \sin\theta_0 \hat{n}_{0z}\hat{m}_{1z}. \tag{3.82b}$$

Substituting the expressions for the vectors $\hat{\boldsymbol{n}}_0$, $\hat{\boldsymbol{n}}_1$ and $\hat{\boldsymbol{m}}_1$ we obtain

$$\hat{\boldsymbol{e}}^{(1)}\Delta\epsilon^{(1)}\hat{\boldsymbol{e}}^{(2)} = 2\phi_1 \sin^2\theta_0 \sin\phi_0 \cos\phi_0 \cos^2\alpha - 2\theta_1 \sin\theta_0 \cos\theta_0 \left(\cos^2\alpha + \sin^2\alpha \cos^2\phi_0\right). \tag{3.83}$$

At this point we can make the following observations: Firstly, if the liquid crystal is aligned symmetrically about the z axis, as would be expected for reasonably large applied field then $\theta_0 = 0$ and $\hat{\boldsymbol{e}}^{(1)} \cdot \Delta\epsilon^{(1)}\hat{\boldsymbol{e}}^{(2)} = 0$ resulting in no beam coupling. Secondly out of plane modulation of the director will induce no coupling if it is symmetric, i.e. $\phi_0 = 0$. Therefore to obtain normal incidence coupling at $O(\eta)$ we require some physical symmetry breaking in the liquid crystal alignment such that $\theta_0 \neq 0$. This can be achieved quite simply by inducing an asymmetry in the anchoring conditions with respect to inversion about the surface normal.

Further insight can be obtained by looking at the terms $O(\eta^2)$ in the modulation strength. Whilst the derivation of these coefficients is quite simple, the equations involved become quite long and cumbersome. As such, only the resulting Fourier coefficients are quoted for the case $\theta_0 = 0$,

$$\hat{\boldsymbol{e}}^{(1)} \cdot \Delta\epsilon^{(1)}\hat{\boldsymbol{e}}^{(2)} = -\sin^2\alpha \cos^2\phi_0 \sum_{n=2}^{\infty} \left(\theta_n\theta_{-n+1} + \theta_n^*\theta_{-n-1}^* + \theta_n\theta_{n-1}^* + \theta_n^*\theta_{n+1}\right), \tag{3.84}$$

where it is important to remember that $\theta_n^* = \theta_{-n}$. In this case equation 3.84 is non–zero and there is some coupling for $\phi_0 \neq \pi/2$. As such, coupling can be observed for normal incidence. The coupling is given by diffraction along the $2K_g$ Fourier component, then back along the

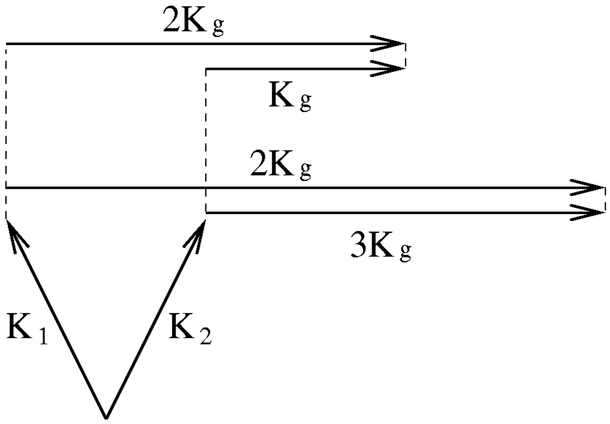

FIGURE 3.18: *Beam coupling at normal incidence can be seen to occur if there are higher Fourier components present in the diffraction medium. Energy is first diffracted by the $2K_g$ Fourier component and then back by the K_g Fourier component. This process can also occur with higher order Fourier components.*

K_g component. This can also occur for higher order Fourier components providing the resulting grating vector is $\pm K_g$, see Figure 3.18. However, this coupling is second order in the modulation amplitude.

At this point it is sensible to ask whether or not the inclusion of terms $O(\eta^2)$ in equation (3.80) would affect this result. By continuing the Taylor expansion it can be seen that the lowest Fourier component in the $O(\eta^2)$ expansion will be $2K_g$. In order to provide a grating vector K_g we require an additional term. The appropriate Fourier component in this case can only be provided by the $O(\eta)$ terms. Therefore, the resulting coupling would be third order in the modulation strength and it's effects will be negligible compared to the $O(\eta^2)$ terms.

In summary we observe that for two beams of equal intensities incident on a photorefractive liquid crystal cell with symmetric director alignment, regardless of the amplitude of the tensor Fourier coefficients we must still see no gain as the system is perfectly symmetric. To observe gain at normal incidence then there must also be an asymmetry in the intensity of the two input beams. The experimentally observed gain is measured for an input beam ratio of 1000 therefore any small coupling effects will be strongly amplified resulting in measurable second order gain.

3.6 Modelling photorefractive liquid crystal cells

The beam coupling model derived in this chapter and the liquid crystal model derived in Chapter 2 have been shown to be accurate. However, they do not completely describe the photorefractive liquid crystal cell. One of the major issues is whether or not we can determine the voltage across the liquid crystal layer. Factors affecting this voltage drop include: the presence of ions in the liquid crystal layer, the relative impedance of each layer and the frequency of the applied field. For AC fields, even of low frequency, the motion of ions is greatly reduced [110]. The effect of increased frequency on the voltage distribution within the layers can be observed by fitting an

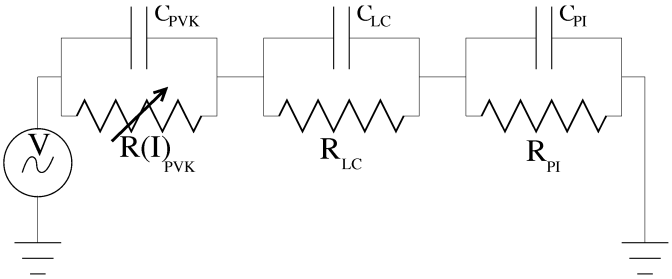

FIGURE 3.19: *Equivalent circuit for RC cell.*

impedance ladder model to the liquid crystal cell [111]. In this section we model each layer of the cell, recall Figure 3.1, as a simple RC circuit as shown in Figure 3.19. This circuit captures the majority of the cells behaviour under the assumption that the slow AC field eliminates the ion motion. The impedance of the each layer is given by

$$Z_j = \frac{R_j}{i\omega R_j C_j + 1}, \tag{3.85}$$

where $R_j = L_j/(\sigma_j A)$ and $C_j = \epsilon_0 \epsilon_j A/L_j$. Here A is the cell area, ϵ_0 is the permittivity of free space, σ_j, ϵ_j and L_j are the conductance, relative permittivity and thickness of layer j, where $j = \{LC, PVK, PI\}$ denotes the liquid crystal, PVK and PI layers respectively. The values of σ_j and ϵ_j and the resulting values for C_j and R_j for $A = 4 \cdot 10^{-4} m^2$ are summarised in Table 3.1 [112, 113]. Note, the measured range of σ_{LC} is quite large. Therefore, we consider a sample of values in this range. The dielectric constant of the liquid crystal corresponds to planar aligned E7.

Layer	L_j	σ_j	ϵ_j	R_j	C_j
LC	$12\mu m$	10^{-5}–$10^{-10} S/m$	5–20	$3 \cdot 10^3$–$3 \cdot 10^8 \Omega$	$5.9 \cdot 10^{-9} F$
PI	$20nm$	$10^{-14} S/m$	3.4	$5 \cdot 10^8 \Omega$	$6.0 \cdot 10^{-7} F$
PVK	$200nm$	$10^{-13} S/m$	5	$5 \cdot 10^8 \Omega$	$8.8 \cdot 10^{-8} F$

TABLE 3.1: Numerical values of cell parameters for typical photorefractive liquid crystal cell.

The steady state voltage across the liquid crystal layer V_{LC} as a function of the applied voltage V is given by $V_{LC} = V Z_{LC}/(Z_{LC} + Z_{PI} + Z_{PVK})$. We want to calculate the effect of a small, intensity dependent, modulation in the resistance of the PVK on the voltage dropped across the liquid crystal layer. We assume that the resistance of the PVK is $R_{PVK} = R_{PVK}(1 + \beta(I))$, where $\beta \ll 1$ is the modulated part of the PVK resistance and I is the intensity of light on the PVK layer. In the limit $\omega = 0$ the voltage drop is determined entirely resistively,

$$V_{LC} = V \frac{R_{LC}}{R_{TOT}} \left[1 - \frac{R_{PVK}}{R_{TOT}} \beta(I) \right] + O(\eta^2), \tag{3.86}$$

where $R_{TOT} = R_{LC} + R_{PI} + R_{PVK}$. Typically as $R_{LC} \ll R_{PI}$ and $R_{LC} \ll R_{PVK}$ the voltage drop across the liquid crystal in the DC regime is very small. Similarly if the frequency of the applied voltage is high enough, typically $\omega \gg 1/(C_j R_j)$ for all j, then the voltage is

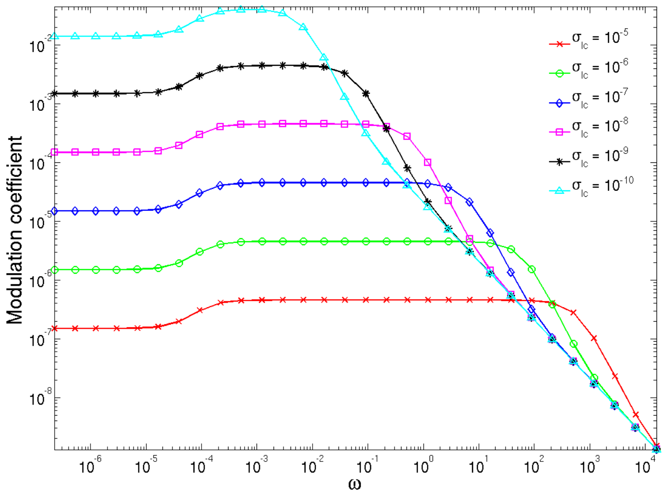

FIGURE 3.20: *Voltage drop across liquid crystal cell. The plot shows the coefficient of $\beta(I)$ against ω. It can be seen that for low, but non-zero, frequency that the modulated part of the voltage dropped across the liquid crystal layer increases. As the frequency increases further the cell behaviour becomes dominated by the capacitance of the layers and the conductivity modulation becomes smaller.*

determined entirely capacitively,

$$V_{LC} = V\frac{C_{PVK}C_{PI}}{C_{PVK}C_{PI} + C_{PVK}C_{LC} + C_{LC}C_{PI}}. \tag{3.87}$$

In this case, as $C_{LC} \ll C_{PVK}$ and $C_{LC} \ll C_{PI}$, the voltage drop across the liquid crystal is large. However, as V_{LC} is independent of the resistance of the photoconductor no diffraction will take place. In the general case, relevant for the slow AC field,

$$V_{LC} = V\frac{Z_{LC}}{Z_{TOT}}\left[1 - \frac{Z_{PVK}}{Z_{TOT}}\left(1 - iZ_{PVK}C_{PVK}\omega\right)\beta(I)\right] + O(\beta^2(I)), \tag{3.88}$$

where $Z_{TOT} = Z_{LC} + Z_{PI} + Z_{PVK}$. The effects of equation (3.88) can be understood by plotting the coefficient of $\beta(I)$ against ω for a range of liquid crystal conductances, see Figure 3.20. It can be seen that, although small, there is a broad peak in the amplitude of the modulation coefficient which narrows and increases in amplitude with the liquid crystal conductance. This suggests that there is a range of frequencies close to zero Hertz for which the diffraction efficiency of the liquid crystal cell is largest. We note that for decreasing the conductance of the liquid crystal increases the range of frequencies over which AC beam coupling can be observed whilst reducing the overall effect of the modulation in the PVK resistance.

Using equation (3.88) we can see that, at zero Hz, a greater voltage modulation across the liquid crystal can be obtained by increasing either the PVK resistance or the liquid crystal resistance with respect to the PI. At low frequencies the increase in voltage across the liquid crystal layer can be attributed to the capacitance of the PVK. Increasing this could provide a method of obtaining a larger voltage drop across the liquid crystal at low frequency.

Whilst this analysis explains some of the features of the cells, there is clearly work to be done in optimising this system. Detailed charge modelling combined with a more thorough analysis of the electric properties of the system will be required to determine the ideal conditions for beam coupling in an AC field.

3.7 Conclusion

In this chapter we have derived an extension to the existing anisotropic coupled wave equations which allow us to model systems in the Bragg, Raman-Nath and intermediate regimes. Comparison to existing theories has been shown analytically in both Bragg and Raman-Nath regimes. Finite element simulations have also been used to confirm the model's validity for all regimes.

The regime independent model developed here is a useful tool for studying the effects of beam coupling in any geometry. The derivation, based on the assumption that the modulation is small, does not make any assumptions regarding the size of the anisotropy. Further, as the liquid crystal model is solved numerically it does not require that the electric field distribution is decoupled from the liquid crystal alignment or that the optical axis of the liquid crystal is restricted to the plane. The assumption that the first order component of the dielectric tensor is restricted to a plane is an assumption included to simplify the number of waves considered for the case of a liquid crystal. However, this is not a requirement of the method and the full equations, where this is not the case, are included in Appendix C. The model takes into account all possible coupling combinations between the various optical waves propagating though the medium. This is achieved by considering higher order grating harmonics as well as all possible mismatch terms. The use of a slowly varying grating profile in the z direction makes the model useful for more complex systems such as the liquid crystal cell. In terms of computation speed the finite element simulation typically takes 1 minute to run whilst the coupled wave approach takes less than 1 second for a non-trivial refractive index profile.

The model shows good agreement with the finite element simulations in all cases tested and will be a useful tool for modelling optical coupling in more complex systems where computational speed and efficiency are required.

In comparison to the existing models of Jones and Cook [68] and Kubystkyi *et al* [99] this model has the advantage that it is more versatile and relies on fewer assumptions. On the other hand, unlike the existing models, the final equation must be solved numerically. Whilst it is clear that under certain assumptions, e.g. small phase detuning, equation (3.61) can be solved analytically this work is beyond the scope of this thesis. Researchers who wish to obtain a good understanding of the dependence of gain on different system parameters should read the paper by Jones and Cook if working in the Bragg regime [68] and the paper by Kubytskyi et al for the Raman-Nath regime [99].

Chapter 4

Surface plasmon polaritons at a metal–liquid crystal interface

A Surface Plasmon Polariton (SPP) is an electromagnetic excitation restricted to the boundary between a metal and a dielectric. By adding a thin gold layer to the boundary of a photorefractive liquid crystal cell a SPP can be excited that sees a refractive index which is dependent on the alignment of the liquid crystal layer. Manipulating the liquid crystal alignment using external beams whose energies are close to the excitation energy of the PVK allows control of the SPP. Current application of SPPs are limited because they have very short propagation lengths due to the optical absorption in the metal. In this chapter we consider how photorefractive liquid crystal cells can be used to overcome these losses. This is a joint work split between theory and experiment. The experimental results are provided by Dr David Smith and Stephen Abbot from the school of Physics and Astronomy.

This chapter is arranged as follows: In Section 4.1 we provide an introduction to the existing literature and a more formal introduction to the system we are studying. Section 4.2 provides an introduction to the methods used to model SPP propagation. In Section 4.3 we describe a numerical code based on the work of Moharam and Glytsis [2, 102] capable of modelling the propagation of SPP at the interface between a photorefractive liquid crystal cell and a metal. In Section 4.4 the SPP propagation model is combined with the liquid crystal model developed in Chapter 2 to allow for experimental comparison. The final part of this chapter, Section 4.5, is devoted to considering analytic and semi–analytic models to describe the propagation of SPP in geometries which provide a good approximation to that of the photorefractive liquid crystal cells, these models are compared to the numerical codes developed in Section 4.3 and show good agreement.

4.1 Introduction

The term Surface Plasmon Polariton (SPP) refers to the coupled oscillation of an electromagnetic field with the electron cloud at the surface of a metal [114]. These excitations propagate along a metal–dielectric interface and have amplitude which decays exponentially in both materials. The discovery of SPPs is directly linked to the prediction of Surface Plasmons (SPs) by Ritchie in 1957 [115]. Whilst studying the loss mechanisms of electromagnetic radiation in thin metal films Ritchie predicted the existence of localised, non-propagating, plasma oscillations. This prediction was experimentally verified in 1959 in two experimental papers, concerned with the loss spectra of Aluminium and Magnesium, by Powell and Swan [116, 117].

The prediction and description of SPPs did not occur until 1960. In a paper based on the earlier work of Ritchie, Stern and Farrell describe the energy loss of non–normal incidence electromagnetic radiation [118]. Here the loss mechanism is the same with the exception that the optical energy is transfered to a propagating SPP rather than a stationary SP. SPPs may be thought of as propagating SPs. Alternatively SPs may be considered as the limiting case of SPPs as the group velocity becomes infinitely large.

Since their discovery a huge number of papers on the properties and applications of SPPs have emerged. Whilst the relevant concepts and properties of SPPs will be reviewed and discussed here, the reader is directed towards two review articles [114, 119]. The first, published by Zayats et al in 2004, describes the optics of SPPs including details about the excitation and optical characterisation techniques. The second, published by Pitarke et al in 2006, describes the physical properties of the solids which allow the excitation of these modes.

Due to their unique properties, such as their sensitivity to small changes in dielectric constants, $\sim O(10^{-14})$ [120, 121], SPPs have a wide variety of applications in both industry and academia. These include resonance sensors [122], enhanced spectroscopy techniques capable of detecting single molecules [123], waveguides [124], biosensors [125] and sub-wavelength optical applications such as nanoscale lithograthy [126].

The major limitation to the use of SPPs is their short propagation length which is typically of the order of microns [126, 127]. Long range SPP modes can be found to exist in thin metallic films [128]. These modes have propagation length of the order of millimetres [129, 130]. However, this is still too short. For the majority of potential SPP applications to become reality the propagation lengths need to be increased.

One way to increase the propagation length of a SPP is by constantly coupling energy into it. In general this is a non–trivial problem as the SPP wavenumber at a metal dielectric interface is larger than the wavenumber of a propagating wave in the dielectric medium. As such the only way SPP can be excited is via an evanescent wave in either the dielectric or the metal [126].

There are several ways to do this. The first of these, the Kretchmann configuration, Figure 4.1A, makes use of a dielectric prism adjacent to a metallic film and an incidence angle greater

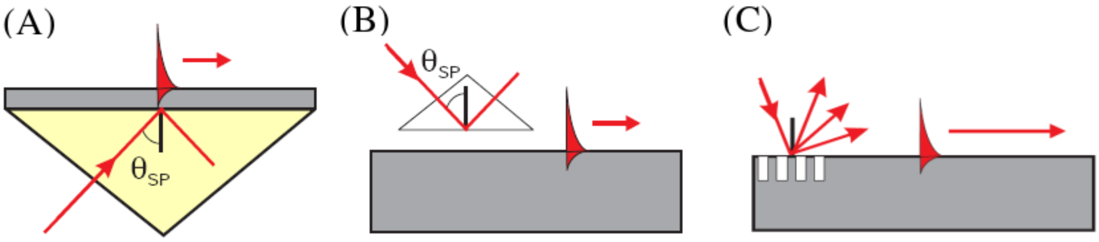

FIGURE 4.1: *Plasmon excitation methods (taken from [114]) A) Kretchmann configuration. B) Otto configuration. C) Grating coupler*

than that for total internal reflection in the prism. At the angle of incidence for which the in plane component of the optical wave vector is equal to the SPP wave vector, optical tunnelling through the metal film will occur and the energy will couple into an SPP at the opposite side of the film. The original paper by Kretchmann is only available in German [131]. However, a good description of the method can be found in [114].

The Otto configuration [132] works in a similar way to the Kretchmann geometry, Figure 4.1B. A SPP is excited in a thick metallic layer using a prism, a thin air gap and a thick metal layer. Here total internal reflection occurs in the prism and the evanescent field in the air gap is coupled to the SPP via optical tunnelling.

The method of SPP generation which is of interest in the context of this work is SPP excitation using a diffraction grating [133] as shown in Figure 4.1C. Here we can illuminate the diffraction grating with light from a much wider range of angles and couple energy from one of the various diffracted orders into the SPP.

Grating couplers take two forms. Metallic grating couplers, where the grating is formed by a corrugation at the metal surface, were first discovered in the context of “Wood’s anomalies” in 1902 [134, 135]. These anomalies refer to the large discrepancies between the total amount of light incident on a metallic grating compared to the total amount reflected, a discrepancy now known to be due to SPP generation. Such gratings have been widely studied in the literature [136, 137, 138, 139]. The majority of these studies consider only shallow gratings where the Rayleigh hypothesis holds. According to this hypothesis the electromagnetic field can be written as the sum of the incoming wave and a series of reflected or transmitted outgoing waves [140]. If this holds then the corrugation can be “flattened” by means of a coordinate transform. In general this is not the case and in deep gratings the fields within the grooves of the grating must also be considered. Studies concerned with deep gratings have been carried out [141]. These studies discovered that SPPs can be generated not only along the surface but also within the grooves of the grating.

The other form of grating couplers, which are relevant in this work, are dielectric gratings [142, 143, 144, 145]. These have been widely studied as a means to pump energy into plasmons. However, typically these gratings are non–configurable and as such have limited application. The use of diffraction gratings with SPPs leads to the possibility of SPP-SPP or SPP-light scattering. For configurable gratings, such as the photorefractive liquid crystal grating coupler, energy can be coupled into signal carrying SPPs increasing their propagation length.

Here we are interested in the coupling of energy into an SPP using a photorefractive liquid crystal cell. The use of SPPs applicable to liquid crystals have been widely studied by the group of Barnes and Sambles. These studies include: SPP propagation in anisotropic materials [146], the use of SPPs to probe the surface alignment [147], SPP induced non–linearity [148] and bistability [149] and theoretical and experimental observation of guided mode resonances and plasmonic resonance shift [150]. These studies clearly show the use of liquid crystal cells as a versatile tool for manipulating plasmonic and optical guided modes.

From an optical point of view the liquid crystal cell can be considered simply as a series of different layered media. Extensive numerical studies have been carried out regarding SPP interactions in layered media. These Transmission matrix (or T–matrix) approaches involve writing the solutions to Maxwell's equations in each homogeneous layer as a Fourier series and matching the tangential components of the fields at the boundaries. The resulting linear system of equations can be solved to obtain the reflection and transmission of these structures. This method can be extended to non-homogeneous materials, using the method of Berreman, by slicing them into a large number of thin layers, each of which may be considered homogeneous [151].

T–matrix methods have been widely used in isotropic materials [3], anisotropic materials [152, 153] and chiral materials [154]. However, these methods become numerically unstable for a large number of layers once the fields become evanescent. This is because both the exponentially decaying and exponentially growing solutions to Maxwell's equations must be considered in each material. Although these exponentially unbounded terms must have zero amplitude, their presence in the equations becomes a problem due to the finite numerical precision of a computer.

To overcome this the Scattering matrix (or S–matrix) approach was developed [155, 156, 157]. This method considers the field in terms of only decaying solutions, creating a stable numerical code. These codes have been implemented by a number of different groups to study different plasmonic systems [158, 159] and have been extended to include surface corrugations [160, 161]. A generalisation of these techniques, which is also easy to implement, is the rigorous diffraction theory developed by Moharam et al [2, 102]. This method is particularly well suited to grating structures and has been used to study single and cascaded anisotropic diffraction gratings [103, 162, 163].

Whilst numerical methods provide a good model for the system as a whole it is important to gain an understanding of the physical processes which affect the SPP propagation. Analytic treatment of plasmons at the interface between a metal and an anisotropic dielectric have also been considered. In general SPPs at such an interface can be described exactly [164]. However, the equations involved in such a theory often become cumbersome and hard to deal with. To overcome this, typical studies of such materials require that the optical axis of the anisotropic medium is restricted to a plane [165, 166]. Using these simplifications dispersion relations for SPP in anisotropic dielectric–metal–dielectric and metal–dielectric–metal structures have also

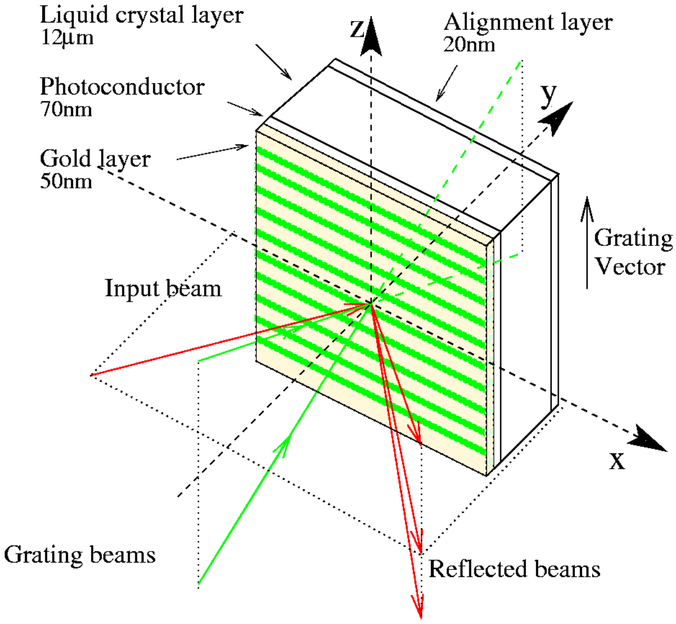

FIGURE 4.2: *Geometry of photorefractive liquid crystal cell used for SPP diffraction. A diffraction grating is created within the liquid crystal layer using two external beams. The effects of SPP diffraction can be studied by considering the reflected and diffracted intensity from the cell.*

been considered [167].

Perturbation techniques have been used extensively to help understand the reflection spectrum of different SPP. These include studies of SPP resonance width [168, 169] and the change in SPP propagation vector [170, 171] due to various perturbations. These papers consider the standard analytic SPP resonance conditions derived for a single isotropic dielectric–metal interface as the leading order solution. This result is then perturbed due to absorption in the metal and finite width, non–ideal, metal films. However, in many cases, due to the powerful numerical tools now available, these methods and results are often overlooked.

In this chapter we study the coupling properties of photorefractive–plasmonic liquid crystal cells formed by adding a thin gold layer to the photoconducting surface of the photorefractive liquid crystal cell. These devices, shown in Figure 4.2, provide an extremely versatile method for manipulating SPP propagation. SPPs are excited by the input beam and propagate along the interface between the gold and the photoconducting layer. For a thin enough photoconducting layer, approximately 70nm in our cells, the SPP will extend into the liquid crystal region allowing it to be manipulated through the liquid crystal alignment.

By applying a strong external field across the liquid crystal layer the refractive index near the cell surface can be altered. Spatial modulation of this applied voltage, and therefore the liquid crystal alignment, is achieved by varying the optical intensity on the photoconducting layer, as in the beam coupling problem discussed in Chapter 3. This allows a number of optically reconfigurable devices to be created, e.g. grating couplers, lenses and waveguides. Further, for sufficiently large optical fields, non-linear interactions through the photoconducting layer will allow photorefractive SPP interactions to be observed.

To understand the behaviour of these devices we consider a simplified system both theoretically and experimentally. A refractive index grating is created by two external grating beams, shown in Figure 4.2. The SPP is excited using a, relatively weak, probe beam. The experimentally measured intensity of the reflected and diffracted beams can then be used, in combination with various modelling techniques, to understand the diffractive properties of the cell.

We model these devices in three stages. First the voltage drop across the liquid crystal is calculated using a simple impedance ladder model, as described in Section 4.4. The liquid crystal alignment is then calculated using the code described in Chapter 2. Finally the diffraction is modelled using both the rigorous coupled wave theory of Moharam and Glytsis [2, 102] and analytic techniques that provide a greater insight into the underlying physics.

4.2 Modeling surface plasmon polaritons

4.2.1 Optics of metals

To understand how SPP propagate at an interface it is important to first understand how electromagnetic radiation propagates in a metal, this can be modelled in the same way as in a dielectric. The main difference is that the dielectric constant becomes complex and typically has a negative real part. There is also a much stronger frequency dependence than is usually found in dielectric materials [3]. These differences are due to the non-zero conductivity of the metal and can be understood by considering Maxwell's curl equations in a conducting medium:

$$\begin{aligned} \boldsymbol{\nabla} \times \boldsymbol{E}(\boldsymbol{x},t) &= -\mu_0\mu_r \frac{\partial \boldsymbol{H}(\boldsymbol{x},t)}{\partial t} \\ \boldsymbol{\nabla} \times \boldsymbol{H}(\boldsymbol{x},t) &= \epsilon_0\epsilon_r \frac{\partial \boldsymbol{E}(\boldsymbol{x},t)}{\partial t} + \boldsymbol{J}(\boldsymbol{x},t) \end{aligned} \tag{4.1}$$

where $\boldsymbol{J}(\boldsymbol{x},t)$ is the current density and is approximately $\sigma(\omega)\boldsymbol{E}(\boldsymbol{x},t)$. Combining the two equations to eliminate $\boldsymbol{H}(\boldsymbol{x},t)$ yields:

$$\boldsymbol{\nabla} \times \boldsymbol{\nabla} \times \boldsymbol{E}(\boldsymbol{x},t) = -\frac{1}{c^2}\mu_r\epsilon_r \frac{\partial^2 \boldsymbol{E}(\boldsymbol{x},t)}{\partial t^2} - \mu_r\sigma(\omega)\frac{\partial \boldsymbol{E}(\boldsymbol{x},t)}{\partial t}, \tag{4.2}$$

which, using the substitution $\boldsymbol{E}(\boldsymbol{x},t) = \boldsymbol{E}(\boldsymbol{x})e^{-i\omega t}$, gives the Helmholtz equation

$$\boldsymbol{\nabla} \times \boldsymbol{\nabla} \times \boldsymbol{E}(\boldsymbol{x}) = \frac{\omega^2}{c^2}\mu_r \left[\epsilon_r + \frac{i\sigma(\omega)}{\omega\epsilon_0}\right] \boldsymbol{E}(\boldsymbol{x}). \tag{4.3}$$

Under these conditions the permittivity and conductivity may be combined as a single, frequency dependent, dielectric constant,

$$\epsilon(\omega) = \epsilon_r + \frac{i\sigma(\omega)}{\omega\epsilon_0}. \tag{4.4}$$

This will, in general, be a complex quantity with strong frequency dependence due to the non-zero conductivity. Throughout the remainder of this chapter we will assume that the permittivity of the metal can be treated as a single dielectric constant. Where numerical values are required we use experimentally measured values for the real and imaginary parts of the refractive index as a function of ω [172].

4.2.2 Surface plasmon polaritons

We now wish to determine the conditions required for a SPP to propagate along an interface. We choose the coordinate system so that the boundary between the two materials is at $y = 0$. We also assume that the magnetic field is transverse, i.e. it is polarised in the z–direction. It will be shown later that this is the only type of SPP wave which can propagate. The electric and magnetic fields at the boundary may be written as:

$$\boldsymbol{E}\left(\boldsymbol{x},t\right) = \frac{-A^{(n)}}{i\omega\epsilon_0\epsilon^{(n)}}\left(-\text{sgn}(y)k_y^{(n)}, ik_x, 0\right)^T e^{-\text{sgn}(y)k_y^{(n)}y}e^{i(k_x x-\omega t)}, \tag{4.5a}$$

$$\boldsymbol{H}\left(\boldsymbol{x},t\right) = \left(0,0,A^{(n)}\right)^T e^{-\text{sgn}(y)k_y^{(n)}y}e^{i(k_x x-\omega t)}, \tag{4.5b}$$

where the superscript refers to the material of interest and sgn$(y) = 1$ and $n = 1$ for $y > 0$, sgn$(y) = -1$ and $n = 2$ for $y < 0$. Substituting equations (4.5) into the wave equation allows us to obtain the dispersion relationship for propagation in each material,

$$k_y^{(n)} = \left(k_x^2 - \epsilon^{(n)}\frac{\omega^2}{c^2}\right)^{\frac{1}{2}}, \tag{4.6}$$

which relates the decay of the electric and magnetic fields away from the boundary to the optical wave number k_x. For exponential decay away from the boundary we require that k_y is both positive and real. To proceed we make use of Maxwell's boundary conditions, i.e. the tangential components of $\boldsymbol{E}$ and $\boldsymbol{H}$ at the boundaries are continuous. These allow us to obtain the following matrix relationship,

$$\begin{pmatrix} 1 & -1 \\ \frac{k_y^{(1)}}{\epsilon^{(1)}} & \frac{k_y^{(2)}}{\epsilon^{(2)}} \end{pmatrix}\begin{pmatrix} A^{(1)} \\ A^{(2)} \end{pmatrix} = 0. \tag{4.7}$$

For SPP to propagate with non-zero amplitude we require that equation (4.7) has a non-trivial solution, i.e.

$$\frac{k_y^{(1)}}{k_y^{(2)}} = -\frac{\epsilon^{(1)}}{\epsilon^{(2)}}. \tag{4.8}$$

This equation tells us that $\epsilon^{(1)}$ must have a different sign to $\epsilon^{(2)}$. Therefore, one of the materials must be a metal and the other a dielectric. This is the general requirement for SPP propagation. It can be seen that if either $\epsilon^{(n)}$ has a non-zero imaginary component then at least one of the y components of the wave numbers will be imaginary and as such the SPP will no longer be localised at the boundary. Using equations (4.6) and (4.8) we can obtain an expression for k_x, the SPP wave number,

$$k_x = \frac{\omega}{c}\sqrt{\frac{\epsilon^{(1)}\epsilon^{(2)}}{\epsilon^{(1)} + \epsilon^{(2)}}}, \tag{4.9}$$

where, for a propagating mode, we require that the term inside the square root is negative. As mentioned in Section 4.2.1 the metal layer will have a complex dielectric constant $\epsilon^{(2)}$ with negative real part. Therefore, assuming $\epsilon^{(1)}$ is positive and real, we require $|\Re(\epsilon^{(2)})| > \epsilon^{(1)}$. Metals used for SPP excitation are typically those with small imaginary terms at optical frequencies. This reduces the absorption losses allowing the SPP to propagate a useful distance. Typical metals used for such experiments are gold or silver. To understand the effects of the small imaginary term on the SPP we consider the effect of a small perturbation in $\epsilon^{(2)}$ on the SPP wave number, equation (4.9). This approximation neglects the variation in the decay lengths of the plasmon induced by the absorption and any propagation away from the boundary which may also result. We substitute $\epsilon^{(2)} = \epsilon_r^{(2)}(1 + \eta i \epsilon_i^{(2)})$ into equation (4.9) where typically $\eta \ll 1$. After some manipulation, this yields

$$k_x = \frac{\omega}{c}\sqrt{\left[\frac{\epsilon^{(1)}\epsilon_r^{(2)}}{\epsilon^{(1)} + \epsilon_r^{(2)}}\right]}\left[1 + \eta\frac{1}{2}\frac{\epsilon^{(1)}\epsilon_i^{(2)}}{\epsilon^{(1)} + \epsilon_r^{(2)}} i + O\left(\eta^2\right)\right]. \tag{4.10}$$

From here we can obtain an approximation for the propagation length of the SPP. The $1/e$ decay length L_{SPP} is given by [114]

$$\frac{1}{L_{SPP}} = 2\Im(k_x) = \frac{\omega}{c}\frac{(\epsilon^{(1)})^{\frac{3}{2}}\epsilon_i^{(2)}|\epsilon_r^{(2)}|^{\frac{1}{2}}}{(|\epsilon_r^{(2)}| - \epsilon^{(1)})^{\frac{3}{2}}}. \tag{4.11}$$

Typically, the propagation length of a SPP is small, of the order of 10μ m for $\lambda = 632.8n$ m and 200μ m for $\lambda = 1.55\mu$ m for a gold metal layer [127].

We have shown that a SPP can exist at the interface between two different materials, one of which has dielectric constant with negative real part, with decay length L_{SPP} given by equation (4.11), if the electromagnetic excitation is transverse magnetic. We now show that such an excitation does not exist for a transverse electric field. We start from a transverse electric solution to Maxwell's equations,

$$\boldsymbol{E}\left(\boldsymbol{x}, t\right) = \left(0, 0, A^{(n)}\right)^T e^{-\text{sgn}(y)k_y^{(n)}y} e^{i(k_x x - \omega t)}, \tag{4.12a}$$

$$\boldsymbol{H}\left(\boldsymbol{x}, t\right) = \frac{A^{(n)}}{i\omega}\left(-\text{sgn}(y)k_y^{(n)}, ik_x, 0\right)^T e^{-\text{sgn}(y)k_y^{(n)}y} e^{i(k_x x - \omega t)}, \tag{4.12b}$$

where the symbols have the same meaning as used above. Again using the boundary conditions on the transverse components of the two fields we obtain a matrix equation

$$\begin{pmatrix} 1 & 1 \\ k_y^{(1)} & -k_y^{(2)} \end{pmatrix}\begin{pmatrix} A^{(1)} \\ A^{(2)} \end{pmatrix} = 0. \tag{4.13}$$

This time however, the solvability condition leads to the equation

$$k_y^{(1)} + k_y^{(2)} = 0. \tag{4.14}$$

As such there is no solution for transverse electric fields in which the decay constants k_z are both positive, and therefore, no SPP relating to this type of wave. This section describes the properties of an ideal SPP at the interface between two semi–infinite materials. In this case the polarisation and propagation vectors can be determined analytically. We can also approximate the propagation length of the SPP in terms of the absorption in the metal. This illustrates the properties of the SPP which we build on throughout this chapter.

4.3 Numerical methods for surface plasmon propagation

The problem of modelling the interaction of SPP at the surface of a photorefractive liquid crystal cell is not a trivial one. Before we develop approximate solutions to describe the physics of these systems it is useful to formulate a numerical model of them. The method we use to model the optical response of a plasmon LC cell is the rigorous diffraction theory [2, 102]. Before we consider the implementation of this method we first look at general T–matrix methods for layered materials.

4.3.1 T–matrix model for surface plasmon interaction

The T–matrix method is based on matching the wave–like solutions to Maxwell's equations in stratified homogeneous or harmonic media. The geometry is broken down into a series of different layers which are homogeneous in the direction normal to the layer surface. For the photorefractive liquid crystal cell the alignment layers and the gold may each be considered as a single layer. However, the liquid crystal must be sliced into a large number of very thin layers. These layers are small enough such that the variation of the liquid crystal alignment in each layer is negligible, see Figure 4.3. The requirement that the fields are matched at the boundary allows the field to be written as a linear combination of forward and reverse propagating waves in the homogeneous case and a sum of linearly independent Fourier components in harmonic materials.

To ensure that Maxwell's equations are satisfied at the boundaries we require that the tangential components of the $\boldsymbol{E}$ and $\boldsymbol{H}$ fields are continuous. Before we consider the more complex case of an harmonic anisotropic material we consider the simplest possible case, homogeneous isotropic dielectrics.

The starting point for such an expansion is the field representation in the layers. Here we are interested in isotropic homogeneous materials. Therefore, the fields break down to TE and TM modes. As we are interested in systems which can support SPP it is appropriate to consider only

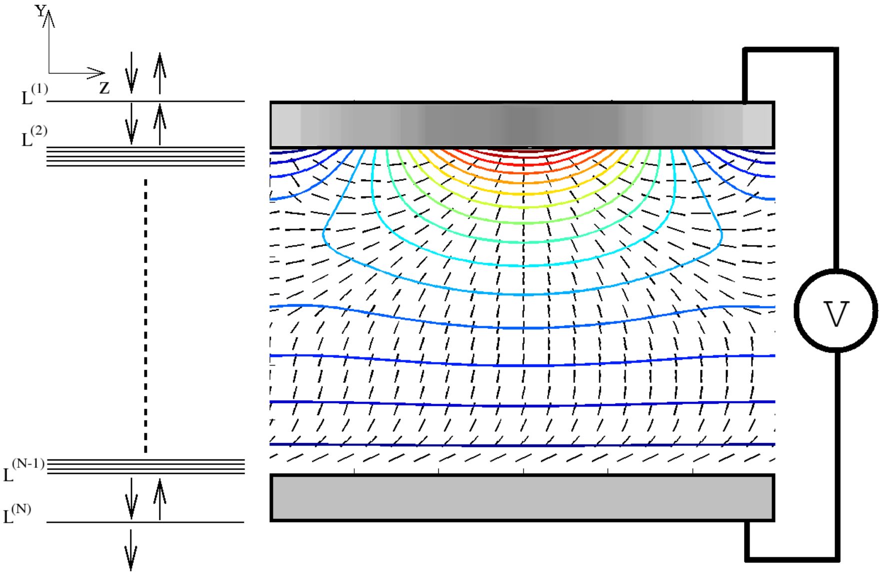

FIGURE 4.3: *The photorefractive liquid crystal cell is broken down into layers. These are homogeneous in the y–direction but may be periodically modulated in the (x, z) plane. The liquid crystal must be sliced into a large number of thin layers, each of which may be considered homogeneous in the y–direction.*

the TM modes. Their fields can be expressed entirely in terms of the magnetic field. In the more general case, which we will consider in Section 4.3.2, both the electric and the magnetic field must be taken into account to allow for the coupling between TE and TM modes. We consider a field which propagates in the x direction with wavenumber α_0 and has transverse wave vector $\beta^{(n)}$ in material n. The magnetic fields in each material can be written in the form

$$\boldsymbol{H}^{(n)} = \hat{\boldsymbol{e}}_z F^{(n)} e^{i\left(\alpha_0 x+\beta^{(n)} y-\omega t\right)} + \hat{\boldsymbol{e}}_z R^{(n)} e^{i\left(\alpha_0 x-\beta^{(n)} y-\omega t\right)}, \tag{4.15}$$

where $F^{(n)}$ and $R^{(n)}$ are the amplitudes of the forward or backward propagating waves and $\beta^{(n)}$ is found from the dispersion relation

$$\beta^{(n)} = \sqrt{\frac{\omega^2}{c^2}\epsilon^{(n)} - \alpha_0^2}. \tag{4.16}$$

In the case of propagating waves it makes sense to talk about forward and backwards waves. When these fields become evanescent this distinction is less clear. From here on we define the forward wave to be the wave which decays exponentially with increasing y if the field is evanescent and the field that propagates in the y direction for purely real modes. This distinction becomes important in the more general case considered in Section 4.3.2. The problem now reduces to finding $F^{(n)}$ and $R^{(n)}$ by solving Maxwell's boundary conditions at each interface. In the case of the TM modes we have to require that the tangential components of the magnetic field and the corresponding electric field are continuous. In terms of the magnetic field these

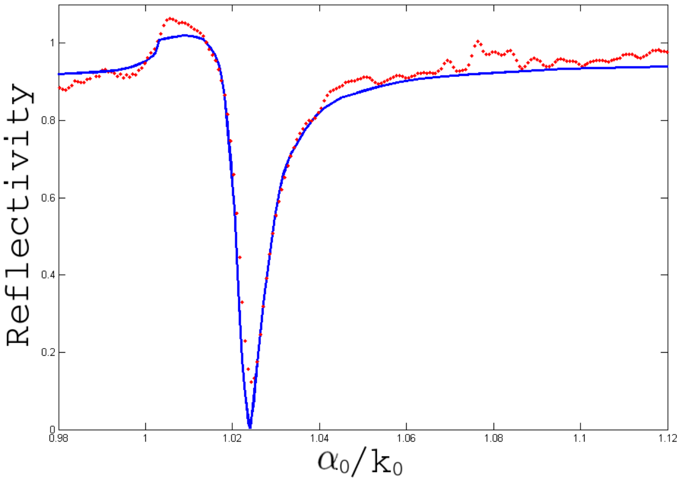

FIGURE 4.4: *Typical reflection spectrum from a three layer Kretschmann geometry. The solid line shows the theoretical results. The dotted line shows the experimental results (courtesy of Dr David Smith and Stephen Abbot).*

equations can be written as

$$\boldsymbol{H}^{(n)}\Big|_{y=L^{(n)}} = \boldsymbol{H}^{(n+1)}\Big|_{y=L^{(n)}} \tag{4.17}$$

and

$$\frac{1}{\epsilon^{(n)}}\frac{d}{dy}\boldsymbol{H}^{(n)}\Big|_{y=L^{(n)}} = \frac{1}{\epsilon^{(n+1)}}\frac{d}{dy}\boldsymbol{H}^{(n+1)}\Big|_{y=L^{(n)}}. \tag{4.18}$$

These continuity conditions at each boundary can be expressed as a linear system,

$$\begin{pmatrix} e^{i\beta^{(n)}W^{(n)}} & e^{-i\beta^{(n)}W^{(n)}} \\ \frac{\beta^{(n)}}{\epsilon^{(n)}}e^{i\beta^{(n)}W^{(n)}} & -\frac{\beta^{(n)}}{\epsilon^{(n)}}e^{-i\beta^{(n)}W^{(n)}} \end{pmatrix}\begin{pmatrix} F^{(n)} \\ R^{(n)} \end{pmatrix} = \begin{pmatrix} 1 & 1 \\ \frac{\beta^{(n+1)}}{\epsilon^{(n+1)}} & -\frac{\beta^{(n+1)}}{\epsilon^{(n+1)}} \end{pmatrix}\begin{pmatrix} F^{(n+1)} \\ R^{(n+1)} \end{pmatrix} \tag{4.19}$$

where $W^{(n)} = L^{(n)} - L^{(n-1)}$ is the thickness of the layer n. Note, from here we could rederive the plasmon conditions by setting $F^{(n+1)}$ and $R^{(n)}$ to zero, using equation (4.16) and solving the resulting system of equations for α_0. However, as we are interested in the methods to generate plasmons we want to study the response of this system to a variety of different α_0. Equation (4.19) is the standard T–matrix method. This can be written as $T^{(n)}\boldsymbol{h}^{(n)} = \boldsymbol{h}^{(n+1)}$, where $\boldsymbol{h}^{(n)} = (F^{(n)}, R^{(n)})^T$. This equation describes the propagating electromagnetic fields on one side of a layer in terms of the fields on the other side.

The simple isotropic homogeneous T–matrix equations have been derived for an arbitrary number of layers. Although this result is not of direct relevance in studying the photorefractive liquid crystal cell problem it can be used to accurately predict the excitation of surface plasmons.

We consider a three layer structure consisting of a glass prism of refractive index 1.9, a metal layer of thickness 50nm adjacent to air ($\epsilon = 1$). The reflection spectrum for light of wavelength 832nm we obtain the theoretical and experimental reflection spectra shown in Figure 4.4. The sharp dip observed is at the SPP resonance angle defined by equation (4.9). These reflection curves are typical of surface plasmons. The peak reflection seen is the onset of total internal reflection at the metal air interface. Increasing the angle slightly takes us closer to the SPP resonance and we see a dip in reflectivity as energy is coupled to the surface mode. The quality of the fit should not be surprising since for this simple structure the matrix theory is identical to the Fresnel reflection coefficients which are used to experimentally obtain the thickness of the various layers.

4.3.2 Rigorous diffraction theory

Using the ideas of the last section we now want to derive and implement the rigorous diffraction theory of Moharam et al [2, 102]. The liquid crystal cell is divided into homogeneous layers and we look for the general solution to Maxwell's equations in each layer. Assuming harmonic propagation it is enough to consider only the curl equations,

$$\boldsymbol{\nabla} \times \boldsymbol{E} = -i\omega\mu_0 \boldsymbol{H} \quad \text{and} \quad \boldsymbol{\nabla} \times \boldsymbol{H} = i\omega\epsilon_0\epsilon_r \boldsymbol{E} \tag{4.20}$$

The dielectric tensor in each layer is written as a Fourier series with fundamental Fourier component $\boldsymbol{K}_g$. Adopting the notation used in [162] the dielectric tensor in region n takes the form

$$\epsilon_{\delta\gamma}^{(n)} = \sum_{l=-\infty}^{\infty} \epsilon_{\delta\gamma,l}^{(n)} \exp\left(il\boldsymbol{K}_g \cdot \boldsymbol{x}\right), \tag{4.21}$$

where $\epsilon_{\delta\gamma,l}^{(n)}$ are the l–th Fourier coefficients in medium n of the dielectric tensor and $\delta, \gamma = x, y, z$. Scaling space $\tilde{\boldsymbol{x}} = k_0\boldsymbol{x}$, where $k_0 = 2\pi/\lambda$ is the wavenumber in free space and λ is the wavelength, $\tilde{\boldsymbol{K}}_g = \lambda/\Lambda$, where Λ is the fundamental grating pitch, and the electric and magnetic fields $\tilde{\boldsymbol{E}} = \sqrt{\epsilon_0}\boldsymbol{E}$ and $\tilde{\boldsymbol{H}} = \sqrt{\epsilon_0}\boldsymbol{H}$ allows us to obtain the scaled derivatives $\tilde{\boldsymbol{\nabla}} = k_0\boldsymbol{\nabla}$ and the scaled equations

$$\tilde{\boldsymbol{\nabla}} \times \tilde{\boldsymbol{E}} = -i\tilde{\boldsymbol{H}} \quad \text{and} \quad \tilde{\boldsymbol{\nabla}} \times \tilde{\boldsymbol{H}} = i\epsilon_r\tilde{\boldsymbol{E}}. \tag{4.22}$$

For compactness of notation we shall omit the tilde and deal only with the scaled fields for the remainder of this chapter. The fields in each layer are written as a Fourier series and broken down into the components along the coordinate axes. It is assumed that the propagation vector in the plane of the interface is known. It is only the field dependence in the direction normal to the interface which is unknown. For an interface in the (x, z) plane the electric and magnetic fields can be written as

$$\begin{aligned} \boldsymbol{E}^{(n)}(\boldsymbol{x}) = & \sum_{p=-\infty}^{\infty} \left[E_{x,p}^{(n)}(y)\hat{\boldsymbol{e}}_x + E_{y,p}^{(n)}(y)\hat{\boldsymbol{e}}_y + E_{z,p}^{(n)}(y)\hat{\boldsymbol{e}}_z\right] \\ & \exp\left\{i\left[\left(k_x + pK_{gx}\right)x + pK_{gy}y + \left(k_z + pK_{gz}\right)z\right]\right\} \end{aligned} \tag{4.23a}$$

and

$$\boldsymbol{H}^{(n)}(\boldsymbol{x}) = \sum_{p=-\infty}^{\infty} \left[H_{x,p}^{(n)}(y)\hat{\boldsymbol{e}}_x + H_{y,p}^{(n)}(y)\hat{\boldsymbol{e}}_y + H_{z,p}^{(n)}(y)\hat{\boldsymbol{e}}_z\right] \exp\left\{i\left[\left(k_x + pK_{gx}\right)x + pK_{gy}y + \left(k_z + pK_{gz}\right)z\right]\right\}, \tag{4.23b}$$

where $\boldsymbol{k}$ is the propagation vector in the (x, z) plane and K_{gx} refers to the x component of K_g. To proceed we decompose Maxwell's equations (4.22) into their x, y, z components:

$$\frac{dH_{z,p}^{(n)}}{dy} = -ipK_{gy}H_{z,p}^{(n)} + i\left(k_z + pK_{gz}\right)H_{y,p}^{(n)} + i\sum_{q=-\infty}^{\infty} \epsilon_{xx,pq}E_{x,q}^{(n)} + \epsilon_{xy,pq}E_{y,q}^{(n)} + \epsilon_{xz,pq}E_{z,q}^{(n)}, \tag{4.24a}$$

$$i\left(k_z + pK_{gz}\right)H_{x,p}^{(n)} - i\left(k_x + pK_{gx}\right)H_{z,p}^{(n)} = i\sum_{q=-\infty}^{\infty} \epsilon_{yx,pq}E_{x,q}^{(n)} + \epsilon_{yy,pq}E_{y,q}^{(n)} + \epsilon_{yz,pq}E_{z,q}^{(n)}, \tag{4.24b}$$

$$\frac{dH_{x,p}^{(n)}}{dy} = -ipK_{gy}H_{x,p}^{(n)} + i\left(k_x + pK_{gx}\right)H_{y,p}^{(n)} - i\sum_{q=-\infty}^{\infty} \epsilon_{zx,pq}E_{x,q}^{(n)} + \epsilon_{zy,pq}E_{y,q}^{(n)} + \epsilon_{zz,pq}E_{z,q}^{(n)}, \tag{4.24c}$$

$$\frac{dE_{z,p}^{(n)}}{dy} = -ipK_{gy}E_{z,p}^{(n)} + i\left(k_z + pK_{gz}\right)E_{y,p}^{(n)} - iH_{x,p}^{(n)}, \tag{4.24d}$$

$$i\left(k_z + pK_{gz}\right)E_{x,p}^{(n)} - i\left(k_x + pK_{gx}\right)E_{z,p}^{(n)} = -iH_{y,p}^{(n)}, \tag{4.24e}$$

and

$$\frac{dE_{x,p}^{(n)}}{dy} = -ipK_{gy}E_{x,p}^{(n)} + i\left(k_x + pK_{gx}\right)E_{y,p}^{(n)} + iH_{z,p}^{(n)}. \tag{4.24f}$$

Here the tensor Fourier coefficients are $\epsilon_{\delta\gamma,pq} = \epsilon_{\delta\gamma,p-q}$. For these equations to be considered exact under the assumptions we have already made the summations on the right hand side of equations (4.24a), (4.24b) and (4.24c) must be between $\pm\infty$. However, these equations will be accurate for a non-infinite summation providing that a sufficiently large number of terms is considered. Here we sum between $\pm N$ and therefore consider $2N+1$ different Fourier components. Typically, in simulations this value is increased until convergence is reached. Equations (4.24b) and (4.24e) are two algebraic equations for the polarisation components $E_{y,p}^{(n)}(y)$ and $H_{y,p}^{(n)}(y)$ respectively. The remaining equations (4.24a), (4.24c), (4.24d) and (4.24e) form a system of differential equations for the remaining polarisation components. After some manipulation this system can be expressed as a differential eigenvalue problem for the tangential components of the fields and a linear algebraic system for the normal components,

$$\frac{d\boldsymbol{A}_{\parallel}^{(n)}}{d\tilde{y}} = iC^{(n)}\boldsymbol{A}_{\parallel}^{(n)}, \tag{4.25a}$$

$$\boldsymbol{A}_{\perp}^{(n)} = D^{(n)}\boldsymbol{A}_{\parallel}^{(n)}, \tag{4.25b}$$

where $\boldsymbol{A}_{\parallel}^{(n)}$, $\boldsymbol{A}_{\perp}^{(n)}$, $C^{(n)}$ and $D^{(n)}$ in each layer are of the form given in [162], reproduced here for convenience. We omit the superscript (n) in the submatrices for compactness,

$$\boldsymbol{A}_{\perp}^{(n)} = \begin{pmatrix} e_y(\tilde{y}) \\ h_y(\tilde{y}) \end{pmatrix}, \qquad \boldsymbol{A}_{\parallel}^{(n)} = \begin{pmatrix} e_x(\tilde{y}) \\ h_z(\tilde{y}) \\ e_z(\tilde{y}) \\ h_x(\tilde{y}) \end{pmatrix}, \tag{4.26}$$

$$C^{(n)} = \begin{pmatrix} k_x\epsilon_{yy}^{-1}\epsilon_{yx} + k_y & k_x\epsilon_{yy}^{-1}k_x - I & k_x\epsilon_{yy}^{-1}\epsilon_{yz} & -k_x\epsilon_{yy}^{-1}k_z \\ \epsilon_{xy}\epsilon_{yy}^{-1}\epsilon_{yx} - \epsilon_{xx} + k_z^2 & \epsilon_{xy}\epsilon_{yy}^{-1}k_x + k_y & \epsilon_{xy}\epsilon_{yy}^{-1}\epsilon_{yz} - \epsilon_{xz} - k_zk_x & -\epsilon_{xy}\epsilon_{yy}^{-1}k_z \\ k_z\epsilon_{yy}^{-1}\epsilon_{yx} & k_z\epsilon_{yy}^{-1}k_x & k_z\epsilon_{yy}^{-1}\epsilon_{yz} + k_y & -k_z\epsilon_{yy}^{-1}k_z + I \\ \epsilon_{zx} - \epsilon_{zy}\epsilon_{yy}^{-1}\epsilon_{yx} + k_xk_z & -\epsilon_{zy}\epsilon_{yy}^{-1}k_x & \epsilon_{zz} - \epsilon_{zy}\epsilon_{yy}^{-1}\epsilon_{yz} - k_x^2 & \epsilon_{zy}\epsilon_{yy}^{-1}k_z + k_y \end{pmatrix} \tag{4.27}$$

and

$$D^{(n)} = \begin{pmatrix} -\epsilon_{yy}^{-1}\epsilon_{yx} & -\epsilon_{yy}^{-1}k_x & -\epsilon_{yy}^{-1}\epsilon_{yz} & \epsilon_{yy}^{-1}k_z \\ -k_z & 0 & k_x & 0 \end{pmatrix} \tag{4.28}$$

The sub-matrices, k_δ, are $M \times M$ diagonal matrices, where $M = 2N + 1$, whose elements are given by k_δ of the pth wave, I is the $M \times M$ identity matrix, the components of the $M \times M$ matrix $\epsilon_{\delta\gamma}$ are $\epsilon_{\delta\gamma,pq}$, the tensor Fourier coefficients that match plane wave m to plane wave n and $e_\delta(\tilde{y})$ and $h_\delta(\tilde{y})$ are vectors of dimension M with elements given by the polarisation components of the pth wave.

Equation (4.25a) can be solved as an eigenvalue problem using the substitution

$$\boldsymbol{A}_{\parallel}^{(n)}(y) = \sum_{j=-N}^{N} \boldsymbol{u}_j^{(n)} a_j^{(n)} e^{i\beta_j^{(n)} y}, \tag{4.29}$$

where the eigenvector $\boldsymbol{u}_j^{(n)}$ is the mode polarisation amplitude in the interface plane and $\beta_j^{(n)}$ is the wavenumber of mode j in the y–direction. The undetermined coefficients $a_j^{(n)}$ are found by matching the tangential components of the field at the boundaries. This leads to the condition

$$\boldsymbol{A}_{\parallel}^{(n)}(y)\bigg|_{y=L^{(n)}} = \boldsymbol{A}_{\parallel}^{(n+1)}(y)\bigg|_{y=L^{(n)}}, \tag{4.30}$$

where the $L^{(n)}$ is the y–coordinate of the boundary, see Figure 4.3. The equations are now in the form of a standard T–matrix approach,

$$\tilde{U}^{(n)}\tilde{C}^{(n)}\tilde{\boldsymbol{a}}^{(n)} = \tilde{U}^{(n+1)}\tilde{\boldsymbol{a}}^{(n+1)}, \tag{4.31}$$

where $\tilde{U}_{kj}^{(n)}$ is the kth element of the jth eigenvector $\boldsymbol{u}_j^{(n)}$, $\tilde{C}_{kj}^{(n)}$ is a diagonal matrix with elements $\exp\left(i\beta_j^{(n)}W^{(n)}\right)$ for $k = j$ and 0 otherwise and $\tilde{\boldsymbol{a}}^{(n)}$ is a vector whose elements are the undetermined coefficients $a_j^{(n)}$. This method works well assuming the geometry does not become large. If it does then, for evanescent waves, the matrix $\tilde{C}^{(n)}$ becomes ill conditioned. To overcome this we use an S–matrix approach [155]. Firstly, we split the fields into forward and backward waves. We also separate the electric and magnetic field components using row and column operations such that

$$\tilde{U}^{(n)} = \begin{pmatrix} U_n^+ & U_n^- \\ V_n^+ & V_n^- \end{pmatrix}, \tag{4.32}$$

where the block matrices U_n^+ and U_n^- are the forward and backward parts of the electric field and V_n^+ and V_n^- are the forward and backward parts of the magnetic field respectively. These have undetermined coefficients $\boldsymbol{a}_n^{\pm}$. The complex eigenvalues of equation (4.25a) can be written as $\beta_j^{(n)\pm} = \beta_{j,c}^{(n)} \pm \beta_{j,d}^{(n)}$, where $\beta_j^{\pm}$ are the forward and backwards eigenvalues and have a common part $\beta_{j,c}$ and a difference $\beta_{j,d}$. The matrix of complex phases can therefore be written as

$$\tilde{C}^{(n)} = \begin{pmatrix} \varphi_n C_n & 0 \\ 0 & \varphi_n C_n^{-1} \end{pmatrix}, \tag{4.33}$$

where φ_n is a diagonal matrix with elements $\exp\left(i\beta_{j,c}^{(n)}W^{(n)}\right)$ and C_n is a diagonal matrix with elements $\exp\left(i\beta_{j,d}^{(n)}W^{(n)}\right)$. In general we want to avoid exponentially growing or decaying phase terms. These occur when the fields become evanescent and $\beta_j^{(n)\pm}$ become complex conjugate pairs. Therefore, the common terms will be real and matrix φ_n will be well conditioned. The differences will be complex causing the matrix C_n to be ill conditioned. therefore we must write the boundary conditions such that we can calculate the reflection spectrum without having to calculate C_n^{-1}. Using this notation the boundary conditions can be written as

$$U_n^+\varphi_n C_n \boldsymbol{a}_n^+ + U_n^-\varphi_n C_n^{-1}\boldsymbol{a}_n^- = U_{n+1}^+\boldsymbol{a}_{n+1}^+ + U_{n+1}^-\boldsymbol{a}_{n+1}^- \tag{4.34a}$$

and

$$V_n^+\varphi_n C_n \boldsymbol{a}_n^+ + V_n^-\varphi_n C_n^{-1}\boldsymbol{a}_n^- = V_{n+1}^+\boldsymbol{a}_{n+1}^+ + V_{n+1}^-\boldsymbol{a}_{n+1}^-. \tag{4.34b}$$

The need to calculate C_n^{-1} can be overcome by defining the S–matrix [155, 156, 157] which relates the reflected field $\boldsymbol{a}_n^-$ to the input fields

$$\boldsymbol{a}_n^- = S_n \boldsymbol{a}_n^+. \tag{4.35}$$

Physically this is equivalent to considering the exponentially growing fields as a linear combination of the exponentially decaying fields. Therefore, the ill conditioned part of the system, associated with the exponentially growing waves, is eliminated. Substituting into equation (4.34) allows us to eliminate C_n^{-1} and obtain a well conditioned system to solve:

$$\left[U_n^+ \varphi_n C_n + U_n^- \varphi_n C_n^{-1} S_n\right] \boldsymbol{a}_n^+ = \left[U_{n+1}^+ + U_{n+1}^- S_{n+1}\right] \boldsymbol{a}_{n+1}^+ \tag{4.36a}$$

$$\left[V_n^+ \varphi_n C_n + V_n^- \varphi_n C_n^{-1} S_n\right] \boldsymbol{a}_n^+ = \left[V_{n+1}^+ + V_{n+1}^- S_{n+1}\right] \boldsymbol{a}_{n+1}^+ \tag{4.36b}$$

By eliminating $\boldsymbol{a}_{n+1}^+$ we obtain

$$\begin{aligned} &\left[U_{n+1}^+ + U_{n+1}^- S_{n+1}\right]^{-1} \left[U_n^+ \varphi_n C_n + U_n^- \varphi_n C_n^{-1} S_n\right] - \\ &\left[V_{n+1}^+ + V_{n+1}^- S_{n+1}\right]^{-1} \left[V_n^+ \varphi_n C_n + V_n^- \varphi_n C_n^{-1} S_n\right] = 0 \end{aligned} \tag{4.37}$$

which, after some algebra, can be written as

$$S_n = C_n M(S_{n+1})^{-1} N(S_{n+1}) C_n, \tag{4.38}$$

where

$$M(S_{n+1}) = \left[U_{n+1}^+ + U_{n+1}^- S_{n+1}\right]^{-1} U_n^+ \varphi_n - \left[V_{n+1}^+ + V_{n+1}^- S_{n+1}\right]^{-1} V_n^+ \varphi_n \tag{4.39a}$$

$$N(S_{n+1}) = \left[V_{n+1}^+ + V_{n+1}^- S_{n+1}\right]^{-1} V_n^- \varphi_n - \left[U_{n+1}^+ + U_{n+1}^- S_{n+1}\right]^{-1} U_n^- \varphi_n \tag{4.39b}$$

Using the fact that the backward propagating field in the final layer must be zero we can compute the S–matrices in an iterative manner. Note we do not need to compute C_n^{-1} at any point. Using a similar method the transmitted field can be calculated iteratively from the input field,

$$\boldsymbol{a}_{n+1}^+ = \left[U_{n+1}^+ + U_{n+1}^- S_{n+1}\right]^{-1} \left[U_n^+ \varphi_n C_n + U_n^- M(S_{n+1})^{-1} N(S_{n+1}) C_n\right] \boldsymbol{a}_n^+. \tag{4.40}$$

These equations are well conditioned and can be used for general anisotropic harmonic media. We implement the equations in MATLAB using standard build in functions to calculate the eigenvalues and, hence, the field in each layer.

4.4 Experimental comparison

Using the numerical model described in the previous section as well as experimental data, obtained by Dr David Smith and Stephen Abbot, we can study the reflection spectrum of a photorefractive liquid crystal cell. Whilst an exact quantitative comparison between theory and experiment is not possible, as discussed in Section 3.6, we can obtain qualitative agreement.

The numerical code we have implemented is suitable for any configuration of grating and any liquid crystal alignment. However, here we only study the system where the grating vector is in the z direction, see Figure 4.2. The liquid crystal is modelled using the code developed in Chapter 2. Once the liquid crystal alignment is found, its Fourier transform is used to describe the dielectric profile of the liquid crystal layer. In this geometry the grating is created by the interaction of two coherent beams in the (y, z) plane. The reflective and diffractive properties of the grating are then probed using a separate input beam.

Before we consider the case of the grating it is interesting to see the response of the SPP to a uniform applied voltage. This allows us to confirm that the theoretical predictions agree with the experimental measurements. Experimentally we measure the reflection of a white light source from the surface of a photorefractive plasmonic liquid crystal cell. This allows us to obtain the reflected intensity as a function of the optical wavelength. This is measured for a variety of different incidence angles and applied voltages. It is expected that, as observed in previous work by Welford et al [150], at low voltages we will see a series of sharp reflectivity resonances in the reflection spectrum. These correspond to the coupling to a series of different guided modes. These modes are only expected at low voltages where the variation in the liquid crystal alignment occurs away from the cell boundaries. Once the voltage is increased above a certain threshold the liquid crystal alignment varies sharply close to the boundary and a shift in the SPP resonance is expected.

The results obtained for this experiment are shown in Figure 4.5. Here reflection spectra are shown for three different applied voltages; 0 Volts, 10 Volts and 20 Volts. Unfortunately, due to the presence of interference fringes, generated from a misalignment of the experimental apparatus, it is not possible to say for certain that the guided mode resonances are visible. It may also be possible that, at these voltages, too much voltage is dropped across the liquid crystal layer and the guided modes have already been cut off. The shift in the SPP resonance is much more obvious. It can be seen that at 20 Volts the resonance angle has shifted significantly. This is important as it shows that the SPP can be manipulated by the presence of the liquid crystal layer.

Similar experimental results can be obtained for the SPP resonance shift due to an applied optical field. For a fixed voltage the reflection spectrum is measured both with and without an external 20mW beam. The effect of the external beam is to change the resistance of the photoconductor. This changes the voltage dropped across the liquid crystal causing a change in alignment. For a high enough applied voltage, such that the liquid crystal is realigning close to the cell surface,

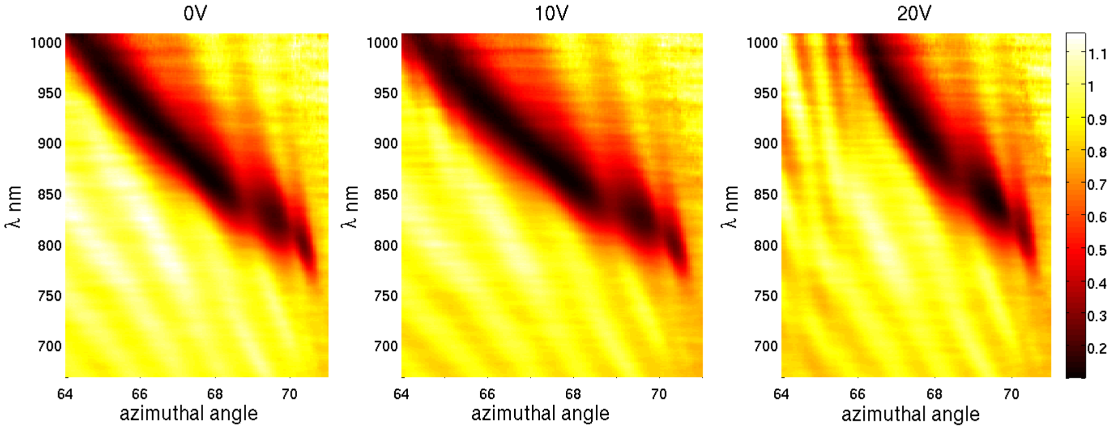

FIGURE 4.5: *Experimental observation of the shift in SPP resonance with applied voltage. For sufficiently large applied voltage the alignment of the liquid crystal near the cell surface is altered. This changes the refractive index seen by the SPP and, hence, changes the resonance conditions. Experimental data by Dr David Smith and Stephen Abbot.*

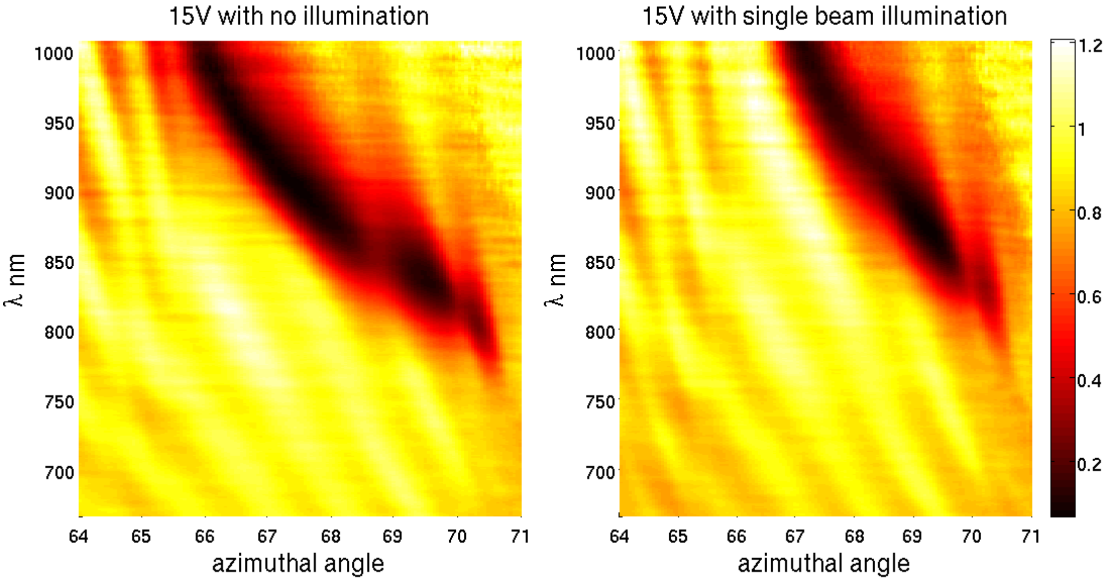

FIGURE 4.6: *Experimental observation of the shift in SPP resonance with* $20mW$ *illumination at a fixed applied voltage. The effect of the external illumination is to change the resistance of the photoconductive layer. This changes the voltage seen across the liquid crystal layer. Physically this effect is seen to be similar to the effect of changing the applied voltage. Experimental data by Dr David Smith and Stephen Abbot.*

the refractive index seen by the plasmon is changed and the resonance position shifts. This is clearly observed in the experimental results shown in Figure 4.6 and confirms that it is possible to manipulate the SPP using an external optical field.

Theoretically the SPP resonance can be modelled for a variety of different applied voltages. Figure 4.7 shows the effects of the applied voltage on the reflected intensity for a single wavelength (800nm). The applied voltage causes the liquid crystal to realign slightly. At low voltages this

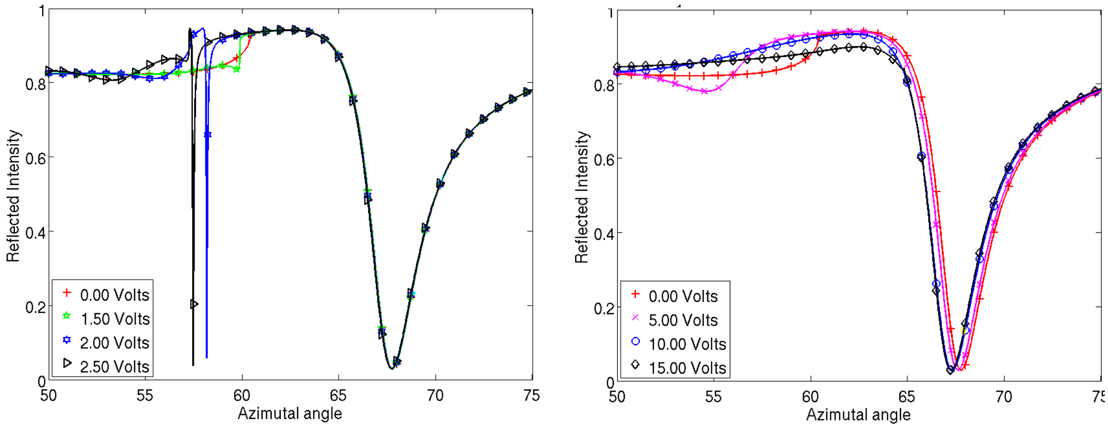

FIGURE 4.7: *Theoretical shift of SPP due to applied voltage at fixed frequency. At low voltage it can be seen that sharp resonances appear in the reflection spectrum before the onset of total internal reflection. These are the result of small realignments in the centre of the liquid crystal cell, too far away from the surface to directly affect the SPP resonance conditions.*

effect causes a strong coupling to the guided modes which can be seen as a series of resonances before the onset of total internal reflection. As the voltage increases the plasmon resonance shifts in agreement with the experimental observations.

For a large enough voltage drop across the liquid crystal is is possible to obtain qualitative fits for the SPP resonance shifts observed both theoretically and experimentally. Figure 4.8 shows the comparison of a reflection spectrum for 0 and 30 Volts. Based on the assumption that this voltage is large enough to ensure complete realignment of the liquid crystal a qualitative fit can be obtained.

The purpose of this work is to understand the effects of diffraction from a liquid crystal cell. Experimentally diffraction has been observed, Figure 4.9, for a 4.5μm grating with $\approx 3\%$ diffraction efficiency for power transfer into the first diffracted order. This diffraction, however low, is important as it provides a way of pumping energy into the SPP. Increased diffraction efficiency, coupled with non–linear feedback between the SPP and the photoconductive layer are the necessary conditions for photorefractive plasmonic gain.

Interestingly theoretical predictions of plasmonic gain show a similar percentage of diffracted output power for a fully aligned liquid crystal. Whilst this is at a lower voltage than used in the experiment it is expected that both these situations correspond to a fully aligned liquid crystal layer. Figure 4.10 shows these results for a single optical wavelength (800nm). Again guided modes can be seen to form at low voltages, an effect not yet observed in our experiments. At high voltages there are two effects: The first is a shift of the SPP resonance due to the change in the non modulated part of the liquid crystal alignment. The second is the diffraction of energy into the higher diffracted orders.

Qualitatively the effects predicted theoretically agree with the experimental observations. However, at this stage it is not possible to obtain a quantitative theoretical experimental verification.

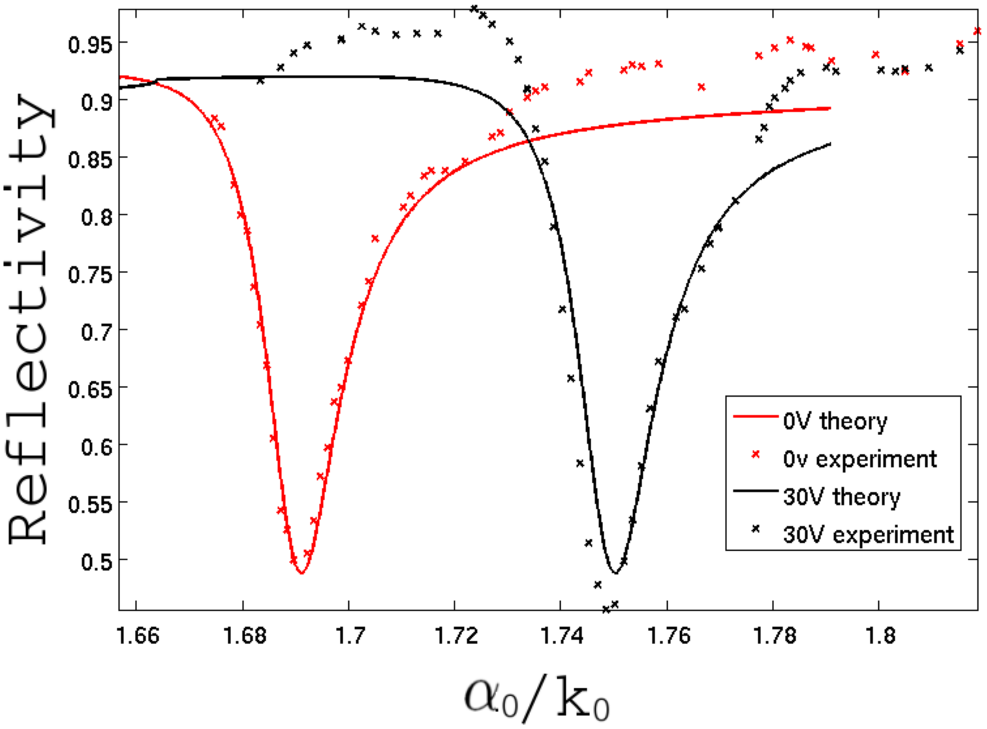

FIGURE 4.8: *Comparison between theoretical shift and experimental shift. For a sufficiently large voltage drop across the liquid crystal layer the SPP resonance asymptotes to the resonance associated with a cell with homeotropic alignment. In this situation the SPP reflection spectra can be matched between theory and experiment. Experimental data by Dr David Smith and Stephen Abbot.*

As with the beam coupling experiments, see Section 3.6, one method to overcome some of these difficulties is to use a slow AC field rather than a DC field to align the liquid crystals. This has two effects: The first is to fix the time frame over which the ions can move reducing the complexity of the system. The second effect, as shown in Section 3.6, is to provide a small increase in the voltage dropped across the liquid crystal layer. These effects will increase the stability and predictability of the experiments whilst decreasing the complexity of the cell modelling allowing a quantitative comparison in the future.

4.5 Asymptotic methods for surface plasmon propagation

Exact theories for SPP propagation in anisotropic media do exist [164]. However, they are overly complicated and highly cumbersome to work with. Here we develop approximation techniques which can be used for SPP propagation in anisotropic media with either homogeneous or periodically modulated permittivity. In Section 4.5.1 we consider the propagation of a SPP at the interface between a semi–infinite metal and a semi–infinite anisotropic dielectric. In Section 4.5.2 we extend this work to consider the case where the permittivity of the dielectric is

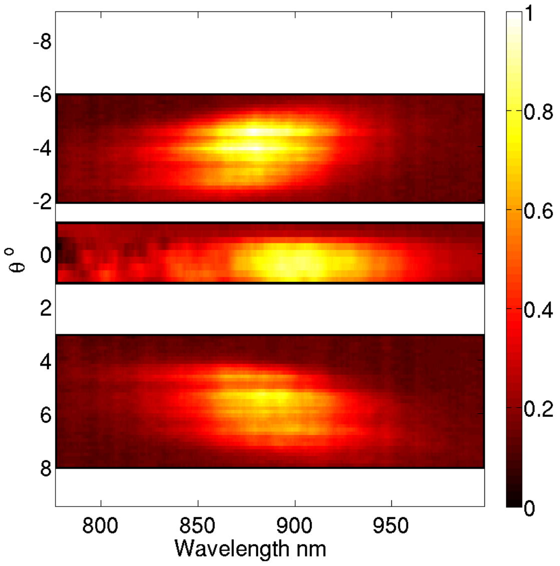

FIGURE 4.9: *Diffraction of a SPP by liquid crystal dielectric grating. Diffraction peaks are observed at with the correct angular separation for the* ± 1 *beams diffracted by a* $4.5\mu m$ *grating. The* 0^o *plot shows the absorption of the plasmon, i.e.* $1 - I$ *where* I *is the normalised intensity. The* ± 1 *diffracted images show the intensity of the* $+1$ *and* -1 *diffracted orders. These intensities have been scaled for visualisation purpose. The measured diffraction efficiency is* $\approx 3\%$*. Experimental data by Dr David Smith and Stephen Abbot.*

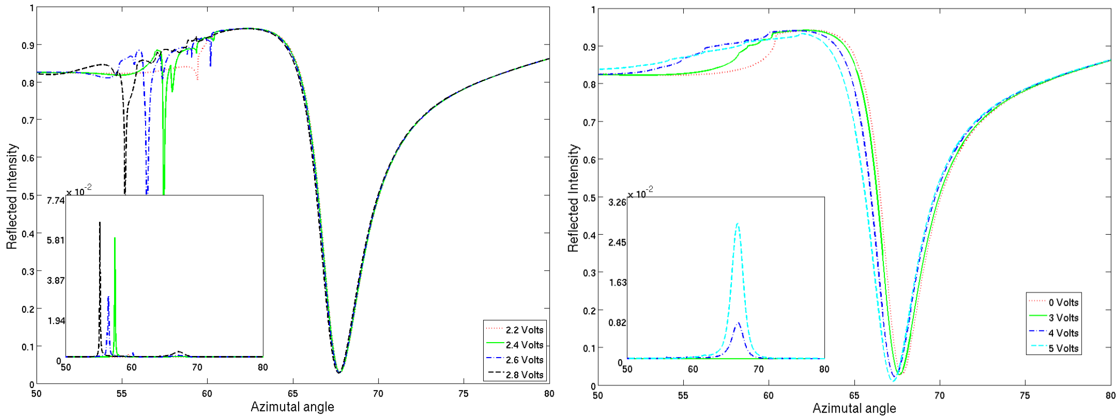

FIGURE 4.10: *Theoretical prediction of diffracted energy by liquid crystal grating at a variety of voltages. Main figure shows the reflection spectrum. The inset shows the intensity of the first diffracted order.*

periodically modulated.

4.5.1 Plasmon propagation in anisotropic media

Using the birefringence as a small parameter we can use perturbation techniques to approximate the effect of anisotropy on the SPP. This is a valid approximation as the birefringence is typically small, even in the case of high anisotropy liquid crystals. We consider a single interface between two semi–infinite materials, a metal and a dielectric. The permittivity in the dielectric medium can be written as

$$\begin{aligned} \epsilon_d = &\left\{ n_o \left[I + \left(\frac{n_e - n_o}{n_o} \right) \hat{\boldsymbol{c}} \otimes \hat{\boldsymbol{c}} \right] \right\}^2 \\ = &\ \epsilon_{d,0} \left[I + \eta \epsilon_{d,1} \hat{\boldsymbol{c}} \otimes \hat{\boldsymbol{c}} + O(\eta^2) \right] \end{aligned} \tag{4.41}$$

where $\epsilon_{d,0} = n_o^2$, $\eta\epsilon_{d,1} = 2\left(\frac{n_e - n_o}{n_o}\right)$, $\eta \ll 1$ is a smallness parameter, $\epsilon_{d,1} \sim O(1)$ and

$$\epsilon_m = \epsilon_{m,0} \tag{4.42}$$

in the metal. Here I is the identity matrix and $\hat{\boldsymbol{c}}$ is the optical axis with components c_x, c_y and c_z. All dielectric constants are assumed real and positive with the exception of $\epsilon_{m,0}$ which is complex and has negative real part. We look for solutions which propagate along the boundary between the two materials and decay exponentially away from the boundary. The interface is in the (x, z) plane with the metal in the region $y > 0$ and the dielectric in the region $y < 0$. The only solution at leading order is the standard isotropic transverse magnetic SPP.

We consider the effects of the perturbation to the operator $C^{(n)}$, equation (4.27), developed in the Section 4.3 where we wrote $C^{(n)}$ such that, for a known propagation vector in the plane of the interface, the field dependence orthogonal to the interface is found via an eigenvalue problem. Here we want to rewrite $C^{(n)}$ such that it is a self adjoint operator $\mathcal{H}_0^{(n)}$ which acts on the electric and magnetic fields to determine the modes at the interface. We find $\mathcal{H}_0^{(n)}$ using the transformation $\mathcal{H}_0^{(n)} = LC^{(n)}R$ where

$$L = \begin{pmatrix} 1 & 0 & 0 & 0 \\ 0 & -1 & 0 & 0 \\ 0 & 0 & 1 & 0 \\ 0 & 0 & 0 & 1 \end{pmatrix}, \qquad R = \begin{pmatrix} 0 & -1 & 0 & 0 \\ 1 & 0 & 0 & 0 \\ 0 & 0 & 0 & 1 \\ 0 & 0 & 1 & 0 \end{pmatrix}. \tag{4.43}$$

Note here we use the same scalings as in Section 4.3. The resulting operator $\mathcal{H}_0^{(n)}$ acts on the fields parallel to the interface plane, $\boldsymbol{A}^{(n)} = R^T \boldsymbol{A}_\parallel^{(n)}$, where $\boldsymbol{A}_\parallel^{(n)}$ is defined in Section 4.3. The properties of the parallel fields are enough to describe the propagation of the surface plasmons. The perpendicular components of the fields can be described using a method similar to the one used in Section 4.3, $\boldsymbol{A}_\perp^{(n)} = D^{(n)} R \boldsymbol{A}^{(n)}$, where $D^{(n)}$ is defined in equation (4.28).

We consider a SPP propagating along the plane and decaying with distance from it. Under an appropriate rotation of coordinate system we may consider only SPP propagating in the x direction. We want to study the effects of the anisotropy as a correction on the slow spatial scale $\boldsymbol{x}_1$. Therefore, as in the beam coupling problem, Section 3.4, we set up a multiple scales expansion scheme in the scaled spatial variables: $\boldsymbol{x}_0 = \boldsymbol{x}$ and $\boldsymbol{x}_1 = \eta \boldsymbol{x}$ and the scaled derivatives

$$\frac{\partial}{\partial \boldsymbol{x}} = \frac{\partial \boldsymbol{x}_0}{\partial \boldsymbol{x}} \frac{\partial}{\partial \boldsymbol{x}_0} + \frac{\partial \boldsymbol{x}_1}{\partial \boldsymbol{x}} \frac{\partial}{\partial \boldsymbol{x}_1} = \frac{\partial}{\partial \boldsymbol{x}_0} + \eta \frac{\partial}{\partial \boldsymbol{x}_1}. \tag{4.44}$$

The operator $\mathcal{H}_0^{(n)}$ can be written as $\mathcal{H}_0^{(n)} = \mathcal{H}^{(n)} + \eta \left(\bar{\mathcal{H}}^{(n)} + \bar{\mathcal{D}}^{(n)} \right)$, where $\mathcal{H}^{(n)}$ and $\bar{\mathcal{H}}^{(n)}$ are self adjoint algebraic operators,

$$\mathcal{H}^{(n)} = \begin{pmatrix} \frac{\epsilon_{n,0}-k_x^2}{\epsilon_{n,0}} & k_y & 0 & 0 \\ k_y & \epsilon_{n,0} & 0 & 0 \\ 0 & 0 & 1 & k_y \\ 0 & 0 & k_y & \epsilon_{n,0}-k_x^2 \end{pmatrix} \tag{4.45a}$$

and

$$\bar{\mathcal{H}}^{(n)} = \begin{pmatrix} \frac{k_x^2 c_y^2}{\epsilon_{n,0}} & c_x c_y k_x & 0 & k_x c_z c_y \\ c_x c_y k_x & \epsilon_{n,0} c_x^2 & 0 & \epsilon_{n,0} c_x c_z \\ 0 & 0 & 0 & 0 \\ k_x c_z c_y & \epsilon_{n,0} c_x c_z & 0 & \epsilon_{n,0} c_z^2 \end{pmatrix} \epsilon_{p,1}, \tag{4.45b}$$

where for compactness of notation we have omitted the superscripts (n) within the operators. The linear differential operator $\bar{\mathcal{D}}^{(n)}$ can be written as $\bar{\mathcal{D}}^{(n)} = \bar{\mathcal{D}}_x^{(n)} \partial_{x_1} + \bar{\mathcal{D}}_y^{(n)} \partial_{y_1}$, where

$$\bar{\mathcal{D}}_x^{(n)} = \begin{pmatrix} \frac{2ik_x}{\epsilon_{n,0}} & 0 & 0 & 0 \\ 0 & 0 & 0 & 0 \\ 0 & 0 & 0 & 0 \\ 0 & 0 & 0 & 2ik_x \end{pmatrix}, \qquad \bar{\mathcal{D}}_y^{(n)} = \begin{pmatrix} 0 & -i & 0 & 0 \\ -i & 0 & 0 & 0 \\ 0 & 0 & 0 & -i \\ 0 & 0 & -i & 0 \end{pmatrix}, \tag{4.46}$$

again for compactness of notation we have omitted the superscript (n) within the operators. We now expand $\mathcal{H}_0^{(n)} \boldsymbol{A}_0^{(n)} = 0$ in powers of η to obtain

$$\mathcal{H}^{(n)} \boldsymbol{A}^{(n)} + \eta \left[\bar{\mathcal{H}}^{(n)} \boldsymbol{A}^{(n)} + \bar{\mathcal{D}}^{(n)} \boldsymbol{A}^{(n)} + \mathcal{H}^{(n)} \bar{\boldsymbol{A}}^{(n)} \right] + O(\eta^2) = 0. \tag{4.47}$$

The isotropic plasmonic modes are found from the requirement that the leading order equation $\mathcal{H}^{(n)} \boldsymbol{A}^{(n)} = 0$ has non–trivial solutions in each material, $\mathrm{Det}(\mathcal{H}^{(n)}) = 0$. From which we obtain the dispersion relation $(k_x^{(n)})^2 + (k_y^{(n)})^2 = \epsilon_{n,0}$. Finally we obtain the polarisations of the fields from the requirement $\boldsymbol{A}^{(n)} \in \ker\left(\mathcal{H}^{(n)}\right)$ and the boundary condition $\boldsymbol{A}^{(m)} = \boldsymbol{A}^{(d)}$.

From here we notice that there are two polarisation vectors which satisfy $\boldsymbol{A}^{(n)} \in \ker(\mathcal{H}^{(n)})$. These correspond to the Transverse Electric (TE) and Transverse Magnetic (TM) modes which have tangential polarisations

$$\hat{\boldsymbol{U}}_1^{(n)} = \frac{k_y^{(n)}}{\sqrt{\epsilon_{n,0}^2 + (k_y^{(n)})^2}} \begin{pmatrix} -\frac{\epsilon_{n,0}}{k_y^{(n)}} \\ 1 \\ 0 \\ 0 \end{pmatrix}, \quad \hat{\boldsymbol{U}}_2^{(n)} = \frac{1}{\sqrt{1 + (k_y^{(n)})^2}} \begin{pmatrix} 0 \\ 0 \\ -k_y^{(n)} \\ 1 \end{pmatrix}. \tag{4.48}$$

We will need to consider both of these polarisations when it comes to the first order equations. However, at leading order, we find that only the transverse magnetic field satisfies the boundary conditions. Therefore, $\hat{\boldsymbol{U}}_1^{(d)} = \hat{\boldsymbol{U}}_1^{(m)} = \hat{\boldsymbol{U}}_1$ and we write $\boldsymbol{A}^{(n)} = \hat{\boldsymbol{U}}_1 A^{(n)}$ with the constraint

$A^{(d)} = A^{(m)} = A^{(S)}$ at $y = 0$. At this point, after some manipulation, we can obtain the standard SPP magnetic fields

$$\boldsymbol{H}^{(n)}(\boldsymbol{x}, t) = A^{(S)}(\boldsymbol{x}_1)\boldsymbol{h}^{(n)} e^{i(\boldsymbol{k}^{(n)}\cdot\boldsymbol{x}_0 - \omega t)} \tag{4.49a}$$

and electric fields

$$\boldsymbol{E}^{(n)}(\boldsymbol{x}, t) = \frac{A^{(S)}(\boldsymbol{x}_1)}{\epsilon_{n,0}} \boldsymbol{e}^{(n)} e^{i(\boldsymbol{k}^{(n)}\cdot\boldsymbol{x}_0 - \omega t)}, \tag{4.50a}$$

where $A^{(S)}$ is the amplitude at the surface and the polarisation and wave vectors are defined as

$$\boldsymbol{e}^{(m)} = \begin{pmatrix} i\delta_m \\ -\alpha_0 \\ 0 \end{pmatrix}, \boldsymbol{k}^{(m)} = \begin{pmatrix} \alpha_0 \\ i\delta_m \\ 0 \end{pmatrix}, \boldsymbol{h}^{(m)} = \begin{pmatrix} 0 \\ 0 \\ 1 \end{pmatrix} \tag{4.51}$$

in the metal and

$$\boldsymbol{e}^{(d)} = \begin{pmatrix} -i\delta_d \\ -\alpha_0 \\ 0 \end{pmatrix}, \boldsymbol{k}^{(d)} = \begin{pmatrix} \alpha_0 \\ -i\delta_d \\ 0 \end{pmatrix}, \boldsymbol{h}^{(d)} = \begin{pmatrix} 0 \\ 0 \\ 1 \end{pmatrix} \tag{4.52}$$

in the dielectric. Here

$$\alpha_0 = \sqrt{\frac{\epsilon_{d,0}\epsilon_{m,0}}{\epsilon_{d,0} + \epsilon_{m,0}}}, \quad \delta_m = \sqrt{-\frac{\epsilon_{m,0}\epsilon_{m,0}}{\epsilon_{d,0} + \epsilon_{m,0}}}, \quad \delta_d = \sqrt{-\frac{\epsilon_{d,0}\epsilon_{d,0}}{\epsilon_{d,0} + \epsilon_{m,0}}}. \tag{4.53}$$

From equation (4.53) we obtain the constraint $|\epsilon_{m,0}| > |\epsilon_{d,0}|$ for propagating solutions. We now consider the effect of the first order perturbation in both the metal and the dielectric. From equation (4.47) the first order equations are

$$\left(\bar{\mathcal{H}}^{(n)} + \bar{\mathcal{D}}^{(n)}\right)\hat{\boldsymbol{U}}_1 A^{(n)} + \mathcal{H}^{(n)}\bar{\boldsymbol{A}}^{(n)} = 0. \tag{4.54}$$

Equation (4.54) is a vector equation which must be satisfied in all directions. We choose two of these directions to be the leading order polarisation vectors. As $\mathcal{H}^{(n)}$ is self adjoint the projection of the final term in equation (4.54) onto the polarisations is zero. Therefore we would expect these two projections to relate the x_1 and y_1 derivatives in $\bar{\mathcal{D}}^{(n)}$. The remaining two projections define the calculable part of the polarisation corrections. We require that these are equal in both materials, this gives the $O(\eta)$ condition $\bar{\boldsymbol{A}}^{(m)} = \bar{\boldsymbol{A}}^{(d)}$.

At this point we could project directly onto the TE and TM polarisations and solve the resulting equations for the correction to the wave vector and the decay constants. However, in the dielectric medium it is clear that for an optical axis which has a component orthogonal to the plane formed by the leading order polarisation and wave propagation vectors then there will be some TE–TM mixing. If this is the case then the equation $\hat{\boldsymbol{U}}_2^{(d)} \cdot (\bar{\mathcal{H}}^{(d)} + \bar{\mathcal{D}}^{(d)})\hat{\boldsymbol{U}}_1 A^{(d)} = 0$ has no solution. This is because, as the TE amplitude is zero, there is nothing to balance the perturbation $\epsilon_{d,1}$ projected in this direction.

To overcome this we define the basis polarisation vectors $\boldsymbol{V}_1^{(d)} = \left(\hat{\boldsymbol{U}}_1 + \hat{\boldsymbol{U}}_2^{(d)}\right)/2$ and $\boldsymbol{V}_2^{(d)} = \left(\hat{\boldsymbol{U}}_2^{(d)} - \hat{\boldsymbol{U}}_1\right)/2$ such that $\boldsymbol{V}_1^{(d)} + \boldsymbol{V}_2^{(d)} = \boldsymbol{U}_1$. In general we can assume that the component of the field associated with each polarisation component may have a different decay constant

$$\hat{\boldsymbol{U}}_1 A^{(d)}(x_1, y_1) = \boldsymbol{V}_1^{(d)} A_1^{(d)}(x_1, y_1) + \boldsymbol{V}_2^{(d)} A_2^{(d)}(x_1, y_1), \tag{4.55}$$

with the constraint that $A_1^{(d)}(x_1, 0) = A_2^{(d)}(x_1, 0)$. The choice of $\boldsymbol{V}_1$ and $\boldsymbol{V}_2$ is arbitrary and has the drawback that the expressions for the corrections to the decay constants become somewhat complicated. This is not a problem as in general it is only the correction to the surface plasmon wavenumber that we require.

Projecting onto the polarisations $\boldsymbol{V}_j^{(d)}$ gives us the equations for the first order dispersion relation

$$\boldsymbol{V}_j^{(d)} \cdot \left(\bar{\mathcal{H}}^{(d)} + \bar{\mathcal{D}}^{(d)}\right) \hat{\boldsymbol{U}}_1 A^{(d)} = 0, \tag{4.56}$$

where $j = 1, 2$ in the dielectric and

$$\hat{\boldsymbol{U}}_1 \cdot \bar{\mathcal{D}}^{(m)} \hat{\boldsymbol{U}}_1 A^{(m)} = 0 \tag{4.57}$$

in the metal. Only a single field needs to be considered in the metal as it is optically isotropic. These two equations define the relationship between the variation of the two differently decaying plasmonic components and the component of the wave vector in the plane. The expressions for $\partial_{x_1} A_j^{(n)}$ in terms of $\partial_{y_1} A^{(m)}$, $\partial_{y_1} A_1^{(d)}$ and $\partial_{y_1} A_2^{(d)}$ are

$$\partial_{y_1} A^{(m)} = i\frac{\alpha_0}{\delta_m}\partial_{x_1} A^{(m)} \tag{4.58a}$$

$$\partial_{y_1} A_1^{(d)} = \left[i\frac{\alpha_0}{\delta_d}\partial_{x_1} - \left(\frac{(\delta_d c_x + i\alpha_0 c_y)^2}{\delta_d} - \frac{\epsilon_d c_z (i c_x \delta_d - \alpha_0 c_y)\sqrt{1-\delta_d^2}}{\delta_d\sqrt{\epsilon_{d,0}^2 - \delta_d^2}}\right)\frac{\epsilon_{d,1}}{2}\right] A_1^{(d)} \tag{4.58b}$$

$$\partial_{y_1} A_2^{(d)} = \left[i\frac{\alpha_0}{\delta_d}\partial_{x_1} - \left(\frac{(\delta_d c_x + i\alpha_0 c_y)^2}{\delta_d} + \frac{\epsilon_d c_z (i c_x \delta_d - \alpha_0 c_y)\sqrt{1-\delta_d^2}}{\delta_d\sqrt{\epsilon_{d,0}^2 - \delta_d^2}}\right)\frac{\epsilon_{d,1}}{2}\right] A_2^{(d)} \tag{4.58c}$$

The boundary condition here is non-obvious as we can only determine the components of $\bar{\boldsymbol{A}}^{(n)}$ which are orthogonal to ker($\mathcal{H}^{(n)}$),

$$\tilde{\boldsymbol{A}}^{(n)} = -\mathcal{P}^{(n)}\left(\bar{\mathcal{H}}^{(n)} + \bar{\mathcal{D}}^{(n)}\right)\hat{\boldsymbol{U}}_1 A^{(n)}, \tag{4.59}$$

where $\tilde{\boldsymbol{A}}^{(n)}$ is the calculable part of the polarisation correction and $\mathcal{P}^{(n)} = \text{Pinv}\left(\mathcal{H}^{(n)}\right)$ is the

Moore–Penrose pseudo inverse. We write the vectors $\hat{\boldsymbol{U}}_1^{(n)}$, $\hat{\boldsymbol{U}}_2^{(n)}$ and $\tilde{\boldsymbol{A}}^{(n)}$ as

$$\hat{\boldsymbol{U}}_1^{(n)} = \begin{pmatrix} \hat{\boldsymbol{u}}_1^{(n)} \\ 0 \\ 0 \end{pmatrix}, \quad \hat{\boldsymbol{U}}_2^{(n)} = \begin{pmatrix} 0 \\ 0 \\ \hat{\boldsymbol{u}}_2^{(n)} \end{pmatrix}, \quad \tilde{\boldsymbol{A}}^{(n)} = \begin{pmatrix} \boldsymbol{S}_1^{(n)} \\ \boldsymbol{S}_2^{(n)} \end{pmatrix}, \tag{4.60}$$

where $\boldsymbol{S}_1^{(n)} \cdot \hat{\boldsymbol{u}}_1^{(n)} = 0$ and $\boldsymbol{S}_2^{(n)} \cdot \hat{\boldsymbol{u}}_2^{(n)} = 0$, recall equation (4.48). The TM vectors in the metal and the dielectric are equal. Therefore, $\hat{\boldsymbol{S}}_1^{(m)} = \hat{\boldsymbol{S}}_1^{(d)} = \hat{\boldsymbol{S}}_1$. The TE vectors in general are not equal, $\boldsymbol{S}_2^{(m)} \neq \boldsymbol{S}_2^{(d)}$. This leads to the boundary conditions

$$\boldsymbol{S}_1 + C_{1m}\hat{\boldsymbol{u}}_1 = \boldsymbol{S}_1 + C_{1d}\hat{\boldsymbol{u}}_1 \tag{4.61}$$

and

$$\boldsymbol{S}_2^{(m)} + C_{2m}\hat{\boldsymbol{u}}_2^{(m)} = \boldsymbol{S}_2^{(d)} + C_{2d}\hat{\boldsymbol{u}}_2^{(d)}, \tag{4.62}$$

where C_{1m}, C_{1d}, C_{2m} and C_{2d} are arbitrary constants. Equation (4.61) must be satisfied in all directions, therefore it makes sense to project onto $\hat{\boldsymbol{S}}_1$ and $\hat{\boldsymbol{u}}_1$. This leads to the boundary condition

$$|\boldsymbol{S}_1^{(m)}| = |\boldsymbol{S}_1^{(d)}| \tag{4.63}$$

and the relation $C_{1m} = C_{1d}$. Similarly equation (4.62) must be satisfied in all directions. However, in this case $\hat{\boldsymbol{u}}_2^{(m)} \neq \hat{\boldsymbol{u}}_2^{(d)}$. Therefore, we can always find a C_{2m} and C_{2d} such that equation (4.62) is satisfied and the only requirement at $O(\eta)$ is equation (4.63). Using (4.58), (4.63) and the requirement that $\partial_{x_1}A^{(m)} = \partial_{x_1}A_1^{(d)} = \partial_{x_1}A_2^{(d)} = \partial_{x_1}A^{(S)}$, we obtain the resulting equation for the variation in x_1;

$$\partial_{x_1}A^{(S)} = i\alpha_0\frac{1}{2}\frac{\epsilon_{m,0}\left(\epsilon_{d,0}c_x^2 - \epsilon_{m,0}c_y^2\right)}{\epsilon_{d,0}^2 - \epsilon_{m,0}^2}\epsilon_{d,1}A^{(S)}. \tag{4.64}$$

From which we obtain the first order correction to the surface plasmon wave vector, $k_{SPP} = \alpha_0(1 + \eta k_{x,1})$, where

$$k_{x,1} = \frac{1}{2}\frac{\epsilon_{m,0}\left(\epsilon_{d,0}c_x^2 - \epsilon_{m,0}c_y^2\right)}{\epsilon_{d,0}^2 - \epsilon_{m,0}^2}\epsilon_{d,1}. \tag{4.65}$$

The perturbation due to the presence of $\epsilon_{d,1}$ can be verified by comparison to numerical simulations, see Section 4.3. Figures 4.11, 4.12 and 4.13 show the comparison for different values of $\epsilon_{d,1}$. In the first two cases the numerics agree well with the analytic approximation. In the third case however, it can be seen that there is a qualitative difference in the results. This is because, for large enough anisotropy, the input beam used to numerically excite the plasmon can couple to a propagating mode rather than directly to the plasmon. This causes the perturbation expansion to fail as the qualitative behaviour of the solution has changed. Therefore, the expansion is only valid if the SPP wavenumber is larger than the corresponding wavenumber for a propagating field. In general terms this can be expressed as the the following inequality constraint;

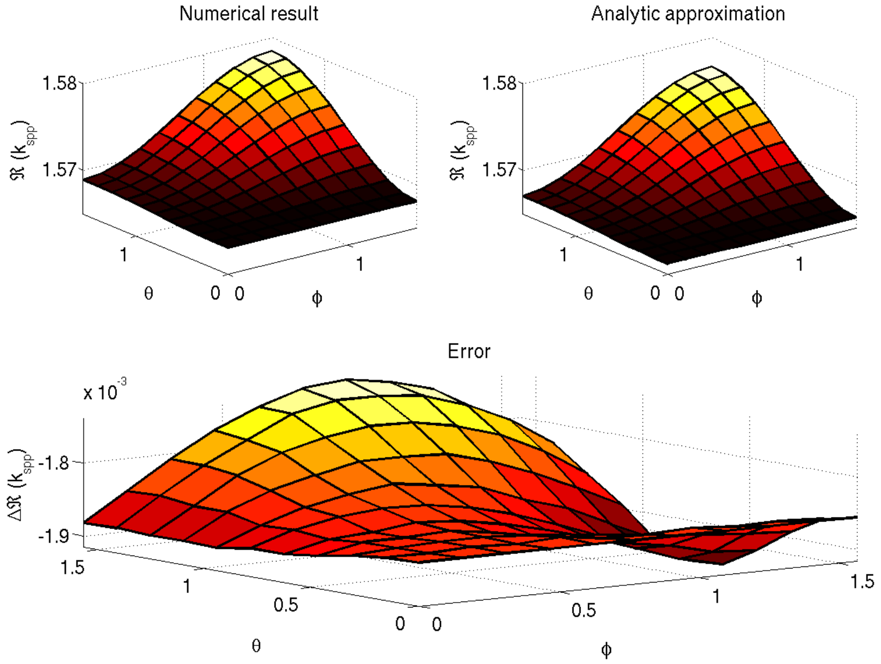

FIGURE 4.11: *Comparison of analytic perturbation expansion and numerical T-matrix calculation of SPP wave vectors. Here we have used* $\eta = 0.013$ *to test our perturbation expansion with a real small number, in this case the maximum error is* $0.0011k_0$.

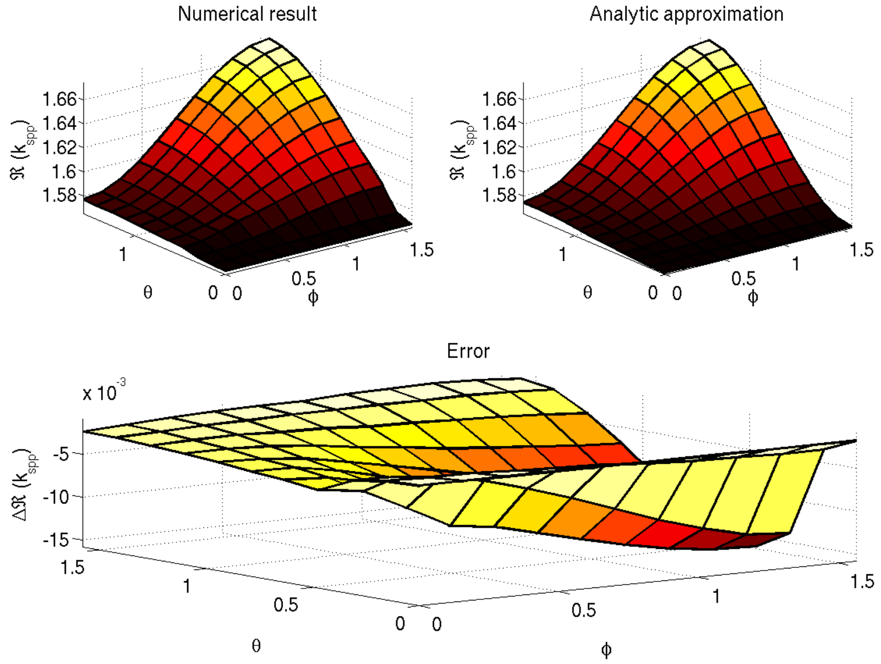

FIGURE 4.12: *Comparison of analytic perturbation expansion and numerical T-matrix calculation of SPP wave vectors. In this case we have used a much larger* $\eta = 0.130$ *to test the perturbation expansion for a more interesting case, here we see a maximum error of* $0.0090k_0$.

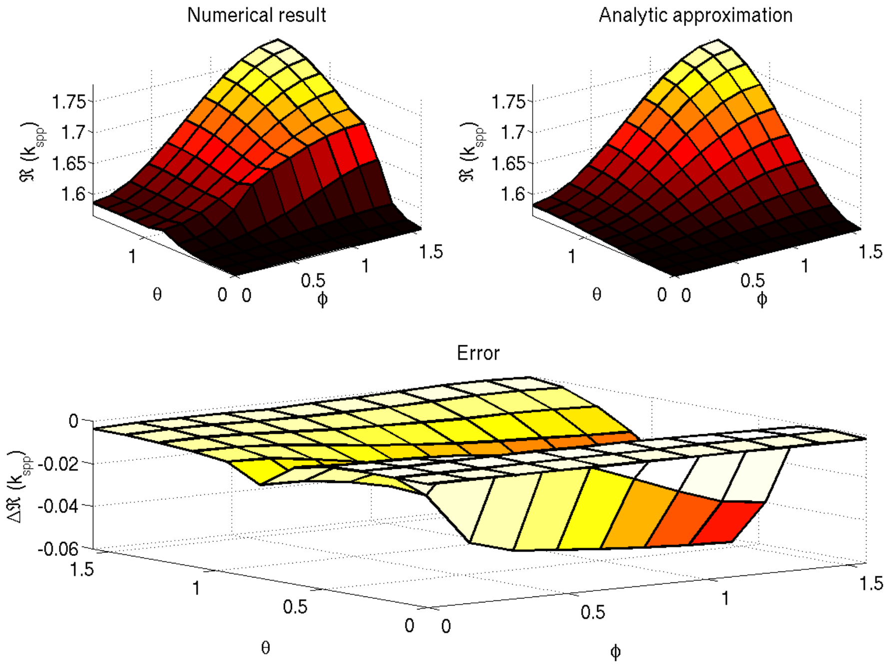

FIGURE 4.13: *Comparison of analytic perturbation expansion and numerical T-matrix calculation of SPP wave vectors. In this case η is no longer small, $\eta = 0.267$, with $\eta^2 = 0.07$. Our maximum calculated error is $0.0446k_0$, however, by looking at the numerical values of K_{SPP} we can see that there are features of the graph we have not yet captured in the perturbation expansion, it could be that although there is an SPP here we are unable to excite it as the energy couples to a propagating mode in the anisotropic crystal.*

$$\sqrt{\frac{\epsilon_{m,0}\epsilon_{d,0}}{\epsilon_{m,0}+\epsilon_{d,0}}} > \sqrt{\epsilon_{d,0}\left(1+\eta\epsilon_{d,1}\right)}, \tag{4.66}$$

i.e. the minimum possible SPP wavenumber must be greater than the largest possible optical wavenumber for any orientation of the crystal axis. If this constraint is not satisfied then equation (4.65) will become invalid for certain orientations of the optical axis. Equation (4.65) describes the perturbation of the surface plasmon mode due to the presence of a homogeneous anisotropic layer with arbitrary optical axis. This is shown to be quantitatively accurate when compared to the numerical simulation as long as the condition (4.66) is satisfied. That is, the presence of the anisotropy does not qualitatively change the behaviour of the system.

4.5.2 Coupled plasmonic equations

The coupled plasmonic equations are derived using the same procedure as in the anisotropic case. The equations are solved at each order in each material and the boundary conditions are matched. Conceptually the only difference is that instead of a single SPP propagating in the x–direction there is a discrete set of SPPs propagating in the (x, z) plane. The interaction between these SPP is included as a coupling term in the first order perturbation, $\bar{\mathcal{H}}$. We consider a discrete number of SPPs propagating along the metal–dielectric interface in the (x, z) plane.

The dielectric is assumed to have a small modulated component and can be written in a similar way to equation (4.21),

$$\epsilon_d = \epsilon_{d,0}\left[I + \eta \sum_{l=-\infty}^{\infty} \epsilon_{\delta\gamma,l}^{(d)} \exp\left(ilK_g z\right)\right]. \tag{4.67}$$

The first stage in the derivation of the coupled plasmon equations is to understand how the leading order equations change for a SPP propagating in the (x, z) plane at an angle θ_p to the x–axis,

$$\boldsymbol{k}_p^{(d)} = \begin{pmatrix} \alpha_0 \cos\theta_p \\ -i\delta_d \\ \alpha_0 \sin\theta_p \end{pmatrix}, \quad \boldsymbol{k}_p^{(m)} = \begin{pmatrix} \alpha_0 \cos\theta_p \\ i\delta_m \\ \alpha_0 \sin\theta_p \end{pmatrix} \tag{4.68}$$

The polarisation and linear operators which describe the SPP propagation are rotated by the rotation matrix

$$\mathcal{R}_p = \begin{pmatrix} \cos\theta_p & 0 & -\sin\theta_p & 0 \\ 0 & \cos\theta_p & 0 & -\sin\theta_p \\ \sin\theta_p & 0 & \cos\theta_p & 0 \\ 0 & \sin\theta_p & 0 & \cos\theta_p \end{pmatrix}, \tag{4.69}$$

such that $\boldsymbol{A}_p^{(n)} = \mathcal{R}_p \hat{\boldsymbol{U}}_1 A_p^{(n)}$ and $\mathcal{H}_p^{(n)} = \mathcal{R}_p \mathcal{H}^{(n)} \mathcal{R}_p^T$. Therefore, the leading order equation for the propagation of a SPP in anisotropic homogeneous media at angle θ_p is $\mathcal{H}_p^{(n)} \boldsymbol{A}_p^{(n)} = 0$ or

$$\mathcal{R}_p \mathcal{H}^{(n)} \mathcal{R}_p^T \mathcal{R}_p \hat{\boldsymbol{U}}_1^{(n)} A_p^{(n)} = 0. \tag{4.70}$$

The rotation matrix $\mathcal{R}_p$ is orthogonal, therefore, equation (4.70) simplifies to $\mathcal{R}_p \mathcal{H}^{(n)} \hat{\boldsymbol{U}}_1 A_p^{(n)} = 0$. This is identical to the leading order equation for a SPP propagating along the x–axis which has already been solved in Section 4.5.1. The propagation and decay constants are unchanged by this rotation and are defined in equation (4.53). Therefore the leading order solution is a series of SPP with amplitudes $A_p^{(S)}(\boldsymbol{x}_1)$ propagating in different directions along the interface.

The perturbation to the leading order operator which couples mode q into mode p is written as

$$\bar{\mathcal{H}}_{pq}^{(n)} = \begin{pmatrix} \frac{\alpha_0^2 \cos^2\theta_p \epsilon_{yy,(p-q)}^{(n)}}{\epsilon_{n,0}} & \epsilon_{xy,(p-q)}^{(n)} \alpha_0 \cos\theta_p & 0 & \alpha_0 \cos\theta_p \epsilon_{zy,(p-q)}^{(n)} \\ \epsilon_{xy,(p-q)}^{(n)} \alpha_0 \cos\theta_p & \epsilon_{n,0} \epsilon_{xx,(p-q)}^{(n)} & 0 & \epsilon_{n,0} \epsilon_{xz,(p-q)}^{(n)} \\ 0 & 0 & 0 & 0 \\ \alpha_0 \cos\theta_p \epsilon_{zy,(p-q)}^{(n)} & \epsilon_{n,0} \epsilon_{xz,(p-q)}^{(n)} & 0 & \epsilon_{n,0} \epsilon_{zz,(p-q)}^{(n)} \end{pmatrix} e^{i(p-q)K_g z}. \tag{4.71}$$

We proceed as in Chapter 3. The SPP are diffracted in the bulk of the dielectric as in the case of the beam coupling equations. We consider only the case where the grating vector is in the z–direction. The effect of this grating is to couple energy from the qth SPP into the pth SPP. As in the case of the coupled wave equations we may not obtain perfect phase matching and we need to consider the phase detuning in the x– direction. This is shown in Figure 4.14. The

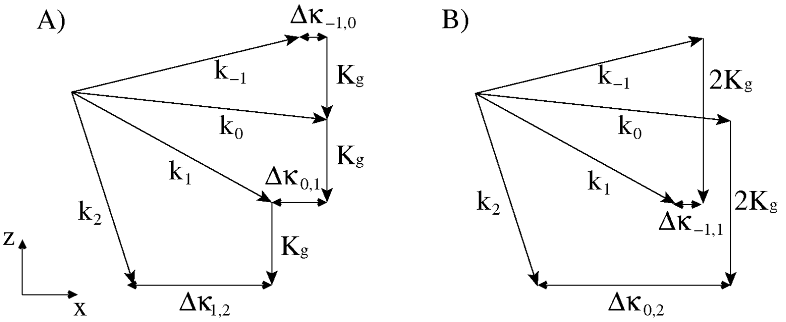

FIGURE 4.14: *Coupling of SPP due to a periodically perturbed dielectric. Figure (A) shows the coupling due to the fundamental Fourier component. Figure (B) shows the coupling due the second harmonic.*

coupling identity in this case is

$$\boldsymbol{k}^{(d)}_q = \boldsymbol{k}^{(d)}_p + (q-p)K_g\hat{\boldsymbol{e}}_z + \eta\Delta k_{pq}\hat{\boldsymbol{e}}_x, \tag{4.72}$$

where

$$\Delta k_{pq} = \alpha_0(\cos\theta_q - \cos\theta_p) \tag{4.73}$$

is the phase detuning term and is assumed to be first order. As discussed in Chapter 3 this may not be the case. However, as the phase detuning becomes large the coupling becomes small. Therefore, we would expect the error induced by this assumption to be negligible. Summing the fields with equal spatial dependence and writing the first order polarisation correction $\bar{\boldsymbol{A}}^{(n)}_p = \mathcal{R}_p\bar{\boldsymbol{U}}^{(n)}A^{(n)}_p$, allows us to obtain the first order equation;

$$\bar{\mathcal{H}}^{(n)}_{pq}\mathcal{R}_q\hat{\boldsymbol{U}}_1A^{(n)}_q e^{i\Delta k_{pq}x_1} + \bar{\mathcal{D}}^{(n)}\mathcal{R}_p\hat{\boldsymbol{U}}_1A^{(n)}_p + \mathcal{R}_p\mathcal{H}^{(n)}\bar{\boldsymbol{U}}^{(n)}A^{(n)}_p = 0. \tag{4.74}$$

The leading order equation is satisfied for two vectors in the kernel of $\mathcal{H}^{(n)}$, the TE and TM modes, which have vectors $\hat{\boldsymbol{U}}^{(n)}_2$ and $\hat{\boldsymbol{U}}^{(n)}_1$ respectively. As described in the previous section the projection along the TE wave is singular and we obtain an equation which does not balance at first order. Therefore, we need to consider two waves whose polarisation is formed from a linear combination of the TE and TM waves, $\boldsymbol{V}_1$ and $\boldsymbol{V}_2$. Projecting equation (4.74) onto these vectors we obtain

$$\boldsymbol{V}^{(d)}_1 \cdot \mathcal{R}^T_p\bar{\mathcal{H}}^{(d)}_{pq}\mathcal{R}_q\hat{\boldsymbol{U}}_1A^{(d)}_q e^{i\Delta k_{pq}x_1} + \boldsymbol{V}^{(d)}_1 \cdot \mathcal{R}^T_p\bar{\mathcal{D}}^{(d)}\mathcal{R}_p\hat{\boldsymbol{U}}_1A^{(d)}_p = 0 \tag{4.75a}$$

and

$$\boldsymbol{V}^{(d)}_2 \cdot \mathcal{R}^T_p\bar{\mathcal{H}}^{(d)}_{pq}\mathcal{R}_q\hat{\boldsymbol{U}}_1A^{(d)}_q e^{i\Delta k_{pq}x_1} + \boldsymbol{V}^{(d)}_2 \cdot \mathcal{R}^T_p\bar{\mathcal{D}}^{(d)}\mathcal{R}_p\hat{\boldsymbol{U}}_1A^{(d)}_p = 0. \tag{4.75b}$$

The differential operator is written as $\bar{\mathcal{D}}^{(n)} = \bar{\mathcal{D}}^{(n)}_x\partial_{x_1} + \bar{\mathcal{D}}^{(n)}_y\partial_{y_1} + \bar{\mathcal{D}}^{(n)}_z\partial_{z_1}$. As we have expressed the field as a Fourier series in the z–direction the geometry is translationally symmetric and, hence, the only variation in the z–direction will be a phase shift. Therefore, there is no amplitude variation in the direction of the grating vector and $\bar{\mathcal{D}}_z = 0$. We can simplify equation (4.75) by observing that the y_1 derivative corresponds to variation orthogonal to the plane of rotation. As such, $\bar{\mathcal{D}}_y$ must be invariant with respect to the conjugacy action of the rotation matrices, $\mathcal{R}_p^T \bar{\mathcal{D}}_y^{(n)} \mathcal{R}_p = \bar{\mathcal{D}}_y^{(n)}$. The only effect of the rotation on the first order derivatives is the effect on $\bar{\mathcal{D}}_x$. Using this simplification equations (4.75) become

$$\boldsymbol{V}_1^{(d)} \cdot \mathcal{R}_p^T \bar{\mathcal{H}}_{pq}^{(d)} \mathcal{R}_q \hat{\boldsymbol{U}}_1 A_q^{(d)} e^{i\Delta k_{pq} x_1} + \boldsymbol{V}_1^{(d)} \cdot \left[\mathcal{R}_p^T \bar{\mathcal{D}}_x^{(d)} \mathcal{R}_p + \bar{\mathcal{D}}_y^{(d)} \right] \hat{\boldsymbol{U}}_1 A_p^{(d)} = 0 \tag{4.76a}$$

and

$$\boldsymbol{V}_2^{(d)} \cdot \mathcal{R}_p^T \bar{\mathcal{H}}_{pq}^{(d)} \mathcal{R}_q \hat{\boldsymbol{U}}_1 A_q^{(d)} e^{i\Delta k_{pq} x_1} + \boldsymbol{V}_2^{(d)} \cdot \left[\mathcal{R}_p^T \bar{\mathcal{D}}_x^{(d)} \mathcal{R}_p + \bar{\mathcal{D}}_y^{(d)} \right] \hat{\boldsymbol{U}}_1 A_p^{(d)} = 0. \tag{4.76b}$$

Similarly, the equation in the metal is

$$\hat{\boldsymbol{U}}_1 \cdot \left[\mathcal{R}_p^T \bar{\mathcal{D}}_x^{(m)} \mathcal{R}_p + \bar{\mathcal{D}}_y^{(m)} \right] \hat{\boldsymbol{U}}_1 A_p^{(m)} = 0 \tag{4.77}$$

We require the continuity of the polarisation amplitudes, using the same argument as presented in Section 4.5.1 we only require this to be the case in the direction orthogonal to the TM mode. This gives us the equation

$$\begin{gathered} \hat{\boldsymbol{V}}_\perp \cdot \mathcal{P}^{(d)} \mathcal{R}_p^T \bar{\mathcal{H}}_{pq}^{(d)} \mathcal{R}_q \hat{\boldsymbol{U}}_1 A_q^{(d)} e^{i\Delta k_{pq} x_1} + \hat{\boldsymbol{V}}_\perp \cdot \mathcal{P}^{(d)} \mathcal{R}_p^T \bar{\mathcal{D}}^{(d)} \mathcal{R}_p \hat{\boldsymbol{U}}_1 A_p^{(d)} = \\ \hat{\boldsymbol{V}}_\perp \cdot \mathcal{P}^{(m)} \mathcal{R}_p^T \bar{\mathcal{D}}^{(m)} \mathcal{R}_p \hat{\boldsymbol{U}}_1 A_p^{(m)}, \end{gathered} \tag{4.78}$$

where $\mathcal{P}^{(n)} = \text{Pinv}\left(\mathcal{H}^{(n)}\right)$ is the Moore–Penrose pseudo inverse and $\hat{\boldsymbol{V}}_\perp = \left(\hat{\boldsymbol{S}}_1^T, 0, 0\right)^T$. Equations (4.76), (4.77) and (4.78) form a coupled system of partial differential equations for the variation of the SPP amplitude in the x and y directions. We are only interested in the variation of the amplitudes in the plane of propagation. As the SPP decay exponentially in the y direction on the fast scale then any coupling will quickly become negligible with distance away from the boundary.

As in the homogeneous anisotropic case we must consider two different SPP components in the dielectric which decay with different decay constants. Therefore, we write $\hat{\boldsymbol{U}}_1 A_p^{(d)} = \boldsymbol{V}_1 A_{p1}^{(d)}(x_1, y_1) + \boldsymbol{V}_2 A_{p2}^{(d)}(x_1, y_1)$. We require that these amplitudes are equal at the boundary to ensure the leading order equations are satisfied, $A_{p1}^{(d)}(x_1, 0) = A_{p2}^{(d)}(x_1, 0) = A_p^{(m)}(x_1, 0) = A_p^{(S)}$ and $\partial_{x_1} A_{p1}^{(d)} = \partial_{x_1} A_{p2}^{(d)} = \partial_{x_1} A_p^{(m)} = \partial_{x_1} A_p^{(S)}$. The system we must now solve is a 4×4 system for the derivatives $\partial_{y_1} A_{p1}^{(d)}$, $\partial_{y_1} A_{p2}^{(d)}$, $\partial_{y_1} A_p^{(m)}$, and $\partial_{x_1} A_p^{(S)}$.

Before we proceed we need to make a few simplifying observations. As $\bar{\mathcal{D}}_y$ is block diagonal and the first two entries of the $\boldsymbol{V}_1$ and $\boldsymbol{V}_2$ are identical we obtain

$$\boldsymbol{V}_1 \cdot \bar{\mathcal{D}}_y^{(d)} \boldsymbol{V}_1 = \boldsymbol{V}_2 \cdot \bar{\mathcal{D}}_y^{(d)} \boldsymbol{V}_2, \tag{4.79a}$$

$$\boldsymbol{V}_1 \cdot \bar{\mathcal{D}}_y^{(d)} \boldsymbol{V}_2 = \boldsymbol{V}_2 \cdot \bar{\mathcal{D}}_y^{(d)} \boldsymbol{V}_1, \tag{4.79b}$$

and

$$\boldsymbol{V}_1 \cdot \mathcal{R}_p^T \bar{\mathcal{D}}_x^{(d)} \mathcal{R}_p \hat{\boldsymbol{U}}_1 = \boldsymbol{V}_2 \cdot \mathcal{R}_p^T \bar{\mathcal{D}}_x^{(d)} \mathcal{R}_p \hat{\boldsymbol{U}}_1. \tag{4.79c}$$

Adding and subtracting equations (4.76a) and (4.76b) and using equations (4.79) we obtain

$$\begin{gathered}\hat{\boldsymbol{U}}_1 \cdot \mathcal{R}_p^T \bar{\mathcal{H}}_{pq}^{(d)} \mathcal{R}_q \hat{\boldsymbol{U}}_1 A_q^{(S)} e^{i\Delta k_{pq} x_1} + \hat{\boldsymbol{U}}_1 \cdot \mathcal{R}_p^T \bar{\mathcal{D}}_x^{(d)} \mathcal{R}_p \hat{\boldsymbol{U}}_1 A_p^{(S)} + \\ \hat{\boldsymbol{U}}_1 \cdot \bar{\mathcal{D}}_y \hat{\boldsymbol{U}}_1 \left(\partial_{y_1} A_{p1}^{(d)} + \partial_{y_1} A_{p2}^{(d)} \right) = 0\end{gathered} \tag{4.80a}$$

and

$$\hat{\boldsymbol{U}}_2 \cdot \mathcal{R}_p^T \bar{\mathcal{H}}_{pq}^{(d)} \mathcal{R}_q \hat{\boldsymbol{U}}_1 A_q^{(S)} e^{i\Delta k_{pq} x_1} + \hat{\boldsymbol{U}}_2 \cdot \bar{\mathcal{D}}_y \hat{\boldsymbol{U}}_2 \left(\partial_{y_1} A_{p1}^{(d)} - \partial_{y_1} A_{p2}^{(d)} \right) = 0 \tag{4.80b}$$

respectively. Equations (4.80a) defines the common part of the y–variation of the amplitudes in the dielectric. Equation (4.80b) defines the difference between the two y derivatives. Using equation (4.79) we notice that only the common part of the y–derivative appears in the boundary conditions. As the field decays exponentially away from the boundary we do not need to consider variation in this direction. Therefore, we only consider equation (4.80a). This leads to an interesting observation. Although considering the fields in terms of TE and TM modes in the dielectric turns out to be a singular choice of basis vectors the error induced by this does not affect the final equation for the x derivative of the field amplitudes.

Equations (4.77), (4.78) and (4.80b) form a 3×3 linear system of equations, $A\boldsymbol{x} = \boldsymbol{b}$, for the spatial derivatives. After some simplification to the left hand side we can write

$$A = \begin{pmatrix} \dfrac{\epsilon_{d,0}\delta_d}{\delta_d^2 - \epsilon_{d,0}^2} & 0 & \dfrac{-2i\epsilon_{d,0}\alpha_0}{\delta_d^2 - \epsilon_{d,0}^2} \\ 0 & -\dfrac{\epsilon_{m,0}\delta_m}{\delta_m^2 - \epsilon_{m,0}^2} & \dfrac{-2i\epsilon_{m,0}\alpha_0}{\delta_m^2 - \epsilon_{m,0}^2} \\ \dfrac{i\epsilon_{d,0}\left(\delta_d^2 + \epsilon_{d,0}^2\right)}{2\left(\delta_d^2 - \epsilon_{d,0}^2\right)^2} & -\dfrac{i\epsilon_{m,0}\left(\delta_m^2 + \epsilon_{m,0}^2\right)}{2\left(\delta_m^2 - \epsilon_{m,0}^2\right)^2} & \dfrac{2\epsilon_{d,0}\delta_d\alpha_0}{\left(\delta_d^2 - \epsilon_{d,0}^2\right)^2} + \dfrac{2\epsilon_{m,0}\delta_m\alpha_0}{\left(\delta_m^2 - \epsilon_{m,0}^2\right)^2} \end{pmatrix}, \tag{4.81}$$

and

$$\boldsymbol{x} = \begin{pmatrix} \partial_{y_1} A_p^{(m)} \\ \partial_{y_1}(A_{p1}^{(d)} + A_{p2}^{(d)}) \\ \cos\theta_p \partial_{x_1} A_p^{(S)} \end{pmatrix}. \tag{4.82}$$

The right hand side contains the coupling terms which, on the boundary, can be written as

$$\boldsymbol{b} = \begin{pmatrix} \hat{\boldsymbol{U}}_1 \cdot \mathcal{R}_p^T \bar{\mathcal{H}}_{pq}^{(d)} \mathcal{R}_q \hat{\boldsymbol{U}}_1 A_q^{(S)} e^{i\Delta k_{pq} x_1} \\ 0 \\ \hat{\boldsymbol{V}}_\perp \cdot \mathcal{P}^{(d)} \mathcal{R}_p^T \bar{\mathcal{H}}_{pq}^{(d)} \mathcal{R}_q \hat{\boldsymbol{U}}_1 A_q^{(S)} e^{i\Delta k_{pq} x_1} \end{pmatrix}. \tag{4.83}$$

Using a Gaussian elimination procedure we can obtain a simple equation for the x derivative

$$\left[\frac{\alpha_0\left(\epsilon_{m,0}\delta_d^3-\epsilon_{m,0}\epsilon_{d,0}^2\delta_d+\epsilon_{d,0}\delta_m^3-\epsilon_{d,0}\epsilon_{m,0}^2\delta_m\right)}{\delta_m\epsilon_{m,0}\left(\delta_m^2-\epsilon_{m,0}^2\right)\left(\delta_d^2-\epsilon_{d,0}^2\right)}\cos\theta_p\right]\partial_{x_1}A_p^{(S)}=$$
$$\left[-i\frac{\epsilon_{d,0}^2+\delta_d^2}{2\left(\delta_d^2-\epsilon_{d,0}^2\right)\delta_d}\hat{\boldsymbol{U}}_1-\frac{\delta_d^2+\epsilon_{d,0}^2}{\left(\delta_d^2-\epsilon_{d,0}^2\right)}\hat{\boldsymbol{V}}_\perp^T\mathcal{P}^{(d)}\right]\cdot\mathcal{R}_p^T\bar{\mathcal{H}}_{pq}^{(d)}\mathcal{R}_q\hat{\boldsymbol{U}}_1A_q^{(S)}e^{i\Delta k_{pq}x_1}. \tag{4.84}$$

The bracketed terms on the right hand side describe the coupling of the of the plasmons due to the presence of the grating and the boundary perturbation respectively. The term on the left hand side provides the correction due to the fields in the metal. Using the change of variable

$$A_p^{(S)}=\tilde{A}_p^{(S)}e^{-i\alpha_0\cos(\theta_p)x_1} \tag{4.85}$$

and equation (4.73) we can simplify equation (4.84) to obtain

$$\cos\theta_p\partial_{x_1}\tilde{A}_p^{(S)}=\frac{i}{2}\sqrt{\frac{\epsilon_{d,0}\epsilon_{m,0}}{\epsilon_{d,0}+\epsilon_{m,0}}}\left\{2\cos^2(\theta_p)\tilde{A}_p^{(S)}+\frac{\epsilon_{m,0}}{\epsilon_{d,0}^2-\epsilon_{m,0}^2}\boldsymbol{U}_{cp}\cdot\mathcal{R}_p^T\bar{\mathcal{H}}_{pq}^{(d)}\mathcal{R}_q\hat{\boldsymbol{U}}_1\tilde{A}_q^{(S)}\right\}, \tag{4.86}$$

where the coupling direction $\boldsymbol{U}_{cp}=\left(\epsilon_{m,0}+\epsilon_{d,0}\right)\boldsymbol{V}_c+\boldsymbol{V}_d$ and

$$\boldsymbol{V}_c=\left(2\epsilon_{d,0}/\sqrt{\epsilon_{m,0}+\epsilon_{d,0}}\right)\hat{\boldsymbol{V}}_\perp^T\mathcal{P}^{(d)}+\hat{\boldsymbol{U}}_1,\quad \boldsymbol{V}_d=\left(2\epsilon_{d,0}/\sqrt{\epsilon_{m,0}+\epsilon_{d,0}}\right)\hat{\boldsymbol{V}}_\perp^T\mathcal{P}^{(d)}-\hat{\boldsymbol{U}}_1 \tag{4.87}$$

Equation (4.86) describes the coupling of SPPs at the interface between a semi infinite metal and a semi infinite dielectric with periodically modulated permittivity. There are two different sources of coupling, the permittivity grating in the bulk of the dielectric material and the modulated permittivity at the interface. Had we considered only the bulk dielectric grating we would have obtained coupled wave equations as described in Chapter 3. The effect of the boundary condition is to induce a perturbation into the coupling direction $\boldsymbol{U}_{cp}$. Understanding the effect of this term should enable us to tailor the properties of the grating to maximise the energy transfer.

This method provides a quantitative understanding of the coupling process. The resulting equation can be solved as a single eigenvalue problem for the variation in SPP amplitude with propagation. This is a much simpler expression than the one used in the rigorous coupled wave theory and will allow us to obtain a better understanding of the coupling mechanisms.

4.6 Conclusion

In this chapter we have implemented existing models to study the propagation of SPP at the interface between a photorefractive liquid crystal cell and a thin gold layer. The resulting numerical code has been shown to agree qualitatively with experimental observations and provides a great deal of information about the system. The S–matrix method used, in combination with Berreman's method, allows us to model complicated dielectric profiles such as the ones observed in photorefractive liquid crystal cells.

To complement the existing numerical models we have also developed new analytic approximations to describe the propagation of SPP at an interface between a semi–infinite metal and a semi–infinite dielectric. The resulting equations, derived assuming the birefringence of the dielectric is small, are suitable for periodically modulated anisotropic materials. For the homogeneous anisotropic case these equations have been compared to the numerical code showing good agreement with the calculated variation in the SPP wavenumber.

Approximation techniques provide a great deal of insight into the behaviour and coupling mechanisms between the SPP as they propagate along the surface. Therefore, these equations will be of fundamental importance in understanding the conditions required to maximise the coupling of energy into a SPP.

The approximation techniques developed here make the assumption that the dielectric is homogeneous in the direction normal to the interface. This assumption, whilst qualitatively correct, does not model the liquid crystal variation in the liquid crystal profile in the direction normal to the boundary. Understanding the effect of this non-homogeneity will involve a detailed study of the SPP response to different liquid crystal alignments on both the short and long spatial scales. Once an understanding of the SPP response has been developed suitable approximation techniques may be found to model this effect.

The work carried out in this chapter, and the ongoing experimental work of Dr David Smith and Stephen Abbot, suggests that the use of photorefractive liquid crystal cells will be an important technique for the manipulation and amplification of SPPs. Further theoretical and experimental work is required to optimise these systems and obtain true photorefractive gain where the diffraction grating is generated directly by the SPP.

Chapter 5

Conclusion and future work

In this thesis we have considered the interaction of electromagnetic fields with liquid crystals in photorefractive cells. Two different optical geometries were studied and semi analytic models were developed to describe these systems. Each of the three technical chapters of this thesis was concerned with the modelling of one of the different aspects of these problems. In this chapter we summarise the results and consider ways in which this work can be extended in the future.

In Chapter 2 we derived an approximation to the $\mathcal{Q}$–tensor equations which describe liquid crystal alignment. The resulting equations, published in SIAM Journal on Applied Mathematics, reduce the computation time by a factor of 100 whilst maintaining an error of order (10^{-4}). These equations were derived based on the assumption that the elastic and electrostatic energies remain small, recall equation (2.18). This observation is true in defect-free geometries. If however, due to geometrical constraints or external fields, the liquid crystal alignment varies sharply this assumption no longer holds and the equations we have derived break down. From a matched asymptotic point of view this is equivalent to having only considered the outer expansion. The corresponding inner expansion, valid only close to the defect core, could be used as a starting point to extend this model so that it can be applied to structures in which defects form.

The liquid crystal model derived in Chapter 2 was used to predict the liquid crystal alignment in a photorefractive liquid crystal cell. In Chapter 3 we combined this with a semi-analytic model, published in Applied Physics B, which describes beam coupling. This approximate model was shown to be accurate when compared to existing models and a finite element simulation of Maxwell's equations. The optical model is accurate and can be solved quickly using a numerical code. However, it does not have an exact analytic solution which would provide a more complete description of the physics. Although an exact analytic solution cannot be found, approximate solutions may exist. Using appropriate perturbation techniques [173] it may be possible to derive solutions which are valid in the regions of interest in photorefractive liquid crystal cells.

The comparison of the optical coupling model with experimental data is important if this theory is to be used to predict the response of photorefractive liquid crystal cells. However, the models we are using do not fully describe the charge migration processes and electrochemestry at the boundaries in the photorefractive cell. There is also a noticeable variation in the measured values of the liquid crystal conductivity making it difficult to obtain reproducible experimental results. The final part of Chapter 3 describes the possibility of using a slow AC field rather than a DC field to reduce the effects if charge migration, simplifying the modelling required and stabilising the experimental setup. The observation of higher photorefractive gain can be explained qualitatively using the simplest of theoretical models. However, a much more in depth analysis of the electrochemical properties is required in order to obtain a working electrical model of the cell.

The final technical section to this thesis, Chapter 4, is concerned with the modelling of surface plasmon polaritons at the interface between a photorefractive liquid crystal cell and a thin gold layer. Powerful numerical techniques have been implemented to allow us to understand the optical properties of these systems. The propagation of the surface plasmons at the interface between a semi–infinite metal and a semi–infinite anisotropic dielectric with periodic modulation has been studied analytically. The coupled plasmonic equations derived predict the ability to produce gain using the liquid crystal as a photorefractive medium. These equations have been derived assuming that the dielectric is homogeneous in the direction normal to the interface. Therefore whilst these equations provide an approximation to the coupling mechanisms they cannot predict the coupling strength quantitatively. To understand these effects the first step would be to perform a detailed analysis of the mode structure and SPP response to variations in the dielectric permittivity on both the long and short scales would need to be obtained. Once the response is fully characterised and understood the appropriate approximations to describe such a system may be found.

Finally we observe that there is great scope for future work if we wish to model the non-linear interactions between the surface plasmon polariton and the photoconducting layer. This opens up the possibility of creating true photorefractive gain which could be used to overcome the short propagation length of the plasmon.

Appendix A

Minimising the free energy

To find the critical points of the liquid crystal free energy we consider the minimisation of a general system of equations

$$F(\boldsymbol{x}) = \int_V f\left[y_n(\boldsymbol{x})\right] dV, \tag{A.1}$$

where $n = 1, 2, 3, ..., N$ and $y_n(\boldsymbol{x})$ are the N scalar functions of space. The critical points of the system of equations are found by considering the points where the variation of the functions due to a small perturbation is zero. We write this perturbation in the form

$$y_n(\boldsymbol{x}) = y_n(0) + \eta\alpha(\boldsymbol{x}), \tag{A.2}$$

where $\eta \ll 1$ and $\alpha(\boldsymbol{x})$ is any smooth, differentiable function which vanishes at the boundaries of our domain. By differentiating $F(\boldsymbol{x})$ with respect to η, we obtain:

$$\frac{\partial F}{\partial \eta} = \int_V \frac{\partial f}{\partial y_n}\frac{\partial y_n}{\partial \eta} + \frac{\partial f}{\partial(\partial_i y_n)}\frac{\partial(\partial_i y_n)}{\partial \eta} dV = 0, \tag{A.3}$$

Substituting equation (A.2) into (A.3) allows us to write:

$$\int_V \left[\frac{\partial f}{\partial y_n} - \partial_i \frac{\partial f}{\partial(\partial_i y_n)}\right] \alpha(\boldsymbol{x}) dV = 0. \tag{A.4}$$

This can only be true for all $\alpha(\boldsymbol{x})$ if the term inside the square bracket is zero. This gives N equations which must be simultaneously satisfied for equation (A.1) to be satisfied.

Appendix B

Numerical Algorithm

B.1 Introduction

The numerical models used throughout this thesis rely on the ability to differentiate and integrate smooth continuous functions quickly and accurately. As the domains of interest in this thesis are relatively simple we use spectral collocation methods. We choose a Fourier discretisation in the x–direction and a Gauss–Lobatto grid in the z–direction. The Gauss–Lobatto grid-points are defined as the roots of the first derivative of the Chebyshev polynomial $T_n(x)$ and the end points -1 and 1 [174]. The high accuracy of these methods ensures that fewer spatial points are required than would be the case for a finite difference method allowing us to obtain high accuracy without incurring large computation times.

In this appendix we describe the methods used for the numerical algorithms. First, section B.2 provides a brief description of the general collocation algorithm used to approximate the derivatives. These approximations are looked at in more detail in sections B.3 and B.4. To calculate the cross polarised intensity we need a way to approximate the integral in equation (3.33). The method used for this is a Clenshaw-Curtis quadrature, which is described in section B.5.

B.2 Differentiation

In solving the equations which determine the liquid crystal alignment we need to approximate the derivatives using a numerical method. We have chosen to use spectral collocation methods as they offer high accuracy and efficiency. The methods are straightforward: given a function $f(x)$, defined in an interval $[a, b]$, we approximate its derivatives with

$$\frac{\partial f}{\partial x} \simeq \mathcal{D}\boldsymbol{v}, \tag{B.1}$$

where, $\boldsymbol{v}$ is a vector whose components are the values of f evaluated at discrete points in x, $v_j = f(x_j)$. Here we use two different spectral methods, one on a periodic grid, and one with fixed boundary conditions on a Gauss-Lobatto grid. For convenience, the derivation of these two differentiation matrices is summarised below. Full details can be found in [75].

The implementation of the derivatives on a two dimensional grid requires us to define the one dimensional derivatives in both the x and z direction acting on a function $f(x,z)$ defined on a grid (x_i, z_i). The derivatives over the entire grid are then found by taking the Kronecker product of each derivative with the identity matrix. If the derivatives over the whole grid are denoted by $\mathcal{D}X$ and $\mathcal{D}Z$, we can relate them to the one dimensional derivatives using

$$\begin{aligned}\mathcal{D}X &= \text{Id}(N_z) \otimes \mathcal{D}x,\\ \mathcal{D}Z &= \mathcal{D}z \otimes \text{Id}(N_x),\end{aligned} \tag{B.2}$$

where Id(N_x) and Id(N_z) are identity matrices with the same dimensions as $\mathcal{D}x$ and $\mathcal{D}z$ respectively.

B.3 Periodic differentiation

The differentiation matrix, $\mathcal{D}x$, for a periodic grid, $[0, 2\pi]$ is determined using a trigonometric interpolant. The interval is discritised into $N = 2\pi/h$ points where h is the grid spacing, and for simplicity we assume that N is always even. We can interpolate any function $f(x_j)$ on our grid using a linear combination of the periodic delta function which we define as:

$$\delta_j = \begin{cases} 1 & \text{if } j = 0 \text{ (mod } N) \\ 0 & \text{if } j \neq 0 \text{ (mod } N). \end{cases} \tag{B.3}$$

We wish to find a continuous periodic function which will interpolate the delta, from this we may then write any function as a linear combination of these interpolants. The discrete Fourier transform of the delta function is a constant, h. We take the inverse Fourier transform to find its continuous interpolant:

$$p(x) = v_j = \frac{h}{2\pi}\left[\frac{1}{2}\sum_{k=-N/2}^{N/2-1} e^{ikx} + \frac{1}{2}\sum_{k=-(N/2-1)}^{N/2} e^{ikx}\right],$$

$$= \frac{h}{2\pi}\cos(x/2)\sum_{k=-(N/2-1/2)}^{N/2-1/2} e^{ikx},$$

$$= \frac{h}{2\pi}\cos(x/2)\frac{e^{-i(N/2+1/2)} - e^{i(N/2+1/2)}}{1-e^{ix}},$$

$$= \frac{h}{2\pi}\cos(x/2)\frac{e^{-i(N/2)x} - e^{i(N/2)x}}{e^{-ix/2}-e^{ix/2}},$$

$$= \frac{h}{2\pi}\cos(x/2)\frac{\sin(Nx/2)}{\sin(x/2)},$$

$$= \frac{h}{2\pi}\frac{\sin(Nx/2)}{\tan(x/2)} = \text{Sn}(x).$$

This is the periodic sinc function, any smooth periodic function can be represented as a linear combination of these:

$$p(x) = \sum_{m=1}^{N} V_m \text{Sn}(x - x_m), \tag{B.4}$$

where v_m is the amplitude of the function at the point x_m. We now differentiate and write in matrix form to obtain our matrix $\mathcal{D}x$:

$$\begin{aligned} p'(x) &= \sum_{m=1}^{N} V_m \text{Sn}'(x - x_m), \\ &= \sum_{m=1}^{N} V_m \frac{h}{2\pi}\left[\frac{N}{2}\cos(nx_j/2)\text{cot}(x_j/2) - \frac{1}{2}\sin(Nx_j/2)\text{cosec}^2(x_j/2)\right], \end{aligned} \tag{B.5}$$

where $x_j = jh$. Using $N = 2\pi/h$ allows us to write the sinc function's derivative as

$$Sn'(x_j) = \begin{cases} 0 & \text{if } x_j = 0 \text{ (mod } N) \\ \frac{1}{2}(-1)^j\cot(x_j/2) & \text{if } x_j \neq 0 \text{ (mod } N). \end{cases} \tag{B.6}$$

Using equations (B.5) and (B.6) we can write $\mathcal{D}x$ in terms of the toeplitz matrix

$$\mathcal{D}x = \begin{pmatrix} 0 & & \frac{1}{2}\cot(\frac{Nh}{2}) \\ \frac{1}{2}\cot(\frac{1h}{2}) & \ddots & \vdots \\ -\frac{1}{2}\cot(\frac{2h}{2}) & \ddots & -\frac{1}{2}\cot(\frac{2h}{2}) \\ \vdots & \ddots & \frac{1}{2}\cot(\frac{1h}{2}) \\ \frac{1}{2}\cot(\frac{Nh}{2}) & & 0 \end{pmatrix}. \tag{B.7}$$

This method of differentiation is exact for periodic functions which can be interpolated by a trigonometric function with maximum wavenumber N. For a smooth function with infinitely many continuous derivatives, the Fourier differentiation matrix has error $||\mathcal{D}x\boldsymbol{v} - \partial_x f(x)|| \leq O(h^m)$ as $h \to 0$ for any m. For further details on the accuracy of spectral methods see [75] page 34.

B.4 Chebyshev differentiation

Differentiation on the Gauss-Lobatto grid is performed by finding an unique polynomial which interpolates the function we wish to differentiate. The derivative of the function is then approximately the derivative of the interpolated polynomial. The z component of the Gauss-Lobatto grid is defined as

$$z_j = \cos(j\pi/N), \tag{B.8}$$

where $j = 0, 1, 2, ..., N$. Here we write the interpolating polynomial in terms of the Lagrange polynomials

$$p_j(z) = \frac{v_j}{a_j} \prod_{\substack{k=0 \\ k\neq j}}^{N} (z - z_k), \tag{B.9}$$

where

$$a_j = \prod_{\substack{k=0 \\ k\neq j}}^{N} (z_j - z_k). \tag{B.10}$$

We wish to write the derivative in terms of a matrix equation. Taking logs of equation (B.9) and differentiating yields:

$$\ln\left[p_j(z)\right] = \ln\left[v_j \prod_{\substack{k=0 \\ k\neq j}}^{N} (z - z_k)\right] - \ln\left[a_j\right],$$

$$p_j'(z) = \frac{v_j}{a_j} \prod_{\substack{k=0 \\ k\neq j}}^{N} (z - z_k) \sum_{\substack{k=0 \\ k\neq j}}^{N} (z - z_k)^{-1}. \tag{B.11}$$

By discretising in space we can write this as a differentiation matrix which takes the form

$$\begin{aligned} \mathcal{D}z_{jj} &= \sum_{\substack{k=0 \\ k\neq j}}^{N} (z_j - z_k)^{-1} \\ \mathcal{D}z_{ij} &= \frac{1}{a_j} \prod_{\substack{k=0 \\ k\neq j}}^{N} (z_i - z_k)^{-1} = \frac{a_i}{a_j(z_i - z_j)}. \end{aligned} \tag{B.12}$$

This method of differentiation is exact for functions which can be interpolated by polynomials of maximum degree N. The accuracy of this method is comparable with the Fourier method, this is based on the equivalence of Fourier points with Chebyshev points, for details see [75] page 48.

B.5 Clenshaw-Curtis quadrature

The numerical quadrature used to calculate the cross polarised intensity in equation (3.33) is a Clenshaw-Curtis quadrature. The Clenshaw-Curtis quadrature formula is the formula of optimal order, based on the fixed set of Chebyshev nodes. As opposed to the Gaussian quadrature which is the formulae of optimal order based on an optimally chosen set of nodes. As the grid used in this quadrature is the Gauss-Lobatto grid, we do not need to interpolate the solution to the liquid crystal equations onto a different grid. We wish to calculate the integral

$$I = \int_{-1}^{1} f(z) dz \tag{B.13}$$

using the coordinate transform $z = \cos\theta$, $0 \leq \theta \leq 2\pi$. As such we can represent equation (B.13) in terms of the Fourier transform of $f(\cos\theta)$:

$$I = \int_{0}^{\pi} \sum_{k=0}^{\infty} a_k \cos(2k\theta)\sin(\theta) d\theta, \tag{B.14}$$

where

$$a_k = \frac{2}{\pi} \int_{0}^{\pi} f(\cos\theta)\cos(2k\theta) d\theta. \tag{B.15}$$

We can evaluate equation (B.14) by using standard integration techniques:

$$I = \frac{1}{2} \sum_{k=0}^{\infty} a_k \left[\frac{\cos[(2k-1)\theta]}{2k-1} - \frac{\cos[(2k+1)\theta]}{2k+1} \right]_{0}^{\pi} \tag{B.16}$$

Discretising in space $\theta_j = j\pi/N$ where $j = 0, 1, 2, ..., N$ and substituting into equation (B.16) gives

$$I = \frac{1}{2} \sum_{k=0}^{\infty} \frac{a_k}{1 - 4k^2}. \tag{B.17}$$

As we have discretised on a finite grid we can truncate this series to the Nyquist frequency, which is $N/2$ for N even and $(N+1)/2$ for N odd. All that remains is to calculate the values of the Fourier coefficients a_k. Based on the symmetry of the cosine terms, without loss of accuracy, we can write equation (B.15) as

$$a_k = \frac{2}{\pi} \sum_{j=0}^{N} f(\cos\theta_j)\cos(2k\theta_j)\frac{\pi}{N}. \tag{B.18}$$

This allows us to write the final integral as

$$\begin{aligned} I &= \sum_{j=0}^{N} f(\cos\theta_j)\frac{2}{N}\sum_{k=0}^{\tilde{N}}\frac{\cos(2k\theta_j)}{1-4k^2}, \\ &= \sum_{j=0}^{N} v_j w_j, \end{aligned} \tag{B.19}$$

where v_j are the values of the function at the points z_j, $\tilde{N} = N/2$ for even N, $\tilde{N} = (N+1)/2$ for odd N and

$$w_j = \frac{2}{N}\sum_{k=0}^{\tilde{N}}\frac{\cos(2k\theta_j)}{1-4k^2}. \tag{B.20}$$

Appendix C

Coupled wave equations for general dielectric perturbation

The model derived in Section 3.4 assumes that the perturbation to the dielectric tensor is in the plane of wave propagation. Here we consider the situation where this is not the case and that the first order tensor given in equation (3.49) is as general as possible. However, we retain the assumption that the optical axis of the leading order tensor is in the plane formed by the optical wave vectors. This means that not only do we have coupling between different modes but also between ordinary and extraordinary components of the field. We note that formally to match the boundary conditions for an incident field with general polarisation we need to consider both the fields 1 and 2, see Figure 3.12C. In general however, the effect of these two fields will be a broadening of the output spectrum and as such only field 1 or 2 needs to be considered. Again we work in the framework of the multiple scales expansion which is described in Section 3.4. The electric field in the general case is written as a more general Fourier expansion in x:

$$\begin{aligned}\boldsymbol{E}_j = \sum_{m=-N}^{N} \quad & \left\{ \left[\boldsymbol{A}_{1o,j}^{(m)}\left(\eta z\right) e^{i\left(\boldsymbol{k}_{1o,j}^{(m)} - \boldsymbol{k}_{1e,j}^{(m)}\right)\cdot\boldsymbol{x}} + \boldsymbol{A}_{1e,j}^{(m)}\left(\eta z\right) \right] e^{i\boldsymbol{k}_{1e,j}^{(m)}\cdot\boldsymbol{x}} \right. \\ & \left. + \left[\boldsymbol{A}_{2o,j}^{(m)}\left(\eta z\right) + \boldsymbol{A}_{2e,j}^{(m)}\left(\eta z\right) e^{i\left(\boldsymbol{k}_{2e,j}^{(m)} - \boldsymbol{k}_{2o,j}^{(m)}\right)\cdot\boldsymbol{x}} \right] e^{i\boldsymbol{k}_{2o,j}^{(m)}\cdot\boldsymbol{x}} \right\} e^{-i\omega t},\end{aligned} \tag{C.1}$$

where the subscript j refers to the order of the expansion and the subscripts o, e and $1, 2$ reffer to the ordinary and extraordinary components of the first and second set of waves respectively. We substitute equations (C.1) and (3.49) into (1.3) and using the more general identities (which again can be derived graphically from Figure 3.12)

$$\begin{aligned}
\boldsymbol{k}_{\alpha e}^{(m)} &= \boldsymbol{k}_{\beta e}^{(n)} + (m-n)K\hat{\boldsymbol{e}}_x + \left(k_{\alpha ez}^{(m)} - k_{\beta ez}^{(n)}\right)\hat{\boldsymbol{e}}_z, \\
\boldsymbol{k}_{\alpha o}^{(m)} &= \boldsymbol{k}_{\beta o}^{(n)} + (m-n)K\hat{\boldsymbol{e}}_x + \left(k_{\alpha oz}^{(m)} - k_{\beta oz}^{(n)}\right)\hat{\boldsymbol{e}}_z, \\
\boldsymbol{k}_{\alpha e}^{(m)} &= \boldsymbol{k}_{\beta o}^{(n)} + (m-n)K\hat{\boldsymbol{e}}_x + \left(k_{\alpha ez}^{(m)} - k_{\beta oz}^{(n)}\right)\hat{\boldsymbol{e}}_z,
\end{aligned} \tag{C.2}$$

where $\alpha, \beta = 1, 2$. We expand to first order and, using the solvability condition from Section 3.4, we obtain a set of coupled wave equations for fields oscilating in the direction $\boldsymbol{k}_{1e}$

$$\begin{aligned}
& ik_{1e}^{(m)}\left[(\hat{\boldsymbol{k}}_1^{(m)}\cdot\hat{\boldsymbol{e}}_{1e}^{(m)})\boldsymbol{\nabla}_1 + \hat{\boldsymbol{k}}_1^{(m)}(\hat{\boldsymbol{e}}_{1e}^{(m)}\cdot\boldsymbol{\nabla}_1) - 2\hat{\boldsymbol{e}}_{1e}^{(m)}(\hat{\boldsymbol{k}}_1^{(m)}\cdot\boldsymbol{\nabla}_1)\right]A_{1e}^{(m)} + \\
& ik_{1e}^{(m)}\left[\hat{\boldsymbol{k}}_1^{(m)}(\hat{\boldsymbol{e}}_{1o}^{(m)}\cdot\boldsymbol{\nabla}_1) - 2\hat{\boldsymbol{e}}_{1o}^{(m)}(\hat{\boldsymbol{k}}_1^{(m)}\cdot\boldsymbol{\nabla}_1)\right]A_{1o}^{(m)}e^{i\left(\boldsymbol{k}_{1o,j}^{(m)}-\boldsymbol{k}_{1e,j}^{(m)}\right)\cdot\boldsymbol{x}} = \\
& \frac{k_0^2}{2}\sum_{n=-N}^{N}\Delta\epsilon^{(n-m)}\left[\hat{\boldsymbol{e}}_{1e}^{(n)}A_{1e}^{(n)}e^{i(k_{1ez}^{(n)}-k_{1ez}^{(m)})z} + \hat{\boldsymbol{e}}_{2o}^{(n)}A_{2o}^{(n)}e^{i(k_{2oz}^{(n)}-k_{1ez}^{(m)})z} + \right. \\
& \left.\hat{\boldsymbol{e}}_{1o}^{(n)}A_{1o}^{(n)}e^{i\left(\boldsymbol{k}_{1o}^{(n)}-\boldsymbol{k}_{1e}^{(n)}\right)\cdot\boldsymbol{x}}e^{i(k_{1ez}^{(n)}-k_{1ez}^{(m)})z} + \hat{\boldsymbol{e}}_{2e}^{(n)}A_{2e}^{(n)}e^{i\left(\boldsymbol{k}_{2e}^{(n)}-\boldsymbol{k}_{2o}^{(n)}\right)\cdot\boldsymbol{x}}e^{i(k_{2oz}^{(n)}-k_{1ez}^{(m)})z}\right],
\end{aligned} \tag{C.3}$$

A similar equation can be obtained in the direction of $\boldsymbol{k}_{2o}$.

$$\begin{aligned}
& ik_{2o}^{(m)}\left[(\hat{\boldsymbol{k}}_2^{(m)}\cdot\hat{\boldsymbol{e}}_{2e}^{(m)})\boldsymbol{\nabla}_1 + \hat{\boldsymbol{k}}_2^{(m)}(\hat{\boldsymbol{e}}_{2e}^{(m)}\cdot\boldsymbol{\nabla}_1) - 2\hat{\boldsymbol{e}}_{2e}^{(m)}(\hat{\boldsymbol{k}}_2^{(m)}\cdot\boldsymbol{\nabla}_1)\right]A_{2e}^{(m)}e^{i\left(\boldsymbol{k}_{2e,j}^{(m)}-\boldsymbol{k}_{2o,j}^{(m)}\right)\cdot\boldsymbol{x}} + \\
& ik_{2o}^{(m)}\left[\hat{\boldsymbol{k}}_2^{(m)}(\hat{\boldsymbol{e}}_{2o}^{(m)}\cdot\boldsymbol{\nabla}_1) - 2\hat{\boldsymbol{e}}_{2o}^{(m)}(\hat{\boldsymbol{k}}_2^{(m)}\cdot\boldsymbol{\nabla}_1)\right]A_{2o}^{(m)} = \\
& \frac{k_0^2}{2}\sum_{n=-N}^{N}\Delta\epsilon^{(n-m)}\left[\hat{\boldsymbol{e}}_{1e}^{(n)}A_{1e}^{(n)}e^{i(k_{1ez}^{(n)}-k_{2oz}^{(m)})z} + \hat{\boldsymbol{e}}_{2o}^{(n)}A_{2o}^{(n)}e^{i(k_{2oz}^{(n)}-k_{2oz}^{(m)})z} + \right. \\
& \left.\hat{\boldsymbol{e}}_{1o}^{(n)}A_{1o}^{(n)}e^{i\left(\boldsymbol{k}_{1o}^{(n)}-\boldsymbol{k}_{1e}^{(n)}\right)\cdot\boldsymbol{x}}e^{i(k_{1ez}^{(n)}-k_{2oz}^{(m)})z} + \hat{\boldsymbol{e}}_{2e}^{(n)}A_{2e}^{(n)}e^{i\left(\boldsymbol{k}_{2e}^{(n)}-\boldsymbol{k}_{2o}^{(n)}\right)\cdot\boldsymbol{x}}e^{i(k_{2oz}^{(n)}-k_{2oz}^{(m)})z}\right],
\end{aligned} \tag{C.4}$$

Between them these two equations describe the field variation completely. We can simplify equation (3.55) by introducing the new variables

$$\begin{aligned}
A_{1e}^{(m)} &= \tilde{A}_{1e}^{(m)}e^{-ik_{ez}^{(m)}z}, & A_{2o}^{(m)} &= \tilde{A}_{2o}^{(m)}e^{-ik_{oz}^{(m)}z}, \\
A_{1o}^{(m)} &= \tilde{A}_{1o}^{(m)}e^{-i\left(\boldsymbol{k}_{1o}^{(n)}-\boldsymbol{k}_{1e}^{(n)}\right)\cdot\boldsymbol{x}}e^{-ik_{ez}^{(m)}z}, & A_{2e}^{(m)} &= \tilde{A}_{2e}^{(m)}e^{-i\left(\boldsymbol{k}_{2e}^{(n)}-\boldsymbol{k}_{2o}^{(n)}\right)\cdot\boldsymbol{x}}e^{-ik_{oz}^{(m)}z}
\end{aligned} \tag{C.5}$$

and projecting onto the appropriate basis set for each wave. Equation (C.3) is a vector equation, to ensure this is satisfied in all directions we project onto $\hat{\boldsymbol{k}}_1^{(m)}$, $\hat{\boldsymbol{e}}_{1e}^{(m)}$ and $\hat{\boldsymbol{e}}_{1o}^{(m)}$. We also have the symmetry requirement that the field is invariant in the direction orthogonal to the plane formed by the set of wave vectors i.e. $\hat{\boldsymbol{e}}_{1o}^{(m)} \cdot \boldsymbol{\nabla}_1 A_{1j} = 0$. Similarly equation C.4 is projecting onto $\hat{\boldsymbol{k}}_2^{(m)}$, $\hat{\boldsymbol{e}}_{2e}^{(m)}$ and $\hat{\boldsymbol{e}}_{2o}^{(m)}$ with the requirement that the field is invariant in the $\hat{\boldsymbol{e}}_{2o}^{(m)}$ direction. In both cases the projection onto $\hat{\boldsymbol{k}}_j^{(m)}$, where $j = 1, 2$, gives the divergence equation and hence the variation of the fields in the direction of the electric displacement vectors

$$
\begin{gathered}
ik_{1e}^{(m)} \left[\hat{\boldsymbol{e}}_{1e}^{(m)} - \left(\hat{\boldsymbol{e}}_{1e}^{(m)} \cdot \hat{\boldsymbol{k}}_1^{(m)} \right) \hat{\boldsymbol{k}}_1^{(m)} \right] \cdot \left[-i\hat{\boldsymbol{e}}_z k_{1z} + \boldsymbol{\nabla}_1 \right] \tilde{A}_{1e}^{(m)} = \\
\frac{k_0^2}{2} \sum_{n=-N}^{N} \hat{\boldsymbol{k}}_1^{(m)} \Delta\epsilon^{(n-m)} \left[\hat{\boldsymbol{e}}_{1e}^{(n)} A_{1e}^{(n)} + \hat{\boldsymbol{e}}_{2o}^{(n)} A_{2o}^{(n)} + \hat{\boldsymbol{e}}_{1o}^{(n)} A_{1o}^{(n)} + \hat{\boldsymbol{e}}_{2e}^{(n)} A_{2e}^{(n)} \right]
\end{gathered}
\tag{C.6}
$$

and

$$
\begin{gathered}
ik_{2o}^{(m)} \left[\hat{\boldsymbol{e}}_{2o}^{(m)} - \left(\hat{\boldsymbol{e}}_{2o}^{(m)} \cdot \hat{\boldsymbol{k}}_2^{(m)} \right) \hat{\boldsymbol{k}}_2^{(m)} \right] \cdot \left[-i\hat{\boldsymbol{e}}_z k_{2ez} - (\boldsymbol{k}_{2e}^{(m)} - \boldsymbol{k}_{2o}^{(m)}) + \boldsymbol{\nabla}_1 \right] \tilde{A}_{2e}^{(m)} = \\
\frac{k_0^2}{2} \sum_{n=-N}^{N} \hat{\boldsymbol{k}}_2^{(m)} \Delta\epsilon^{(n-m)} \left[\hat{\boldsymbol{e}}_{1e}^{(n)} A_{1e}^{(n)} + \hat{\boldsymbol{e}}_{2o}^{(n)} A_{2o}^{(n)} + \hat{\boldsymbol{e}}_{1o}^{(n)} A_{1o}^{(n)} + \hat{\boldsymbol{e}}_{2e}^{(n)} A_{2e}^{(n)} \right].
\end{gathered}
\tag{C.7}
$$

The remaining equations describe the variation of the ordinary and extraordinary components of the two fields in their respective directions of energy flow. For the set of fields 1 the projections onto $\hat{\boldsymbol{e}}_{1o}^{(m)}$ and $\hat{\boldsymbol{e}}_{1e}^{(m)}$ are

$$
\begin{gathered}
-2ik_{1e}^{(m)} \hat{\boldsymbol{k}}_1^{(m)} \cdot \left[-i\hat{\boldsymbol{e}}_z k_{1oz} - (\boldsymbol{k}_{1o}^{(m)} - \boldsymbol{k}_{1e}^{(m)}) + \boldsymbol{\nabla}_1 \right] \tilde{A}_{1o}^{(m)} = \\
\frac{k_0^2}{2} \sum_{n=-N}^{N} \hat{\boldsymbol{e}}_{1o}^{(m)} \Delta\epsilon^{(n-m)} \left[\hat{\boldsymbol{e}}_{1e}^{(n)} A_{1e}^{(n)} + \hat{\boldsymbol{e}}_{2o}^{(n)} A_{2o}^{(n)} + \hat{\boldsymbol{e}}_{1o}^{(n)} A_{1o}^{(n)} + \hat{\boldsymbol{e}}_{2e}^{(n)} A_{2e}^{(n)} \right]
\end{gathered}
\tag{C.8}
$$

and

$$
\begin{gathered}
2ik_{1e}^{(m)} \left[\left(\hat{\boldsymbol{e}}_{1e}^{(m)} \cdot \hat{\boldsymbol{k}}_1^{(m)} \right) \hat{\boldsymbol{e}}_{1e}^{(m)} - \hat{\boldsymbol{k}}_1^{(m)} \right] \cdot \left[-i\hat{\boldsymbol{e}}_z k_{1ez} + \boldsymbol{\nabla}_1 \right] \tilde{A}_{1e}^{(m)} = \\
\frac{k_0^2}{2} \sum_{n=-N}^{N} \hat{\boldsymbol{e}}_{1e}^{(m)} \Delta\epsilon^{(n-m)} \left[\hat{\boldsymbol{e}}_{1e}^{(n)} A_{1e}^{(n)} + \hat{\boldsymbol{e}}_{2o}^{(n)} A_{2o}^{(n)} + \hat{\boldsymbol{e}}_{1o}^{(n)} A_{1o}^{(n)} + \hat{\boldsymbol{e}}_{2e}^{(n)} A_{2e}^{(n)} \right]
\end{gathered}
\tag{C.9}
$$

respectively. For the second set of fields we obtain a similar set of equations the projections onto $\hat{\boldsymbol{e}}_{2o}^{(m)}$ and $\hat{\boldsymbol{e}}_{2e}^{(m)}$ are

$$-2ik_{2o}^{(m)}\hat{\boldsymbol{k}}_2^{(m)} \cdot \left[-i\hat{\boldsymbol{e}}_z k_{2oz} + \boldsymbol{\nabla}_1\right] \tilde{A}_{2o}^{(m)} = \frac{k_0^2}{2}\sum_{n=-N}^{N} \hat{\boldsymbol{e}}_{2o}^{(m)} \Delta\epsilon^{(n-m)} \left[\hat{\boldsymbol{e}}_{1e}^{(n)} A_{1e}^{(n)} + \hat{\boldsymbol{e}}_{2o}^{(n)} A_{2o}^{(n)} + \hat{\boldsymbol{e}}_{1o}^{(n)} A_{1o}^{(n)} + \hat{\boldsymbol{e}}_{2e}^{(n)} A_{2e}^{(n)}\right] \tag{C.10}$$

and

$$2ik_{2o}^{(m)} \left[\left(\hat{\boldsymbol{e}}_{2o}^{(m)} \cdot \hat{\boldsymbol{k}}_2^{(m)}\right) \hat{\boldsymbol{e}}_{2e}^{(m)} - \hat{\boldsymbol{k}}_2^{(m)}\right] \cdot \left[-i\hat{\boldsymbol{e}}_z k_{2ez} - (\boldsymbol{k}_{2e}^{(m)} - \boldsymbol{k}_{2o}^{(m)}) + \boldsymbol{\nabla}_1\right] \tilde{A}_{2e}^{(m)} = \frac{k_0^2}{2}\sum_{n=-N}^{N} \hat{\boldsymbol{e}}_{2e}^{(m)} \Delta\epsilon^{(n-m)} \left[\hat{\boldsymbol{e}}_{1e}^{(n)} A_{1e}^{(n)} + \hat{\boldsymbol{e}}_{2o}^{(n)} A_{2o}^{(n)} + \hat{\boldsymbol{e}}_{1o}^{(n)} A_{1o}^{(n)} + \hat{\boldsymbol{e}}_{2e}^{(n)} A_{2e}^{(n)}\right] \tag{C.11}$$

respectively. These equations describe the coupling of energy in all directions and show clearly that for $\Delta\epsilon$ out of the plane the ordinary and extraordinary fields become coupled. It is also clear that for $\Delta\epsilon$ in the plane of propagation that these equations simplify to the equations described in Section 3.4. The analysis of these equations is beyond the scope of this thesis, as for the situations of interest they reduce to the simplified equations presented in Section 3.4. However, it is clear that for the most general case these equations describe the coupling phenomena to first order completely. We also note that whilst we have considered the fields 1 and 2 neccasary to match the boundary conditions here, in reality it is sufficient to consider only one set, field 1 or field 2, see Figure 3.12C. The result of not considering both fields will be a general spectral broadening of the output.

References

[1] R. James, E. Willman, FA Fernández, and SE Day. Finite-element modeling of liquid-crystal hydrodynamics with a variable degree of order. *IEEE Trans. Electron Devices*, 53(7):1575–1582, 2006.

[2] M.G. Moharam and T.K. Gaylord. Rigorous coupled-wave analysis of planar-grating diffraction. *J. Opt. Soc. Am.*, 71(7):811, 1981.

[3] M. Born and E. Wolf. *Principles of Optics, Electromagnetic theory of propagation interference and diffraction of light sixth edition*. Cambridge, 1980.

[4] A.S. Goldhaber and M.M. Nieto. Photon and graviton mass limits. *Rev. Mod. Phys.*, 82(1):939–979, 2010.

[5] E.R. Williams, J.E. Faller, and H.A. Hill. New Experimental Test of Coulomb's Law: A Laboratory Upper Limit on the Photon Rest Mass. *Phys. Rev. Lett.*, 26(12):721–724, 1971.

[6] G. Capriz and P.P. Guidugli. On Signorini's perturbation method in finite elasticity. *Arch. Rat. Mech. Anal.*, 57(1):1–30, 1974.

[7] G. Grioli. *Mathematical theory of elastic equilibrium:(recent results)*. Springer-Verlag, 1962.

[8] A. Signorini. Sulle deformazioni termoelastiche finite. *Proc. 3rd Int. Congr. App. Mech.*, 2:80–89, 1930.

[9] H. Kawamoto. The history of liquid-crystal displays. *P IEEE*, 90(4):460–500, 2002.

[10] B. Bahadur. *Liquid crystals: applications and uses*. World Scientific Pub Co Inc, 1990.

[11] I.C. Khoo. *Liquid Crystals*. Wiley series in pure and applied optics, 2007.

[12] T.J. Sluckin, D.A. Dunmur, and H. Stegemeyer. *Crystals that flow: Classic papers from the history of liquid crystals*. CRC, 2004.

[13] F. Reinitzer. Contributions to the knowledge of cholesterol. *Crystals That Flow*, pages 27–40, 2004.

[14] F. Reinitzer. Contributions to the knowledge of cholesterol. *Liq. Cryst.*, 5(1):7–18, 1989.

[15] O. Lehmann. On flowing crystals. *Crystals That Flow*, pages 43–52, 2004.

[16] O. Lehmann. On flowing crystals. *Zeitschrift für Physikalische Chemie*, 4:462–472, 1889.

[17] G. Friedel. The mesomorphic states of matter. *Crystals That Flow*, pages 163–201, 2004.

[18] G. Friedel. The mesomorphic states of matter. *Ann. Phys.*, 18:273–474, 1922.

[19] M. deBroglie and E. Friedel. Diffraction of x-rays by smectic substances. *Crystals That Flow*, pages 213–215, 2004.

[20] M. deBroglie and E. Friedel. Diffraction of x-rays by smectic substances. *Comptes rendus de l'Academie des Sciences*, 176:738–740, 1923.

[21] C. Mauguin. Orientation of liquid crystals by a magnetic field. *CR Acad. Sci*, 152:1680–1683, 1911.

[22] V. Freedericksz and V. Zolina. On the use of a magnetic field in the measurement of the forces tending to orient an anisotropic liquid in a thin homogeneous layer. *T. Am. Electrochem. Soc.*, 55:85–96, 1929.

[23] M. Schadt and W. Helfrich. Voltage-Dependent Optical Activity of a Twisted Nematic Liquid Crystal. *Appl. Phys. Lett.*, 18:127–128, 1971.

[24] F.M. Leslie. Distortion of twisted orientation patterns in liquid crystals by magnetic fields. *Mol. Cryst. Liq. Cryst.*, 12(1):57–72, 1970.

[25] W. Maier and A. Saupe. A simple molecular theory of the nematic crystalline-liquid state. *Z. Naturf*, 13:564–566, 1958.

[26] P. G. de Gennes and J. Prost. *The Physics of Liquid Crystals*. Oxford University Press New York, second edition, 1993.

[27] C.W. Oseen. The theory of liquid crystals. *Trans. Faraday Soc.*, 29(140):883–899, 1933.

[28] F.C. Frank. On the theory of liquid crystals. *Discuss. Faraday Soc.*, 25:19–28, 1958.

[29] J. Katriel, G.F. Kventsel, G.R. Luckhurst, and T.J. Sluckin. Free energies in the Landau and molecular field approaches. *Liq. Cryst.*, 1(4):337–355, 1986.

[30] A. Majumdar. Equilibrium order parameters of liquid crystals in the Landau-De Gennes theory. *European J. Appl. Mathematics of Computation*, 21:181203, 2010.

[31] J.L. Ericksen. Hydrostatic theory of liquid crystals. *Arch. Ration. Mech. An.*, 9(1):371–378, 1962.

[32] J.L. Ericksen. Conservation laws for liquid crystals. *J. Rheol.*, 5:23–34, 1961.

[33] F.M. Leslie. Some constitutive equations for anisotropic fluids. *Q. J. Mech. Appl. Math.*, 19(3):357, 1966.

[34] F.M. Leslie. Some constitutive equations for liquid crystals. *Arch. Ration. Mech. An.*, 28(4):265–283, 1968.

[35] P.G. de Gennes. Short range order effects in the isotropic phase of nematics and cholesterics. *Mol. Cryst. Liq. Cryst.*, 12(3):193–214, 1971.

[36] N. Schopohl and T. J. Sluckin. Defect core structure in nematic liquid crystals. *Phys. Rev. Lett.*, 59(22):2582–2584, Nov 1987.

[37] A. Sonnet, A. Kilian, and S. Hess. Alignment tensor versus director: Description of defects in nematic liquid crystals. *Phys. Rev. E*, 52(1):718–722, 1995.

[38] L. Longa, D. Monselesan, and H.R. Trebin. An extension of the Landau-Ginzburg-de Gennes theory for liquid crystals. *Liq. Cryst.*, 2(6):769–796, 1987.

[39] L. Longa and H.R. Trebin. Integrity basis approach to the elastic free energy functional of liquid crystals. *Liq. Cryst.*, 5(2):617–622, 1989.

[40] S. Ishihara. How far has the molecular alignment of liquid crystals been elucidated? *J. Display Technol.*, 1(1):30, 2005.

[41] A. Rapini and M. Papoular. Distorsion d'une lamelle nematique sous champ magnetique conditions d'ancrage aux parois. *Le Journal de Physique Colloques*, 30(C4):54–56, 1969.

[42] D.W. Berreman. Solid surface shape and the alignment of an adjacent nematic liquid crystal. *Phys. Rev. Lett.*, 28(26):1683–1686, 1972.

[43] D.W. Berreman. Alignment of liquid crystals by grooved surfaces. *Mol. Cryst. Liq. Cryst.*, 23(3):215–231, 1973.

[44] R. Barberi, I. Dozov, M. Giocondo, M. Iovane, P. Martinot-Lagarde, D. Stoenescu, S. Tonchev, and LV Tsonev. Azimuthal anchoring of nematic on undulated substrate: Elasticity memory. *Eur. Phys. J. B.*, 6(1):83–91, 1998.

[45] M. Nobili and G. Durand. Disorientation-induced disordering at a nematic-liquid-crystal–solid interface. *Phys. Rev. A*, 46(10):6174–6177, 1992.

[46] E. Willman, F.A. Fernández, R. James, and S.E. Day. Modeling of weak anisotropic anchoring of nematic liquid crystals in the Landau–de Gennes theory. *IEEE Trans. Electron Devices*, 54(10):2630–2637, 2007.

[47] S. Kralj, E. G. Virga, and S. Žumer. Biaxial torus around nematic point defects. *Phys. Rev. E*, 60(2):1858–1866, 1999.

[48] S. Kralj, R. Rosso, and E.G. Virga. Finite-size effects on order reconstruction around nematic defects. *Phys. Rev. E*, 81(2):21702, 2010.

[49] E. Penzenstader and H.R. Trebin. Fine structure of point defects and soliton decay in nematic liquid crystals. *J. Phys.*, 50:1027–1040, 1989.

[50] R. Rosso and E.G. Virga. Metastable nematic hedgehogs. *J. Phys. A*, 29:4247–4264, 1996.

[51] S. Mkaddem and E.C. Gartland. Fine structure of defects in radial nematic droplets. *Phys. Rev. E*, 62(5):6694–6705, 2000.

[52] S. Kralj and E.G. Virga. Universal fine structure of nematic hedgehogs. *J. Phys. A: Math. Gen.*, 34:829–838, 2001.

[53] M. Kleman and O. D. Lavrentovich. Topological point defects in nematic liquid crystals. *Philos. Mag.*, 86:4117–4137, 2006.

[54] G. Panasyuk and D. W. Allender. Model for the director and electric field in liquid crystal cells having twist walls or disclination lines. *J. Appl. Phys.*, 91(12):9603–9612, 2002.

[55] D. Svensek and S. Žumer. Instability modes of high-strength disclinations in nematics. *Phys. Rev. E*, 70(6):061707, 2004.

[56] A. de Lózar, W. Schöpf, I. Rehberg, D. Svenšek, and L. Kramer. Transformation from walls to disclination lines: Statics and dynamics of the pincement transition. *Phys. Rev. E*, 72(5):51713, 2005.

[57] F. Bisi, E.C. Gartland, R. Rosso, and E.G. Virga. Order reconstruction in frustrated nematic twist cells. *Phys. Rev. E*, 68(2):021707, 2003.

[58] E.C. Gartland, P. Palffy-Muhoray, and R.S. Varga. Numerical minimization of the landau-de gennes free energy: Defects in cylindrical capillaries. *Mol. Cryst. Liq. Cryst.*, 199:429–452, 1991.

[59] F.A. Fernández, S.E. Day, P. Trwoga, H.F. Deng, and R. James. Three-dimensional modelling of liquid crystal display cells using finite elements. *Mol. Cryst. Liq. Cryst.*, 375(1):291–299, 2002.

[60] R. Barberi, F. Ciuchi, G.E. Durand, M. Iovane, D. Sikharulidze, A.M. Sonnet, and E.G. Virga. Electric field induced order reconstruction in a nematic cell. *Eur. Phys. J. E.*, 13:61–71, 2003.

[61] H. Mori, E.C. Gartland, J.R. Kelly, and P. Bos. Multidimensional director modeling using the q tensor representation in a liquid crystal cell and its application to the π cell with patterned electrodes. *Jpn. J. Appl. Phys.*, 38:135, 1999.

[62] J. Beeckman, R. James, F.A. Fernández, W. De Cort, P.J.M. Vanbrabant, and K. Neyts. Calculation of Fully Anisotropic Liquid Crystal Waveguide Modes. *J. Lightw. Tech.*, 27:3812–3819, 2009.

[63] P.J.M. Vanbrabant, J. Beeckman, K. Neyts, R. James, and F.A. Fernández. A finite element beam propagation method for simulation of liquid crystal devices. *Opt. Express*, 17(13):10895–10909, 2009.

[64] K.R. Daly, G. D'Alessandro, and M. Kaczmarek. Regime independent coupled-wave equations in anisotropic photorefractive media. *Appl. Phys. B: Lasers Opt.*, 95(3):589–596, 2009.

[65] N. Mukohzaka, N. Yoshida, H. Toyoda, Y. Kobayashi, and T. Hara. Diffraction efficiency analysis of a parallel-aligned nematic-liquid-crystal spatial light modulator. *Appl. Opt.*, 33(14):2804–2811, 1994.

[66] G. Vijaya Prakash, M. Kaczmarek, A. Dyadyusha, J. J. Baumberg, and G. D'Alessandro. Control of topological defects in microstructured liquid crystal cells. *Opt. Express*, 13:2201, 2005.

[67] M. Hiroyuki, E.C. Gartland Jr, J.R. Kelly, and J. Philip. Multidimensional director modeling using the Q tensor representation in a liquid crystal cell and its application to the π cell with patterned electrodes. *Jpn. J. Appl. Phys*, 38:135–146, 1999.

[68] D.C. Jones and G. Cook. Theory of beam coupling in a hybrid photorefractive-liquid crystal cell. *Opt. Commun.*, 232:399–409, 2004.

[69] R.H. Self, C.P. Please, and T.J. Sluckin. Deformation of nematic liquid crystals in an electric field. *Eur. J. Appl. Math.*, 13:1–23, 2002.

[70] Y.H. Wan and J.E. Marsden. Symmetry and Bifurcation in Three-Dimensional Elasticity - Part III: Stressed Reference Configurations. *Arch. Rat. Mech. Anal.*, 84:293–233, 1983.

[71] D.R.J. Chillingworth. The Signorini perturbation scheme in an abstract setting. *Proc. Roy. Soc. Edin. A*, 119A:373–395, 1991.

[72] M. Golubitsky and D.G. Schaeffer. A discussion of symmetry and symmetry breaking. In *Proc. Symp. Pure Math*, pages 499–515, 1983.

[73] J.F. Thompson, ZUA Warsi, and C.W. Mastin. *Numerical grid generation: foundations and applications*. North-holland Amsterdam, 1985.

[74] G. Cook, C.A. Wyres, M.J. Deer, and D.C. Jones. Hybrid organic-inorganic photorefractives. *Proc. SPIE*, 5213:63–77, 2003.

[75] L. N. Trefethen. *Spectral Methods in MATLAB*. SIAM, 2000.

[76] K. R. Daly and G. D'Alessandro. http://www.personal.soton.ac.uk/dales/dfqta/.

[77] L. Solymar, D. J. Webb, and A. Grunnet-Jepsen. *The physics and applications of photorefractive materials*. Oxford, 1996.

[78] M. Kaczmarek and R.W. Eason. Conditions for efficient build-up of power in photorefractive ring cavities. *Opt. Commun.*, 154(5-6):334–338, 1998.

[79] X. Sun, C. Ren, Y. Pei, and F. Yao. Electrically controlled dynamic holographic gratings in fullerene C 60-doped nematic liquid crystals. *J. Phys. D: Appl. Phys.*, 41(24):245105, 2008.

[80] I.C. Khoo, K. Chen, and Y.Z. Williams. Orientational Photorefractive Effect in Undoped and CdSe Nanorods-Doped Nematic Liquid CrystalBulk and Interface Contributions. *IEEE J. Sel. Top. Quantum Electron.*, 12(3):443–450, 2006.

[81] A. Redler and H.S. Kitzerow. Influence of doping on the photorefractive properties of a polymer-dispersed liquid crystal. *Appl. Phys. Lett.*, 93:183304, 2008.

[82] M. Talarico and A. Golemme. Photorefractive binary system based on ferroelectric liquid crystals. *J. Phys. Chem. C*, 111(21):7834–7840, 2007.

[83] T.M. Fears, C. Anderson, and J.G. Winiarz. Photorefractivity in a polymeric composite photosensitized with NiS nanocrystals. *J. Chem. Phys.*, 129:154704, 2008.

[84] G. Cook, AV Glushchenko, V. Reshetnyak, AT Griffith, MA Saleh, and DR Evans. Nanoparticle doped organic-inorganic hybrid photorefractives. *Opt. Express*, 16(6):4015–4022, 2008.

[85] O. Buchnev, A. Dyadyusha, M. Kaczmarek, V. Reshetnyak, and Y. Reznikov. Enhanced two-beam coupling in colloids of ferroelectric nanoparticles in liquid crystals. *J. Opt. Soc. Am. B*, 24(7):1512–1516, 2007.

[86] U. Bortolozzo, S. Residori, and J. P. Huignard. Beam coupling in photorefractive liquid crystal light valves. *J. Phys: Appl Phys*, 41:224007, 2008.

[87] A. Miniewicz. Photorefractive-like all-optical switching in nematic-photoconducting polymer liquid crystal cell. *Mol. Cryst. Liq. Cryst.*, 489(1):119–134, 2008.

[88] F. Yao, Y. Pei, Y. Zhang, J. Zhang, C. Hou, and X. Sun. High-resolution photorefractive gratings in nematic liquid crystals sandwiched with photoconductive polymer film. *Appl. Phys. B*, 92(4):573–576, 2008.

[89] D. Jiang, L. Ding, J. Huang, E. Gu, L. Liu, Z. Chai, and D. Liu. Synthesis and characterization of photorefractive polymer based on chemically hybridized cds–pvk nanocomposite with a new azo chromophore. *Polymer*, 48(24):7156–7162, 2007.

[90] D.J. Binks, S.P. Bant, D.P. West, P. O'brien, and M.A. Malik. CdSe/CdS core/shell quantum dots as sensitizer of a photorefractive polymer composite. *J. Mod. Opt.*, 50(2):299–310, 2003.

[91] M. Kaczmarek, A. Dyadyusha, S. Slussarenko, and I. C. Khoo. The role of surface charge field in two-beam coupling in liquid crystal cells with photoconducting polymer layers. *J. Appl. Phys.*, 96:2616–2623, 2004.

[92] G. Cook, A.V. Glushchenko, V.Y. Reshetnyak, E.R. Beckel, M.A. Saleh, and D.R. Evans. Liquid crystal inorganic hybrid photorefractives. *Winter Topical Meeting Series, 2008 IEEE/LEOS*, pages 129–130, 2008.

[93] A. Miniewicz, K. Komorowska, J. Vanhanen, and J. Parka. Surface-assisted optical storage in a nematic liquid crystal cell via photoinduced charge-density modulation. *Organic Electronics*, 2(3-4):155 – 163, 2001.

[94] H. Kogelnik. Coupled wave theory for thick hologram gratings. *Bell. Syst. Tech. J.*, 48:2909–2947, 1969.

[95] G. Montemezzani and M. Zgonik. Light diffraction at mixed phase and absorption gratings in anisotropic media for arbitrary geometries. *Phys. Rev. E*, 55(1):1035–1047, 1997.

[96] C.V. Raman and N.S. Nath. The diffraction of light by high frequency sound waves: part i. *Proc. Indian. Acad. Sci. A*, 3:406–412, 1936.

[97] A.V. Galstyan, G.G. Zakharyan, and R.S. Hakobyan. The theory of light diffraction in thin anisotropic medium. *Mol. Cryst. Liq. Cryst.*, 453:203–213, 2006.

[98] G.G. Zakharyan and A.V. Galstyan. Mixed phase and absorption thin gratings diffraction. *Opto-electronics Rev.*, 15:20–26, 2007.

[99] V.O. Kubytskyi, V.Y. Reshetnyak, T.J. Sluckin, and S.J. Cox. Theory of surface-potential-mediated photorefractivelike effects in liquid crystals. *Phys. Rev. E*, 79(1):11703, 2009.

[100] T.K. Gaylord and M.G. Moharam. Thin and thick gratings: terminology clarification. *Appl. Opt.*, 20(19):3271, 1981.

[101] M.G. Moharam, T.K. Gaylord, and R. Magnusson. Criteria for bragg regime diffraction by phase gratings. *Opt. Commun.*, 32:14–18, 1980.

[102] E.N. Glytsis and T.K. Gaylord. Three-dimensional (vector) rigorous coupled-wave analysis of anisotropic grating diffraction. *J. Opt. Soc. Am. A*, 7(8):1399, 1990.

[103] E.N. Glytsis and T.K. Gaylord. Rigorous three-dimensional coupled-wave diffraction analysis of single and cascaded anisotropic gratings. *J. Opt. Soc. Am. A*, 4(11):2061, 1987.

[104] D.R. Evans and G. Cook. Bragg-matched photorefractive two-beam coupling in organic-inorganic hybrids. *J. nonlinear opt. phys. Mater.*, 16(03):271–280, 2007.

[105] S. Bartkiewicz, K. Matczyszyn, A. Miniewicz, and F. Kajzar. High gain of light in photoconducting polymer-nematic liquid crystal hybrid structures. *Opt. Commun.*, 187:257–261, 2001.

[106] V.O. Kubytskyi, V.Y. Reshetnyak, T.J. Sluckin, and S.J. Cox. Simulation of photorefractive effect in thin liquid crystal film. *Mol. Cryst. Liq. Cryst.*, 489(0):204–213, 2008.

[107] E.P. Raynes, C.V. Brown, and J.F. Stromer. Method for the measurement of the K_{22} nematic elastic constant. *Appl. Phys. Lett.*, 82(1):13–15, 2003.

[108] A. Yariv and P. Yeh. Optical waves in crystals: propagation and control of laser radiation. *John Wiley & Sons, Inc., New York*, 12:5448–5456, 1984.

[109] I.C. Khoo. Wave mixing in non-linear media. *IEEE Journal of quantum electronics*, 25:484–519, 1989.

[110] A.R.M. Verschueren and R. Niessen. Experiments and modeling of conduction and charge accumulation in liquid crystal cells. *IEEE T. Dielect. El. In.*, 10(6):963–969, 2003.

[111] P. Aubourg, J.P. Huignard, M. Hareng, and R.A. Mullen. Liquid crystal light valve using bulk monocrystalline Bi_12SiO_20 as the photoconductive material. *Appl. Opt.*, 21(20):3706–3712, 1982.

[112] L.B. Rothman. Properties of polyimide films. *J. Electrochem. Soc*, 127(10):2216–2220, 1980.

[113] S. Santos, C. Gomez, and I. Salazar. DC Conductivity in Poly-N-Vinylcarbazole: A Study of Dielectric Measurements. *International Journal of Polymeric Materials*, 51(6):567–575, 2002.

[114] A.V. Zayats, I.I. Smolyaninov, and A.A. Maradudin. Nano-optics of surface plasmon polaritons. *Phys. Rep.*, 408(3-4):131–314, 2005.

[115] R.H. Ritchie. Plasma losses by fast electrons in thin films. *Phys. Rev.*, 106(5):874–881, 1957.

[116] C.J. Powell and J.B. Swan. Origin of the characteristic electron energy losses in aluminum. *Phys. Rev.*, 115(4):869–875, 1959.

[117] C.J. Powell and J.B. Swan. Origin of the characteristic electron energy losses in magnesium. *Phys. Rev.*, 116(1):81–83, 1959.

[118] E.A. Stern and R.A. Ferrell. Surface plasma oscillations of a degenerate electron gas. *Phys. Rev.*, 120(1):130–136, 1960.

[119] J.M. Pitarke, V.M. Silkin, E.V. Chulkov, and P.M. Echenique. Theory of surface plasmons and surface-plasmon polaritons. *Rep. Prog. Phys.*, 70:1–87, 2007.

[120] I.R. Hooper and J.R. Sambles. Differential ellipsometric surface plasmon resonance sensors with liquid crystal polarization modulators. *Appl. Phys. Lett.*, 85:3017, 2004.

[121] X. Fan, I.M. White, S.I. Shopova, H. Zhu, J.D. Suter, and Y. Sun. Sensitive optical biosensors for unlabeled targets: a review. *analytica chimica acta*, 620(1-2):8–26, 2008.

[122] J. Homola, S.S. Yee, and G. Gauglitz. Surface plasmon resonance sensors: review. *Sensor. Actuator. B*, 54(1-2):3–15, 1999.

[123] K. Kneipp, H. Kneipp, I. Itzkan, R.R. Dasari, and M.S. Feld. Surface-enhanced Raman scattering and biophysics. *J. Phys.: Condens. Matter*, 14:R597, 2002.

[124] S.A. Maier, P.G. Kik, H.A. Atwater, S. Meltzer, E. Harel, B.E. Koel, and A.A.G. Requicha. Local detection of electromagnetic energy transport below the diffraction limit in metal nanoparticle plasmon waveguides. *Nat. Mater.*, 2(4):229–232, 2003.

[125] M. Malmqvist. Biospecific interaction analysis using biosensor technology. *Nature*, 361(6408):186–187, 1993.

[126] W.L. Barnes, A. Dereux, and T.W. Ebbesen. Surface plasmon subwavelength optics. *Nature*, 424(6950):824–830, 2003.

[127] M. Kuttge, E.J.R. Vesseur, J. Verhoeven, H.J. Lezec, H.A. Atwater, and A. Polman. Loss mechanisms of surface plasmon polaritons on gold probed by cathodoluminescence imaging spectroscopy. *Appl. Phys. Lett.*, 93:113110, 2008.

[128] F. Yang, J.R. Sambles, and G.W. Bradberry. Long-range surface modes supported by thin films. *Phys. Rev. B*, 44(11):5855–5872, 1991.

[129] G.G. Nenninger, P. Tobika, J. Homola, and S.S. Yee. Long-range surface plasmons for high-resolution surface plasmon resonance sensors. *Sensor. Actuat. B-CHEM.*, 74(1-3):145–151, 2001.

[130] A.W. Wark, H.J. Lee, and R.M. Corn. Long-range surface plasmon resonance imaging for bioaffinity sensors. *Anal. Chem*, 77(13):3904–3907, 2005.

[131] E. Kretschmann and H. Raether. Radiative decay of non radiative surface plasmons excited by light. *Zeitschrift Fuer Naturforshung, Teil A*, 23:2135, 1968.

[132] A. Otto. Excitation of nonradiative surface plasma waves in silver by the method of frustrated total reflection. *Zeitschrift für Physik A Hadrons and Nuclei*, 216(4):398–410, 1968.

[133] Y.Y. Teng and E.A. Stern. Plasma radiation from metal grating surfaces. *Phys. Rev. Lett.*, 19(9):511–514, 1967.

[134] R.W. Wood. XLII. On a remarkable case of uneven distribution of light in a diffraction grating spectrum. *Philosophical Magazine Series 6*, 4(21):396–402, 1902.

[135] R.W. Wood. Anomalous diffraction gratings. *Physical Review*, 48(12):928–936, 1935.

[136] T.W. Preist, N.P.K. Cotter, and J.R. Sambles. Periodic multilayer gratings of arbitrary shape. *JOSA A*, 12(8):1740–1748, 1995.

[137] I.R. Hooper and J.R. Sambles. Surface plasmon polaritons on thin-slab metal gratings. *Phys. Rev. B*, 67(23):235404, 2003.

[138] I.R. Hooper and J.R. Sambles. Coupled surface plasmon polaritons on thin metal slabs corrugated on both surfaces. *Phys. Rev. B*, 70(4):45421, 2004.

[139] Z. Chen, I.R. Hooper, and J.R. Sambles. Strongly coupled surface plasmons on thin shallow metallic gratings. *Phys. Rev. B*, 77(16):161405, 2008.

[140] P.M. Van Den Berg and J.T. Fokkema. The Rayleigh hypothesis in the theory of diffraction by a perturbation in a plane surface. *Radio Sci*, 15:723–732, 1980.

[141] M.R. Gadsdon, I.R. Hooper, A.P. Hibbins, and J.R. Sambles. Surface plasmon polaritons on deep, narrow-ridged rectangular gratings. *JOSA B*, 26(6):1228–1237, 2009.

[142] J. Yoon, G. Lee, S.H. Song, C.H. Oh, and P.S. Kim. Surface-plasmon photonic band gaps in dielectric gratings on a flat metal surface. *J. Appl. Phys.*, 94:123, 2003.

[143] S. Park, G. Lee, S.H. Song, C.H. Oh, and P.S. Kim. Resonant coupling of surface plasmons to radiation modes by use of dielectric gratings. *Opt. Lett.*, 28(20):1870–1872, 2003.

[144] B. Fischer, B. Rothenhäusler, and W. Knoll. Surface-plasmon-enhanced diffraction orders in polymer gratings. *Thin Solid Films*, 258(1-2):247–251, 1995.

[145] F. Wu, D. Han, X. Hu, X. Liu, and J. Zi. Complete surface plasmon-polariton band gap and gap-governed waveguiding, bending and splitting. *J. Phys.: Condens. Matter*, 21:185010, 2009.

[146] S.J. Elston and J.R. Sambles. Surface plasmon-polaritons on an anisotropic substrate. *J. Mod. Opt.*, 37(12):1895–1902, 1990.

[147] K.R. Welford and J.R. Sambles. Detection of surface director reorientation in a nematic liquid crystal. *Appl. Phys. Lett.*, 50:871, 1987.

[148] R.A. Innes and J.R. Sambles. Optical nonlinearity in a nematic liquid crystal using surface plasmon-polaritons. *Opt. Commun.*, 64(3):288–292, 1987.

[149] R.A. Innes, S.P. Ashworth, and J.R. Sambles. Large optical bistability in a nematic liquid crystal using surface plasmon-polaritons. *Phys. Lett. A*, 135(6-7):357–362, 1989.

[150] KR Welford, JR Sambles, and MG Clark. Guided modes and surface plasmon-polaritons observed with a nematic liquid crystal using attenuated total reflection. *Liquid Crystals*, 2(1):91–105, 1987.

[151] D.W. Berreman. Optics in stratified and anisotropic media: 4 x 4-matrix formulation. *JOSA B*, 64:502–510, 1972.

[152] J.M. Simon and V.A. Presa. Surface electromagnetic waves at the interface with anisotropic media. *J. Mod. Opt.*, 42(11):2201–2211, 1995.

[153] M.L. Gigli and R.A. Depine. Excitation of eigenmodes at uniaxial crystal-metal-isotropic films. *J. Mod. Opt.*, 45:2281–2299, 1998.

[154] A. Lakhtakia. Surface-plasmon wave at the planar interface of a metal film and a structurally chiral medium. *Opt. Commun.*, 279(2):291–297, 2007.

[155] D.Y.K. Ko and J.R. Sambles. Scattering matrix method for propagation of radiation in stratified media: attenuated total reflection studies of liquid crystals. *J. Opt. Soc. Am. A*, 5(11):1863–1866, 1988.

[156] L. Li. Formulation and comparison of two recursive matrix algorithms for modeling layered diffraction gratings. *interfaces*, 16:17, 1996.

[157] M. Auslender and S. Hava. Scattering-matrix propagation algorithm in full-vectorial optics of multilayer grating structure. *Opt. Lett.*, 21:1765–1767, 1996.

[158] M.E. Caldwell and E.M. Yeatman. Surface-plasmon spatial light modulators based on liquid crystal. *Appl. Opt.*, 31(20):3880–3891, 1992.

[159] F. Yang and J.R. Sambles. Optical fully leaky mode characterization of a standard liquid-crystal cell. *J. Opt. Soc. Am. B*, 16(3):488–497, 1999.

[160] J. Chandezon, MT Dupuis, G. Cornet, and D. Maystre. Multicoated gratings: a differential formalism applicable in the entire optical region. *JOSA*, 72(7):839–846, 1982.

[161] N.P.K. Cotter, T.W. Preist, and J.R. Sambles. Scattering-matrix approach to multilayer diffraction. *J. Opt. Soc. Am. A*, 12(5):1097–1103, 1995.

[162] K. Rokushima and J. Yamakita. Analysis of anisotropic dielectric gratings. *J. Opt. Soc. Am.*, 73(7):901, 1983.

[163] M.G. Moharam and T.K. Gaylord. Coupled-wave analysis of reflection gratings. *Appl. Opt.*, 20(2):240, 1981.

[164] R.F. Wallis and J.J. Brion. Theory of surface polaritons in anisotropic dielectric media with applications to surface magnetoplasmons in semiconductors. *Phys. Rev. B*, 9:3429–3473, 1974.

[165] A.A. Krokhin, A. Neogi, and D. McNeil. Long-range propagation of surface plasmons in a thin metallic film deposited on an anisotropic photonic crystal. *Phys. Rev. B*, 75(23):235420, 2007.

[166] R. Li, C. Cheng, F.F. Ren, J. Chen, Y.X. Fan, J. Ding, and H.T. Wang. Hybridized surface plasmon polaritons at an interface between a metal and a uniaxial crystal. *Appl. Phys. Lett.*, 92:141115, 2008.

[167] J. Jacob, A. Babu, G.l Mathew, and V. Mathew. Propagation of surface plasmon polaritons in anisotropic mim and imi structures. *Superlattices Microstruct.*, 44(3):282 – 290, 2008.

[168] W.P. Chen and J.M. Chen. Use of surface plasma waves for determination of the thickness and optical constants of thin metallic films. *JOSA*, 71:189–191, 1981.

[169] E. Fontana. Thickness optimization of metal films for the development of surface-plasmon-based sensors for nonabsorbing media. *Applied Optics*, 45(29):7632–7642, 2006.

[170] I. Pockrand. Surface plasma oscillations at silver surfaces with thin transparent and absorbing coatings. *Surface Science*, 72(3):577–588, 1978.

[171] W.P. Chen and J.M. Chen. Surface plasma wave study of submonolayer Cs and Cs O covered Ag surfaces. *Surf. Sci.*, 91(2-3):601–617, 1980.

[172] P.B. Johnson and R.W. Christy. Optical constants of the noble metals. *Physical Review B*, 6:4370–4379, 1972.

[173] L. I. Schiff. *Quantum Mechanics*. McGraw Hill Book Company, 1949.

[174] J.P. Boyd and J.P. Boyd. *Chebyshev and Fourier spectral methods*. Dover Pubns, 2001.

Appl Phys B (2009) 95: 589–596
DOI 10.1007/s00340-009-3492-1

Applied Physics B
Lasers and Optics

Regime independent coupled-wave equations in anisotropic photorefractive media

K.R. Daly · G. D'Alessandro · M. Kaczmarek

Received: 29 January 2009 / Revised version: 17 February 2009 / Published online: 3 April 2009

Abstract An extension to coupled wave theory suitable for all regimes of diffraction is presented. The model assumes that the refractive index grating has an arbitrary profile in one direction and is periodic (but not necessarily sinusoidal) in the other. Higher order diffracted terms are considered and appropriate mismatch terms dealt with. It is shown that this model is analytically equivalent to both the Bragg and Raman–Nath regime coupling models under an appropriate set of assumptions. This model is applied to cases such as optical coupling in liquid crystal cells with photoconductive layers. Its predictions are successfully compared to finite element simulations of the full Maxwell's equations.

PACS 42.25.-p · 42.25.Fx · 42.25.Lc · 42.65.Hw · 42.70.Df

1 Introduction

The coupling of light due to diffraction from inhomogeneous, anisotropic materials has been studied for many years [1–4] and is often referred to as occurring in one of two distinct regimes, Bragg and Raman-Nath.

Bragg regime coupling is characterised by the presence of only two beams and was initially described in 1969 by the coupled-wave theory of Kogelnik [1] for an isotropic medium. This work was extended in 1997 by Montemezzani and Zgonik [2] to include optically anisotropic materials.

Raman-Nath diffraction occurs in cases of thin gratings with multiple diffracted output beams for a single input beam. Diffraction in this regime was first studied in 1936 [3]. This system is modelled by considering the modulated refractive index as a phase grating and neglecting any anisotropy in the materials. In the past couple of years modelling in the Raman–Nath regime has been extended using an approach similar to that of Kogelnik and Montemezzani to describe Raman–Nath diffraction in anisotropic media [4].

Although the models just described offer ease of implementation and high computational efficiency they are restricted to specific regimes. Differentiation between the Bragg and Raman–Nath regimes is not always straight forward as both the thickness of the medium and the refractive index profile affect the nature of the diffracted beams. The first criteria used to distinguish the two regimes were suggested by Kogelnik [1]. However, since then a variety of ways have been suggested, as reviewed in [5], and more appropriate criteria for both Bragg and Raman–Nath [6] coupling regimes have been established.

From the analysis of these criteria, it is clear that there is no distinct cut off point between Bragg and Raman–Nath regimes. Indeed, there is an intermediate regime in which neither theory is appropriate. A more rigorous method has been developed, based on direct substitution of the refractive index profile into Maxwell's equations, for both isotropic [7] and anisotropic [8] materials. It has been shown to agree numerically with both the coupled-wave approach and the Raman–Nath phase grating approach. Although offering good agreement with the simpler theories this approach is less computationally efficient as it involves solving $4n$ coupled ODEs for n discrete wave vectors.

Bragg geometries were extensively used to observe two-beam coupling gain in photorefractive crystals. For exam-

---

K.R. Daly (✉) · G. D'Alessandro
School of Mathematics, University of Southampton,
Southampton, SO17 1BJ, UK
e-mail: krd103@soton.ac.uk

M. Kaczmarek
School of Physics and Astronomy, University of Southampton,
Southampton, SO17 1BJ, UK

ple in $BaTiO_3$ and $Rh:BaTiO_3$ crystals very high coupling coefficients and diffraction efficiencies were observed [9]. More recently efficient beam coupling was shown in a wide range of organic materials, such as fullerene [10] and CdSe doped [11] liquid crystals, polymer-dispersed [12] and ferroelectric liquid crystals [13], polymeric composites [14], hybrids with liquid crystals [15–17], light valves [17], photoconductive polymer-liquid crystal structures [18, 19] and photorefractive polymers [20, 21]. In most of these materials either Bragg or Raman–Nath gratings could be created.

However, not all experimental geometries used in beam coupling are simple. Recently, photorefractive effects have been demonstrated using low power lasers in nematic liquid crystal cells in both the Bragg [22] and the Raman–Nath [23] regimes. Optical coupling is achieved by sandwiching the liquid crystals between photoconductive or photorefractive layers. In the case of the photoconductive layer, such as $PVK:C_{60}$, which also serves as an alignment layer for the liquid crystal, the interference of two incident beams will create a region of modulated conductivity. A voltage applied across the cell provides a modulated electric field across the bulk liquid crystal sample which aligns the molecules and, as such, affects the refractive index in the cell. As shown in Fig. 1, such interaction leads to several diffracted orders being present: simple changes in the geometry of the incident beams will move the system continuously from the Bragg to the Raman–Nath regime, through the intermediate regime. Application of a simple Bragg diffraction theory to a system in the intermediate regime could lead to incorrect values of coupling coefficients to be deduced.

This system has a number of features which complicate the modelling. Firstly, due to the non-linear alignment of the liquid crystals with the applied electric field, liquid crystal refractive index profiles are non-uniform in the z-direction and contain many harmonics of the fundamental grating vector in the x-direction. Secondly, as nematic liquid crystal molecules are symmetric with respect to inversion, it is necessary to have a non-normal incidence angle for the bisector of the two incident beams in order to obtain the correct grating vector [24]. This means that as the grating is created by the superposition of the beams at the cell surface, there are no waves which can be perfectly matched by the fundamental grating vector. Finally, as has already been mentioned, in structures with liquid crystals beam coupling behaviour has been observed in both the Bragg and Raman-Nath regimes, so a model has to be capable of describing both of these behaviours.

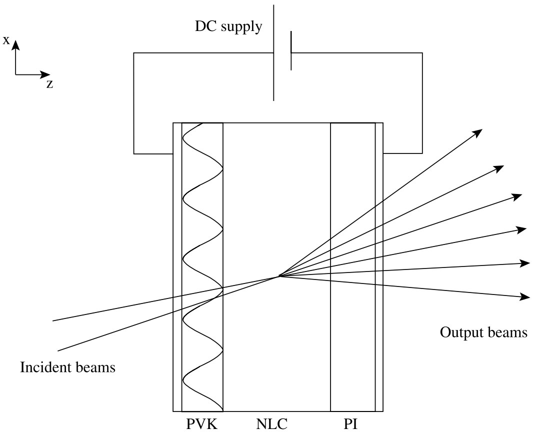

Fig. 1 Schematic of liquid crystal beam coupling cell. The nematic liquid crystal (NLC) is aligned by the Polyimide (PI) layer and the photoconducting Polyvinyl Carbazole (PVK) layers

In this paper, we present an extension to the coupled-wave theory of Kogelnik and Montemezzani, which can be used in the cases of Bragg, Raman–Nath and intermediate regime coupling. This method is capable of handling refractive index profiles containing a fundamental sinusoidal modulation and any higher harmonics that may be present. As an example we use the structure and geometry of a liquid crystal cell with a photoconductive alignment layer. A finite element simulation which solves Maxwell's equations is then used to verify the models predictions.

In Sect. 2 we develop the beam coupling model from Maxwell's equations and show comparison to the existing coupled-wave models of Montemezzani, and Kogelnik, and the Raman–Nath phase grating approach. In Sect. 3 a model for the liquid crystal cell is developed. Finally Sect. 4 provides details of the comparison between the method presented here and the finite element approach.

2 Beam coupling model

2.1 Derivation

We consider a medium which contains a periodic refractive index grating in the x-, z-plane with a fundamental grating wave number $K = \frac{2\pi}{\Lambda}$ and any number of higher grating harmonics pK where $p = 2, 3, \ldots$ and Λ is the grating period. The method we have developed is valid for gratings aligned in any direction. However, to simplify the algebra, we assume that the grating is aligned in the x-direction. This is, for example, the case in photorefractive liquid crystal cells. We further assume that the medium is birefringent and that each Fourier component of the dielectric tensor, $\Delta\epsilon^{(p)}(z)$, may have a different profile in the z-direction so that the dielectric tensor may be expressed as

$$\epsilon_r = \epsilon_u + \frac{1}{2}\sum_{p=-\infty}^{\infty} \Delta\epsilon^{(p)}(z) e^{i(pKx+\phi^{(p)})}, \tag{1}$$

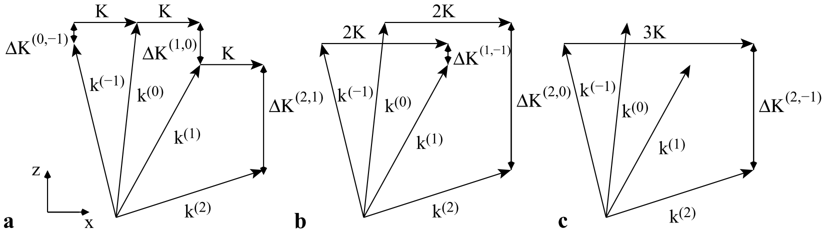

Fig. 2 Possible couplings and associated mismatch terms for (**a**) the fundamental grating period. (**b**) The second harmonic. (**c**) The third harmonic

where ϵ_u is the uniform part of the dielectric tensor and $\phi^{(p)}$ is the phase shift of the p-th grating Fourier component. We choose our coordinate axes such that they coincide with the principal axes of ϵ_u. Coupling can be achieved by diffraction from the fundamental grating vector and any of its higher harmonics, as illustrated in Fig. 2. It should be noted that as the bisector of the two incident waves is not normal, none of these terms are perfectly matched by the fundamental grating vector. Therefore the coupling strength will depend on not only the amplitude of the appropriate coupling harmonic, but also on the size of the mismatch term $\Delta K^{(m,n)} = k_z^{(m)} - k_z^{(n)}$.

The electric field in the material is assumed to be a superposition of the plane waves which may be perfectly matched by the grating vectors in the x-direction. Hence the field is periodic in x with fundamental wave number K. We expand it in a Fourier series in x as

$$\boldsymbol{E} = \sum_{m=-N}^{N} \boldsymbol{A^{(m)}}(z) e^{i(\boldsymbol{k^{(m)}} \cdot \boldsymbol{x} - \omega t)}, \tag{2}$$

where ω is the optical angular frequency and $\boldsymbol{k^{(m)}} = mK\hat{\boldsymbol{x}} + k_z^{(m)}\hat{\boldsymbol{z}}$, with the constraint that $|\boldsymbol{k^{(m)}}| = k_0 n^{(m)}$. Here k_0 is the free space wave number and $n^{(m)}$ is the refractive index seen by the m-th wave. The total number of optical components is $2N+1$ where $N = \frac{k_0}{|\boldsymbol{K}|}$. Substituting (2) and (1) into Maxwell's equations and using

$$\boldsymbol{k}^{(m)} = \boldsymbol{k}^{(n)} + (m-n)K\hat{\boldsymbol{x}} + \big(k_z^{(m)} - k_z^{(n)}\big)\hat{\boldsymbol{z}}, \tag{3}$$

we obtain a set of coupled-wave equations for the amplitudes $\boldsymbol{A^{(m)}}$:

$$\begin{aligned}
&\big[i\boldsymbol{k^{(m)}} \times i\boldsymbol{k^{(m)}} \times \boldsymbol{A^{(m)}}\big] + \big[i\boldsymbol{k^{(m)}} \times \nabla \times \boldsymbol{A^{(m)}}\big] \\
&\quad + \big[\nabla \times i\boldsymbol{k^{(m)}} \times \boldsymbol{A^{(m)}}\big] + \big[\nabla \times \nabla \times \boldsymbol{A^{(m)}}\big] \\
&= \frac{\omega^2}{c^2}\epsilon_u \boldsymbol{A^{(m)}} \\
&\quad + \frac{k_0^2}{2} \sum_{n=-N}^{N} \Delta\epsilon^{(n-m)} \boldsymbol{A^{(n)}} e^{i\Gamma\phi^{(n-m)}} e^{i(k_z^{(n)} - k_z^{(m)})z},
\end{aligned} \tag{4}$$

where $\Gamma = \operatorname{sgn}(m-n)$ and $\Gamma(0) = 0$. We may neglect the final bracketed term on the left hand side of this equation as its terms consist of second derivatives, which, using the slowly varying amplitude approximation, will be small. The first term on each side of the equation describes the propagation of light in an anisotropic medium [25],

$$i\boldsymbol{k^{(m)}} \times i\boldsymbol{k^{(m)}} \times \boldsymbol{A^{(m)}} = \frac{\omega^2}{c^2}\epsilon_u \boldsymbol{A^{(m)}}. \tag{5}$$

This relates the optical wave vector to the wave polarisation and dielectric tensor. As such the eigenvalues of this equation will determine the refractive indices and hence, the velocities at which the light may propagate through the material. The remaining terms in (4) describe the optical coupling between the various plane wave amplitudes:

$$\begin{aligned}
&i\boldsymbol{k^{(m)}} \times \nabla \times \boldsymbol{A^{(m)}} + \nabla \times i\boldsymbol{k^{(m)}} \times \boldsymbol{A^{(m)}} \\
&\quad = \frac{k_0^2}{2} \sum_{n=-N}^{N} \Delta\epsilon^{(n-m)} \boldsymbol{A^{(n)}} e^{i\Gamma\phi^{(n-m)}} e^{i(k_z^{(n)} - k_z^{(m)})z}.
\end{aligned} \tag{6}$$

We perform some vector algebra on the left hand side of (6) and use $\boldsymbol{k^{(m)}} = \hat{\boldsymbol{k}}^{\boldsymbol{(m)}} k^{(m)}$ and $\boldsymbol{A^{(m)}} = \hat{\boldsymbol{A}}^{\boldsymbol{(m)}} A^{(m)}$, where $\hat{\boldsymbol{k}}^{\boldsymbol{(m)}}$ is the unit wave vector, $\hat{\boldsymbol{A}}^{\boldsymbol{(m)}}$ the unit polarisation vector, $k^{(m)}$ the optical wave number and $A^{(m)}$ the optical amplitude of the m-th wave. Taking the dot product of $\hat{\boldsymbol{A}}^{\boldsymbol{(m)}}$ with both sides of (6) gives

$$\begin{aligned}
&2ik^{(m)}\big[\big(\hat{\boldsymbol{k}}^{\boldsymbol{(m)}} \cdot \hat{\boldsymbol{A}}^{\boldsymbol{(m)}}\big)\hat{\boldsymbol{A}}^{\boldsymbol{(m)}} - \hat{\boldsymbol{k}}^{\boldsymbol{(m)}}\big] \cdot \nabla A^{(m)} \\
&\quad = \frac{k_0^2}{2} \sum_{n=-\infty}^{\infty} \mathcal{G}^{(n,m)} A^{(n)} e^{i\Gamma\phi^{(n-m)}} e^{i(k_z^{(n)} - k_z^{(m)})z},
\end{aligned} \tag{7}$$

where, to simplify notation, we have written $\mathcal{G}^{(n,m)} = \hat{\boldsymbol{A}}^{\boldsymbol{(m)}} \Delta\epsilon^{(n-m)} \hat{\boldsymbol{A}}^{\boldsymbol{(n)}}$. The bracketed term on the left hand side of (7) can be written as $\hat{\boldsymbol{u}}^{\boldsymbol{(m)}} g^{(m)}$, where $\hat{\boldsymbol{u}}$ is the unit Poynting vector, $g^{(m)} = \hat{\boldsymbol{A}}^{\boldsymbol{(m)}} \cdot \hat{\boldsymbol{D}}^{\boldsymbol{(m)}}$ and $\hat{\boldsymbol{D}}$ is the electric displacement unit vector. By writing $k^{(m)} = n^{(m)}k_0$ we can simplify (7) further to give

$$\begin{aligned}
&n^{(m)} g^{(m)} \hat{u}_z^{(m)} \frac{dA^{(m)}}{dz} \\
&\quad = \frac{ik_0}{4} \sum_{n=-N}^{N} \mathcal{G}^{(n,m)} A^{(n)} e^{i\Gamma\phi^{(n-m)}} e^{i(k_z^{(n)} - k_z^{(m)})z},
\end{aligned} \tag{8}$$

where, as $A^{(m)}$ is a function of only z, we have simplified the derivative. We can simplify this system by introducing the new variable

$$A^{(m)} = \tilde{A}^{(m)} e^{-ik_z^{(m)} z}. \tag{9}$$

Substituting (9) into (8) gives the simplified equations

$$\hat{u}_z^{(m)} \frac{d\tilde{A}^{(m)}}{dz} = ik_z^{(m)} \tilde{A}^{(m)} + \frac{ik_0}{4n^{(m)} g^{(m)}} \sum_{n=-N}^{N} \mathcal{G}^{(n,m)} \tilde{A}^{(n)} e^{i\Gamma\phi^{(n-m)}}, \tag{10}$$

which for the simple case of $\Delta\epsilon^{(n-m)}$ being constant can be solved as an eigenvalue eigenvector problem. For all other cases the equations are solved using a Runge–Kutta method in MATLAB.

Equation (10) describes the coupling of an arbitrary number of beams in a system whose dielectric profile is arbitrary in the z-direction and modulated with fundamental period Λ in the x-direction.

2.2 Comparison to existing models

Before we consider the application of this model we first aim to show that under suitable approximations it may be reduced to the commonly used Bragg and Raman–Nath models. Here we show that as well as being numerically equivalent for these geometries and optical incidence angles, the equations are analytically identical for an appropriate set of assumptions.

The Bragg case is straightforward. Under the assumption of a single grating Fourier component, a constant dielectric profile in the z-direction and the presence of only two waves, (8) becomes

$$\begin{aligned} \hat{u}_z^{(1)} \frac{dA^{(1)}}{dz} &= \frac{ik_0}{4n^{(1)} g^{(1)}} \mathcal{G}^{(1,2)} A^{(2)} e^{i\phi} e^{i\Delta K z}, \\ \hat{u}_z^{(2)} \frac{dA^{(2)}}{dz} &= \frac{ik_0}{4n^{(2)} g^{(2)}} \mathcal{G}^{(2,1)} A^{(1)} e^{-i\phi} e^{-i\Delta K z}. \end{aligned} \tag{11}$$

These expressions become equal to those derived by Montemezzani [2], once the assumption of zero absorption has been made.

The comparison to Raman–Nath phase grating theory is less obvious. Again, we begin by making the assumptions of a single grating Fourier component of large wavelength, and a constant dielectric profile in the z-direction. As the grating wavelength is large the deviation in propagation angles of the beams is small. Hence the mismatch term $k_z^{(n)} - k_z^{(m)}$ is small and may be neglected for thin materials. For comparison, the system is simplified for an isotropic material with all waves polarised in the same direction. If we then make the normal Raman–Nath assumptions, i.e. we assume normal incidence and a $\pi/2$ phase shift, we may write (8) as

$$2\cos\theta^{(m)} \frac{2n}{k_0 \Delta\epsilon} \frac{dA^{(m)}}{dz} = \left[A^{(m-1)} - A^{(m+1)}\right], \tag{12}$$

where $\theta^{(m)}$ is the angle with respect to the surface normal at which the m-th wave propagates. Using the assumption that the wave propagation directions differ by a small amount we may approximate $\theta^{(m)}$ by the propagation angle of the incident beam $\theta^{(i)} = 0$. To proceed we make the following change of variable:

$$\zeta = \frac{k_0 \Delta\epsilon}{2n} z. \tag{13}$$

Making use of the Bessel recurrence relations it can be seen that (12) is satisfied by the m-th order Bessel function $J_m(\zeta)$. This gives the optical envelope

$$A^{(m)} = J_m(\zeta) = J_m\left(\frac{k_0 \Delta\epsilon}{2n} z\right) \tag{14}$$

which is identical to the optical envelope predicted by the Raman–Nath phase grating theory [3].

This analysis demonstrated how (8) is, under realistic assumptions, equivalent to either Bragg or Raman–Nath theory. The next step is to compare the model to finite element simulations for the example system of a photorefractive liquid crystal cell.

3 Liquid crystal model

To demonstrate the applications of this model we wish to model a non-trivial beam coupling system. A typical liquid crystal cell provides the perfect example of this due to its highly non-linear alignment and high optical anisotropy.

We use a Landau–DeGennes $\mathcal{Q}$ tensor model [26] for which the liquid crystal director field $\hat{\boldsymbol{n}}$ is modelled by a traceless symmetric tensor

$$\mathcal{Q} = \sqrt{2} S \left(\hat{\boldsymbol{n}} \otimes \hat{\boldsymbol{n}} - \frac{1}{2}\delta\right), \tag{15}$$

where δ is Kronecker's δ function and S is the scalar order parameter. Here we have used a 2 × 2 tensor which restricts the liquid crystals reorientation to within a plane. The liquid crystal alignment is then found through a minimisation of the free energy in the system. The total free energy in the cell may be expressed as [26]

$$F = \int_V [F_e + F_d + F_t] dV, \tag{16}$$

where F_e is the electrostatic free energy, F_d is the elastic free energy and F_t is the thermotropic free energy. These may be expressed in non-dimensional form as

$$F_d = \frac{1}{2}\xi_0^2 |\nabla \mathcal{Q}|^2, \tag{17}$$

$$F_e = -\frac{1}{2}\chi_i (\nabla\phi)^2 - \chi_a \mathrm{Tr}(\mathcal{Q}\mathcal{E}), \tag{18}$$

and

$$F_t = \frac{1}{2}T_0 \mathrm{Tr}\big(\mathcal{Q}^2\big) - \sqrt{6}\mathrm{Tr}\big(\mathcal{Q}^3\big) + \frac{1}{2}\big[\mathrm{Tr}\big(\mathcal{Q}^2\big)\big]^2, \tag{19}$$

where ξ_0^2 is the non-dimensional elastic constant, χ_i and χ_a are the non-dimensional isotropic and anisotropic electrostatic constants respectively, T_0 the non-dimensional temperature, and $\mathcal{E}$ is the electrostatic tensor

$$\mathcal{E} = \sqrt{2}|\boldsymbol{E}|^2\left(\hat{\boldsymbol{E}} \otimes \hat{\boldsymbol{E}} - \frac{1}{2}\delta\right). \tag{20}$$

We represent the alignment tensor $\mathcal{Q}$ on the basis of 2×2 traceless symmetric tensors [27],

$$\mathcal{Q} = \sum_{p=0}^{1} a_p T^{(p)}, \tag{21}$$

where

$$T^{(0)} = \frac{1}{\sqrt{2}}\begin{pmatrix} -1 & 0 \\ 0 & 1 \end{pmatrix}, \qquad T^{(1)} = \frac{1}{\sqrt{2}}\begin{pmatrix} 0 & 1 \\ 1 & 0 \end{pmatrix}. \tag{22}$$

Note that in this notation the scalar order parameter is $S = a_0^2 + a_1^2$. We then express the Euler–Lagrange equations which minimise the free energy as

$$\xi_0^2 \nabla^2 a_n - T_0 a_n - 2a_n\big(a_0^2 + a_1^2\big) + \chi_a e_n = 0. \tag{23}$$

One of the major problems with solving these equations is that the non-dimensional elastic and electrostatic constants are several orders of magnitude smaller than the thermotropic coefficients. Various methods exist to overcome this obstacle including; the use of adaptive finite element meshing techniques [28], the scaling of the thermotropic coefficients [29] and the renormalisation of variables at each step [30].

Here we use this difference in magnitudes to setup a multiple scales perturbation expansion in terms of the small parameter ξ_0^2. This has the advantage of simplifying the equations and the method of solution. However, a consequence of the approximation is that we must assume that the scalar order parameter has only small variations across the cell. This prevents us from modelling any defects in the liquid crystal alignment. At leading order this defines the scalar order parameter as

$$T_0 + a_0^2 + a_1^2 = 0. \tag{24}$$

The first order correction determines the molecular alignment,

$$a_0 \nabla^2 a_1 - a_1 \nabla^2 a_0 + a_0 \chi_0 a_1 - a_1 \chi_0 a_0 = 0, \tag{25}$$

where $\chi_0 = \chi_a/\xi_0^2$. The electric field within the cell can be found by direct substitution of the dielectric tensor

$$\epsilon = \epsilon_0 \epsilon_I \delta + \frac{1}{\sqrt{2}}\epsilon_0 \epsilon_A \mathcal{Q}, \tag{26}$$

where ϵ_A and ϵ_I are the anisotropic and isotropic dielectric coefficients respectively, into Maxwell's equation $\nabla \cdot \boldsymbol{D} = 0$ to give

$$\nabla^2 \phi + \alpha \nabla \mathcal{Q} \cdot \nabla \phi = 0, \tag{27}$$

where α is the non-dimensional, non-homogeneous dielectric coefficient and ϕ is the electric potential in the cell. Equations (24), (25) and (27) are solved numerically by first discretising in space and then solving for steady state using Broyden's root finding method. The numerical differentiation is carried out using a spectral collocation method [31] for improved computational efficiency and accuracy.

4 Finite element comparison

The regime independent model has been compared against the existing models for Bragg and Raman-Nath diffraction. We now use comsol multiphysics, a finite element modelling package to solve Maxwell's equations directly and hence verify its accuracy for the intermediate regime.

We define a rectangular geometry with sides parallel to the x- and z-axis. The boundary conditions are periodic in the x-direction with periodicity of the refractive index. The finite element simulations are carried out with an optical wavelength of 1 μm, as shorter wavelengths would require an extremely fine finite element mesh and, hence, considerable computation time.

In order to verify the intermediate regime, we must first define it using the dimensionless parameter q, as suggested by Kogelnik [1], where

$$q = \frac{2\pi\lambda L}{n_u \Lambda^2}, \tag{28}$$

and n_u is the average refractive index. Typically the Bragg regime is defined for $q \geq 10$ and the Raman–Nath regime for $q \leq 0.1$. The intermediate regime lies between these two values.

We first verify that the model behaves correctly for a single grating component K which is constant for all z. To ensure that q lies in the intermediate regime the following parameters are used: $L = 12$ μm, $\Lambda = 11.5$ μm, which give

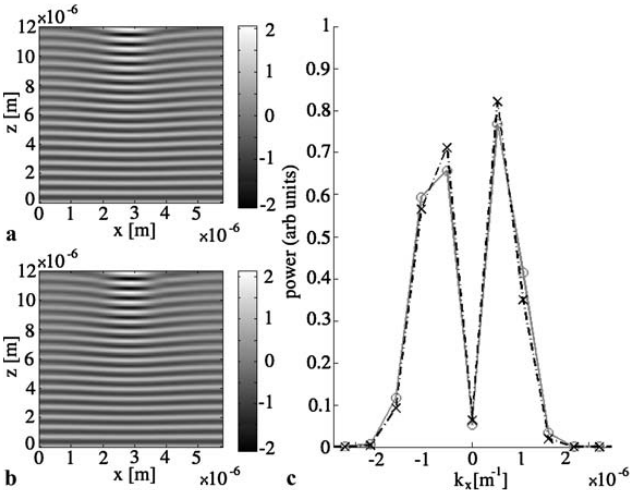

Fig. 3 x-Component of electric field in cell for:
(**a**) coupled-wave model.
(**b**) Finite element simulation.
(**c**) Optical power spectrum at output of cell where '∘' is the coupled-wave approximation and '×' is the finite element simulation

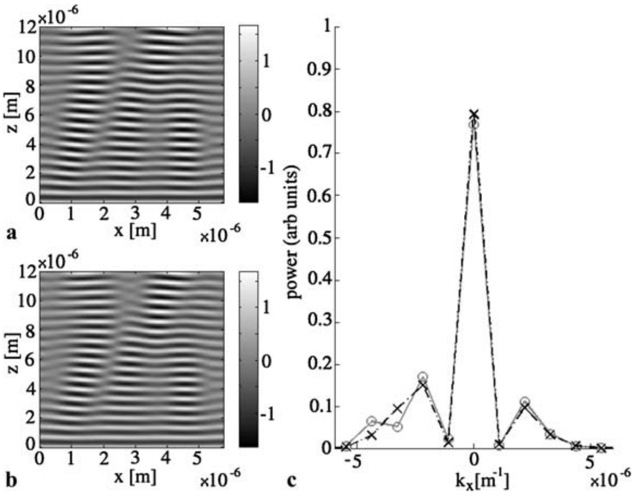

Fig. 4 x-Component of electric field in cell for:
(**a**) coupled-wave model.
(**b**) Finite element simulation.
(**c**) Optical power spectrum at output of cell where '∘' is the coupled-wave approximation and '×' is the finite element simulation

the regime parameter $q = 1.4210$. The incident electric field is normal to the cell boundary $z = 0$. The refractive indices chosen in this system correspond to those of a typical liquid crystal, $n_o = 1.5$ and $n_e = 1.7$ giving the dielectric profile as

$$\epsilon_r = \begin{pmatrix} n_o^2 & 0 \\ 0 & n_e^2 \end{pmatrix} + \begin{pmatrix} -0.1 & 0.05 \\ 0.05 & 0.1 \end{pmatrix} \cos(Kx). \tag{29}$$

Figure 3 compares the field calculated within the cell by the coupled-wave model and the finite element method. From the power spectrum it can be seen that the optical energy has coupled almost completely from the incident beam into its two closest neighbours, with asymmetry observed between the $+1$ and -1 diffracted orders due to the small off-diagonal component of the dielectric tensor interacting with the polarisation asymmetry. The optical power spectrum and field inside the cell show good agreement with the finite element simulation. The difference in the power spectra are less than 10%. This verifies the model's ability to predict the component amplitudes of each wave and hence the electric field within the medium. We now wish to make full use of the model's features, by considering a system with the same fundamental period, but also with second and third harmonics present. Furthermore, to make the system even more realistic with respect to the experimental system we choose some arbitrary profiles for these higher harmonics. Therefore we choose as the non-homogeneous part of the dielectric tensor

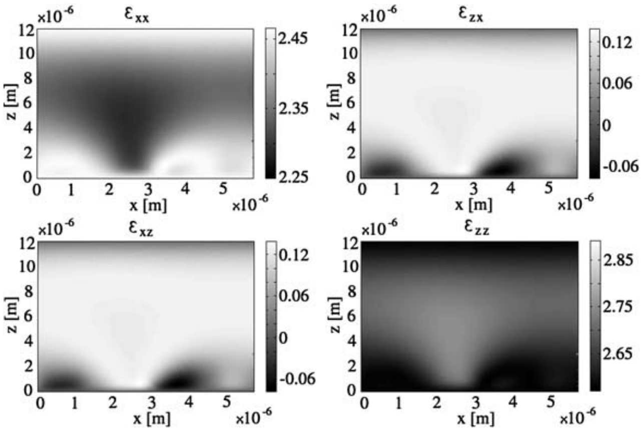

Fig. 5 In plane dielectric profile for the anisotropic liquid crystal. The four images show the different profiles seen by the light depended on its direction of motion

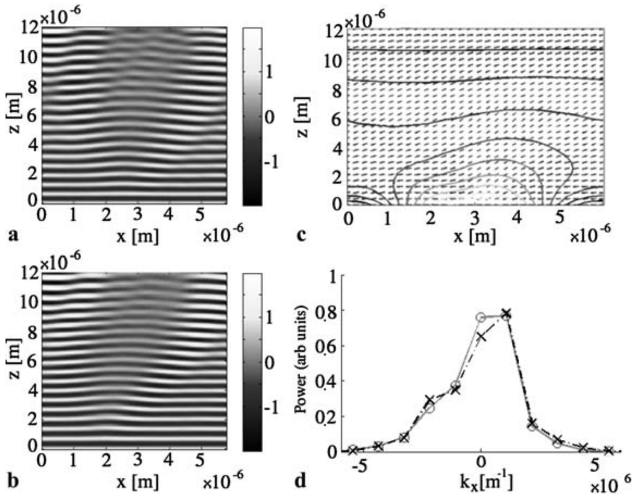

Fig. 6 (**a**) x-Component of electric field in cell for: (**a**) coupled-wave model. (**b**) Finite element simulation. (**c**) Liquid crystal director profile showing molecular orientation and contour lines showing equipotentials. (**d**) Optical power spectrum at output of cell where '∘' is the coupled-wave approximation and '×' is the finite element simulation

$$\begin{aligned}\Delta\epsilon &= \begin{pmatrix} -0.05 & 0.03 \\ 0.03 & 0.05 \end{pmatrix} \cos(\boldsymbol{K}\cdot\boldsymbol{x}) \\ &\quad + \begin{pmatrix} -0.1 & 0.05 \\ 0.05 & 0.1 \end{pmatrix} e^{-\frac{(z-L_z/2)^2}{L_z^2}} \cos(2\boldsymbol{K}\cdot\boldsymbol{x}) \\ &\quad + \begin{pmatrix} -0.05 & 0.1 \\ 0.1 & 0.05 \end{pmatrix} e^{\frac{z}{Lz}} \cos(3\boldsymbol{K}\cdot\boldsymbol{x}). \end{aligned} \tag{30}$$

The field throughout the cell and the comparison with the finite element modelling in this case is shown in Fig. 4. Unlike the previous test case the majority of the energy remains in the incident beam $k_x = 0$ with energy transferring past the nearest neighbours into the second diffracted order beams. Again we see good agreement between the electric fields and the optical power spectrum with error less than one part in ten. This comparison verifies the models ability to handle the higher harmonics and arbitrary spatial profiles of the grating. The only difference between this and the liquid crystal profile is the addition of higher harmonics and the possibility of less smooth spatial profiles. For the liquid crystal test case, we solve (24), (25) and (27) with an applied voltage of the form

$$V_{\mathrm{app}} = V_0 \cos^2\left(\frac{\pi}{\Lambda}x\right). \tag{31}$$

The voltage amplitude $V_0 = 5$ has been chosen to give an interesting dielectric profile containing harmonics of the grating vector and a non-uniform profile in the z-direction (see Fig. 5). The component values a_0 and a_1 are substituted into (10), this is then solved to give the amplitude of the different optical wave vectors. Figure 6 shows the comparison of the electric field in the liquid crystal with the finite element modelling. In this case the energy can be seen to transfer asymmetrically. This is because of the size of the off-diagonal terms in the dielectric tensor in comparison to the diagonal elements.

5 Conclusion

An extension to the anisotropic coupled-wave theory has been derived allowing us to model systems in the Bragg, Raman–Nath and intermediate regimes. Comparison to existing theories has been shown analytically in both Bragg and Raman–Nath regimes. Finite element simulations have confirmed the model validity for all regimes.

The model developed here takes into account all possible coupling combinations between the various optical waves propagating though the medium. This is achieved by considering higher order grating harmonics as well as all possible mismatch terms. The use of an arbitrary grating profile in the z-direction makes the model useful for more complex systems such as the liquid crystal cell. In terms of computation speed the finite element simulation typically takes 1 minute to run, whilst the coupled-wave approach takes <1 second for a non-trivial refractive index profile.

The model shows good agreement with the finite element simulations in all cases tested and will be a useful tool for modelling optical coupling in more complex systems where computational speed and efficiency are required.

References

1. H. Kogelnik, Coupled wave theory for thick hologram gratings. Bell. Syst. Tech. J. **48**, 2909–2947 (1969)
2. G. Montemezzani, M. Zgonik, Light diffraction at mixed phase and absorption gratings in anisotropic media for arbitrary geometries. Phys. Rev. E **55**, 1035–1047 (1997)
3. C.V. Raman, N.S. Nath, The diffraction of light by high frequency sound waves: part I. Proc. Indian Acad. Sci. A **3**, 406–412 (1936)
4. A.V. Galstyan, G.G. Zakharyan, R.S. Hakobyan, The theory of light diffraction in thin anisotropic medium. Mol. Cryst. Liq. Cryst. **453**, 203–213 (2006)
5. T.K. Gaylord, M.G. Moharam, Thin and thick gratings: terminology clarification. Appl. Opt. **20**(19), 3271 (1981)
6. M.G. Moharam, T.K. Gaylord, R. Magnusson, Criteria for Bragg regime diffraction by phase gratings and Criteria for Raman-Nath regime diffraction by phase gratings. Opt. Commun. **32**, 14–23 (1980)
7. M.G. Moharam, T.K. Gaylord, Rigorous coupled-wave analysis of planar-grating diffraction. J. Opt. Soc. Am. **71**(7), 811 (1981)
8. E.N. Glytsis, T.K. Gaylord, Three-dimensional (vector) rigorous coupled-wave analysis of anisotropic grating diffraction. J. Opt. Soc. Am. A **7**(8), 1399 (1990)
9. M. Kaczmarek, R.W. Eason, Conditions for efficient build-up of power in photorefractive ring cavities. Opt. Commun. **154**(5-6), 334–338 (1998)
10. X. Sun, C. Ren, Y. Pei, F. Yao, Electrically controlled dynamic holographic gratings in fullerene C 60-doped nematic liquid crystals. J. Phys. D, Appl. Phys. **41**(24), 245105 (2008)
11. I.C. Khoo, K. Chen, Y.Z. Williams, Orientational photorefractive effect in undoped and CDSE nanorods-doped nematic liquid crystal–bulk and interface contributions. IEEE J. Sel. Top. Quantum Electron. **12**(3), 443–450 (2006)
12. A. Redler, H.S. Kitzerow, Influence of doping on the photorefractive properties of a polymer-dispersed liquid crystal. Appl. Phys. Lett. **93**, 183304 (2008)
13. M. Talarico, A. Golemme, Photorefractive binary system based on ferroelectric liquid crystals. J. Phys. Chem. C **111**(21), 7834–7840 (2007)
14. T.M. Fears, C. Anderson, J.G. Winiarz, Photorefractivity in a polymeric composite photosensitized with NiS nanocrystals. J. Chem. Phys. **129**, 154704 (2008)
15. G. Cook, A.V. Glushchenko, V. Reshetnyak, A.T. Griffith, M.A. Saleh, D.R. Evans, Nanoparticle doped organic-inorganic hybrid photorefractives. Opt. Express **16**(6), 4015–4022 (2008)
16. O. Buchnev, A. Dyadyusha, M. Kaczmarek, V. Reshetnyak, Y. Reznikov, Enhanced two-beam coupling in colloids of ferroelectric nanoparticles in liquid crystals. J. Opt. Soc. Am. B **24**(7), 1512–1516 (2007)
17. U. Bortolozzo, S. Residori, J.P. Huignard, Beam coupling in photorefractive liquid crystal light valves. J. Phys., Appl. Phys. **41**, 224007 (2008)
18. A. Miniewicz, Photorefractive-like all-optical switching in nematic-photoconducting polymer liquid crystal cell. Mol. Cryst. Liq. Cryst. **489**(1), 119–134 (2008)
19. F. Yao, Y. Pei, Y. Zhang, J. Zhang, C. Hou, X. Sun, High-resolution photorefractive gratings in nematic liquid crystals sandwiched with photoconductive polymer film. Appl. Phys. B **92**(4), 573–576 (2008)
20. D. Jiang, L. Ding, J. Huang, E. Gu, L. Liu, Z. Chai, D. Liu, Synthesis and characterization of photorefractive polymer based on chemically hybridized cds–pvk nanocomposite with a new azo chromophore. Polymer **48**(24), 7156–7162 (2007)
21. D.J. Binks, S.P. Bant, D.P. West, P. O'brien, M.A. Malik, CdSe/CdS core/shell quantum dots as sensitizer of a photorefractive polymer composite. J. Mod. Opt. **50**(2), 299–310 (2003)
22. D.R. Evans, G. Cook, Bragg-matched photorefractive two-beam coupling in organic-inorganic hybrids. J. Nonlinear Opt. Phys. Mater. **16**(03), 271–280 (2007)
23. S. Bartkiewicz, K. Matczyszyn, A. Miniewicz, F. Kajzar, High gain of light in photoconducting polymer-nematic liquid crystal hybrid structures. Opt. Commun. **187**, 257–261 (2001)
24. G. Cook, A.V. Glushchenko, V.Y. Reshetnyak, E.R. Beckel, M.A. Saleh, D.R. Evans, Liquid crystal inorganic hybrid photorefractives, in *Winter Topical Meeting Series, IEEE/LEOS 2008*, pp. 129–130 (2008)
25. M. Born, E. Wolf, *Principles of Optics. Electromagnetic Theory of Propagation Interference and Diffraction of Light*, 6th edn. (Cambridge University Press, Cambridge, 1980)
26. P.G. deGennes, J. Prost, *The Physics of Liquid Crystals*, 2nd edn. Oxford Science Publications (Clarendon, Oxford, 1993)
27. A. Sonnet, A. Kilian, S. Hess, Alignment tensor versus director: Description of defects in nematic liquid crystals. Phys. Rev. E **52**(1), 718–722 (1995)
28. R. James, E. Willman, F. Anibal-Fernandez, S.E. Day, Finite element modeling of liquid crystal hydrodynamics with a variable degree of order. IEEE Trans. Electron Dev. **53**, 15751582 (2006)
29. G. Vijaya Prakash, M. Kaczmarek, A. Dyadyusha, J.J. Baumberg, G. D'Alessandro, Control of topological defects in microstructured liquid crystal cells. Opt. Express **13**, 2201 (2005)
30. H. Mori, E. Gartland Jr., J. Kelly, P. Bos, Multidimensional director modeling using the Q tensor representation in a liquid crystal cell and its application to the π cell with patterned electrodes. Jpn. J. Appl. Phys. **38**, 135 (1999)
31. L.N. Trefethen, *Spectral Methods in MATLAB* (SIAM, Philadelphia, 2000)

SIAM J. APPL. MATH.
Vol. 70, No. 8, pp. 2844–2860

AN EFFICIENT $\mathcal{Q}$-TENSOR-BASED ALGORITHM FOR LIQUID CRYSTAL ALIGNMENT AWAY FROM DEFECTS[*]

K. R. DALY[†], G. D'ALESSANDRO[†], AND M. KACZMAREK[‡]

Abstract. We develop a fast and accurate approximation of the normally stiff equations which minimize the Landau–de Gennes free energy of a nematic liquid crystal. The resulting equations are suitable for all configurations in which defects are not present, making them ideal for device simulation. Specifically they offer an increase in computational efficiency by a factor of 100 while maintaining an error of order (10^{-4}) when compared to the full stiff equations. As this approximation is based on a $\mathcal{Q}$-tensor formalism, the sign reversal symmetry of the liquid crystal is respected. In this paper we derive these equations for a simple two-dimensional case, where the director is restricted to a plane, and also for the full three-dimensional case. An approximation of the error in the perturbation scheme is derived in terms of the first order correction, and a comparison to the full stiff equations is given.

Key words. $\mathcal{Q}$-tensor, nematic liquid crystals, alignment, approximation methods, numerical methods

AMS subject classifications. 35Q99, 35B38, 82D30, 58Z05

DOI. 10.1137/100796467

1. Introduction.

The modeling and simulation of liquid crystals for device purposes is an active area of research with a wide variety of applications [1, 14]. In most applications macroscopic continuum models are used to determine liquid crystal alignment under the influence of an applied electric or magnetic field. There are two main approaches to continuum modeling. The Frank–Oseen (FO) model [8, 20] describes the liquid crystal in terms of a unit vector $\hat{\boldsymbol{n}}$, also referred to as the director. This model is computationally very efficient. However, although the vector representation of the liquid crystal may be considered quite intuitive, it is physically incorrect as it does not respect the inversion symmetry of the liquid crystal; i.e., $\hat{\boldsymbol{n}}$ and $-\hat{\boldsymbol{n}}$ represent the same state of the liquid crystal. This limits the application of the FO model to geometries in which the liquid crystal orientation angle is bounded between 0 and $\pi/2$. Further, the microscopic order of the nematic phase, which depends on temperature, is not considered. This makes the model unsuitable for geometries in which defects, nonsmooth variations in $\hat{\boldsymbol{n}}$, can occur.

To overcome these problems an approach was developed by de Gennes in which the liquid crystal alignment is represented by a tensor, $\mathcal{Q}$, which is proportional to $\hat{\boldsymbol{n}}\otimes\hat{\boldsymbol{n}}$ [7]. This tensor is invariant with respect to the transformation $\hat{\boldsymbol{n}} \to -\hat{\boldsymbol{n}}$. Further, this theory takes into account the orientational order of the liquid crystal through the temperature-dependent bulk energy, sometimes referred to as the thermotropic energy, and can therefore be used to describe situations in which sharp variations in the liquid crystal alignment—otherwise known as defects—occur. The main disadvantage of this method is that, due to the difference in time scales between the thermotropic

---

[*] Received by the editors May 25, 2010; accepted for publication June 28, 2010; published electronically September 16, 2010.
http://www.siam.org/journals/siap/70-8/79646.html

[†] School of Mathematics, University of Southampton, Southampton SO17 1BJ, UK (krd103@soton.ac.uk, dales@soton.ac.uk).

[‡] School of Physics, University of Southampton, Southampton SO17 1BJ, UK (M.Kaczmarek@soton.ac.uk).

and elastic properties of the liquid crystals, the final equations are numerically stiff, making computation expensive.

Often the advantages of using a $\mathcal{Q}$-tensor model outweigh the disadvantage of increased computation time. However, there are devices, such as photorefractive cells [6] or spatial light modulators [19], in which the FO model is inappropriate as the liquid crystals may rotate in an unbounded way. However, as there are no defects in these cells, the Landau–de Gennes $\mathcal{Q}$-tensor model is unnecessarily expensive to compute.

Numerical methods to overcome the stiffness of the full $\mathcal{Q}$-tensor equations include the scaling of the elastic and electrostatic coefficients [25] and the renormalization of the liquid crystal director after each time step [11]. Codes also exist which solve the full stiff equations. These are usually based around finite element simulations with adaptive meshing techniques to eliminate the need for dense grids away from defects [12, 27].

Although the separation in scales makes the $\mathcal{Q}$-tensor equations computationally expensive, the small parameters involved can be used to our advantage. Here we use a multiple scales expansion technique to separate the two timescales. On the timescale of interest, i.e., the slow reorientation time of the liquid crystal, the fast timescale equations, which determine the order parameter, can be considered as having reached equilibrium. The resulting equations for the slow timescale are nonstiff and can be solved in a fraction of the time of the full equations. This approximation reduces the computation time by a factor of approximately one hundred and is suitable for any geometry in which the variation in the scalar order parameter may be assumed to be small.

The paper is arranged as follows: In section 2 we introduce the equations governing the free energy of the liquid crystal and make an analogy between our approximation method and the Signorini method originally developed in elasticity [2, 10, 21]. In section 3, to illustrate the method, we derive a simplified two-dimensional model for the case where liquid crystal alignment is restricted to a plane. Equations for alignment are given and an estimate of the accuracy of the method is derived. In section 4 we apply the ideas and methods used in the two-dimensional case to derive equations for the three-dimensional case. A method to approximate the error is also given. Finally section 5 details comparison with the FO and $\mathcal{Q}$-tensor models that show that the approximation we derive is both fast and accurate.

2. Free energy.

We consider the dimensional liquid crystal free energy of the form $\tilde{\mathcal{F}} = \tilde{\mathcal{F}}_e(\tilde{\mathcal{Q}}) + \tilde{\mathcal{F}}_d(\tilde{\mathcal{Q}}) + \tilde{\mathcal{F}}_t(\tilde{\mathcal{Q}})$, where $\tilde{\mathcal{F}}_e$, $\tilde{\mathcal{F}}_d$, and $\tilde{\mathcal{F}}_t$ are, respectively, the electrostatic, elastic, and bulk free energies. The general form of the biaxial liquid crystal alignment tensor, $\tilde{\mathcal{Q}}$, written in terms of the orthogonal unit directors $\hat{\boldsymbol{n}}$ and $\hat{\boldsymbol{m}}$, which define the major and minor crystal axes, respectively, is

$$\tilde{\mathcal{Q}} = \sqrt{\frac{3}{2}}\tilde{S}\left(\overline{\hat{\boldsymbol{n}} \otimes \hat{\boldsymbol{n}}}\right) + \sqrt{\frac{3}{2}}\tilde{\beta}\left(\overline{\hat{\boldsymbol{m}} \otimes \hat{\boldsymbol{m}}}\right), \tag{2.1}$$

where $\tilde{S}$ is the scalar order parameter, $\tilde{\beta}$ is the biaxiality parameter, I is the identity matrix, and $\overline{\hat{\boldsymbol{n}} \otimes \hat{\boldsymbol{n}}} = (\hat{\boldsymbol{n}} \otimes \hat{\boldsymbol{n}} - 1/3I)$ denotes a traceless symmetric tensor. The total free energy may be obtained by integrating over the cell volume. In the absence of external forces, such as electromagnetic fields or boundaries, this free energy reduces to just the elastic and thermotropic free energies which are $SO(3)$ invariant. Much work has been done to obtain comprehensive expressions for the thermotropic and elastic free energies. Details, including a full derivation of all possible $SO(3)$ invariants up to powers of $\tilde{\mathcal{Q}}^4$, can be found in [13, 15, 16].

Throughout the remainder of this paper we shall assume the simplest possible expressions for these free energies. It should be noted, however, that this restriction is not a necessary condition for this method to work; rather it is a simplification used to clarify the derivation.

The elastic free energy in its simplest form is derived using the one elastic constant approximation. This can be written as

$$\tilde{\mathcal{F}}_d = \frac{L}{2}\left|\boldsymbol{\nabla}\tilde{\mathcal{Q}}\right|^2, \tag{2.2}$$

where L is defined as $L = K/(3\tilde{S}^2)$ and K is the liquid crystal elastic constant. The electrostatic free energy of the liquid crystal takes the form

$$\tilde{\mathcal{F}}_e = -\frac{1}{3}\epsilon_0\Delta\epsilon\mathrm{Tr}\left(\tilde{\mathcal{Q}}\tilde{\mathcal{E}}\right), \tag{2.3}$$

where

$$\tilde{\mathcal{E}} = \sqrt{\frac{3}{2}}\,\overline{\tilde{\boldsymbol{E}}\otimes\tilde{\boldsymbol{E}}}, \tag{2.4}$$

ϵ_0 is the permittivity of free space, $\Delta\epsilon$ is the anisotropic relative permittivity, and the electric field is denoted $\tilde{\boldsymbol{E}} = -\boldsymbol{\nabla}\tilde{\psi}$, where $\tilde{\psi}$ is the electric potential. The effect of temperature on the liquid crystal alignment is described by the bulk free energy, written in terms of a Landau power series expansion of $\tilde{\mathcal{Q}}$ [7] with $SO(3)$ invariance,

$$\tilde{\mathcal{F}}_t = \frac{1}{2}A(T-T^*)\mathrm{Tr}\left(\tilde{\mathcal{Q}}^2\right) - \sqrt{6}B\mathrm{Tr}\left(\tilde{\mathcal{Q}}^3\right) + \frac{1}{2}C\mathrm{Tr}^2\left(\tilde{\mathcal{Q}}^2\right), \tag{2.5}$$

where A, B, and C are the bulk thermotropic coefficients which are assumed to be independent of temperature. The temperature dependence of this energy is described entirely by $T - T^*$, where T^* is the pseudocritical temperature at which the isotropic phase becomes unstable.

To ensure the traceless symmetric properties of our $\tilde{\mathcal{Q}}$ and $\tilde{\mathcal{E}}$ are respected, we express the free energy on the basis of traceless symmetric tensors [22],

$$\tilde{\mathcal{Q}} = \sum_{p=1}^{5}\tilde{a}_p T^{(p)} \quad \text{and} \quad \tilde{\mathcal{E}} = \sum_{p=1}^{5}\tilde{e}_p T^{(p)},$$

where

$$\begin{aligned} T^{(1)} &= \frac{1}{\sqrt{6}}\left(-\boldsymbol{e}_x\otimes\boldsymbol{e}_x - \boldsymbol{e}_y\otimes\boldsymbol{e}_y + 2\boldsymbol{e}_z\otimes\boldsymbol{e}_z\right),\\ T^{(2)} &= \frac{1}{\sqrt{2}}\left(\boldsymbol{e}_x\otimes\boldsymbol{e}_x - \boldsymbol{e}_y\otimes\boldsymbol{e}_y\right), \quad T^{(3)} = \frac{1}{\sqrt{2}}\left(\boldsymbol{e}_x\otimes\boldsymbol{e}_y + \boldsymbol{e}_y\otimes\boldsymbol{e}_x\right),\\ T^{(4)} &= \frac{1}{\sqrt{2}}\left(\boldsymbol{e}_x\otimes\boldsymbol{e}_z + \boldsymbol{e}_z\otimes\boldsymbol{e}_x\right), \quad T^{(5)} = \frac{1}{\sqrt{2}}\left(\boldsymbol{e}_y\otimes\boldsymbol{e}_z + \boldsymbol{e}_z\otimes\boldsymbol{e}_y\right). \end{aligned} \tag{2.6}$$

We rescale the order parameter $S = \frac{3C}{2B}\tilde{S}$, the biaxiality parameter $\beta = \frac{3C}{2B}\tilde{\beta}$, the tensor field $\mathcal{Q} = \frac{3C}{2B}\tilde{\mathcal{Q}}$, and the component fields $a_p = \frac{3C}{2B}\tilde{a}_p$ and $e_p = \tilde{e}_p/\psi_0^2$, where ψ_0 is a typical potential, $\psi = \tilde{\psi}/\psi_0$. For compactness of notation, from now on we adopt the convention of summing over repeated indices, unless stated otherwise.

We also indicate with $\boldsymbol{a}$ and $\boldsymbol{e}$ the vectors with components a_p and e_p. Finally we nondimensionalize to obtain the scaled free energy,

$$\mathcal{F} = \frac{\xi_0^2}{2}|\boldsymbol{\nabla a}|^2 - \chi_a \boldsymbol{a} \cdot \boldsymbol{e} + \frac{T_0}{2}|\boldsymbol{a}|^2 + \frac{1}{2}|\boldsymbol{a}|^4 - \sqrt{6}\sum_{p,q,r} \mathrm{Tr}\left(T^{(p)}T^{(q)}T^{(r)}\right) a_p a_q a_r. \tag{2.7}$$

The nondimensional elastic constant ξ_0^2, the electrostatic coefficient χ_a, and the scaled temperature T_0 are

$$\xi_0^2 = \frac{9C}{2B^2}\frac{L}{L_x^2}, \quad \chi_a = \frac{9\epsilon_0 \Delta\epsilon C^2}{2L_x^2 B^3}\psi_0^2, \quad T_0 = \frac{T - T^*}{T_c - T^*},$$

where T_c is the clearing point temperature and L_x is the characteristic length of the geometry studied. We have rescaled space so that $(\hat{x}, \hat{z}) = (x, z)/L_x$. Typically $T_0 \sim O(1)$, while $\xi_0^2 \sim O(10^{-7})$ and $\chi_a \sim O(10^{-6})$.

The separation in scales between the various terms in the free energy cause the Euler–Lagrange equations, which minimize (2.7), to be stiff. As a result the computing times required for even relatively simple geometries become very large. In situations where the elastic and electrostatic free energies remain small we can initially consider only the critical points of the bulk free energy. The elastic and electrostatic free energies can then be considered as a perturbation. It is this assumption that makes this method inappropriate for defect modeling.

2.1. Critical points under slightly broken symmetry. Before we consider the case of the liquid crystal it is useful to consider a general free energy of the type given in (2.7). The free energy $\mathcal{F}(\boldsymbol{a})$ consists of a symmetric bulk free energy perturbed by a small symmetry breaking contribution from the elastic and electrostatic energies. We denote these terms $\mathcal{F}_t(\boldsymbol{a})$ and $\mathcal{L}(\boldsymbol{a})$, respectively, where $\mathcal{L}(\boldsymbol{a})\ \mathcal{F}_t(\boldsymbol{a}) \in \mathbb{R}^5$ in the three-dimensional case and $\mathcal{L}(\boldsymbol{a})\ \mathcal{F}_t(\boldsymbol{a}) \in \mathbb{R}^2$ in the two-dimensional case. For simplicity we consider here the case that $\mathcal{L}(\boldsymbol{a})$ has only the electrostatic energy component, so that the liquid crystal state is described by a single five-dimensional vector $\boldsymbol{a}$, rather than a five-component vector field $\boldsymbol{a}(\boldsymbol{x})$. This allows us to describe the perturbation scheme in very general terms as the effect of a symmetry-breaking perturbation on an invariant manifold of solutions of a set of ordinary differential equations. In the more general case where the elastic energy is also considered we would have to deal with partial differential equations for vector fields; however, we expect that the main ideas outlined here would remain valid.

As the bulk energy is $SO(3)$ invariant the critical points of $\mathcal{F}_t(\boldsymbol{a})$ will form an orbit of solutions in the five-dimensional component space. Specifically, for the general case corresponding to a biaxial minimizer, the group orbit will be a 3-manifold, while in the special case corresponding to uniaxial minimizers the orbit reduces to a 2-manifold.

The effect of the first order perturbation $\mathcal{L}(\boldsymbol{a})$ is to break the symmetry and to collapse the invariant manifold of critical points to a smaller set near the manifold. This setting is very similar to the Signorini perturbation scheme, originally derived in the context of elastostatics [2, 10, 21, 26], but of wider potential application [3]. This scheme determines the equilibrium configuration of an elastic body under the effect of applied stresses using a perturbation expansion in powers of the applied stress. In the context of liquid crystals, the role of the "applied stresses" is played by the (small) elastic and electrostatic forces, and our approximation is the first step of a standard Signorini expansion.

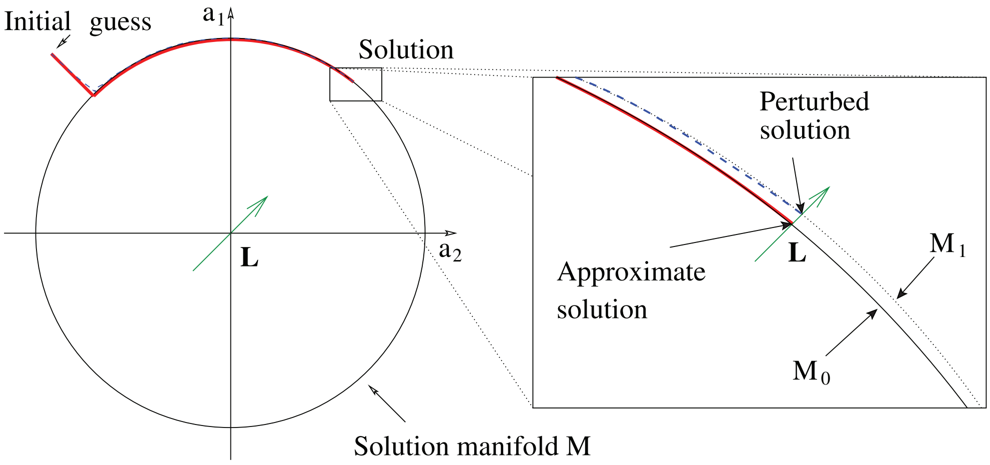

FIG. 1. *Graphical representation of the Signorini perturbation scheme. For some initial point in the phase space* (a_1, a_2) *there is rapid convergence at a rate* τ_0 *to the solution manifold. Motion along the manifold, driven by the flow* $\boldsymbol{L}$*, occurs much more slowly at a rate* τ_1*. The critical point on* M_0 *is found when* $\boldsymbol{L}$ *is orthogonal to* $T_{\boldsymbol{a}}$*. As* M_0 *is close to* M_1 *the solution can be approximated by the point on* M_0 *whose surface normal intersects* M_1 *close to the perturbed solution.*

We consider an orbit M_0 consisting of the critical points of the bulk energy $\mathcal{F}_t(\boldsymbol{a})$ with tangent space $T_{\boldsymbol{a}}M_0$ at $\boldsymbol{a} \in M_0$. As M_0 consists entirely of critical points, then $T_{\boldsymbol{a}}M_0 \subset \ker(\mathcal{H})$, where $\mathcal{H}$ is the Hessian of the bulk free energy. If the critical points of the bulk free energy are nondegenerate in the direction normal to the manifold, then the tangent space coincides with the kernel, $T_{\boldsymbol{a}}M_0 = \ker(\mathcal{H})$. Therefore, M_0 is a normally hyperbolic invariant manifold for the flow, $-\boldsymbol{\nabla}_{\boldsymbol{a}}\mathcal{F}_t(\boldsymbol{a})$, where $\boldsymbol{\nabla}_{\boldsymbol{a}}$ denotes differentiation with respect to the components of the vector $\boldsymbol{a}$.

The effects of the perturbative terms can be understood by the invariant manifold theory. If the perturbed flow, $-\boldsymbol{\nabla}_{\boldsymbol{a}}(\mathcal{F}_t + \mathcal{L})$, and its first derivative are sufficiently close to the unperturbed flow, then there exists a smooth invariant manifold M_1 close to M_0. The behavior of the perturbed flow along M_1 will be comparable to the flow restricted to M_0 [26]. Specifically, a point p_0 on M_0 will correspond to a point p_1 on M_1, where p_1 is the intersection of the normal to M_0 at p_0 and M_1. If all nonzero eigenvalues of $\mathcal{H}$ are positive, then the dynamical behavior of the flow close to the manifold will consist of exponential attraction towards the manifold followed by a slow drift along it [9].

As the perturbation $-\boldsymbol{\nabla}_{\boldsymbol{a}}\left(\mathcal{F}_t + \mathcal{L}\right)$ is also a gradient vector field, then the local minima on M_1 will be attracting stationary points. For nondegenerate critical points these are in $1:1$ correspondence with the local minima of the perturbed function restricted to the unperturbed manifold M_0. The critical points restricted to M_0 are found when the flow $\boldsymbol{L} = -\boldsymbol{\nabla}_{\boldsymbol{a}}\mathcal{L}$ is orthogonal to $T_{\boldsymbol{a}}$. This is represented graphically for the simplified two-dimensional case in Figure 1.

In the simple two-dimensional case considered in section 3 the symmetry group is $SO(2)$ under the action of rotation on $\mathbb{R}^2$. In this case there will be two critical points on the perturbed manifold. These correspond to an unstable maximum and a stable minimum.

In the three-dimensional case (see section 4), the situation is more complicated. The bulk energy minimizers form an orbit of the conjugacy action of $SO(3)$ on the five-dimensional space of traceless symmetric matrices (see section 4.2). This orbit is parametrized locally by the direction of the major axis of the liquid crystal molecule (two dimensions) together with a circle corresponding to the orientation of the minor axis. For uniaxial minimizers of the bulk free energy, these circles of critical points shrink to radius 0. The result is that liquid crystal orientation can be determined only in terms of the major axis. To determine the orientation of the minor axis in cases where the perturbation induces biaxiality, a further step in the expansion is required.

3. Two-dimensional case. As an example to illustrate the approximation method it is helpful to look at a simplified two-dimensional case where the liquid crystal director is restricted to the x, z plane. The alignment tensor is a 2×2 uniaxial tensor,

$$\mathcal{Q}_{ij} = \sqrt{2}S\left(\hat{n}_i\hat{n}_j - \frac{1}{2}\delta_{ij}\right). \tag{3.1}$$

We can proceed exactly as in section 2 with the simplified basis set of 2×2 traceless symmetric tensors:

$$T_1 = \tfrac{1}{\sqrt{2}}\begin{pmatrix} -1 & 0 \\ 0 & 1 \end{pmatrix}, \qquad T_2 = \tfrac{1}{\sqrt{2}}\begin{pmatrix} 0 & 1 \\ 1 & 0 \end{pmatrix}. \tag{3.2}$$

Hence

$$\mathcal{Q} = \sum_{p=1}^{2} a_p T^{(p)}.$$

In this notation the scalar order parameter is $S^2 = \mathrm{Tr}(\mathcal{Q}^2) = a_1^2 + a_2^2$. The Euler–Lagrange equations of motion, derived using the simplest form of the free energy, are

$$\partial_\tau a_n = \xi_0^2\nabla^2 a_n - T_0 a_n - 2a_n\left(a_1^2 + a_2^2\right) + \chi_a e_n, \tag{3.3}$$

where $n = 1, 2$, $\tau = t/\tau_d$, $\tau_d = \left[9C/(2B^2)\right]\zeta$, and the viscosity, ζ, is related to Leslie's rotational viscosity γ_1 by $\zeta = \gamma_1/(3\tilde{S}^2)$.

3.1. Invariant manifold. Due to the smallness of ξ_0^2 and χ_a, equation (3.3) can be seen to have two different timescales. Taking $\eta = \xi_0^2$ as the small parameter, we can write the time derivatives in (3.3) as $\partial_\tau = \partial_{\tau,0} + \eta\partial_{\tau,1}$. Substituting into (3.3) gives

$$\partial_{\tau_0} a_n + \eta\partial_{\tau_1} a_n = \eta\nabla^2 a_n - T_0 a_n - 2a_n\left(a_1^2 + a_2^2\right) + \eta\chi_0 e_n, \tag{3.4}$$

where $\chi_0 = \chi_a/\xi_0^2$ is $O(1)$. Observing that only the bulk free energy changes on the fast timescale, we assume that this scale determines only the scalar order parameter. As we are interested only in the slow timescale, i.e., the timescale over which the liquid crystal aligns, we can make the assumption that the fast timescale behavior has reached equilibrium, i.e., $\partial_{\tau_0} = 0$. The slow scale behavior, which is present due to the small elastic and electrostatic terms, will be obtained from the first order correction.

To proceed the component representation of the liquid crystal is rewritten as a power series expansion in η:

$$a_n = a_{n,0} + \eta a_{n,1} + O(\eta^2), \tag{3.5}$$

where $a_{n,j}$ is the nth component of jth order. Substituting into (3.4) and retaining terms only to $O(\eta^0)$ allows us to write

$$\left[T_0 + 2\left(a_{1,0}^2 + a_{2,0}^2\right)\right] a_n = 0, \tag{3.6}$$

which is satisfied if $\left(a_{1,0}^2 + a_{2,0}^2\right) = -T_0/2$. As $S^2 = a_1^2 + a_2^2$, equation (3.6) defines the leading order approximation to the scalar order parameter,

$$S_0^2 = -T_0/2. \tag{3.7}$$

This equation can also be derived by minimizing the corresponding Landau–de Gennes free energy in terms of the scalar order parameter. As described in section 2.1, (3.7) defines a manifold of critical points in the component space $(a_{1,0}, a_{2,0})$. For uniaxial liquid crystals the critical points of the free energy are nondegenerate as $T_0 < 0$. We consider the effects of the elastic and electrostatic free energies as a symmetry-breaking perturbation. In the context of the Signorini expansion this defines the flow along the manifold with, in this case, a single unique minimum, found using the first step of the Signorini expansion.

3.2. Kernel of adjoint (tangent space).

This minimum, and hence the liquid crystal alignment, can be found from the first order expansion of (3.3). Retaining terms to $O(\eta)$ and using (3.6) we obtain

$$4\begin{pmatrix} a_{1,0}^2 & a_{1,0}a_{2,0} \\ a_{1,0}a_{2,0} & a_{2,0}^2 \end{pmatrix}\begin{pmatrix} a_{1,1} \\ a_{2,1} \end{pmatrix} = \begin{pmatrix} \nabla^2 a_{1,0} + \chi_0 e_1 - \partial_{\tau_1} a_{1,0} \\ \nabla^2 a_{2,0} + \chi_0 e_2 - \partial_{\tau_1} a_{2,0} \end{pmatrix}. \tag{3.8}$$

This is a system of linear equations for $a_{n,1}$ that can be written as $\mathcal{H}\boldsymbol{a}_1 = \boldsymbol{L}$. Recall that $\mathcal{H}$ is the Hessian of the bulk free energy. However, in this case this equation has no unique solution as $\det(\mathcal{H}) = 0$. The Hessian is a symmetric real valued function, and therefore $\mathcal{H}^\dagger = \mathcal{H}$, where $\mathcal{H}^\dagger$ denotes the adjoint of $\mathcal{H}$. Therefore, as stated in section 2.1, for a nontrivial solution to exist, $\boldsymbol{L} \cdot \ker(\mathcal{H}) = 0$. As this is a two-dimensional system, the kernel of $\mathcal{H}$ is a single vector $\boldsymbol{V}$. This gives us the solvability condition $\boldsymbol{L} \cdot \boldsymbol{V} = 0$, where $\boldsymbol{V} = (-a_{2,0}, a_{1,0})^T$ is the eigenvector of zero eigenvalue of $\mathcal{H}$.

Using the solvability condition, $\boldsymbol{L} \cdot \boldsymbol{V} = 0$, we obtain the following equation for $a_{1,0}$ and $a_{2,0}$:

$$a_{1,0}\partial_{\tau_1} a_{2,0} - a_{2,0}\partial_{\tau_1} a_{1,0} = a_{1,0}\nabla^2 a_{2,0} - a_{2,0}\nabla^2 a_{1,0} + a_{1,0}\chi_0 e_2 - a_{2,0}\chi_0 e_1. \tag{3.9}$$

Equation (3.9) can be solved simultaneously with (3.6) to determine the liquid crystal dynamics on the solution manifold.

3.3. Parameterization of the solution.

By correctly parameterizing the components $a_{1,0}$ and $a_{2,0}$ we can force the director onto the solution manifold, removing the need to solve the leading order equation. As the leading order solution manifold is $SO(2)$ invariant, we parameterize the solutions in terms of the polar angle $\vartheta \in [0, 2\pi]$. If we write

$$a_{1,0} = S_0 \sin\vartheta \quad \text{and} \quad a_{2,0} = S_0 \cos\vartheta,$$

then (3.7) is automatically satisfied. This representation can be used in (3.9) to determine the time evolution of $a_{n,0}$:

$$S_0^2 \frac{\partial a_{n,0}}{\partial \tau_1} = V_n \left(a_{1,0}\nabla^2 a_{2,0} - a_{2,0}\nabla^2 a_{1,0} + a_{1,0}\chi_0 e_2 - a_{2,0}\chi_0 e_1\right), \tag{3.10}$$

where V_n is the nth component of $\boldsymbol{V}$. This equation confirms that the motion of the director field is in the direction tangent to the manifold.

Equation (3.10) is an initial value problem for $a_{n,0}$ which can be solved using standard numerical techniques for an initial set of $a_{n,0}$ on the manifold. It is important to note that we need never calculate ϑ, as (3.10) is solved purely in terms of the component representation, $a_{n,0}$. This ensures that the singularities expected in a director model are overcome. It is possible to solve (3.10) for either $n = 1$ or $n = 2$ and calculate $a_{2,0}$ or $a_{1,0}$, respectively, from (3.7). However, this method is not recommended, as computing the square root in (3.7) will introduce a sign ambiguity. The extra computation required to correct this is inefficient and could potentially make the code unstable.

3.4. Order one accuracy check. To determine the accuracy of the expansion, we consider the perturbed manifold M_1. The equations derived above are suitable only in the case where M_1 is sufficiently close to M_0.

Physically the minimum distance between the leading order solution and M_1 represents the correction S_1 to the scalar order parameter, $S = S_0 + \eta S_1 + O(\eta^2)$. In general this can be calculated from the singular value decomposition of the $O(\eta)$ equation (3.8). However, in two dimensions the correction can be calculated analytically. After a little algebra we obtain

$$S_1 = \frac{1}{\sqrt{-2T_0^3}} \left[\boldsymbol{a}_0 \cdot \nabla^2 \boldsymbol{a}_0 + \chi_0 \boldsymbol{a}_0 \cdot \boldsymbol{e}\right]. \tag{3.11}$$

The magnitude of S_1 can be used to determine the validity of the perturbation expansion. If ηS_1 becomes comparable with S_0, then the expansion breaks down and the liquid crystal has large variation in order parameter. If this happens, then the full stiff equations (3.3) must be solved.

4. Three-dimensional case.

The three-dimensional Euler–Lagrange equations are computed in a similar way to the two-dimensional case:

(4.1a)

$$\eta \frac{\partial a_1}{\partial \tau_1} = \eta \left(\nabla^2 a_1 + \chi_0 e_1\right) - T_0 a_1 + 3\left(a_1^2 - a_2^2 - a_3^2\right) + \frac{3}{2}\left(a_4^2 + a_5^2\right) - 2a_1 \sum_{k=1}^{5} a_k^2,$$

(4.1b)

$$\eta \frac{\partial a_2}{\partial \tau_1} = \eta \left(\nabla^2 a_2 + \chi_0 e_2\right) - T_0 a_2 - 6a_1 a_2 + \frac{3\sqrt{3}}{2}\left(a_4^2 - a_5^2\right) - 2a_2 \sum_{k=1}^{5} a_k^2,$$

(4.1c)

$$\eta \frac{\partial a_3}{\partial \tau_1} = \eta \left(\nabla^2 a_3 + \chi_0 e_3\right) - T_0 a_3 - 3\left(2a_1 a_3 - \sqrt{3} a_4 a_5\right) - 2a_3 \sum_{k=1}^{5} a_k^2,$$

(4.1d)

$$\eta \frac{\partial a_4}{\partial \tau_1} = \eta \left(\nabla^2 a_4 + \chi_0 e_4\right) - T_0 a_4 + 3a_1 a_4 + 3\sqrt{3}\left(a_2 a_4 + a_3 a_5\right) - 2a_4 \sum_{k=1}^{5} a_k^2,$$

(4.1e)

$$\eta \frac{\partial a_5}{\partial \tau_1} = \eta \left(\nabla^2 a_5 + \chi_0 e_5\right) - T_0 a_5 + 3a_1 a_5 + 3\sqrt{3}\left(a_3 a_4 - a_2 a_5\right) - 2a_5 \sum_{k=1}^{5} a_k^2,$$

where, as in the two-dimensional case, $\eta = \xi_0^2$ and $\chi_0 = \chi_a/\xi_0^2$. The fast time derivatives have been neglected as, on the timescale of interest, these variations will have reached equilibrium. At this point, for compactness of notation, it is useful to define the first order perturbation L_m in terms of the elastic and electrostatic contributions,

$$L_m = \nabla^2 a_{m,0} + \chi e_m - \frac{\partial a_{m,0}}{\partial \tau_1}, \tag{4.2}$$

where $m = 1, \ldots, 5$.

4.1. Invariant manifold. In the two-dimensional case the leading order equations are those which minimize the free energy in terms of the scalar order parameter. This minimization fixes the liquid crystal director onto the solution manifold in the two-dimensional space (a_1, a_2). A similar method can be used in the three-dimensional case using the biaxial $\mathcal{Q}$-tensor representation (2.1). It can be shown that the stationary points of the leading order free energy function, of the form given in (2.5), are either uniaxial or isotropic [17]. As such the biaxiality parameter β must vanish at leading order. Minimizing the free energy in terms of the scalar order parameter S, as in the two-dimensional case, allows us to obtain the fast timescale equations. The Euler–Lagrange equation of motion that minimizes the leading order scalar order parameter, S_0, is

$$\frac{\partial S_0}{\partial \tau_0} = -2{S_0}^3 + 3{S_0}^2 - T_0 S_0, \tag{4.3}$$

which can be solved for a steady uniaxial state to obtain

$$S_0 = \frac{3 + \sqrt{9 - 8T_0}}{4}. \tag{4.4}$$

Equation (4.4) defines the solution manifold in the five-dimensional component space. The critical points on this manifold are nondegenerate, providing T_0 is below the superheating limit, $T_0 = 9/8$ [18]. In terms of the component representation, the scalar order parameter is given by

$$S_0^2 = \sum_{n=1}^{5} a_n^2. \tag{4.5}$$

To fix the biaxiality order parameter to zero, we require

$$a_{1,0}^3 + 3a_{1,0}^2 \left(S_0 - a_{1,0}\right) + \frac{3\sqrt{3}}{2} \left[a_{2,0}\left(a_{4,0}^2 - a_{5,0}^2\right) + 2a_{3,0}a_{4,0}a_{5,0}\right] = S_0^3. \tag{4.6}$$

These two equations define a 3-manifold in the five-dimensional component space. However, as the leading order minimizers are uniaxial, there are only two undefined parameters which relate to the angles the liquid crystal makes with the coordinate axes. Therefore, as described in section 2.1, the 3-manifold corresponding to the biaxial stationary points must reduce to a 2-manifold, leading to a degeneracy in the first order correction. Specifically this allows us to determine only the direction of the major crystal axis uniquely.

4.2. Kernel of adjoint (tangent space). As in the two-dimensional case we now need to find the first order correction to the leading order terms which will determine the unique solution on the manifold. Motion across the manifold is determined by the first order perturbation L_m. The first order contribution from the bulk energy is invariant with respect to motion on the leading order manifold. Therefore, for the equation to have a nontrivial solution, we require that the perturbation L_m be orthogonal to the kernel of $\mathcal{H}$. As $\mathrm{Ker}(\mathcal{H}) = T_{\boldsymbol{a}}M_0$ the solvability condition is

$$L_m \frac{\partial a_{m,0}}{\partial s} = 0, \tag{4.7}$$

where s parameterizes motion along the tangent space to the manifold. The derivative of $a_{m,0}$ is found by considering the tensor $\mathcal{Q}_{ij}(0)$, which satisfies the perturbed Euler–Lagrange equations. The motion of $\mathcal{Q}_{ij}(0)$ along the manifold by rotation in a spherical coordinate system is defined by the rotation matrix $R_{ij}(s)$, which acts on $Q_{ij}(0)$ by the conjugacy action $\mathcal{Q}_{ij}(s) = R_{ip}(s)R_{jq}(s)\mathcal{Q}_{pq}(0)$. The rotation matrix $R_{ij}(s)$ is orthogonal, i.e., $R_{ik}(s)R_{jk}(s) = \delta_{ij}$ and $R_{ij}(0) = \delta_{ij}$. Motion along the manifold written in terms of the component representation is

$$a_{m,0}(s) = \left[T^{(m)}_{ji} R_{ip}(s) R_{jq}(s) T^{(l)}_{pq}\right] a_{l,0}(0). \tag{4.8}$$

The derivative of $a_{m,0}$ is found by differentiating (4.8) at $s = 0$:

$$\frac{\partial a_{m,0}}{\partial s} = T^{(m)}_{ji}\left[R'_{ip}(0)\delta_{jq}T^{(l)}_{pq} + \delta_{ip}R'_{jq}(0)T^{(l)}_{pq}\right] a_{l,0}(0). \tag{4.9}$$

To proceed we need to determine $R'_{ij}(0)$; this can be obtained by differentiating the identity $R_{ip}(s)R_{jp}(s) = \delta_{ij}$ at $s = 0$:

$$R'_{ip}(0)\delta_{jp} + \delta_{ip}R'_{jp}(0) = 0. \tag{4.10}$$

For this equation to be satisfied $R'_{ij}(0)$ must be a skewsymmetric tensor expressed on the basis $W^{(n)}$, defined as

$$\begin{aligned} W^{(1)} &= \frac{1}{\sqrt{2}}\left(\boldsymbol{e}_y \otimes \boldsymbol{e}_x - \boldsymbol{e}_x \otimes \boldsymbol{e}_y\right), \\ W^{(2)} &= \frac{1}{\sqrt{2}}\left(\boldsymbol{e}_x \otimes \boldsymbol{e}_z - \boldsymbol{e}_z \otimes \boldsymbol{e}_x\right), \\ W^{(3)} &= \frac{1}{\sqrt{2}}\left(\boldsymbol{e}_z \otimes \boldsymbol{e}_y - \boldsymbol{e}_y \otimes \boldsymbol{e}_z\right). \end{aligned} \tag{4.11}$$

For each $W^{(n)}$ we obtain a different $\partial a_{m,0}/\partial s$ and thus three vectors, $\boldsymbol{V}^{(n)}$, that span the kernel. The solvability conditions can be written as

$$L_m V^{(n)}_m = 0, \tag{4.12}$$

where the spanning vectors can be explicitly written as

$$V^{(n)}_m = T^{(m)}_{ki}\left(T^{(p)}_{ij}W^{(n)}_{jk} - W^{(n)}_{ij}T^{(p)}_{jk}\right) a_{p,0}, \tag{4.13}$$

In terms of the $O(\eta^0)$ components the spanning vectors $\boldsymbol{V}^{(n)}$ formed by each $W^{(n)}$ are

$$\boldsymbol{V}^{(1)} = \begin{pmatrix} 0 \\ -2a_{3,0} \\ 2a_{2,0} \\ -a_{5,0} \\ a_{4,0} \end{pmatrix}, \quad \boldsymbol{V}^{(2)} = \begin{pmatrix} -\sqrt{3}a_{4,0} \\ a_{4,0} \\ a_{5,0} \\ \sqrt{3}a_{1,0} - a_{2,0} \\ -a_{3,0} \end{pmatrix}, \quad \boldsymbol{V}^{(3)} = \begin{pmatrix} \sqrt{3}a_{5,0} \\ a_{5,0} \\ -a_{4,0} \\ a_{3,0} \\ -\sqrt{3}a_{1,0} - a_{2,0} \end{pmatrix}. \tag{4.14}$$

The first order equations require (4.12) to be satisfied in the direction of each spanning vector. This gives us three equations, one for each of the skewsymmetric tensors $W^{(n)}$. Substituting (4.2) into (4.12), the time-dependent equations are obtained:

$$V_m^{(n)} \frac{\partial}{\partial \tau_1} a_{m,0} = V_m^{(n)} \Big(\nabla^2 a_{m,0} + \chi e_m \Big), \tag{4.15}$$

where $m = 1, \dots, 5$.

4.3. How to solve equations/parameterization of equations. Equations (4.15) describe the dynamics of the critical point structure on the generic 3-manifold. However, as the bulk minimizers are uniaxial, these 3 equations must reduce to 2 corresponding to the reduction in the dimension of the manifold. Using guidance from the two-dimensional case we exploit the $SO(3)$ invariance of the bulk energy and parameterize the component representation $\boldsymbol{a}_0$ in terms of the uniaxial $\mathcal{Q}$-tensor with principal axis defined by the spherical coordinate angles $[\theta, \phi]$:

$$\boldsymbol{a}_0 = S_0 \begin{pmatrix} 1 - \frac{3}{2}\sin^2\theta \\ \frac{\sqrt{3}}{2}\sin^2\theta \left(2\cos^2\phi - 1\right) \\ \sqrt{3}\sin^2\theta\cos\phi\sin\phi \\ \sqrt{3}\cos\theta\sin\theta\sin\phi \\ \sqrt{3}\cos\theta\sin\theta\cos\phi \end{pmatrix}. \tag{4.16}$$

For a free energy which supports biaxial phases the appropriate representation for the component field would be a biaxial tensor expressed in terms of all three Euler angles. Substituting into (4.15), we can simplify the time derivatives to obtain equations for the time derivatives of θ and ϕ:

$$\begin{aligned} 3S_0^2 \frac{\partial\theta}{\partial\tau_1} &= \Big(\cos\phi V_m^{(2)} - \sin\phi V_m^{(3)}\Big)\Big(\nabla^2 a_{m,0} + \chi e_m\Big), \\ 3S_0^2 \frac{\partial\phi}{\partial\tau_1} &= \frac{1}{\sin^2\theta} V_m^{(1)} \Big(\nabla^2 a_{m,0} + \chi e_m\Big). \end{aligned} \tag{4.17}$$

These can be used to describe the time-dependent liquid crystal alignment in all cases except where the liquid crystal is aligned close to the coordinate singularity $\theta = 0, \pi$. If this is the case, then we need to use a multigrid method [23]. We choose a different set of coordinates $(\tilde{\theta}, \tilde{\phi})$, formed by rotating the existing coordinates about the y axis. This second coordinate system produces a set of components which give time-dependent equations:

$$
\begin{aligned}
3S_0^2 \frac{\partial \tilde{\theta}}{\partial \tau_1} &= \left(\cos\tilde{\phi} V_m^{(2)} - \sin\tilde{\phi} V_m^{(1)}\right)\left(\nabla^2 a_{m,0} + \chi e_m\right), \\
3S_0^2 \frac{\partial \tilde{\phi}}{\partial \tau_1} &= -\frac{1}{\sin^2\tilde{\theta}} V_m^{(3)}\left(\nabla^2 a_{m,0} + \chi e_m\right).
\end{aligned} \tag{4.18}
$$

The second coordinate system is singular at $\tilde{\theta} = 0, \pi$, equivalent to $\theta = \pi/2$ and $\phi = 0, \pi$. As such the two coordinate systems cannot be simultaneously singular for a given director. Using the different coordinate systems, the time derivatives of $a_{p,0}$ can be found from the least singular coordinate system as either

$$
\frac{\partial a_p}{\partial \tau_1} = V_p^{(1)} \frac{\partial \phi}{\partial \tau_1} - \left(\sin\phi V_p^{(3)} - \cos\phi V_p^{(2)}\right)\frac{\partial \theta}{\partial \tau_1} \tag{4.19a}
$$

or

$$
\frac{\partial a_p}{\partial \tau_1} = -V_p^{(3)} \frac{\partial \tilde{\phi}}{\partial \tau_1} + \left(\cos\tilde{\phi} V_p^{(2)} - \sin\tilde{\phi} V_p^{(1)}\right)\frac{\partial \tilde{\theta}}{\partial \tau_1}. \tag{4.19b}
$$

The strength of the singularity in each coordinate system is determined by the size of θ and $\tilde{\theta}$. This can be directly measured from the size of the x and z components of the director. An appropriate choice of representation, chosen arbitrarily to allow for some overlap between the two, is to use $[\theta, \phi]$ if $|n_z| \leq 4/(3\sqrt{2})$ and $[\tilde{\theta}, \tilde{\phi}]$ if $|n_x| \leq 4/(3\sqrt{2})$. If both of these conditions are satisfied, an average value of $\partial a_p/\partial \tau_1$ obtained from each of the two representations is used.

4.4. Order one accuracy check. As in the two-dimensional case, we wish to determine the correction to the scalar order parameter as an approximation of the accuracy of our method. Unlike the two-dimensional case an analytic expression cannot be obtained. Instead we use the method of singular value decomposition. Given the degenerate $O(\eta)$ equation $\mathcal{H}\boldsymbol{a}_1 = \boldsymbol{L}$, we calculate the perturbed manifold M_1 corresponding to the $O(\eta)$ correction to the components $\boldsymbol{a}_1$, where

$$
\begin{aligned}
\mathcal{H}_{11} &= (4a_{1,0} - 6)a_{1,0} + T_0 + 2\textstyle\sum_{n=1}^4 a_{n,0}^2, \\
\mathcal{H}_{22} &= 4a_{2,0}^2 + 6a_{1,0} + T_0 + 2\textstyle\sum_{n=1}^4 a_{n,0}^2, \\
\mathcal{H}_{33} &= 4a_{3,0}^2 + 6a_{1,0} + T_0 + 2\textstyle\sum_{n=1}^4 a_{n,0}^2, \\
\mathcal{H}_{44} &= 4a_{4,0}^2 - 3a_{1,0} - 3\sqrt{3}a_{2,0} + T_0 + 2\textstyle\sum_{n=1}^4 a_{n,0}^2, \\
\mathcal{H}_{55} &= 4a_{5,0}^2 - 3a_{1,0} + 3\sqrt{3}a_{2,0} + T_0 + 2\textstyle\sum_{n=1}^4 a_{n,0}^2,
\end{aligned}
$$

$$
\begin{aligned}
\mathcal{H}_{12} &= (6 + 4a_{1,0})a_{2,0}, & \mathcal{H}_{24} &= (4a_{2,0} - 3\sqrt{3})a_{4,0}, \\
\mathcal{H}_{13} &= (6 + 4a_{1,0})a_{3,0}, & \mathcal{H}_{25} &= (4a_{2,0} + 3\sqrt{3})a_{5,0}, \\
\mathcal{H}_{14} &= (4a_{1,0} - 3)a_{4,0}, & \mathcal{H}_{34} &= 4a_{3,0}a_{4,0} - 3\sqrt{3}a_{5,0}, \\
\mathcal{H}_{15} &= (4a_{1,0} - 3)a_{5,0}, & \mathcal{H}_{35} &= 4a_{3,0}a_{5,0} - 3\sqrt{3}a_{4,0}, \\
\mathcal{H}_{23} &= 4a_{2,0}a_{3,0}, & \mathcal{H}_{45} &= 4a_{4,0}a_{5,0} - 3\sqrt{3}a_{3,0},
\end{aligned}
$$

and $\mathcal{H}_{ij} = \mathcal{H}_{ji}$. The order parameter correction S_1 is then determined from the components of $\boldsymbol{a}_1$ orthogonal to the manifold, $S_1 = \boldsymbol{a}_0 \cdot \boldsymbol{a}_1/S_0$.

TABLE 1

Numerical values of nondimensional constants for a typical photorefractive liquid crystal cell.

$K = 20 \times 10^{-12}\text{N}$	$\epsilon_\perp = 4.1$	$\zeta = 0.037\text{Pa s}$
$A = 0.13 \times 10^6\text{J K}^{-1}\text{m}^{-3}$	$S = 3.65\hat{S}$	$\tau_d = 2.56 \times 10^{-7}\text{s}$
$B = 1.6 \times 10^6\text{Jm}^{-3}$	$L = 6.05 \times 10^{-12}\text{N}$	$\xi_0^2 = 4.39 \times 10^{-7}$
$C = 3.9 \times 10^6\text{Jm}^{-3}$	$L_x = 12 \times 10^{-6}\text{m}$	$\chi_a = 5.13 \times 10^{-6}\psi_0^2$
$T_0 = -10$	$L_z = 12 \times 10^{-6}\text{m}$	$\chi_I = 3.25 \times 10^{-5}\psi_0^2$
$\epsilon_\parallel = 9.1$	$\gamma_1 = 0.081\text{Pa s}$	$\psi_0 = 1\text{V}$

5. Examples.

To demonstrate the use of the nonstiff approximate liquid crystal equations, we consider a planar cell filled with liquid crystals. A spatially periodic voltage is applied to one boundary, while the other is set to a uniform zero volts. This is a realistic model for a photorefractive liquid crystal cell [6, 4], a device used for optical coupling and as an optically addressable spatial light modulator. This is an interesting device for testing this algorithm as it allows for three-dimensional orientation of the liquid crystal directors and has a simple geometry.

Under appropriate conditions the test geometry is a square in the x, z plane. Periodic conditions are imposed in the x direction such that $\boldsymbol{a}(x + L_x, z) = \boldsymbol{a}(x, z)$, and Dirichlet boundary conditions, corresponding to infinite anchoring strength, are imposed at $z = 0$ and $z = L_z$. The liquid crystal is aligned by application of a spatially modulated voltage $\psi(x, L_z) = \psi_a \sin^2(\pi x/L_x)$ at one boundary, where ψ_a is the applied voltage amplitude, while the other is earthed, $\psi(x, 0) = 0$.

First we verify the two-dimensional liquid crystal model derived in section 3. This is done through comparison to the full stiff time-dependent $\mathcal{Q}$-tensor equations and through comparison to a time-dependent FO model. In this case the director orientation is restricted to the x, z plane by the planar, in plane boundary conditions. As is typical, due to the alignment layers used in these cells, a small pretilt is applied at $z = L_z$. The parameters used in our simulation are given in Table 1. The spatial derivatives are calculated using a pseudospectral method [24] and, for ease of implementation, the time derivative is calculated using the MATLAB multistep solver ODE113. A public domain version of the MATLAB code is available at [5].

The FO model is derived by minimizing the FO free energy [8, 20],

$$\tilde{\mathcal{F}}_{FO} = \frac{K}{2}(\boldsymbol{\nabla}\theta_{FO})^2 - \frac{1}{2}\epsilon_0\epsilon_u(\tilde{\boldsymbol{E}})^2 - \frac{1}{2}\epsilon_0\Delta\epsilon\left(\hat{\boldsymbol{n}} \cdot \tilde{\boldsymbol{E}}\right)^2, \tag{5.1}$$

in terms of the director angle θ_{FO},

$$\frac{\partial\theta_{FO}}{\partial\tau_{FO}} = \nabla^2\theta_{FO} + \frac{1}{2}\delta_1\left[\sin 2\theta_{FO}\left(E_x^2 - E_z^2\right) + 2\cos 2\theta_{FO}E_xE_z\right], \tag{5.2}$$

where $\delta_1 = (\epsilon_0\Delta\epsilon/K)\psi_0^2$ and $\tau_{FO} = t\left[K/(L_x^2\gamma_1)\right]$. Starting from the same initial conditions, the FO and $\mathcal{Q}$-tensor models are integrated till steady state is reached. The resulting configurations are compared and the differences are computed.

First we compare the FO model with the approximate $\mathcal{Q}$-tensor model. We observe that there is an area of the FO model which does not show good agreement with the $\mathcal{Q}$-tensor model. By plotting the resulting director field as vectors and comparing the numerical gradient, it can be seen that these errors correspond to the points where the FO model predicts unphysical gradients; see Figure 2.

Similarly we can compare the full stiff $\mathcal{Q}$-tensor equations with the nonstiff approximate equations derived in section 3. Figure 3 shows a plot of the error in the

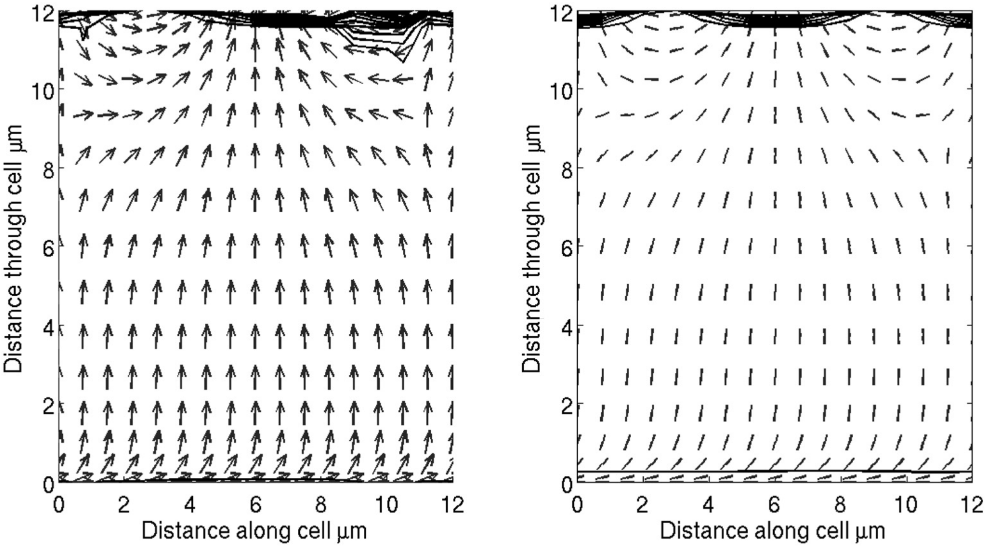

FIG. 2. *Comparison of liquid crystal alignment. The left and right images show the director alignment for the FO model and the approximate Q-tensor model, respectively. Director fields for both models are plotted, contour lines show areas of equal elastic energy,* $|\boldsymbol{\nabla}\theta_{FO}|^2 = C$ *in the FO model, and* $|\boldsymbol{\nabla a}|^2 = C$ *in the Landau–de Gennes model. The inaccuracy of the FO model can be seen in the asymmetry of* $|\boldsymbol{\nabla}\theta_{FO}|^2$ *near the boundary.*

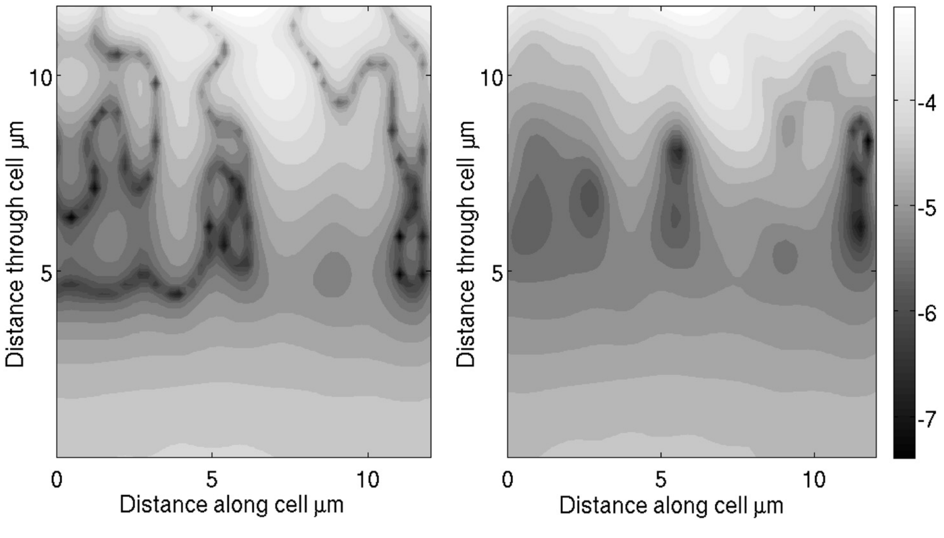

FIG. 3. *Two-dimensional director field error calculation for a* 10 *volt spatially modulated electric field plotted on a logarithmic scale. The liquid crystal has strong planar anchoring boundary conditions at* $z = 0$ *and* $z = L_z$ *and periodic boundary conditions in the* x *direction. The error is calculated both through calculation of the correction to the scalar order parameter* S_1/S_0 *(left) and through comparison to the full stiff equations* δa *(right).*

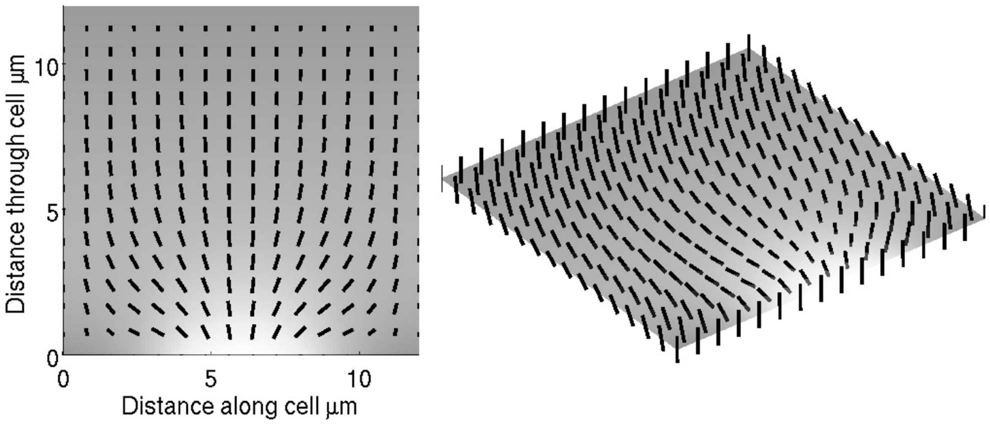

FIG. 4. *Typical director field plot calculated using approximate equations for a* 5 *volt spatially modulated electric field. The shading corresponds to the voltage throughout the cell. The liquid crystal alignment is parallel to the surface but twisted out of plane. This forces full three-dimensional orientation of the liquid crystal when subject to a spatially modulated electric field.*

approximate equation calculated using both the first order correction to the order parameter, (3.11), and the difference in the two simulations divided by the leading order scalar order parameter, (3.7),

$$\delta a = \frac{1}{S_0} \left|\left|\boldsymbol{a}_{approx} - \boldsymbol{a}_{stiff}\right|\right| . \tag{5.3}$$

Not only is the error very low, but when the two error plots are compared it can be seen that the approximate error is qualitatively comparable with the difference between the full stiff equations and the approximations derived here. In both plots the error peaks around the points of highest liquid crystal variation. This is expected, as these points correspond to those with highest elastic energy.

Second we compare the three-dimensional model, derived in section 4, with the full stiff $\mathcal{Q}$-tensor model. In this case the boundary conditions fix the director out of plane in the y direction to allow for full three-dimensional reorientation.

The steady state alignment results are shown in Figure 4. The comparison to the full stiff equations is shown in Figure 5 with error calculated using both the correction to the scalar order parameter, calculated using singular value decomposition, and the percentage error given in (5.3), where S_0 for the three-dimensional case is given in (4.4). Again it can be seen that the difference between the two methods is very low and that the error approximation using the singular value decomposition method is comparable to the true error. We find for the same number of grid points, 12 in each spatial dimension, that the stiff code takes over an hour to converge, while the approximate code converges to a solution with $\delta a \sim O(10^{-4})$ in a time of $\approx$45 seconds.

6. Conclusion. The approximate equations derived in this paper determine the liquid crystal alignment, which minimizes the Landau–de Gennes free energy in the absence of defects. They can be solved in a fraction of the time required to solve the full stiff equations.

We have derived equations for both a two- and three-dimensional case and have implemented both as nonstiff initial value problems in MATLAB. Estimates of the accuracy of these equations have been derived in terms of the first order correction

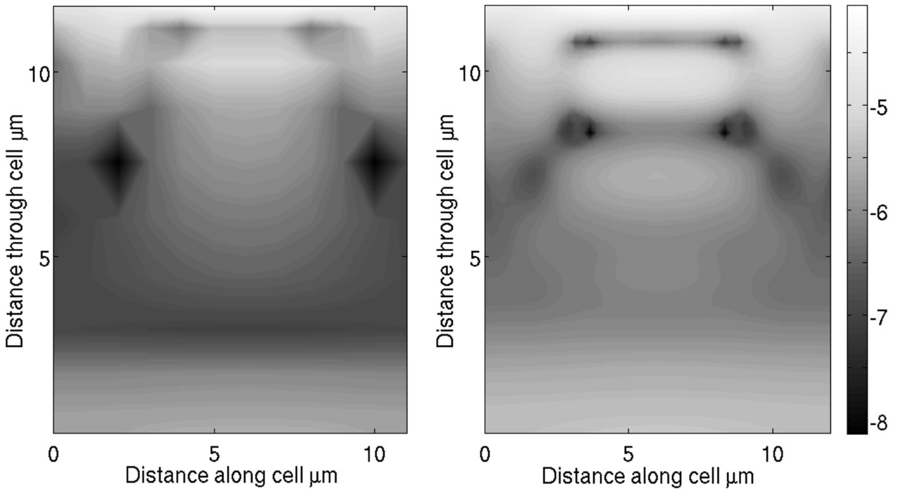

FIG. 5. *Three-dimensional director field error calculation for a* 5 *volt spatially modulated electric field plotted on a logarithmic scale. The liquid crystal has strong out-of-plane anchoring boundary conditions at* $z = 0$ *and* $z = L_z$ *and periodic boundary conditions in the* x *direction. The error is calculated both through calculation of the correction to the scalar order parameter* S_1/S_0 *(left) and through comparison to the full stiff equations* δa *(right).*

to the component values and have been shown to give strong qualitative agreement with the deviation of the approximation from the full stiff equations.

It should be noted that the free energy functions used in this paper are the simplest possible forms of the free energy. However, generalization to other free energy functions, whose bulk energy minimizers are uniaxial, is relatively straightforward. Generalizing this method to situations where the free energy supports biaxial states is also possible. In this case M_0 is a 3-manifold and expressions must be found for the equations of motion using a biaxial tensor representation with major and minor axes determined using all three Euler angles.

The major advantage of these equations with respect to the full stiff minimizers is that they can be computed in a fraction of the time while producing results with error $\sim O(10^{-4})$. This will be of great importance in medium- to large-scale models where computational efficiency becomes an issue. The assumption that the elastic and electrostatic free energies remain small makes these equations suitable for geometries in which defects do not occur. As such these approximate equations will be of most use in applications where defects are undesirable. This is the case in many optical devices where smooth alignment of the liquid crystal is important, but the FO model predicts nonphysical configurations.

Acknowledgments. The authors would like to thank Dr. David Chillingworth, Dr. Ian Hawke, Prof. Tim Sluckin, and Mr. Richard Slessor for helpful discussions and suggestions.

REFERENCES

[1] B. BAHADUR, *Liquid Crystals: Applications and Uses*, World Scientific, River Edge, NJ, 1990.
[2] G. CAPRIZ AND P. PODIO GUIDUGLI, *On Signorini's perturbation method in finite elasticity*, Arch. Rational Mech. Anal., 57 (1974), pp. 1–30.

[3] D. R. J. Chillingworth, *The Signorini perturbation scheme in an abstract setting*, Proc. Roy. Soc. Edinburgh Sect. A, 119 (1991), pp. 373–395.

[4] G. Cook, C. A. Wyres, M. J. Deer, and D. C. Jones, *Hybrid organic-inorganic photorefractives*, Proc. SPIE, 5213 (2003), pp. 63–77.

[5] K. R. Daly and G. D'Alessandro, *Homepage of the Defect Free Q-Tensor Approximation Code*, http://www.personal.soton.ac.uk/dales/DFQTA/.

[6] K. R. Daly, G. D'Alessandro, and M. Kaczmarek, *Regime independent coupled-wave equations in anisotropic photorefractive media*, Appl. Phys. B Lasers Opt., 95 (2009), pp. 589–596.

[7] P. G. de Gennes and J. Prost, *The Physics of Liquid Crystals*, 2nd ed., Oxford University Press, New York, 1993.

[8] F. C. Frank, *On the theory of liquid crystals*, Discuss. Faraday Soc., 25 (1958), pp. 19–28.

[9] M. Golubitsky and D. G. Schaeffer, *A discussion of symmetry and symmetry breaking*, in Singularities, Part 1 (Arcata, CA, 1981), Proc. Symp. Pure Math. 40, AMS, Providence, RI, 1983, pp. 499–515.

[10] G. Grioli, *Mathematical Theory of Elastic Equilibrium (Recent Results)*, Springer-Verlag, Berlin, 1962.

[11] M. Hiroyuki, E. C. Gartland, Jr., J. R. Kelly, and J. Philip, *Multidimensional director modeling using the Q tensor representation in a liquid crystal cell and its application to the π cell with patterned electrodes*, Japan. J. Appl. Phys., 38 (1999), pp. 135–146.

[12] R. James, E. Willman, F. A. Fernández, and S. E. Day, *Finite-element modeling of liquid-crystal hydrodynamics with a variable degree of order*, IEEE Trans. Electron Devices, 53 (2006), pp. 1575–1582.

[13] J. Katriel, G. F. Kventsel, G. R. Luckhurst, and T. J. Sluckin, *Free energies in the Landau and molecular field approaches*, Liq. Cryst., 1 (1986), pp. 337–355.

[14] I.-C. Khoo, *Liquid Crystals*, Wiley Ser. Pure Appl. Optics, John Wiley, Hoboken, NJ, 2007.

[15] L. Longa, D. Monselesan, and H. R. Trebin, *An extension of the Landau-Ginzburg-de Gennes theory for liquid crystals*, Liq. Cryst., 2 (1987), pp. 769–796.

[16] L. Longa and H. R. Trebin, *Integrity basis approach to the elastic free energy functional of liquid crystals*, Liq. Cryst., 5 (1989), pp. 617–622.

[17] A. Majumdar, *Equilibrium order parameters of liquid crystals in the Landau-De Gennes theory*, European J. Appl. Math., 21 (2010), pp. 181–203.

[18] S. Mkaddem and E. C. Gartland, *Fine structure of defects in radial nematic droplets*, Phys. Rev. E, 62 (2000), pp. 6694–6705.

[19] N. Mukohzaka, N. Yoshida, H. Toyoda, Y. Kobayashi, and T. Hara, *Diffraction efficiency analysis of a parallel-aligned nematic-liquid-crystal spatial light modulator*, Appl. Opt., 33 (1994), pp. 2804–2811.

[20] C. W. Oseen, *The theory of liquid crystals*, Trans. Faraday Soc., 29 (1933), pp. 883–899.

[21] A. Signorini, *Sulle deformazioni termoelastiche finite*, in Proceedings 3rd International Congress for Applied Mechanics, Vol. 2, 1930, pp. 80–89.

[22] A. Sonnet, A. Kilian, and S. Hess, *Alignment tensor versus director: Description of defects in nematic liquid crystals*, Phys. Rev. E, 52 (1995), pp. 718–722.

[23] J. F. Thompson, Z. U. A. Warsi, and C. W. Mastin, *Numerical Grid Generation: Foundations and Applications*, North–Holland, Amsterdam, 1985.

[24] L. N. Trefethen, *Spectral Methods in MATLAB*, SIAM, Philadelphia, 2000.

[25] G. V. Prakash, M. Kaczmarek, A. Dyadyusha, J. J. Baumberg, and G. D'Alessandro, *Control of topological defects in microstructured liquid crystal cells*, Opt. Express, 13 (2005), pp. 2201–2209.

[26] Y. H. Wan and J. E. Marsden, *Symmetry and bifurcation in three-dimensional elasticity.* III. *Stressed reference configurations*, Arch. Rational Mech. Anal., 84 (1983), pp. 203–233.

[27] E. Willman, F. A. Fernandez, R. James, and S. E. Day, *Modeling of weak anisotropic anchoring of nematic liquid crystals in the Landau–de Gennes theory*, IEEE Trans. Electron Devices, 54 (2007), pp. 2630–2637.

Two-beam coupling in nematic crystals with an applied AC field

Mark Herrington,[1*] Keith Daly[2], Oleksandr Buchnev,[1] Giampaolo D'Alessandro[2] and Malgosia Kaczmarek[1]

[1] *School of Physics and Astronomy, Southampton University,*
University Road, Highfield, Southampton, Hampshire, SO17 1BJ, UK
[2] *School of Mathematics, Southampton University,*
University Road, Highfield, Southampton, Hampshire, SO17 1BJ, UK
[*] *Corresponding author: mrh203@soton.ac.uk*

Compiled October 1, 2010

We report the first measurement of two beam coupling in a photorefractive liquid crystal cell with low frequency (1-10 Hz) applied AC field. The gain measured is larger than that observed at equivalent DC fields. A simple impedance ladder model is used to interpret the observed effect of the incident light and AC field. © 2010 Optical Society of America

OCIS codes: 000.0000, 999.9999.

Two beam coupling is a widely studied effect and has applications in holographic data storage and spatial light modulators [1]. It was originally investigated in photorefractive crystals [2], where an interference pattern can create a space charge field in the crystal bulk and via the electro-optic effect modulate the refractive index. This refractive index grating is responsible for two beam coupling. The natural birefringence of liquid crystals makes them highly desirable for two beam coupling: reorienting the liquid crystal molecules with an electric field can lead to a strong refractive index grating and, hence, to large beam coupling gain. This has been achieved by applying a DC field either to liquid crystal systems with photoconductive layers [3, 4] or to liquid crystal doped in the bulk with photosensitive molecules such as fullerenes or dyes [5]. These systems are: cheaper to manufacture than a photorefractive crystal; have comparable gain, which, furthermore, can be enhanced with the addition of ferroelectric nanoparticles [6]; and can operate at low beam intensities. Unfortunately, a long exposure to a DC field can degrade the liquid crystals or the alignment layers, limiting the lifetime of the cells. Therefore, there is a clear need to couple beams without an applied DC field. This has been achieved, for example, by replacing the photoconductive layer with a thin photorefractive window [7]. In this case, the space charge field in the photorefractive crystal applies a modulated electric field to the liquid crystal. However, while the photorefractive windows used in such systems lead to high gain, they are also expensive. In this letter we investigate using a photoconductive alignment layer and an applied sinusoidal AC field to remove the need for expensive photorefractive windows or for an applied DC field. We have measured efficient coupling resulting in significant gain coefficients. Unlike other liquid crystal devices such as SLMs or displays, where a high frequency AC field is applied (tens to hundreds of Hz), we focus here on very low frequencies, between 1 and 10 Hz. The gain measured in the Raman-Nath regime is larger than that generated with an applied DC field.

The cell investigated was made from two ITO covered glass substrates. One was coated with a polyimide (PI) layer and the second with photoconductive polyvinyl carbazole doped with fullerenes (PVK:C60). The substrates were rubbed, separated by 12 μm spacers and filled with nematic liquid crystal E7 by capillary forces. The cell was placed in a standard two beam coupling experimental setup, shown schematically in Figure 1. The beam from the laser diode was split into two equal intensity beams (1mW) using a glass block and mirror (Labelled G and M in Figure 1). The beams were made to intersect in the centre of the cell tilted at 30 ° to the bisector of the incident beams. The angle between the beams was such that an interference pattern with a period of Λ=24μm formed on the cell surface. This long period grating ensures that the electric field penetrates through the whole cell [7]. The gain ratio is defined as $G = I_{B1+B2}/I_{B1-B2}$, where I_{B1+B2} is the intensity of beam 1 in the presence of beam 2 and I_{B1-B2} is the intensity of beam 1 in the absence of beam 2. The exponential gain coefficients is calculated using

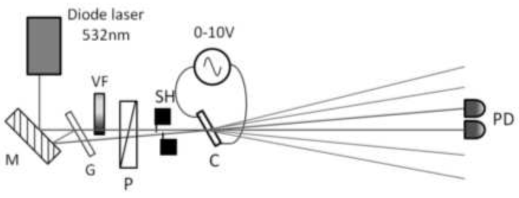

Fig. 1. Experimental set-up. M- Mirror G- Glass block VF- Variable P- Polariser ND filter SH- Shutters C- Cell PD- Photodiodes

$$\Gamma = \frac{1}{L}\ln\left(\frac{Gm}{m-G+1}\right), \qquad (1)$$

where L is the cell thickness and m is the ratio of intensities of the incident beams [8]. As we are interested in the magnitude of energy transfer it is important to ensure that m is close to 1.

With a sinusoidal AC field applied to the cell, whilst illuminated by the two beams, several diffracted orders were observed. This indicates that a diffraction grating in the Raman-Nath regime had formed within the cell. Measuring the gain coefficients shows that energy was transferred from one beam to the other, demonstrating that beam coupling was present. Measurements of the gain coefficients as a function of amplitude shows that below 3V there is no beam coupling with an AC or DC field (see Figure 2). By 4V there is measurable two beam coupling with both AC and DC applied fields. These results indicate the threshold for reorientation is between 3 V and 4 V and that it is not sensitive to frequency. At all applied frequencies of the AC field, the gain coefficients increase with increasing amplitude and appear to be reaching a peak at 10V. For every voltage above the threshold, gain coefficients were larger than those measured in DC. The peak DC gain coefficient, 44 cm^{-1}, was observed at 16V (see Table 1). The same gain coefficient could be achieved with AC field but at much lower amplitudes. For example, at 10Hz it is observed at only 6V and at 2Hz only 4V are required. The maximum gain coefficient observed is 134 cm^{-1} at 2Hz, approximately three times greater than the peak value measured in DC and approximately four and a half times greater than the DC gain coefficient at the same voltage. Once the amplitude of the applied AC exceeds the threshold, there is a very sharp transition to large gain coefficients (see Figure 3). The peak gain coefficient appears to shift slightly to higher frequencies with larger voltage values. While the gain coefficient decreases monotonically for frequencies higher than the peak gain frequency, it is still significantly higher than the DC gain even at 10Hz. For example, the data for 10V shows a peak at 134 cm^{-1} at 2Hz but then decays to 70 cm^{-1} by 10Hz. The data for 4V show the same trend with a peak of 50 cm^{-1} at 1Hz. By 5Hz the rate of decay has decreased, but, there is measurable gain up to 10Hz. The same trend has been observed in a second, validation, cell.

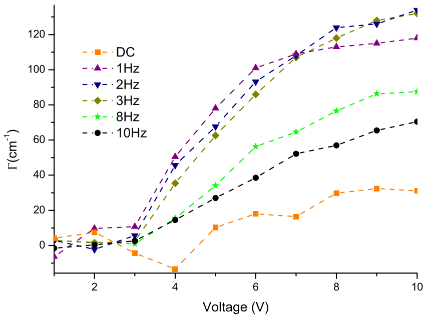

Fig. 2. Gain coefficient vs Amplitude for different applied frequencies.

Table 1. Amplitude necessary to observe the largest DC gain of 44 cm^{-1}

Frequency (Hz)	Voltage(V)	Shift
0	16	N/A
1	3.8	12.2
2	4	12
3	4.3	11.7
8	5.5	10.5
10	6.5	9.5

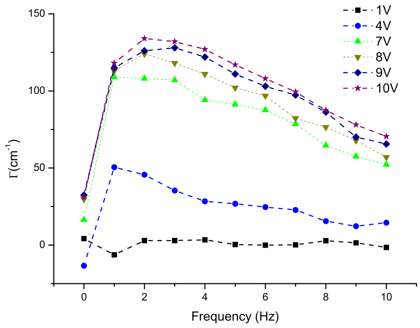

Fig. 3. Gain coefficient vs Amplitude for different applied frequencies.

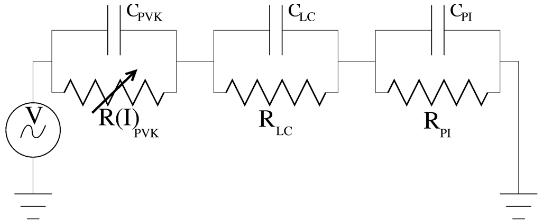

Fig. 4. Equivalent circuit for liquid crystal cell.

The reorientation of the liquid crystal and, hence, the strength of the observed diffraction is strongly related to the voltage drop across the liquid crystal layer. Factors affecting this voltage drop include: the presence of ions in the liquid crystal layer, the relative impedance of each layer and the frequency of the applied field. For an AC field, even of low frequency, the motion of ions is greatly reduced [9]. We can provide a semi-quantitative explaination of the gain vs frequency behaviour using a simple toy model of the electrical coupling between the layers [10]. Here we model each layer in the cell as a simple RC circuit as shown in Figure 4. This circuit captures the majority of the cells electrical behaviour under the assumption that the slow AC field eliminates the ion motion. The impedance of each layer is given by

$$Z_j = \frac{R_j}{i\omega R_j C_j + 1}, \tag{2}$$

where $R_j = L_j/(\sigma_j A)$ and $C_j = \epsilon_0 \epsilon_j A/L_j$. Here A is the cell area, ϵ_0 is the permittivity of free space, σ_j, ϵ_j and L_j are the conductance, relative permittivity and thickness of layer j, with $j = \{LC, PI, PVK\}$. The values of σ_j and ϵ_j and the resulting values for C_j and R_j for $A = 4 \cdot 10^{-4} m^2$ are summarised in Table 2. Note, the exact value of σ_{LC} is not accurately known and varies with different liquid crystal samples. Therefore, we consider a range of liquid crystal conductances. The dielectric constant of the liquid crystal corresponds to planar aligned E7.

The steady state voltage across the liquid crystal layer V_{LC} as a function of the applied voltage V is given by $V_{LC} = VZ_{LC}/(Z_{LC} + Z_{PI} + Z_{PVK})$. We calculate the effect

Table 2. Parameter values for a typical photorefractive liquid crystal cell.

Layer	$L_j(nm)$	$\sigma_j(S/m)$	ϵ_j
LC	$12 \cdot 10^3$	10^{-5}–10^{-10}	5–20
PI [11]	20	10^{-14}	3.4
PVK [12]	200	10^{-13}	5

of a small, intensity dependent, modulation in the resistance of the PVK on the voltage dropped across the liquid crystal layer. We assume that the resistance of the PVK is $R_{PVK} = R_{PVK}\left[1 + \eta\beta(I)\right]$, where $\beta(I)$ is the intensity dependent part of the PVK resistance, $\eta \ll 1$ and I is the optical intensity at the PVK layer. In the limit $\omega = 0$ the voltage drop is determined entirely resistively

$$V_{LC} = V\frac{R_{LC}}{R_{tot}}\left[1 - \frac{R_{PVK}}{R_{tot}}\eta\beta(I)\right] + O(\eta^2), \tag{3}$$

where $R_{tot} = R_{LC}+R_{PI}+R_{PVK}$. Typically, as $R_{lc} \ll R_{PI} \simeq R_{PVK}$, the voltage drop across the liquid crystal in the DC regime is very small. Similarly, if the frequency of the applied voltage is high enough, typically $\omega \gg 1/(C_jR_j)$ for all layers, then the voltage is determined entirely capacitively

$$V_{LC} = V\frac{C_{PVK}C_{PI}}{C_{PVK}C_{PI} + C_{PVK}C_{LC} + C_{LC}C_{PI}}. \tag{4}$$

In this case, as $C_{lc} \ll C_{PVK} \lesssim C_{PI}$, the voltage drop across the liquid crystal is large. However, as V$_{LC}$ is independent of the resistance of the photoconductor, no diffraction will take place. In the general case, relevant for the slow AC field

$$V_{LC} = V\frac{Z_{LC}}{Z_{tot}}\left[1 - \frac{Z_{PVK}}{Z_{tot}}\left(1 - iZ_{PVK}C_{PVK}\omega\right)\eta\beta(I)\right] + O(\eta^2), \tag{5}$$

where $Z_{tot} = Z_{LC} + Z_{PI} + Z_{PVK}$. The significance of equation (5) can be understood by plotting the coefficient of $\eta\beta(I)$ against ω for a range of liquid crystal conductances, see Figure 5. It can be seen that, although small, there is a broad peak in the amplitude of the modulation coefficient which narrows and increases in amplitude with the liquid crystal conductance. This suggests that there is a range of frequencies close to zero Hertz for which the diffraction efficiency of the liquid crystal cell is largest. We note that decreasing the conductance of the liquid crystal increases the range of frequencies over which $\beta(I)$ affects V$_{LC}$, whilst reducing the overall effect of the PVK. This analysis explains some of the features of the cells, clearly more work has to be done in optimising this system. Detailed modelling of charge motion, combined with a more thorough analysis of the electrical properties of the system, will be required to determine the ideal conditions for beam coupling assisted by an AC field.

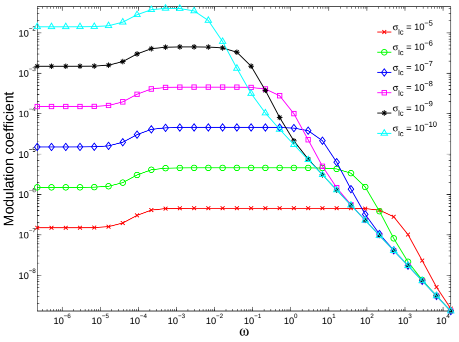

Fig. 5. Modulation coefficient at fix voltage for a planar aligned cell at different frequencies and for different liquid crystal conductances

In summary, efficient two beam coupling has been observed in the Raman-Nath regime in liquid crystal cells with PVK layer and with an applied sinusoidal AC field. A strong dependence of the gain coefficient on frequency was observed with a very sharp transition from the DC to the low frequency AC regime. The largest gain coefficient observed was $134cm^{-1}$ at 2Hz and 10V. There is a clear shift to lower amplitudes in case of an AC field, as compared with the DC regime, to achieve the same value of gain. Furthermore, higher coupling coefficients, up to a factor of three larger, have been observed with AC field than with DC field.A semi–quantitative explanation has been given, assuming the AC field reduces the effect of charge migration, in terms of an impedance ladder model.

Financial support was provided by COI MOD

References

1. U. Bortolozzo, S. Residori and J. P. Huignard, J. Phys. D: Appl. Phys. **41,** (2008)
2. D. L. Staebler and J. J. Amodei , J. Appl. Phys. **43,** (1972)
3. S. Bartkiewicz, K. Matczyszyn, A. Miniewicz and F. Kajzar, Opt. Commun. **187,** 257 (2001)
4. M. Kaczmarek, A. Dyadyusha, S. Slussarenko and I.C. Khoo, JAP **96,** 2616 (2004).
5. I.C. Khoo, Opt. Lett. **20,** 2137 1995
6. O. Buchnev, A. Dyadyusha, M. Kaczmarek, V. Reshetnyak and Y. Reznikov, J. Opt. Soc. Am. **24,** 1512 (2007)
7. G. Cook, C. Wyres, M. Deer and D. Jones, Proceedings of SPIE **5213, 63** (2003)
8. P. Yeh, Introduction to Photorefractive Nonlinear Optics, Wiley, New York, 1993.
9. A.R.M. Verschueren, R.A.H Niessen, P.H.L. Notten, W. Oepts and E.M.L. Alexander-Moonen, IEEE Transactions on Dielectrics and Electrical Insulation **10,** 963 (2003)
10. P. Aubourg, JP Huignard, M. Hareng, and RA Mullen, Applied Optics **21** 3706 (1982)
11. L. B. Rothman, J. Electrochem. Soc. **127** 2216 (1980)
12. S. Santos and C. Gómez and I. Salazar, Int. J. of Polym. Materials **51** 567 (2002)